UNIVERSITY OF CALIFONIA
RIVERSIDE

Spin Transport and Relaxation in Graphene and Germanium

A Dsissertation submitted in partial satisfaction
of the requirements for the degree of

Doctor of Philosophy

in

Physics

by

Wei Han

March 2012

Dissertation Committee:
Dr. Roland K. Kawakami, Chairperson
Dr. Jing Shi
Dr. Chun Ning (Jeanie) Lau

The Dissertation of Wei Han is approved:

_____

_____

_____

Committee Chairperson

University of California, Riverside

Acknowledgement

I want to express my gratitude to many people who have guided or helped me to make this work possible. First of all, I have to thank my advisor Roland K. Kawkami. It is truly my precious experience to be in his group. He is an excellent physicist and a good mentor for young graudate students. I thank him very much for the opportunity to be involved in his research on graphene spintronics. He has taught me how to think of new ideas and how to systematically approach these open questions. The two best lessons I learned from him are: 1) Keep things as simple as possible; 2) Not speak out on anything that I am unsure. I am sure the first lesson helped me make a lot of progress in the graphene spintronics. The second lesson personally helped me not foul myself or give "bad" guidence to other researchers. I also want to particaluly thank him for giving me many opportunites to addend different conferences.

I would like to specially thank Keyu Pi (Kyle), Wei-Hua Wang, and Yan Li for their guidence and training during my earlier PhD studies. Kyle taught me much about the MBE chamber, cleanroom techniques, and magetism. This knowledge opened the door of spintronics to me. Yan taught me about MBE and magnetism. Wei-Hua Wang passed his graphene spin valve knowledge to me. The best lesson I learned from him is that "always do something novel, never spend too much time developing the field that has been done for a long time". This lesson keeped me off a lot of "bad" research directions. I enjoyed working with them and I still remember all those late nights where we vented, pumped down the chamber or did ebeam liothography in the cleanroom.

I am also very greatful to Kathleen McCareay, Jared Wong, and Adrian Swartz. We are kind of the middle age of the lab. I enjoy working in the lab because their accompany. They are always available to discuss the projects with me and to help me with a lot of good ideas. My poor English gets better and better all due to their help. I still remember many times of my bugging them to read my papers, abstracts and emails. Also, I thank them very much for inviting me to their parties.

I would like to thank all of the other labmtaes: Hua Wen, Patrick Odenthal, Jen-Ru Chen, Renjing Zheng, Steven Tjung, Igor Pinchuk, George Christensen, Richard Chiang, Desalegne Teweldebrhan and Walid Amamou. Among them, Hua Wen and Jen-Ru Chen worked with me on some projects. I really enjoyed the time teaching them. They have been working very hard and contributed a lot to this work.

I want to give my spical thanks to our collabrators: Prof. Chun Ning (Jeanie) Lau at UCR, Prof. Kang L. Wang at UCLA and Prof. Jing Shi at UCR. Prof. Lau kindly provided us their graphene during the earlier years. I used her AFM for the study of growing smooth MgO film on top of graphite, which lead to the tunneling spin injection in graphene afterwards. Thanks very much to her students, Feng Miao, Wenzhong Bao, Gang Liu and Jairo Velasco Jr. We shared the experience of making graphene devices and I really enjoyed the discussion and “joking” with them in the cleanroom. Prof. Wang group (Yi Zhou, Faxian Xiu, Li-Te Chang, Jianshi Tang, and Xiaowei Jiang) and I worked on the spin transport in Germanium. From this collaboration, I gained a lot of knowledge of Ge shocttky barrier and Fermi pinning. Yi Zhou is a great researcher and

works very hard. I still remember the 3 weeks we worked on the nonlocal spin transport in Ge and the discussion at “University cafe” during lunch. Prof. Shi goup (Deqi Wang) and I worked on the spin transport in graphene with tunable mobilities together. Thanks very much for their magic molecue to make this project possible.

I would like to thank my dear friends in the physic department: Gang Liu, Feng Miao, Peng Wei, Deqi Wang, Ling Yang, Hsiang-Ku Lin, Yong Pu, Tao Lin, Xinfei Liu, Wenzhong Bao, Xiaoxiao He, Dong Gui, Dezheng Sun, Hang Zhang, et al. Among them, I would like to specially thank Wenzhong Bao, who has been my roommate for more than 3 years. I have been “pushed” by his hard working. Without him, I could not do this amount of work.

I also want to thank the technians in our cleanroom: Dong Yan, and Dexter Humphrey. Dong, sorry for calling you during the weekends and midnight.

I want to also thank Keyu Pi (Kyle) and Cece Chang for their organization of many road trips and backpacking trips. Thanks to Kyle for the amazing road trip to Chicago and many hiking trips. Thanks to Cece for several backpacking trips in the east serria, where I enjoyed the beauty and freedom of nature.

At the end, I would like to thank my parents for their love, which makes me always optimistic.

ABSTRACT OF THE DISSERATATION

Spin Transport and Relaxation in Graphene and Germanium

by

Wei Han

Doctor of Philosophy, Graduate Program in Physics
University of California, Riverside, March 2012
Dr. Roland Kawakami, Chairperson

In this thesis, I summarize our studies investigating the spin dependent properties of graphene over the last five years and the spin transport in germanium in the last three years.

In the field of graphene spintronics, this thesis includes three major advances in these fields. First, room temperature spin transport in single layer graphene (SLG) is achieved using transparent contacts (Co/SLG) and an electron-hole asymmetry of spin transport in SLG is observed. Second, tunneling spin injection into SLG is achieved using TiO2 seeded MgO barriers. A large non-local magnetoresistance (MR) of 130 ohms is observed at room temperature. Third, long spin lifetime in SLG and bilayer graphene (BLG) are observed. Furthermore, strongly contrasting behavior for SLG and BLG is observed, in which SLG is dominant by Elliot-Yafet (EY) spin relaxation at low

temperatures while In BLG is dominant by Dyakonov-Perel spin relaxation at low temperatures.

In the field of spin transport in germanium (Ge), this thesis includes growth of single-crystalline, atomically smooth MgO films on Ge(001) by molecular beam epitaxy, the origin of Fermi level pinning in Ge Schottky junctions using epitaxially grown ultrathin MgO films, and electrical spin injection and transport in Ge using both nonlocal and three terminal spin transport methods.

Table of contents

Chapter 1: Introduction 1

1.1 Spintronics 2

1.2 Lateral spin valves: from metals, semiconductors, organics to graphene 5

1.3 Graphene 14

1.4 Review of the work in graphene spintronics 16

1.5 Motivation and outlines 21

Chapter 2: Theoretical view of spin transport and relaxation 34

2.1 Electrical spin injection and detection 35

2.2 Calculation of the nonlocal MR 39

2.3 The relationship of local MR and nonlocal MR 45

2.4 Spin relaxation mechanisms 47

Chapter 3: Experimental techniques 53

3.1 Fabrication of graphene spin valves 54

3.2 Molecular beam epitaxy (MBE) 64

3.3 Electron beam lithography 66

3.4 The electrical measurements set up 68

Chapter 4: Spin injection and precession in single layer graphene 73

4.1 Introduction 74

4.2 Experiment details 75

4.3 Results and discussion 78

4.4 Conclusion 83

Chapter 5: Electron-hole asymmetry of spin injection and transport in single layer graphene 86

5.1 Introduction 87

5.2 Experiment details 88

5.3 Results and discussion 89

5.4 Conclusion 99

Chapter 6: Growth of atomically smooth MgO films on graphene by molecular beam epitaxy 102

6.1 Introduction 103

6.2 Experiment details 104

6.3 Results and discussion 105

6.4 Conclusion 113

Chapter 7: Tunneling spin injection into single layer graphene 116

7.1 Introduction 117

7.2 Experiment details 118

7.3 Characterization of the tunneling contact 119

7.4 Nonlocal MR and local MR measurement 122

7.5 Gate dependence of spin transport 127

7.6 Spin lifetime measurement with different contacts 133

7.7 Conclusion 136

Chapter 8: Spin relaxation in single layer and bilayer graphene 140

8.1 Introduction 141

8.2 Experiment details 142

8.3 Results and discussion 144

8.4 Conclusion 157

Chapter 9: Spin relaxation in single layer graphene with tunable mobilites 161

9.1 Introduction 162

9.2 Experiment details 163

9.3 Results and discussion 164

9.4 Conclusion 171

Chapter 10: Growth of single-crystalline, atomically smooth MgO films on Ge(001) by molecular beam epitaxy 174

10.1 Introduction 175

10.2 Experiment details 176

10.3 Results and discussion 178

10.4 Conclusion 185

Chapter 11: Investigate the origin of Fermi level pinning in Ge Schottky junctions using epitaxially grown ultrathin MgO films 189

11.1 Introduction 190

11.2 Experiment details 191

11.3 Results and discussion 192

11.4 Conclusion 199

Chapter 12: Electrical spin injection and transport in germanium. 202

12.1 Introduction 203

12.2 Experiment details 205

12.3 Nonlocal MR measurement. 206

12.4 Three-terminal Hanle measurement 216

12.5 Conclusion 220

List of figures

Fig. 1-1, spin-dependent density of states for (a) nonmagnetic materials and (b) ferromagnetic materials.. 2

Fig. 1-2, giant magetoresistance effect observed in thin-film structures 3

Fig. 1-3, tunneling magetoresistance effect observed in a magnetic tunnel junction 4

Fig. 1-4, lateral spin valves 5

Fig. 1-5, nonlocal spin transport in Al spin valve by Johnson and Silsbee 6

Fig. 1-6, electrical spin injection and accumulation in an Py/Cu/Py spin valve 7

Fig. 1-7, electrical spin transport in GaAs 9

Fig. 1-8, electrical spin transport in Si 11

Fig. 1-9, organic semiconductor spin valves 12

Fig. 1-10, electrical spin transport in carbon nanotube spin valve 13

Fig. 1-11, graphene band structure 15

Fig. 1-12, two pioneering work on graphene spintronics 17

Fig. 2-1, local and nonlocal MR measurement 36

Fig. 2-2, description of the background of the nonlocal MR 38

Fig. 2-3, the nonlocal MR calculation 39

Fig. 2-4, the relationship of local MR and nonlocal MR 46

Fig. 2-5, spin relaxation mechanisms 48

Fig. 3-1, characterization of the graphene thickness 55

Fig. 3-2, alignment marks 57

Fig. 3-3, the image of graphene in the alignment marks 57

Fig. 3-4, NPGS design of the graphene spin vale pattern 58

Fig. 3-5, characterization of the undercut formed by the bilayer ebeam resist 59

Fig. 3-6, transparent contacts (Co/SLG) and tunneling contacts (Co/MgO, TiO_2/SLG) . 60

Fig. 3-7, fabrication of graphene spin valve for spin relaxation study 64

Fig. 3-8, MBE 64

Fig. 3-9, the example of an EBL process 66

Fig. 3-10, the electrical measurement setup 68

Fig. 3-11, the electrical measurement geometries 69

Fig. 3-12, the nonlocal MR measurement 70

Fig. 3-13, the nonlocal MR background as a function of the frequency for graphene spin valve with transparent contacts 71

Fig. 4-1, graphene spin valves with transparent contacts 76

Fig. 4-2, electrical characteristics of the SLG spin valves with transparent contacts 77

Fig. 4-3, nonlocal MR of SLG spin valves with transparent contacts 80

Fig. 4-4, Hanle spin precession 81

Fig. 5-1, graphene spin valves 89

Fig. 5-2, electrical characteristics and non-local MR scans of samples A and sample B 91

Fig. 5-3, nonlocal MR as a function of gate voltage 93

Fig. 5-4, electron-hole asymmetry 94

Fig. 5-5, sign reversal of nonlocal MR as a function of bias current for sample B 96

Fig. 5-6, bias dependence in GaAs, Al, Si, graphene spin valves 97

Fig. 5-7, origin of the electron-hole asymmetry 98

Fig. 6-1, the role of surface diffusion on MgO film morphology 106

Fig. 6-2, morphology of MgO films grown on HOPG dressed by Ti atoms 108

Fig. 6-3, MgO films grown on HOPG without or with seeding Ti atoms 109

Fig. 6-4, the rms roughness of 1 nm MgO films as a function of Ti coverage 111

Fig. 6-5, MgO film on single layer graphene 112

Fig. 7-1, tunneling contact for graphene spin valve 119

Fig. 7-2, electrical characterization of the tunneling contact 120

Fig. 7-3, nonlocal MR for SLG spin valve with tunneling contacts 124

Fig. 7-4, nonlocal and local MR for SLG spin valve with tunneling contacts at 4K . . . 126

Fig. 7-5, predictions of the drift-diffusion theory of spin transport 128

Fig. 7-6, gate dependence of the nonlocal MR at 300 K and 4 K 131

Fig. 7-7, gate dependence of the nonlocal MR at 300K for SLG spin valves with transparent contacts (a) and pinhole contacts (b) 132

Fig. 7-8, Hanle spin precession for SLG spin valves with different contacts. 135

Fig. 8-1, device fabrication 143

Fig. 8-2, measurement of spin transport and spin relaxation 145

Fig. 8-3, gate dependence of SLG spin valves 148

Fig. 8-4, temperature dependence of SLG spin valves 149

Fig. 8-5, bilayer graphene 150

Fig. 8-6, gate dependence of BLG spin valves 152

Fig. 8-7, temperature dependence of BLG spin valves 153

Fig. 8-8, gate dependence of BLG spin valves (device C) 155

Fig. 9-1, Hanle spin precession 165

Fig. 9-2, electrical properties of SLG after iron oxide NPs doping 166

Fig. 9-3, electrical properties of SLG after iron oxide NPs doping at 10 K 168

Fig. 9-4, spin depentdent properties of the same SLG spin valve (device A) with different mobilities measured from Hanle spin precession at 10 K 169

Fig. 9-5, spin lifetimes of the same SLG spin valve (device B) measured from Hanle spin precession at 10 K 171

Fig. 10-1, Auger spectra of Ge substrate after annealing at 500 °C for 1 h (black curve) and the typical spectra of 3 nm MgO grown on Ge substrate (red/grey curve) 177

Fig. 10-2, RHEED patterns of Ge substrate and 3 nm MgO grown on Ge at different temperatures (left column in the Ge[1 1 0](0 0 1) and MgO[1 0 0](0 0 1) orientation; right column in the Ge[1 0 0](0 0 1) and MgO[1 1 0](0 0 1) orientation) 179

Fig. 10-3, AFM images of Ge substrate and 3 nm MgO grown on Ge at different temperatures 181

Fig. 10-4, HRTEM and RHEED of Fe/MgO/Ge(0 0 1) 184

Fig. 10-5, interface rotation of Fe/MgO/Ge(0 0 1) 185

Fig. 11-1, epitaxial Fe/MgO/Ge junction 193

Fig. 11-2, J-V Characteristics 194

Fig. 11-3, Richardson plots of a Fe/MgO (0.5 nm)/n-Ge diode under different forward biases (0.15 V – 0.22 V) 196

Fig. 11-4, the SBH as a function of the MgO thickness of the Fe/MgO/n-Ge diodes (solid red squares to the left axis) 198

Fig. 11-5, Fe/n-Ge junction with sulfur passivation 199

Fig. 12-1, Ge spin valve device with Fe/MgO/Ge tunnel junction 207

Fig. 12-2, nonlocal MR measurement 210

Fig. 12-3, nonlocal Hanle spin recession measurement 213

Fig. 12-4, bias dependence of the spin transport in Ge 214

Fig. 12-5, three-terminal Hanle measurement 220

Fig. 12-6, comparison of nonlocal four-terminal and three-terminal spin transport in Ge 221

Chapter 1.

Introduction

Abstract

In this section, I first briefly introduce the history of spintronics. Then, lateral spin valves based on metals, semiconductor, and carbon-based materials are reviewed. A brief introduction to graphene is presented. Then, recent progress in graphene spintronics is reviewed. At the end, I point out the motivations and the outline of this thesis.

1.1 Spintronics

Spintronics utilizes the electron spin degree of freedom for information storage and logic operations, which could decrease the power consumption, increase data processing speed, and increase integration densities [1-5]. The basis of spintronics is related to ferromagnetic (FM) materials because the electronic states within the FM material become spin-dependent under a magnetic field due to time reversal symmetry breaking. Fig. 1-1 shows the spin-dependent density of states (DOS) for non-magnetic and FM metals in the presence of a magnetic field. The asymmetry of the spin dependent DOS allows FM to inject, detect and manipulate spin. Furthermore, from the quantum mechanics standpoints, electrons are spin-1/2 fermions with two degrees of freedom, spin up (1/2) and spin down (-1/2), which can be viewed as quantum bits ("q-bit") and could be useful for a novel type of proposed computation know as quantum computation [6].

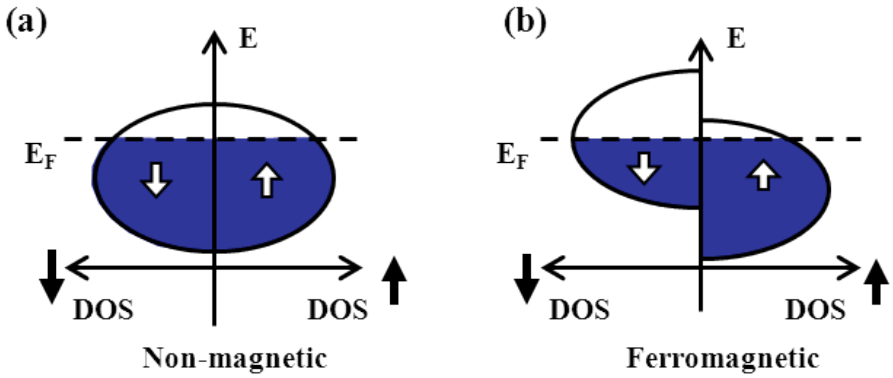

Fig. 1-1, spin-dependent density of states for (a) nonmagnetic materials and (b) ferromagnetic materials.

The history of spintronics can be traced back to 1970s - 1980s. The giant magtoresistance (GMR) effect in in multilayer FM thin metallic films was discovered independently by Fert group and Grünberg group [7, 8]. Tunneling experiments were pioneered by Meservey, Tedrow and Julliere [9, 10].

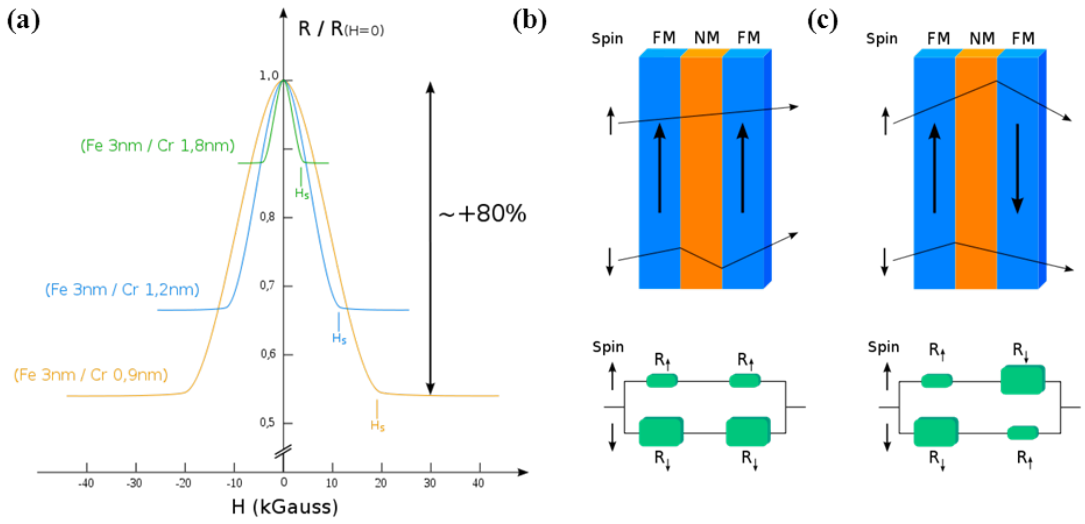

Fig. 1-2, giant magetoresistance effect observed in thin-film structures.

(a) the results of Fert et al in Ref. (b) two-resistance model (spin-up channel and spin-down channel) explaining the GMR effect. Images are taken from Wikipedia.

Fig. 1-2a shows the GMR effect discovered in Fe/Cr multilayers by the group of Albert Fert. When the Cr layer is very thin (~ 1nm), the RKKY (Ruderman and Kittel [11], Kasuya [12] and Yosida [13]) coupling between adjacent Fe layers becomes antiferromagnetic, making them energetically preferable to align in the anti-parallel configureation, which gives a high resistance. A magnetic field is able to align the

magnetization of Fe films to become parallel, which yields a low resistance. Fig. 1-2b and 1-2c show a simple two-resistance model (spin-up channel and spin-down channel) to explain the GMR effect. When the two FM layers both exhibit spin up magnetization, the total resistance will be equal to $R_{AP} = \left(R_{small} + R_{large}\right)/2$. On the other head, if the two FM layers are anti-parallel to each other, the total resistance will be $R_P = 2R_{large}R_{small}/\left(R_{large} + R_{small}\right)$. This effect will usually lead to two levels of resistance: a higher resistance of R_{AP} and a lower resistance of R_P. In 2007, Albert Fert and Peter

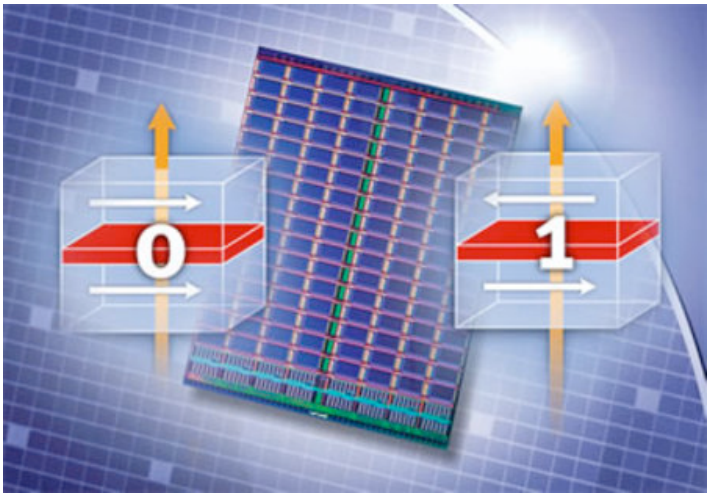

Fig. 1-3, tunneling magetoresistance effect observed in a magnetic tunnel junction. "0" corresponds to a low resistance when the magnetizations are parallel, while "1" corresponds to a high resistance when the magnetizations are anti-parallel. Image via Technolengk.com.

Grünberg were awarded the Nobel Prize in Physics for their discovery of the GMR effects, which has been widely used in sensitive read-out heads for compact hard disks.

The tunneling experiments lead to the Tunneling magnetoresistance (TMR), which is the basis of a new type of non-volatile memory called magnetoresistive random access memory (MRAM). TMR occurs in magnetic tunnel junctions (MTJ), which consist of two FM films separated by a thin insulator. Due to the spin polarized density of states, there will be a low resistance when the magnetizations are parallel ("0" in MRAM, fig. 1-3) and a high resistance when the magnetizations are antiparallel ("1" in MRAM, fig. 1-3). In the early 1990s, Miyazaki and Moodera independently observed room temperature TMR (~10%) across an amorphous aluminum oxide insulator [14, 15]. Later in 2004, much higher TMRs were observed in MgO-based MTJs by the Parkin group and Yuasa group due to the spin-filtering effect based on wavefunction symmetry [16-18]. Currently, the record for room temperature TMR is 600% in Fe/Co/MgO/Co/Fe MTJs grown by molecular beam epitaxy [19].

1.2 Lateral spin valves: from metals, semiconductors, organics to graphene

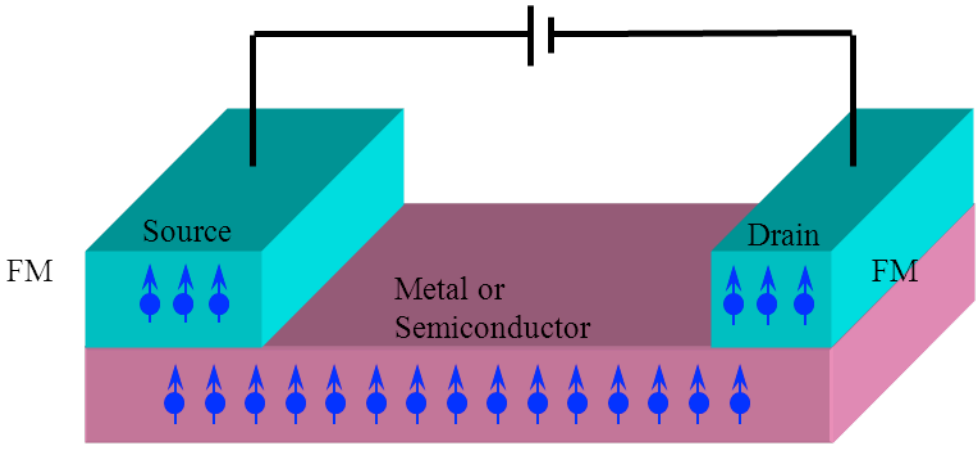

Fig. 1-4, lateral spin valves. The metal or semiconductor is used for the spin transport channel.

Compared to current perpendicular-to-plane spintronics devices, such as GMR and TMR, lateral spin valves are of special interest because of the design flexibility for multi-terminal devices and the ability to manipulate spin during transport [20, 21].

Generally, the lateral spin valves consist of two FM electrodes connected to a nonmagnetic spin transport channel (fig. 1-4). The left FM electrode is used as a "source" for spin injection, while the right FM electrode is used as a "drain" for spin detection. This idea of electrical spin injection as a method to create non-equilibrium spin populations in nonmagnetic metals was first proposed in 1976 by Aronov and Pikus [22]. Experimentally, the first electronic spin injection and detection in nonmagnetic metals was performed by Johnson and Silsbee in 1985 in a single-crystal aluminum bar at temperatures of 77 K [23] (fig. 1-5).

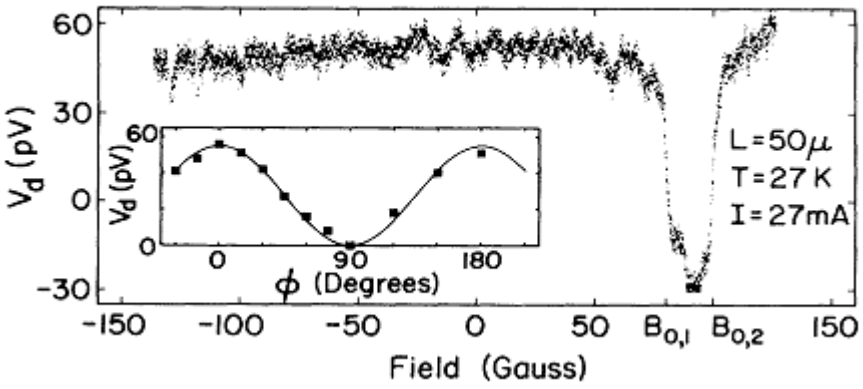

Fig. 1-5, nonlocal spin transport in Al spin valve by Johnson and Silsbee in Ref. [23].

Later in 2001, Jedema and co-workers demonstrated spin injection and nonlocal spin detection in Py/Cu/Py lateral spin valves at RT [24](fig. 1-6). The spin relaxation length of Cu is estimated to be 350 nm at RT and 1000 nm at 4.2 K by studying the spacing dependence of the nonlocal MR. In 2002, Jedema and co-workers performed spin precession measurements in the Al strip, which clearly demonstrated the nonlocal MR signal is from spin injection and transport [21].

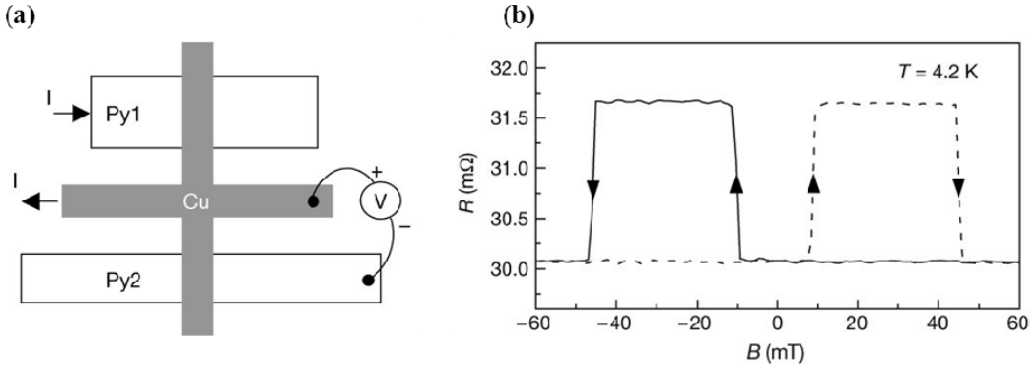

Fig. 1-6, electrical spin injection and accumulation in an Py/Cu/Py spin valve. (a) nonlocal measurement geometry. (b) Nonlocal MR loop measured at 4.2 K. From Ref. [24]

Since the beginning of the twenty-first century, there has been a lot of spin transport work completed in nonmagnetic metals. Kimura and Otani observed large spin accumulation in Py/Ag/Py, and Py/Cu/Py spin valves [25]. Their results indicated that the spin relaxation lengths are about 700 nm for Ag and 400 nm for Cu at RT, 3 μm at 77 K for Ag and 1 μm at 4 K for Cu. They also determined that the spin transport in Cu and Ag spin valves was affected by the contact junction size, temperature, and the relaxation by

an extra FM electrode between the injector and detector. Yi and co-workers studied the spin injection, diffusion, and detection in Au based lateral spin-valves and found that the spin relaxation length is about 60 nm at 10 K [26]. The bias dependence of the spin transport in Al and Cu were studied by different groups including Valenzuela, et al and Casanova, et al [27, 28]. In Valenzuela's work [27], the spin signal is highly dependent on the bias due to reduced polarization for hot electron states and a spin dependent wave-vector mismatch across the Al_2O_3 barrier. In Casanova's work [28] with Py directly contacted to Al or Cu, the spin signal is almost the same at different bias, leading to symmetric spin injection efficiency with positive bias and negative bias. In 2008, the Otani group used a pure spin current to induce the magnetic switching in Py/Cu/Py spin valves by combing the technology of spin torque and nonlocal spin transport, which paved the way for future spin-torque transistors [29]. In 2010, the van Wees group performed thermal spin injection from Py into Cu, which provided a novel way to achieve spin injection [30].

Compared to metal based spin valves, semiconductors are of great interest for spintronics due to its long spin lifetimes [1, 31, 32]. Spin field effect transistor (Spin-FET) was proposed by Datta and Das in 1990 [20]. It uses the Rashba magnetic field generated by the gate voltage and induces the spin precession to obtain on-off states. To achieve this, electrical spin injection and detection has to be achieved. However, one major challenge to perform electron spin injection into semiconductors is the conductivity mismatch problem [33], which means that the conductivity of FM metal electrodes are usually much larger than that of semiconductors. This problem inhibits efficient spin

injection. To enhance the spin injection efficiency [1], one way is to use low conductance FM electrodes, like ferromagnetic semiconductors realized by magnetic doping, or 100% spin polarized source (half metal, such as LSMO, Fe3O4, etc). Another way is to use hot electron spin injection with highly spin polarized "hot" electron with energies that are much greater than E_F. A method commonly used to generate efficient spin injection is utilizing Schottky barrier or oxide tunneling barrier (MgO, Al_2O_3, SiO_2, etc). There have been intensive studies of spin injection in GaAs, Si, and Ge in the last 4 years [34-41].

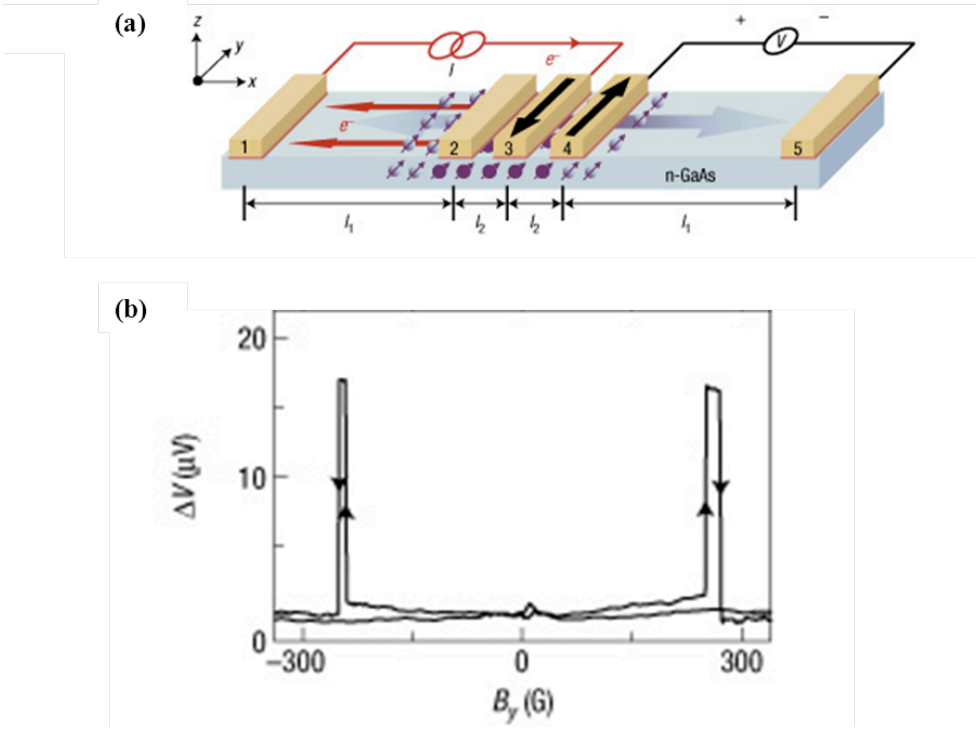

Fig. 1-7, electrical spin transport in GaAs. (a) GaAs spin valve device geometry. (b) Nonlocal MR measured at 50 K. From Lou et al, Ref. [34].

The first all electrical spin injection and detection in semiconductors was accomplished in 2007 by Lou and co-workers on GaAs using an Fe/GaAs Schottky barrier [34] (fig. 1-7). In this work, they performed spin precession up to 70 K, and found that the spin lifetimes in GaAs ($n = 2–4 \times 10^{16}$ cm^{-3}) were 24 ns at 4 K and 4 ns at 70 K. They also observed very interesting bias dependence of spin polarization in GaAs using both electrical detection and optical Hanle effect. This effect motivated several theoretical work afterwards, including spin extraction theory by Dery and Sham, and the spin-dependent interfacial electronics structure proposed by Chantis [42, 43].

In the same year, there were two major advances of spin transport in Si. The first one was done by the Appelbaum group in University of Delaware [37]. They used the hot electron spin injection method and measured the leakage current of the n-Si detector and successfully performed spin transport across 10 μm undoped Si (fig. 1-8a and 1-8b). The other advance was completed by the Jonker group [36] in the Naval research laboratory on the $Fe/Al_2O_3/Si/AlGaAs/GaAs$ quantum well/AlGaAs n–i–p structure using electrical spin injection and spin-LED detection method (fig. 1-8c and 1-8d). Later, electrical spin injection and detection in silicon in a lateral transport geometry was achieved by van't Erve and co-workers using tunnel contacts ($Fe/Al_2O_3/Si$) [35]. In 2009, the Jansen group achieved room temperature spin injection in Si using the 3-terminal technique for the first time. Sasaki and co-workers achieved nonlocal spin transport in Si utilizing a new tunneling contact junction (Fe/MgO/Si) [39]. Tran et al observed a great enhancement of the spin accumulation in GaAs, which was attributed to the localized states at the interface of $Co/Al_2O_3/GaAs$ [44]. In the same year, a spin-FET was experimentally

achieved in the nonlocal geometry on InAs heterostructure with large spin-orbit couplings for the first time [40]. In 2011, Suzuki and co-workers performed the first demonstration of generating a spin current and spin transport in a highly doped Si channel at RT using a four-terminal lateral device [38, 45]. Jonker group performed spin transport in Si using 3-terminal technique with the temperature up to 500 K [46]. As to Ge, there are several advances including spin transport in Ge nanowire, spin injection and precession in bulk Ge using the nonlocal geometry, and 3-terminal technique [41, 47-49].

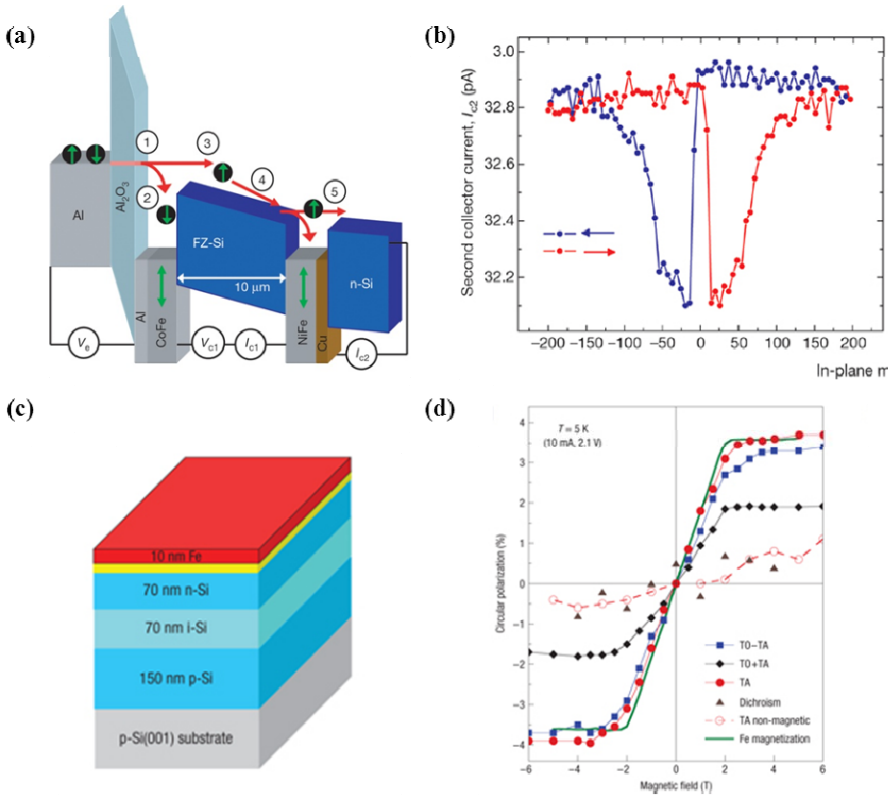

Fig. 1-8, electrical spin transport in Si. (a-b) Hot electron spin injection into Si by appelaum et al. From ref. [37]. (b) Spin LED measurement in Si by Jonker et al from Ref. [36].

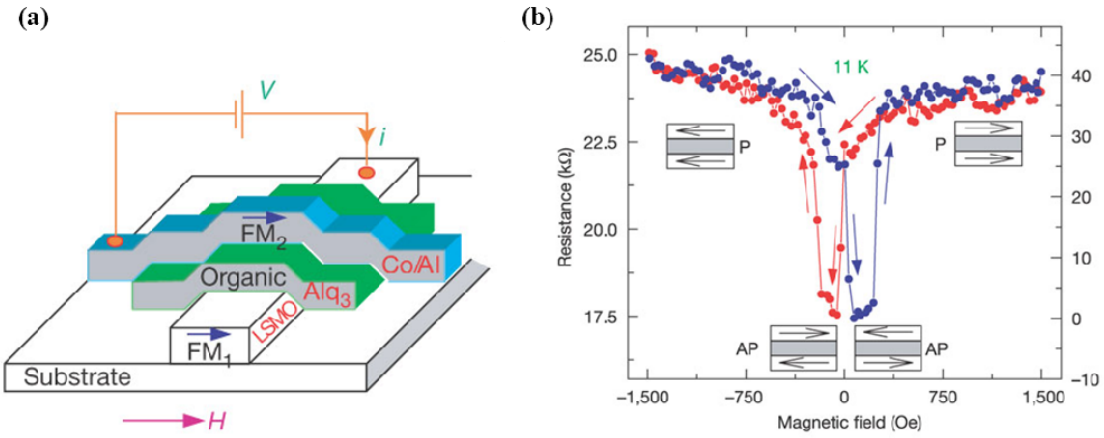

Fig. 1-9, organic semiconductor spin valves. (a) Alq3 device geometry. One FM electrode is LSMO, and the other FM electrode is Co. (b) MR loop measured at 11 K with a negative MR of 40%. From Ref. [50]

Organic semiconductors are interesting to the spintronics community due to long spin lifetimes, the chemical flexibility and optoelectronic properties. In 2004, Xiong et al studied the spin valve based on Alq3 (8-hydroxy-quinoline aluminium) with LSMO and Co as the FM electrodes [50] (fig. 1-9). In 2007 and 2008, Santos et al and Dediu et al independently achieved room temperature spin transport by inserting a thin Al_2O_3 between Co and Alq_3 [51, 52]. In 2009, Sun et al used large Co nanoparticle between Co electrodes and Alq_3 to block the diffusion of Co growth inside Alq3 to form conductance path, and observed large MR [53]. Raman et al studied the effect of molecular ordering on spin injection in rubrene and Yoo et al observed giant MR in the LSMO/LAO/rubrene/Fe junction [54, 55]. In 2010, Yoo et al studied the spin valve effect on rubrene with an organic-based magnetic semiconductor named vanadium

(TCNE: tetracyanoethylene)x (x~2); Tc~400 K) [56]. Barraud et al investigated the Co/Alq3 and LSMO/Alq3 interfaces and concluded that the interfaces were the reason for the observation of both positive and negative MR in previous studies [57].

Carbon based materials (carbon nanotubes, C60, graphene) have attracted considerable interest because they are expected to have long spin lifetimes due to low intrinsic spin orbit coupling and hyperfine couplings [58, 59]. Carbon nanotubes (CNTs) spin valve devices were first reported by Tsukagoshi and co-workers (fig. 1-10) in 1999 [60].

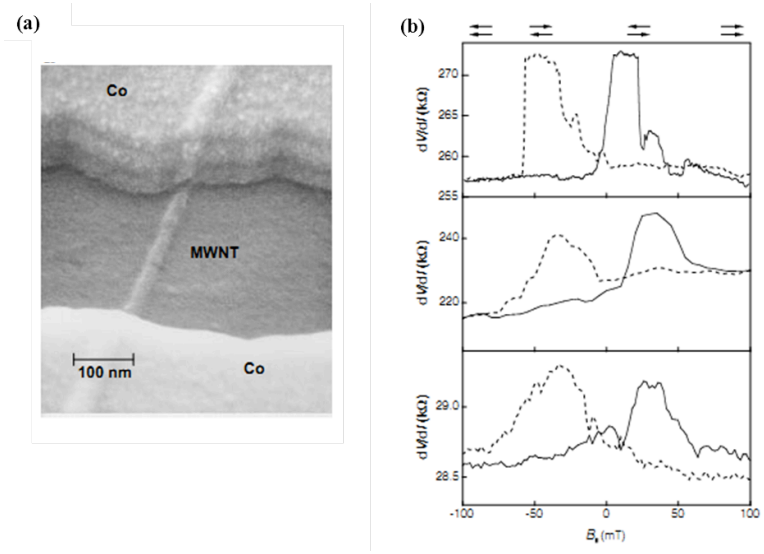

Fig. 1-10, electrical spin transport in carbon nanotube spin valve. (a) Carbon nanotube spin valve geometry. MWNT is connected to two FM Co leads. (b) Local MR measurements for 3 devices. From Tsukagoshi et al, Ref. [60]

After this study, several groups reported MR studied on single wall and multi wall CNTs [61, 62]. Among these works, Sahoo et al [61] and Man et al [62] reported gate

tunable spin transport with PdNi low resistance contacts and the oscillation of the MR followed the oscillation of the conductance. However, there was a debate on whether the observed MR was purely from spin transport or also resulting from spurious signals such as AMR, or Hall effect. In 2006-2007, two important milestones in CNT spintronics were achieved. The first one was detection of the pure spin current using the nonlocal technique by Tombros et al [63]. they studied the spin transport in a single wall nanotube using both local and nonlocal techniques, in which the local MR was about 30 times larger than the nonlocal MR. This was not obeying the theoretical predictions (local MR is equal to 2 times of nonlocal MR) and pointed out that nonlocal MR was more reliable than the local MR to prove spin injection. The other important one was the observation of very large MR ratio in CNT spin valves using half metallic LSMO electrodes [64].

Compared to carbon nanotubes, graphene, a single atomic layer of graphitic carbon, has drawn more attention in the spintronics due to its tunable carrier concentration and conductivity, ultra high mobilities, and sensitive surfaces, etc.

1.3 Graphene

The 2010 Nobel Prize was awarded to Andre Geim and Konstantin Novoselov for their groundbreaking experiments regarding graphene [65, 66]. Physically, graphene is one atom thick sheet of carbon atoms with sp2 bonding in a honeycomb crystal lattice. Its electronic structure is of linear E-k relation for the low energies near the K or K' points of the 2D Brillouin zone (fig. 1-11). The six K or K' points are called Dirac points, due to the fact their behavior is similar to relativistic particles described by the Dirac equation.

Currently, several methods to make graphene have been developed. The first one is generally called “mechanical exfoliation” (tape method), as first invented by Geim group [65]. The second one is epitaxial growth by reducing from SiC at ultrahigh temperatures to fabricate wafer-size graphene [67]. The third one is reduction from graphene oxide flakes done early in 1960s by P. Boehm [68], however, the quality of graphene from this method is not good due to residual of the reduction functional groups. The fourth one is to grow on metal substrates, such as Ni, Ir, etc [69]. Recently, there was a major breakthrough made by the Ruoff group growing large area of high quality single layer graphene on copper using the CVD method [70]. Following this direction, researchers have produced 30-inch graphene, which could be used for transparent electrodes [71].

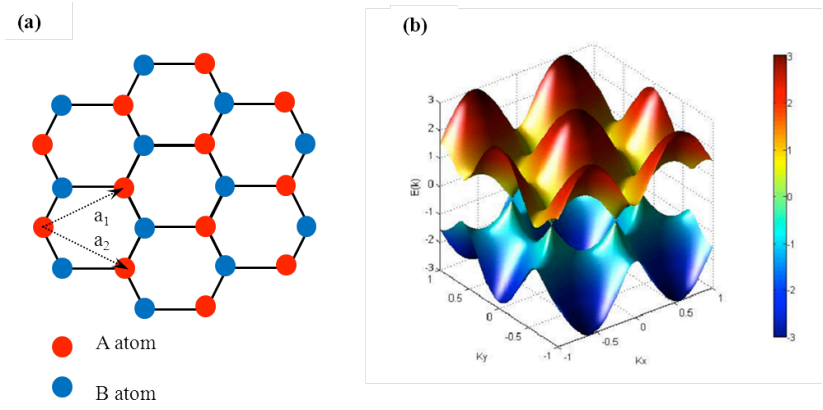

Fig. 1-11, graphene band structure.

(a) Real space lattice of single layer graphene. Red/blue circles correspond to A/B sublattice atom. Vectors a_1 and a_2 are primitive vectors. (b) Energy dispersion relations of graphene.

Since its discovery, graphene has been a promising material for future electronics. In 2010, the Avouris group at IBM created graphene transistors with an on and off rate of 100 G Hz [72]. In 2011, they reported creating the integrated circuit based on graphene [73]. It also has excellent thermal properties, such as ultrahigh thermal conductivity [74].

In the next section, the experimental progress of graphene spintronics is going to be reviewed.

1.4. Review of the work in graphene spintronics

The pioneering work in the field of graphene spintronics was done by the van Wees group in Netherlands [75]. In 2007, they demonstrated both local and nonlocal spin transport in single layer graphene (SLG) at RT (fig. 1-12a and 1-12b). The gate tunable spin transport was also achieved by tuning the conductivity of the graphene. The spin precession in graphene clearly proved the spin injection and the spin lifetimes of 100-200 ps in graphene were obtained. In the same year, Cho et al also achieved gate tunable spin transport in SLG at low temperature, which was related to quantum-coherent transport [76]. Another important progress of the local spin transport in graphene was done by the Kawakami group (fig. 1-12a and 1-12b). They observed a local MR of 7% on a multilayer graphene spin valve at low temperature with tunneling contacts [77]. Similar results have been reported by other groups (the Shiraishi group and the Goldman group) as well [78, 79].

In 2008, there were further advances in this field. Tombros et al discovered the anisotropic spin relaxation, in which spins perpendicular to the graphene layer are 20% smaller than the spins parallel to the graphene layer [80]. Jozsa et al utilized DC electrical

field to manipulate the spin transport in two ways [81, 82]. The first one is using the DC electric field to control the spin injection efficiency by applying the DC current along with the AC current, and the other one is using the DC electric field for drifting along the spin diffusion direction. Goto et al observed the gate tunable spin transport in multilayer graphene nonlocal spin valves, and correlated this effect to the conductivity of graphene [83].

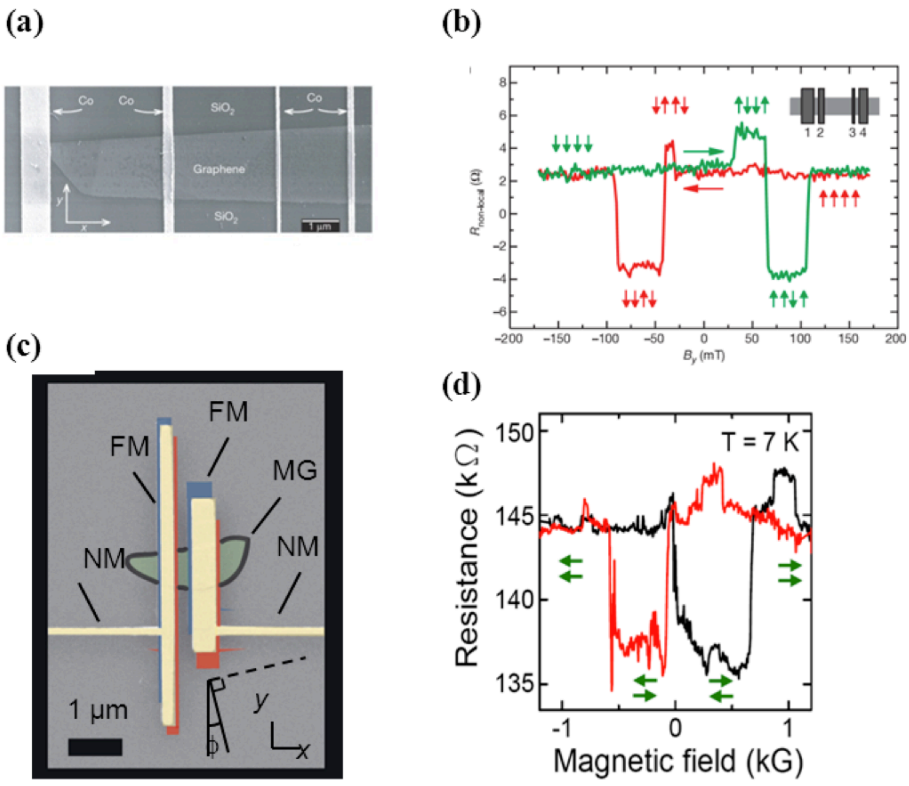

Fig. 1-12, two pioneering work on graphene spintronics.

(a-b) Nonlocal spin transport in single layer graphene spin valve done by Tombros et al, and figures copied from ref. [75]. (c-d) Local spin transport in thin graphite spin valve done by Wang et al. and figures copied from ref. [77]

In 2009, this filed started to grow rapidly. Jozsa et al observed the linear relationship of spin relaxation length and diffusion coefficient, which indicates the dominance of Elliot-Yafet spin relaxation in SLG [84]. Han et al demonstrated spin injection and precession in graphene spin valves with Co/Graphene transparent contacts [85, 86]. The nonlocal MR signal was proportional to the conductivity of single layer graphene, which was expected for spin valves with low resistance transparent contacts. Furthermore, Han et al observed an electron-hole asymmetry, in which the nonlocal MR is roughly independent of bias for electrons, but varies significantly with bias for holes. Shiraishi group found linear relationship of the nonlocal MR and bias current and studied the degradation of the spin valves under high current [87].

These earlier studies identified two critical challenges, which must be overcome in order to realize the full potential of graphene for spintronics. The first important challenge was to enhance the spin injection efficiency, which was low due to the conductance mismatch between the FM metal electrodes and graphene [33]. Although it was expected that the conductance mismatch problem could be alleviated by inserting tunnel barriers into the spin injection interface [88, 89], growing smooth layers on top of graphene was non-trivial because the low surface energy and high surface diffusion led to cluster formation. In 2010, an important progress was made by using a submonolayer Ti seed layer followed by MgO deposition produced atomically smooth MgO films [90]. As a result, tunneling spin injection was achieved with greatly enhanced spin injection efficiencies and I observed a nonlocal MR of 130 ohms for a 2.1 μm spacing between injector and detector, which has been the world record in the field of graphene spintronics

[91]. Later in 2011, Yamaguchi et al achieved tunnel spin injection into graphene using a different barrier [92]. In their work, they used an Al_2O_3 barrier grown by atomic layer deposition on a functionalized graphene surface, and observed a nonlocal MR as high as 30 ohms. Another important achievement was done by the Fert group [93, 94]. They systematically studied the damage to the graphene by growing oxides materials on top of graphene, and observed a very high local MR with high impedance contact junctions.

The second important challenge was to determine the cause of the unexpectedly short spin lifetimes measured by the Hanle effect (spin precession) in SLG (50–200 ps). These lifetimes were orders of magnitude shorter than expected from the intrinsic spin–orbit couplings (~μs). To address this issue, several experimental studies were done [95, 96]. First, Popinciuc et al [95] summarized his work on the spin relaxation in graphene spin valves, and found that the spin relaxation times were not determined by factors including low impendence contacts, spin scattering due to the edge, and the oxide layer on top of graphene. Second, Pi et al studied the effect of charged impurity scattering by adding Au particles on top of SLG spin valves and found that for spin lifetimes on the order of 100 ps, the charged impurity scattering was not the dominant mechanism for spin relaxation in graphene [96]. Third, Han et al observed much longer spin lifetimes in SLG spin valves with tunnel barriers, which indicated that metal contact-induced effects were very important for spin relaxation [91]. Later in 2011, three groups published long spin lifetimes in graphene spin valves. Maassen et al observed 500 ps in 14 layers graphene spin valves [97]. Yang et al observed 2 ns in bilayer graphene (BLG) spin valve at room

temperature [98], and Han et al observed 771 ps at RT in SLG, 1.2 ns at 4 K in SLG, and 6.2 ns at 20 K in BLG [99].

There is still much debate over the dominant spin relaxation mechanism in graphene. In the experimental studies, the van Wees group believes the Elliot-Yafet (EY) spin relaxation is the dominant spin relaxation mechanism in graphene from SLG to 14 layers graphene. The Özyilmaz group and the Kawakami group show the importance of EY spin relaxation in SLG, and Dyakonov–Perel (DP) spin relaxation in BLG. In the theoretical studies, the EY or DP spin relaxation in graphene was also under debate [100-102].

Another three important experimental advances that need to be mentioned are perpendicular spin transport in graphite nanostructures achieved by Banerjee and co-workers [103], spin transport on large area graphene fabricated by CVD method, which made graphene a promising material of choice for large scale spintronic applications [104], and the observation of large spin-Hall effect induced by the Zeeman interaction in graphene [105, 106].

Other topics in the field of graphene spintronics include graphene nanoribbons spintronics and pseudospintronics in graphene. Graphene nanoribbons are predicted to become half-metallic (100% spin-polarized) with the application of a transverse electric field [107]. Spin transport in nanoribbons is also expected to generate extremely large MR ratios of over 10^6 [108]. Pseudo spin valves based bilayer graphene were proposed independently by several groups including San-Jose et al and MacDonald group at UT Austin [109, 110].

1.5. Motivation and outlines

In this thesis, I mainly present the spin transport experimental results on SLG and BLG spin valves, including electron-hole asymmetry of spin transport in SLG, tunneling spin injection into SLG, long spin lifetime in SLG and BLG. I also present measurement of spin injection and transport in bulk Germanium (Ge) at the end. The chapters in this thesis are:

Chapter 2:

I compare the local and nonlocal spin transport measurement. The advantages of nonlocal spin transport method are addressed. I discuss the theoretical calculation of the nonlocal MR using a simple 1D drift and diffusion model. The theoretical view of spin relaxation mechanisms is also discussed.

Chapter 3:

I present the detailed device fabrication of graphene spin valves with either transparent contacts, or tunneling contacts. Two main experimental techniques are briefly discussed, including molecular beam epitaxy (MBE) and electron beam lithography (EBL). I also describe the electrical set up for nonlocal MR measurement.

Chapter 4:

In this chapter, I discuss the experimental results of nonlocal spin transport in graphene spin valves with transparent contacts. Spacing dependence of the nonlocal MR and spin precession in graphene spin valves are presented.

Chapter 5:

In this chapter, the gate tunable spin transport in SLG is discussed with transparent contacts. Also the bias current dependence of spin injection and transport in SLG is discussed, with a comparison of metal and semiconductors. The electron-hole asymmetry is presented and several possible reasons are discussed.

Chapter 6:

In this chapter, I discuss the growth of thin MgO films on top of graphene or graphite. AFM is used to characterize the surface roughness of the MgO film. To reduce the mobility of surface atoms, the graphene surface is dressed by Ti atoms prior to MgO deposition. With as little as 0.5 monolayers of Ti, the MgO overlayer becomes atomically smooth.

Chapter 7:

In this chapter, I discuss the tunneling spin injection using a TiO_2 seeded MgO barrier. Gate tunable spin transport in SLG spin valves with different contacts are discussed. Local and nonlocal MR results are presented. Furthermore, tunnel barriers reduce the contact-induced spin relaxation and are therefore important for future investigations of spin relaxation in graphene.

Chapter 8:

In this chapter, I discuss the long spin lifetimes observed in graphene spin valves. The temperature and gate dependence of the spin dependent properties are studied. I also discuss the different spin relaxation behaviors observed in SLG and BLG by studying the relationship of spin lifetimes and diffusion coefficients. In SLG, the spin lifetimes and diffusion coefficients follow the same curve as a function of gate voltage at low temperatures. While for BLG, these two quantities follow an inverse relationship.

Chapter 9:

In this chapter, I discuss the charged impurities effect on the spin lifetimes in SLG spin valves by studying the SLG with tunable mobilities. The graphene mobility becomes tunable by adding iron oxide nanoparticles on top of SLG surface. The mobility is tuned by changing the amount of charged impurity in graphene. However, the spin lifetimes turn to be in the same range of 0.5-2 ns for SLG at 10 K with mobility from 2000-12000 $cm^2V^{-1}s^{-1}$. These results indicate that the charged impurity scattering is not the dominant spin relaxation in SLG with the mobility less than 12000 $cm^2V^{-1}s^{-1}$.

Chapter 10:

In this chapter, I discuss the growth of MgO film on top of N-type Ge substrate. The effect of growth temperature on the quality of MgO film is discussed. AFM and RHEED results are discussed.

Chapter 11:

In this chapter, I discuss the Schottky characteristics of high quality metal/MgO/n-Ge junctions with the ultrathin MgO epitaxially grown on Ge. The MgO thickness dependence of the depinning effect is studied. Sulfur passivation of the Ge dangling bonds by using aqueous $(NH_4)_2S$ solution is shown.

Chapter 12:

In this chapter, I discuss the spin transport in bulk Ge. The nonlocal spin transport results in Ge are discussed. The temperature dependence of spin transport and spin relaxation are studied. Besides, the three- terminal (3-T) local method and nonlocal spin transport are compared, and the discrepancy between 3-T and nonlocal spin lifetime shows that the 3-T spin relaxation is easily affected by extrinsic factors.

References:

[1] S. A. Wolf, D. D. Awschalom, R. A. Buhrman, J. M. Daughton, S. von Molnar, M. L. Roukes, A. Y. Chtchelkanova, and D. M. Treger, Science **294**, 1488 (2001).

[2] I. Zutic, J. Fabian, and S. Das Sarma, Rev. Mod. Phys **76**, 323 (2004).

[3] C. Chappert, A. Fert, and F. Nguyen Van Dau, Nature Materials **6**, 813 (2007).

[4] A. Fert, Reviews of Modern Physics **80**, 1517 (2008).

[5] S. D. Bader, and S. S. P. Parkin, Annual Review of Condensed Matter Physics **1**, 71 (2010).

[6] C. H. Bennett, and D. P. DiVincenzo, nature **404**, 247 (2000).

[7] M. N. Baibich, J. M. Broto, A. Fert, F. N. Van Dau, and F. Petroff, Phys. Rev. Lett. **61**, (1988).

[8] G. Binasch, P. Grünberg, F. Saurenbach, and W. Zinn, Phys. Rev. B **39**, 4828 (1989).

[9] M. Julliere, Physics Letter A **54**, 225 (1975).

[10] P. M. Tedrow, and R. Meservey, Phys. Rev. Lett. **26**, 192 (1971).

[11] M. A. Ruderman, and C. Kittel, Phys. Rev. **96**, 99 (1954).

[12] T. Kasuya, Prog. Theo. Phys. **16**, 45 (1956).

[13] K. Yosida, Phys. Rev. **106**, 893 (1957).

[14] J. S. Moodera, L. R. Kinder, T. M. Wong, and R. Meservey, Phys. Rev. Lett. **74**, 3273 (1995).

[15] T. Miyazaki, and N. Tezuka, Journal of Magnetism and Magnetic Materials **139**, L231 (1995).

[16] S. S. P. Parkin, C. Kaiser, A. Panchula, P. M. Rice, B. Hughes, M. Samant, and S.-H. Yang, Nature Materials **3**, 862 (2004).

[17] S. Yuasa, T. Nagahama, A. Fukushima, Y. Suzuki, and K. Ando, Nature Materials **3**, 868 (2004).

[18] W. H. Butler, X.-G. Zhang, T. C. Schulthess, and J. M. MacLaren, Phys. Rev. B **63**, 054416 (2001).

[19] S. Ikeda, J. Hayakawa, Y. Ashizawa, Y. M. Lee, K. Miura, H. Hasegawa, M. Tsunoda, F. Matsukura, and H. Ohno, Appl. Phys. Lett. **93**, 082508 (2008).

[20] S. Datta, and B. Das, Appl. Phys. Lett. **56**, 665 (1990).

[21] F. J. Jedema, H. B. Heersche, A. T. Filip, J. J. A. Baselmans, and B. J. van Wees, Nature **416**, 713 (2002).

[22] G. L. Bir, A. G. Aronov, and G. E. Pikus, Sov. Phys. JETP **42**, 705 (1976).

[23] M. Johnson, and R. H. Silsbee, Phys. Rev. Lett. **55**, 1790 (1985).

[24] F. J. Jedema, A. T. Filip, and B. J. van Wees, Nature **410**, 345 (2001).

[25] T. Kimura, and Y. Otani, Phys. Rev. Lett. **99**, 196604 (2007).

[26] Y. Ji, A. Hoffmann, J. S. Jiang, J. E. Pearson, and S. D. Bader, J. Phys. D: Appl. Phys. **40**, 1280 (2007).

[27] S. O. Valenzuela, D. J. Monsma, C. M. Marcus, V. Narayanamurti, and M. Tinkham, Phys. Rev. Lett. **94**, 196601 (2005).

[28] F. Casanova, A. Sharoni, M. Erekhinsky, and I. K. Schuller, Phys. Rev. B **79**, 184415 (2009).

[29] T. Yang, T. Kimura, and Y. Otani, Nature Physics **4**, 851 (2008).

[30] A. Slachter, F. L. Bakker, J. P. Adam, and B. J. Van Wees, Nature Physics, (2010).

[31] J. M. Kikkawa, and D. D. Awschalom, Nature **397**, 139 (1999).

[32] D. D. Awschalom, and M. E. Flatte, Nature Physics **3**, 153 (2007).

[33] G. Schmidt, D. Ferrand, L. W. Molenkamp, A. T. Filip, and B. J. van Wees, Phys. Rev. B **62**, 4790(R) (2000).

[34] X. Lou, C. Adelmann, S. A. Crooker, E. S. Garlid, J. Zhang, K. S. M. Reddy, S. D. Flexner, C. J. Palmstrom, and P. A. Crowell, Nature Physics **3**, 197 (2007).

[35] O. M. J. van't Erve, A. T. Hanbicki, M. Holub, C. H. Li, C. Awo-Affouda, P. E. Thompson, and B. T. Jonker, Appl. Phys. Lett. **91**, 212109 (2007).

[36] B. T. Jonker, G. Kioseoglou, A. T. Hanbicki, C. H. Li, and P. E. Thompson, Nature Physics **3**, 542 (2007).

[37] I. Appelbaum, B. Huang, and D. J. Monsma, Nature **447**, 295 (2007).

[38] T. Sasaki, T. Oikawa, T. Suzuki, M. Shiraishi, Y. Suzuki, and K. Tagami, Appl. Phys. Expr. **2**, 53003 (2009).

[39] S. P. Dash, S. Sharma, R. S. Patel, M. P. d. Jong, and R. Jansen, Nature **462**, 26 (2009).

[40] H. C. Koo, J. H. Kwon, J. Eom, J. Chang, S. H. Han, and M. Johnson, Science **325**, 1515 (2009).

[41] Y. Zhou, W. Han, L.-T. Chang, F. Xiu, M. Wang, M. Oehme, I. A. fischer, J. Schulze, R. K. Kawakami, and K. L. Wang, Phys. Rev. B **84**, 125323 (2011).

[42] H. Dery, and L. J. Sham, Phys. Rev. Lett. **98**, 046602 (2007).

[43] A. N. Chantis, K. D. Belashchenko, D. L. Smith, E. Y. Tsymbal, M. v. Schilfgaarde, and R. C. Albers, Phys. Rev. Lett. **99**, 196603 (2007).

[44] T. Tran, H. Jaffres, C. Deranlot, J.-M. George, A. Fert, A. Miard, and A. Lemaitre, Phys. Rev. Lett. **102**, 036601 (2009).

[45] T. Suzuki, T. Sasaki, T. Oikawa, M. Shiraishi, Y. Suzuki, and K. Noguchi, Appl. Phys. Expr. **4**, 023003 (2011).

[46] C. H. Li, O. M. J. v. t. Erve, and B. T. Jonker, Nature Communications **2**, 245 (2010).

[47] E.-S. Liu, J. Nah, K. M. Varahramyan, and E. Tutuc, Nano Letters **10**, 3297 (2010).

[48] K.-R. Jeon, B.-C. Min, Y.-H. Jo, H.-S. Lee, I.-J. Shin, C.-Y. Park, S.-Y. Park, and S.-C. Shin, Phys. Rev. B **84**, 165315 (2011).

[49] A. Jain, L. Louahadj, J. Peiro, J. C. L. Breton, C. Vergnaud, A. Barski, C. Beigné, L. Notin, A. Marty, V. Baltz, S. Auffret, E. Augendre, H. Jaffrès, J. M. George, and M. Jamet, Appl. Phys. Lett. **99**, 162102 (2011).

[50] Z. H. Xiong, D. Wu, Z. V. Vardeny, and J. Shi, Nature **427**, 821 (2004).

[51] T. S. Santos, J. S. Lee, P. Migdal, C. Lekshmi, B. Satpati, and J. S. Moodera, Phys. Rev. Lett. **98**, 016601 (2007).

[52] V. Dediu, L. E. Hueso, I. Bergenti, A. Riminucci, F. Borgatti, P. Graziosi, C. Newby, F. Casoli, M. P. De Jong, C. Taliani, and Y. Zhan, Phys. Rev. B **78**, 115203 (2008).

[53] D. Sun, L. Yin, C. Sun, H. Guo, Z. Gai, X.-G. Zhang, T. Z. Ward, Z. Cheng, and J. Shen, Phys. Rev. Lett. **104**, 236602 (2010).

[54] K. V. Raman, S. M. Watson, J. H. Shim, J. A. Borchers, J. Chang, and J. S. Moodera, Phys. Rev. B **80**, 195212 (2009).

[55] J.-W. Yoo, H. W. Jang, V. N. Prigodin, C. Kao, C. B. Eom, and A. J. Epstein, Phys. Rev. B **80**, 205207 (2009).

[56] J.-W. Yoo, C.-Y. Chen, H. W. Jang, C. W. Bark, V. N. Prigodin, C. B. Eom, and A. J. Epstein, Nature Materials **9**, 638 (2010).

[57] C. Barraud, P. Seneor, R. Mattana, S. Fusil, K. Bouzehouane, C. Deranlot, P. Graziosi, L. Hueso, I. Bergenti, V. Dediu, F. Petroff, and A. Fert, Nature physics **6**, 615 (2010).

[58] D. Huertas-Hernando, F. Guinea, and A. Brataas, Phys. Rev. B **74**, 155426 (2006).

[59] B. Trauzettel, D. V. Bulaev, D. Loss, and G. Burkard, Nature Physics **3**, 192 (2007).

[60] K. Tsukagoshi, B. W. Alphenaar, and H. Ago, Nature **401**, 572 (1999).

[61] S. Sahoo, T. Kontos, J. Furer, C. Hoffmann, M. Graber, A. Cottet, and C. Schonenberger, Nature Physics **1**, 99 (2005).

[62] H. T. Man, I. J. W. Wever, and A. F. Morpurgo, Phys. Rev. B **73**, 241401(R) (2006).

[63] N. Tombros, S. J. v. d. Molen, and B. J. van Wees, Phys. Rev. B **73**, 233403 (2006).

[64] L. E. Hueso, J. M. Pruneda, V. Ferrari, G. Burnell, J. P. Valdes-Herrera, B. D. Simons, P. B. Littlewood, E. Artacho, A. Fert, and N. D. Mathur, Nature **445**, 410 (2007).

[65] K. S. Novoselov, A. K. Geim, S. V. Morozov, D. Jiang, Y. Zhang, S. V. Dubonos, I. V. Grigorieva, and A. A. Firsov, Science **306**, 666 (2004).

[66] A. K. Geim, and K. S. Novoselov, Nature Materials **6**, 183 (2007).

[67] C. Berger, Z. Song, T. Li, X. Li, A. Y, Ogbazghi, R. Feng, Z. Dai, A. N. Marchenkov, E. H. Conrad, P. N. First, and W. A. d. Heer, J. Phys. Chem. B **108**, 19912 (2004).

[68] Graphene Times (2009-12-07). Retrieved on 2010-12-10.

[69] K. S. Kim, Y. Zhao, H. Jang, S. Y. Lee, J. M. Kim, K. S. Kim, J.-H. Ahn, P. Kim, J.-Y. Choi, and B. H. Hong, Nature **457**, 706 (2009).

[70] X. Li, W. Cai, J. An, S. Kim, J. Nah, D. Yang, R. Piner, A. Velamakanni, I. Jung, E. Tutuc, S. K. Banerjee, L. Colombo, and R. S.Ruoff, Science Express **10.1126/science.1171245**, (2009).

[71] S. Bae, H. K. Kim, X. Xu, J. Balakrishnan, T. Lei, Y. Song, Y. J. Kim, B. Ozyilmaz, J.-H. Ahn, B. H. Hong, and S. Lijima, Nature Nanotech., (2010).

[72] Y.-M. Lin, C. Dimitrakopoulos, K. A. Jenkins, D. B. Farmer, H.-Y. Chiu, A. Grill, and P. Avouris, Science **327**, 662 (2010).

[73] Y.-M. Lin, A. Valdes-Garcia, S.-J. Han, D. B. Farmer, I. Meric, Y. Sun, Y. Wu, C. Dimitrakopoulos, A. Grill, P. Avouris, and K. A. Jenkins, Science **332**, 1294 (2011).

[74] A. A. Balandin, S. Ghosh, W. Bao, I. Calizo, D. Teweldebrhan, F. Miao, and C. N. Lau, Nano Letters **8**, 902 (2008).

[75] N. Tombros, C. Jozsa, M. Popinciuc, H. T. Jonkman, and B. J. van Wees, Nature **448**, 571 (2007).

[76] S. Cho, Y.-F. Chen, and M. S. Fuhrer, Appl. Phys. Lett. **91**, 123105 (2007).

[77] W. H. Wang, K. Pi, Y. Li, Y. F. Chiang, P. Wei, J. Shi, and R. K. Kawakami, Phys. Rev. B **77**, 020402(R) (2008).

[78] M. Ohishi, M. Shiraishi, R. Nouchi, T. Nozaki, T. Shinjo, and Y. Suzuki, Jpn. J. Appl. Phys **46**, L605 (2007).

[79] M. Nishioka, and A. M. Goldman, Appl. Phys. Lett. **90**, 252505 (2007).

[80] N. Tombros, S. Tanabe, A. Veligura, C. Jozsa, M. Popinciuc, H. T. Jonkman, and B. J. van Wees, Phys. Rev. Lett. **101**, 046601 (2008).

[81] C. Jozsa, M. Popinciuc, N. Tombros, H. T. Jonkman, and B. J. van Wees, Phys. Rev. B **79**, 081402(R) (2008).

[82] C. Jozsa, M. Popinciuc, N. Tombros, H. T. Jonkman, and B. J. van Wees, Phys. Rev. Lett. **100**, 236603 (2008).

[83] H. Goto, A. Kanda, T. Sato, S. Tanaka, Y. Ootuka, S. Odaka, H. Miyazaki, K. Tsukagoshi, and Y. Aoyagi, Appl. Phys. Lett. **92**, 212110 (2008).

[84] C. Józsa, T. Maassen, M. Popinciuc, P. J. Zomer, A. Veligura, H. T. Jonkman, and B. J. van Wees, Phys. Rev. B **80**, 241403(R) (2009).

[85] W. Han, W. H. Wang, K. Pi, K. M. McCreary, W. Bao, Y. Li, F. Miao, C. N. Lau, and R. K. Kawakami, Phys. Rev. Lett. **102**, 137205 (2009).

[86] W. Han, K. Pi, W. Bao, K. M. McCreary, Y. Li, W. H. Wang, C. N. Lau, and R. K. Kawakami, Appl. Phys. Lett. **94**, 222109 (2009).

[87] M. Shiraishi, M. Ohishi, R. Nouchi, T. Nozaki, T. Shinjo, and Y. Suzuki, Adv. Funct. Mater. **19**, 3711 (2009).

[88] E. I. Rashba, Phys. Rev. B **62**, 16267(R) (2000).

[89] A. Fert, and H.Jaffres, Phys. Rev. B **64**, 184420 (2001).

[90] W. H. Wang, W. Han, K. Pi, K. M. McCreary, F. Miao, W. Bao, C. N. Lau, and R. K. Kawakami, Appl. Phys. Lett. **93**, 183107 (2008).

[91] W. Han, K. Pi, K. M. McCreary, Y. Li, J. J. I. Wong, A. G. Swartz, and R. K. Kawakami, Phys. Rev. Lett. **105**, 167202 (2010).

[92] T. Yamaguchi, S. Masubuchi, K. Iguchi, R. Moriya, and T. Machida, Journal of Magnetism and Magnetic Materials **324**, 849 (2012).

[93] B. Dlubak, P. Seneor, A. Anane, C. Barraud, C. Deranlot, D. Deneuve, B. Servet, R. Mattana, F. Petroff, and A. Fert, Appl. Phys. Lett. **97**, 092502 (2010).

[94] A. Fert, Imagine NANO talk, (2011).

[95] M. Popinciuc, C. Jozsa, P. J. Zomer, N. Tombros, A. Veligura, H. T. Jonkman, and B. J. van Wees, Phys. Rev. B **80**, 214427 (2009).

[96] K. Pi, W. Han, K. M. McCreary, A. G. Swartz, Y. Li, and R. K. Kawakami, Phys. Rev. Lett. **104**, 187201 (2010).

[97] T. Maassen, F. K. Dejene, M. H. Guimaraes, C. Jozsa, and B. J. van Wees, Phys. Rev. B **83**, 115410 (2011).

[98] T.-Y. Yang, J. Balkrishnna, F. Volmer, A. Avsar, M. Jaiswal, J. Samm, S. R. Ali, A. Pachoud, M. Zeng, M. Popinciuc, G. Guntherodt, B. Beschoten, and B. Ozyilmaz, Phys. Rev. Lett. **107**, 047206 (2010).

[99] W. Han, and R. K. Kawakami, Phys. Rev. Lett. **107**, 047207 (2011).

[100] A. H. Castro Neto, and F. Guinea, Phys. Rev. Lett. **103**, 026804 (2009).

[101] H. Ochoa, A. H. Castro Neto, and F. Guinea, arXiv:1107.3386, (2011).

[102] P. Zhang, and M. W. Wu, arXiv:1108.0283v1, (2011).

[103] T. Banerjee, W. G. van der Wiel, and R. Jansen, Phys. Rev. B **81**, 214409 (2010).

[104] A. Avsar, T.-Y. Yang, S.-K. Bae, J. Balakrishnan, F. Volmer, M. Jaiswal, Z. Yi, S. R. Ali, G. Güntherodt, B.-H. Hong, B. Beschoten, and B. Özyilmaz, arXiv:1104.4715, (2011).

[105] D. A. Abanin, S. V. Morozov, L. A. Ponomarenko, R. V. Gorbachev, A. S. Mayorov, M. I. Katsnelson, K. Watanabe, T. Taniguchi, K. S. Novoselov, L. S. Levitov, and A. K. Geim1, Science **332**, 328 (2011).

[106] D. A. Abanin, R. V. Gorbachev, K. S. Novoselov, A. K. Geim, and L. S. Levitov, Phys. Rev. Lett. **107**, 096601 (2011).

[107] Y.-W. Son, M. L. Cohen, and S. G. Louie, Nature **444**, 347 (2006).

[108] W. Y. Kim, and K. S. Kim, Nature Nanotech. **3**, 408 (2008).

[109] P. San-Jose, E. Prada, E. McCann, and H. Schomerus, Phys. Rev. Lett. **102**, 247204 (2009).

[110] H. Min, G. Borghi, M. Polini, and A. H. MacDonald, Phys. Rev. B **77**, 041407(R) (2008).

Chapter 2.

Theoretical view of spin transport and relaxation

Abstract

In this section, I discuss the theoretical aspects for electrical spin injection and detection in the local and nonlocal geometries. A simple 1D drift and diffusion model is employed in the nonlocal MR calculation. Furthermore, the theoretical view of spin relaxation mechanisms will be discussed.

2.1 Electrical spin injection and detection

Typically, there are two geometries for electrical spin transport measurements. First is the conventional spin transport geometry, known as the "local" measurement, which measures the resistance across two ferromagnetic electrodes (fig. 2-1a). Spin polarized electrons are injected from one electrode, transported across the nonmagnetic channel, and detected by the second electrode. In this thesis, the ferromagnetic electrodes are Co and the nonmagnetic channel is graphene. The spin transport is detected as the difference in resistance between the parallel and anti-parallel magnetization alignments of the two electrodes. This is the geometry used for magnetic tunnel junctions (MTJ) and current-perpendicular-to-the-plane giant magnetoresistance (CPP-GMR) [1, 2]. The second geometry is the "nonlocal" measurement [3, 4] which uses four electrodes, as shown in fig. 2-1b. Here, a current source is applied across Co electrodes E1 and E2 to inject spins at E2. For spin detection, a voltage is measured across Co electrodes E3 and E4, and the signal is due to the transport of spins from E2 to E3. This measurement is called "nonlocal" because the voltage probes lie outside of the current loop. After the spin injection, the spins at E2 are able to diffuse in both directions, toward E1 (as a spin current with charge current) and toward E3 (as a spin current without charge current). This spin diffusion is usually described by a spin dependent chemical potential ($\mu_\uparrow$ and $\mu_\downarrow$), where a splitting of the chemical potential corresponds to the spin density in the graphene. Fig. 2-1c and 2-1d show that as the spins diffuse toward E3, the spin density decays due to spin flip scattering. Thus, the voltage will be positive for the parallel alignment of E2 and E3 ($V_P > 0$, fig. 2-1c, black dots) and negative for the antiparallel

alignment ($V_{AP} < 0$, fig. 2-1d, black dots). The signal generated by the spin transport is the nonlocal MR, defined as $\Delta R_{NL} = (V_P - V_{AP})/I$, where *I* is the injection current.

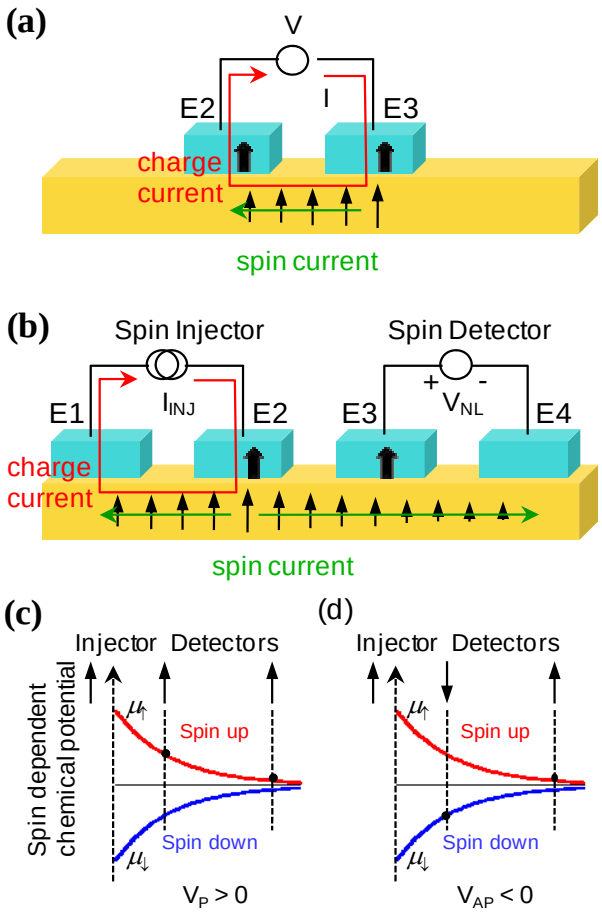

Fig. 2-1, local and nonlocal MR measurement.

(a) Schematic of local spin transport measurements. (b) Schematic of nonlocal spin transport measurements. The red arrow indicates the direction of the charge current and the green arrow indicates the direction of spin current. (c, d) Spin-dependent chemical potential for parallel and antiparallel states of spin injector and detectors in the nonlocal geometry.

Comparing these two geometries, the nonlocal measurement is more sensitive to detect the spin signal because the spin current is isolated from the charge current. As discussed later, the nonlocal MR measurement has much better signal-to-noise ratio compared to the local MR measurement performed on the same device. Also, the nonlocal measurement is less prone to artifacts such as anomalous Hall and anisotropic magnetoresistance (AMR) effects [4].

Experimentally, there is a nonlocal baseline voltage which could be due to non-uniform spin injection or detection, Peltier and Seebeck effects, or nonconserving spin scattering at the interface [5-7]. The non-uniform spin injection or detection was calculated by Johnson and Silsbee [5]. Ideally, spatially uniform spin injection/detection occurs at the FM/NM interface when the tunnel barrier is uniform and the conductivity of the NM is homogenous throughout the channel, as shown in fig. 2-2a. In this case, the nonlocal baseline resistance is 0. However, in experimental studies with the tunnel barrier of nonuniform thickness, spin injection/detection could be non-uniform (fig. 2-2b), which will cause an electric field to exist between the injector and the second detector (point B in fig.2-2b). As a result of this electric field, there would be a non-zero nonlocal baseline resistance. The Peltier and Seebeck effects were calculated by van Wees group in Cu/Py spin vlaves [6]. As shown in fig. 2-2d and 2-3e, a voltage difference exists due to the difference in the Peltier coefficients for Cu and Py at the injector interface, and the thermal Seebeck effect due to the the temperature difference at the detector interface. Another mechanism is related to nonconserving spin scattering for spin up currents and spin down currents at the interface [7].

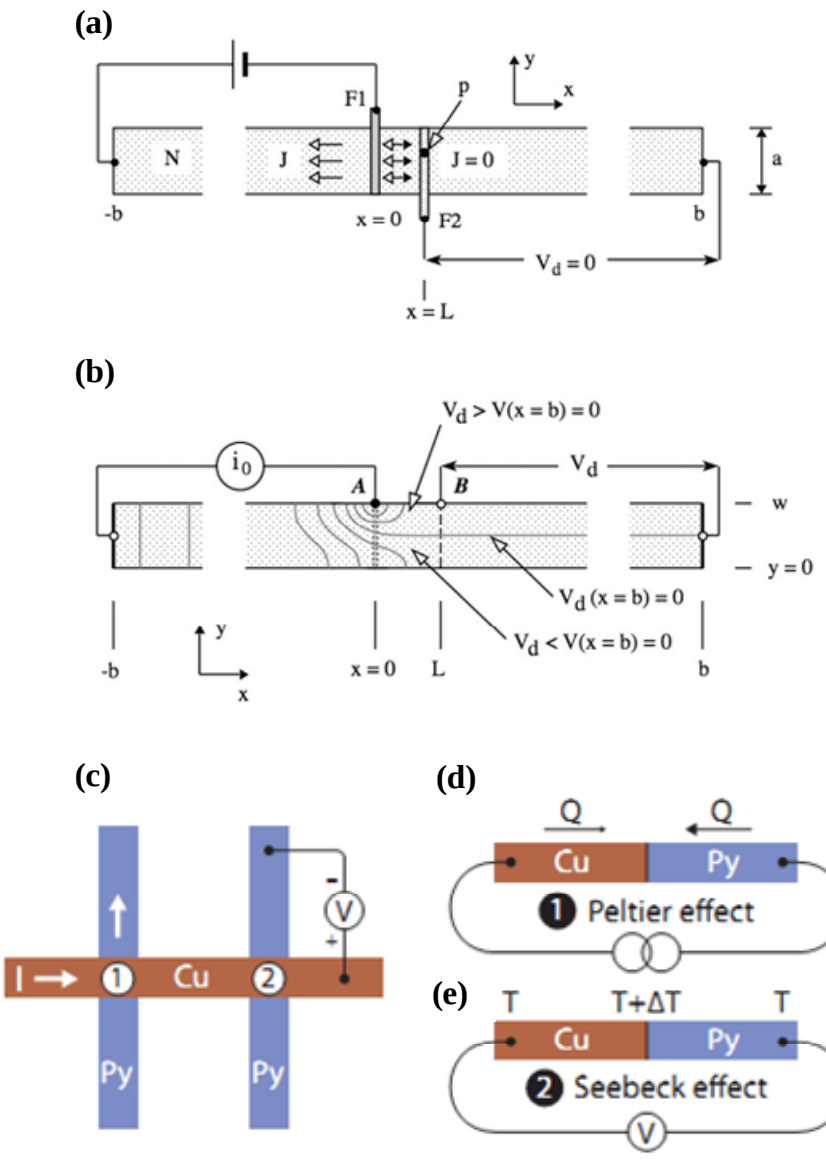

Fig. 2-2, description of the background of the nonlocal MR.

(a-b) Schematics for nonlocal baseline resistance due to non-uniform spin injection or detection by Johnson and Silibee in ref [5]. (c-e) The nonlocal baseline resistance due to Peltier and Seebeck effects by the van Wees group in ref [6].

2.2 Calculation of the nonlocal MR

I calculated the nonlocal MR based on one dimensional spin transport and diffusion model following Takahashi and Maekawa [8]. The graphene spin valve geometry is shown in fig. 2-3.

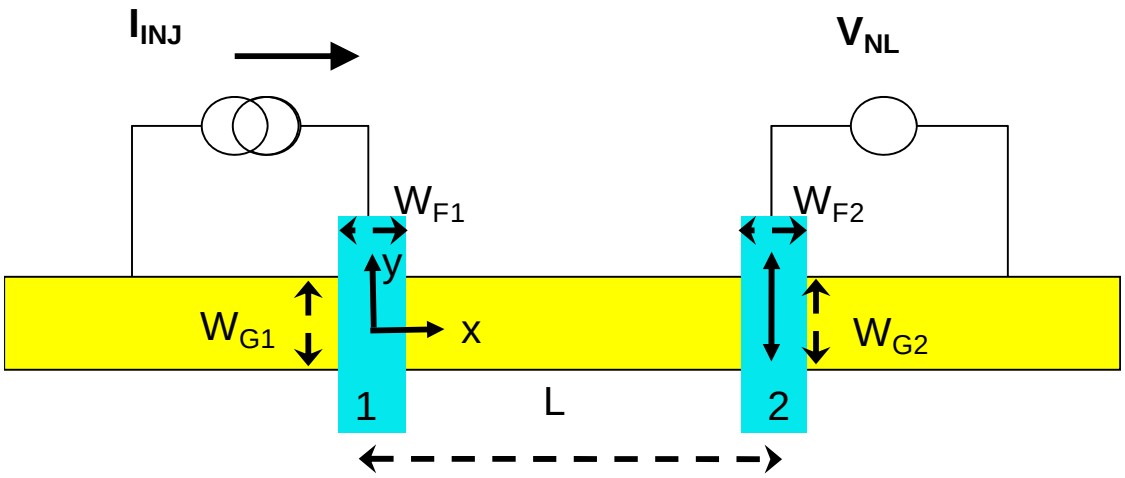

Fig. 2-3, the nonlocal MR calculation.

L is the spacing between the injector 1 and detector 2. W_G is the width of the graphene, and W_F is the width of the Co electrodes.

A current is applied across electrodes E_1 and graphene to generate spin polarization in the graphene beneath electrode E_1 by spin injection/accumulation. This spin-polarization propagates to E_2 (spacing: L) via spin diffusion and generates a non-local voltage across electrodes E_2 and graphene due to the spin-sensitive nature of the ferromagnetic electrodes. For both Co and graphene, according to the ohm's law, the spin current is expressed by:

$$j_{\uparrow\downarrow} = -\frac{\sigma_{\uparrow\downarrow}}{e}\nabla\mu_{\uparrow\downarrow} \tag{2-1}$$

where $\uparrow\downarrow$ corresponds to the spin up and spin down, $\sigma_{\uparrow\downarrow}$, $\mu_{\uparrow\downarrow}$ are the conductivity and the spin dependent chemical potential. Assuming one dimensional drift-diffusion, the spin dependent chemical potential can be expressed by:

$$\nabla^2(\mu_\uparrow - \mu_\downarrow) = \frac{1}{\lambda^2}(\mu_\uparrow - \mu_\downarrow) \tag{2-2}$$

where λ is the spin diffusion length ($\lambda = \sqrt{D\tau_{sf}}$, D is the diffusion coefficient, and τ_{sf} is the spin lifetimes). Here, for simplicity, I assume the uniform spin injection over the contact area and neglect the interfacial spin scattering. In graphene,

$$\mu_{G\uparrow} = \begin{pmatrix} (eI/\sigma_G)x + a_1 e^{-|x|/\lambda_G} + a_2 a_1 e^{-|x-L|/\lambda_G}, x<0 \\ a_1 e^{-|x|/\lambda_G} + a_2 a_1 e^{-|x-L|/\lambda_G}, x>0 \end{pmatrix},$$

$$\mu_{G\downarrow} = \begin{pmatrix} (eI/\sigma_G)x - a_1 e^{-|x|/\lambda_G} - a_2 a_1 e^{-|x-L|/\lambda_G}, x<0 \\ -a_1 e^{-|x|/\lambda_G} - a_2 a_1 e^{-|x-L|/\lambda_G}, x>0 \end{pmatrix} \tag{2-3}$$

In the FM electrodes (Co), the chemical potential is equal to:

$$\mu_{F1\uparrow} = (eI/\sigma_F A_J)z + eV_1 + b_1(\sigma_F/\sigma_{F\uparrow})e^{-z/\lambda_F},$$

$$\mu_{F1\downarrow} = (eI / \sigma_F A_J)z + eV_1 - b_1(\sigma_F / \sigma_{F\uparrow})e^{-z/\lambda_F} \quad (2\text{-}5)$$

$$\mu_{F2\uparrow} = eV_2 - b_2(\sigma_F / \sigma_{F\uparrow})e^{-z/\lambda_F} ,$$

$$\mu_{F2\downarrow} = eV_2 - b_2(\sigma_F / \sigma_{F\downarrow})e^{-z/\lambda_F} \quad (2\text{-}6)$$

in which V_1 and V_2 are the voltage drops at the interface 1 and interface 2. $V = (\overline{\mu_F} - \overline{\mu_G}) / e$. Using equation 2-1, 2-3, 2-5, 2-6 and $j_s = j_\uparrow - j_\downarrow$, one can calculate the following spin current densities. The spin current density at interface E_1 in graphene is equal to:

$$j_{G\_1s} = 2\left(\frac{\sigma_G}{e\lambda_G}\right)a_1 , \quad (2\text{-}7)$$

And the spin current density at interface E_2 in graphene is equal to:

$$j_{G\_2s} = 2\left(\frac{\sigma_G}{e\lambda_G}\right)a_2 , \quad (2\text{-}8)$$

The spin current density at the interface E_1 in the Co electrodes is equal to:

$$j_{F\_1s} = p_F j - 2\left(\frac{\sigma_F}{e\lambda_F}\right)b_1 , \quad (2\text{-}9)$$

in which, the $p_F = \dfrac{\sigma^\uparrow - \sigma^\downarrow}{\sigma^\uparrow + \sigma^\downarrow}$ is the spin polarization of the Co electrodes.

And the spin current density at interface E_2 in the Co electrodes is equal to:

$$j_{G\_2s} = -2\left(\frac{\sigma_F}{e\lambda_F}\right)b_2 , \quad (2\text{-}10)$$

Across the interface 1 and 2 with interface resistance R_1 (G_1^{-1}) and R_2 (G_2^{-1}), the spin current is equal to:

$$I_{\uparrow\downarrow} = \frac{G_{\uparrow\downarrow}}{e}(\mu_{F\uparrow\downarrow}|_{z=0^+} - \mu_{G\uparrow\downarrow}|_{z=0^-}) \tag{2-11}$$

in which $G = G_\uparrow + G_\downarrow = 1/R_\uparrow + 1/R_\downarrow = 1/R$. Combining equation 2-3, 2-5, 2-6, 2-11, we can get the spin current across the interface 1 and 2:

$$I_{1s} = I_{1\uparrow} - I_{1\downarrow} = G_1 P_{J1} V_1 - \frac{G_1}{e}(a_1 + a_2 e^{-L/\lambda_G}) + (\frac{G_1^{\uparrow}}{\sigma_F^{\uparrow}} + \frac{G_1^{\downarrow}}{\sigma_F^{\downarrow}})\frac{\sigma_F}{e} b_1 \tag{2-12}$$

$$I_{2s} = I_{1\uparrow} - I_{1\downarrow} = G_2 P_{J2} V_2 - \frac{G_2}{e}(a_2 + a_1 e^{-L/\lambda_G}) + (\frac{G_2^{\uparrow}}{\sigma_F^{\uparrow}} + \frac{G_2^{\downarrow}}{\sigma_F^{\downarrow}})\frac{\sigma_F}{e} b_2 \tag{2-13}$$

in which $P_{J1} = \frac{G_1^{\uparrow} - G_1^{\downarrow}}{G_1^{\uparrow} + G_1^{\downarrow}}$, and $P_{J2} = \frac{G_2^{\uparrow} - G_2^{\downarrow}}{G_2^{\uparrow} + G_2^{\downarrow}}$.

Due to the spin current conservation, the spin current should be the same across the interface. Hence:

At the interface 1,

$$I_{1s} = 2\left(\frac{\sigma_G}{e\lambda_G}\right) a_1 W_{G1} = p_F I - 2\left(\frac{\sigma_F}{e\lambda_F}\right) b_1 A_1 = G_1 P_{J1} V_1 - \frac{G_1}{e}(a_1 + a_2 e^{-L/\lambda_G}) + (\frac{G_1^{\uparrow}}{\sigma_F^{\uparrow}} + \frac{G_1^{\downarrow}}{\sigma_F^{\downarrow}})\frac{\sigma_F}{e} b_1 \tag{2-14}$$

At the interface 2,

$$I_{2s} = 2\left(\frac{\sigma_G}{e\lambda_G}\right) a_2 W_{G2} = -2\left(\frac{\sigma_F}{e\lambda_F}\right) b_2 A_2 = G_2 P_{J2} V_2 - \frac{G_2}{e}(a_2 + a_1 e^{-L/\lambda_G}) + (\frac{G_2^{\uparrow}}{\sigma_F^{\uparrow}} + \frac{G_2^{\downarrow}}{\sigma_F^{\downarrow}})\frac{\sigma_F}{e} b_2 \tag{2-15}$$

Also, the total current at interface 1 is equal to $I_1 = I_{1\uparrow} + I_{1\downarrow}$. Hence,

At interface 1,

$$I_1 = I_{1\uparrow} + I_{1\downarrow} = G_1 V_1 - \frac{G_1 P_{J1}}{e}(a_1 + a_2 e^{-L/\lambda_G}) + (\frac{G_1^{\uparrow}}{\sigma_F^{\uparrow}} - \frac{G_1^{\downarrow}}{\sigma_F^{\downarrow}})\frac{\sigma_F}{e} b_1 = I \tag{2-16}$$

And at interface 2, the total charge current is 0. Hence,

$$I_2 = I_{2\uparrow} + I_{2\downarrow} = G_2 V_2 - \frac{G_2 P_{J2}}{e}(a_2 + a_1 e^{-L/\lambda_G}) + (\frac{G_2^{\uparrow}}{\sigma_F^{\uparrow}} - \frac{G_2^{\downarrow}}{\sigma_F^{\downarrow}})\frac{\sigma_F}{e} b_2 = 0 \tag{2-17}$$

Now we have equations 2-14, 2-15, 2-16, 2-17 with 6 variables (V_1, V_2, a_1, a_2, b_1, and b_2). Simplify them using the following definitions;

$$R_{F1} = \left(\frac{\sigma_F}{\lambda_F}\right) A_1, R_{F2} = \left(\frac{\sigma_F}{\lambda_F}\right) A_2, R_{G1} = \left(\frac{\sigma_G}{\lambda_G}\right) W_{G1}, R_{G2} = \left(\frac{\sigma_G}{\lambda_G}\right) W_{G2},$$

We can get

$$I = \frac{V_1}{R_1} - \frac{P_{J1}}{R_1 e}(a_1 + a_2 e^{-L/\lambda_G}) + (\frac{1+P_{J1}}{1+p_F} - \frac{1-P_{J1}}{1-p_F})\frac{1}{eR_1} b_1 \tag{2-18}$$

$$0 = \frac{V_2}{R_2} - \frac{P_{J2}}{R_2 e}(a_2 + a_1 e^{-L/\lambda_G}) + (\frac{1+P_{J2}}{1+p_F} - \frac{1-P_{J2}}{1-p_F})\frac{1}{eR_2} b_2 \tag{2-19}$$

$$b_1 = \frac{1}{2} p_F I e R_{F1} - \left(\frac{R_{F1}}{R_{G1}}\right) a_1 \tag{2-20}$$

$$\frac{2a_1 R_1}{R_N} = P_{J1} V_1 - \frac{1}{e}(a_1 + a_2 e^{-L/\lambda_G}) + (\frac{1+P_{J1}}{1+p_F} - \frac{1-P_{J1}}{1-p_F})\frac{b_1}{e} \tag{2-21}$$

$$\frac{R_G}{R_F} a_2 = -b_2 \tag{2-22}$$

$$2\frac{R_2}{R_N} a_2 = P_{J2} V_2 - \frac{1}{e}(a_2 + a_1 e^{-L/\lambda_G}) + (\frac{1+P_{J2}}{1+p_F} - \frac{1-P_{J2}}{1-p_F})\frac{1}{e} b_2 \tag{2-23}$$

Solving these 6 equations for V2 leads to the result.

$$V_2 = \pm 2IR_G e^{-L/\lambda_G} \left(\frac{P_{J1}\frac{R_{J1}}{R_{G1}}}{1-P_{J1}^2} + \frac{P_{F1}\frac{R_{F1}}{R_{G1}}}{1-P_{F1}^2} \right) \times \left(\frac{P_{J2}\frac{R_{J2}}{R_{G2}}}{1-P_{J2}^2} + \frac{P_{F2}\frac{R_{F2}}{R_{G2}}}{1-P_{F2}^2} \right) \times$$

$$\left(\left(1 + \frac{2\frac{R_1}{R_{G1}}}{1-P_{J1}^2} + \frac{2\frac{R_{F1}}{R_{G1}}}{1-P_{F1}^2} \right) \times \left(1 + \frac{2\frac{R_2}{R_{G2}}}{1-P_{J2}^2} + \frac{2\frac{R_{F2}}{R_{G2}}}{1-P_{F2}^2} \right) - e^{-2L/\lambda_G} \right)^{-1} \qquad (2\text{-}24)$$

in which means the parallel state and anti-parallel state for the injector (Co_1) and detector (Co_2). Since the nonlocal MR is defined as $\Delta R_{NL} = (V_{2\uparrow\uparrow} - V_{2\uparrow\downarrow}) / I$, it could be expressed by:

$$\Delta R_{NL} = 4R_G e^{-L/\lambda_G} \left(\frac{P_{J1}\frac{R_{J1}}{R_{G1}}}{1-P_{J1}^2} + \frac{P_{F1}\frac{R_{F1}}{R_{G1}}}{1-P_{F1}^2} \right) \times \left(\frac{P_{J2}\frac{R_{J2}}{R_{G2}}}{1-P_{J2}^2} + \frac{P_{F2}\frac{R_{F2}}{R_{G2}}}{1-P_{F2}^2} \right) \times$$

$$\left(\left(1 + \frac{2\frac{R_1}{R_{G1}}}{1-P_{J1}^2} + \frac{2\frac{R_{F1}}{R_{G1}}}{1-P_{F1}^2} \right) \times \left(1 + \frac{2\frac{R_2}{R_{G2}}}{1-P_{J2}^2} + \frac{2\frac{R_{F2}}{R_{G2}}}{1-P_{F2}^2} \right) - e^{-2L/\lambda_G} \right)^{-1} \qquad (2\text{-}25)$$

There are two limits for the contact resistance of the interface 1 and 2. First, when two contacts are both tunneling contacts, $R_{J1} >> R_{G1}$, and $R_{J2} >> R_{G2}$, then,

$$\Delta R_{NL} = P_{J1} P_{J2} R_G e^{-L/\lambda_G} \qquad (2\text{-}26)$$

When two contacts are both transparent contacts, $R_{J1} = R_{J2} = 0$. then,

$$\Delta R_{NL} = 4\frac{1}{R_G} \left(\frac{P_{F2}R_{F2}}{(1-P_{F2}^2)} \right) \left(\frac{P_{F1}R_{F2}}{(1-P_{F2}^2)} \right) \frac{e^{-L/\lambda_G}}{1-e^{-2L/\lambda_G}} \qquad (2\text{-}27)$$

This part will be discussed in detail in chapter 7.

2.3 The relationship of local MR and nonlocal MR

The local MR is expected theoretically to be twice the nonlocal MR. Following the method of calculating the nonlocal MR by Fert and Lee [9], the nonlocal MR geometry (fig. 2-4c) could be viewed as the sum of the two different geometries in fig. 2-4a and fig. 2-4b.

For geometry shown in fig. 2-4a, there is a current I/2 across the interface of the Co detector and graphene. When the two electrodes are parallel, the voltage difference between the detector electrode and graphene spin dependent chemical potential at the outside is set to be V_P. And when the two electrodes are anti-parallel, the voltage difference is set to be V_{AP}. As the geometry shown in fig. 2-4b, there is a negative current I/2 across the interface of the Co detector and graphene. Hence, the voltage difference between the detector and graphene will be $-V_{AP}$ and $-V_P$ for the parallel state and anti-parallel state due to the time reversal symmetry. Hence, the nonlocal MR will be:

$$\Delta R_{NL} = \frac{\Delta V_{geometry\_a} + \Delta V_{geometry\_b}}{I} = \frac{(V_P - V_{AP}) + (-V_{AP} - (-V_P))}{I}$$

$$= 2\frac{(V_P - V_{AP})}{I} \tag{2-28}$$

Interestingly, geometry b is the same as the local MR measurement. The local MR would be equal to:

$$\Delta R_L = \frac{(V_P - V_{AP}) + (-V_{AP} - (-V_P))}{I/2}$$

$$= 4\frac{(V_P - V_{AP})}{I} \tag{2-29}$$

From equation 2-27 and 2-28, we can reach the conclusion that the local MR is twice the nonlocal MR ($\Delta R_L = 2\Delta R_{NL}$). If there is anomalous MR effect, or Hall effect existing

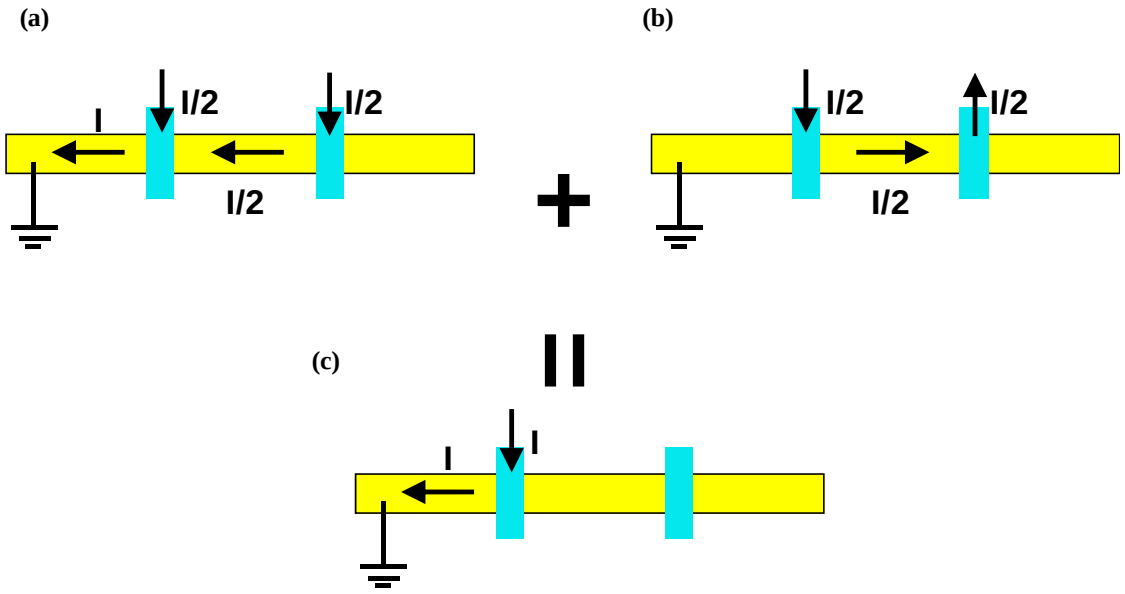

Fig. 2-4, the relationship of local MR and nonlocal MR.

(a) The current distribution of I/2 across injector/graphene and detector/graphene. A net current I will flow between injector and graphene left side. (b) Local MR measurement geometry. The current distribution of I/2 across injector/graphene and detector/graphene. A net current 0 will flow between injector and graphene left side. (c) the nonlocal MR measurement geometry. It is approximately equal to adding up the current distributions of (a) and (b).

at the interface or the Co electrodes, this relationship does not hold, as demonstrated in previous experiments [10].

2.4 Spin relaxation mechanisms

In this section, I discuss possible spin relaxation mechanisms in graphene. Spin relaxation in graphene is a process that brings a non-equilibrium population of spins into a uniform distribution. There are four major spin relaxation mechanisms [11].

(i) The Elliot-Yafet (EY) mechanism, in which the electron has a chance to flip its spin at each scattering by impurities or phonons. Hence, more momentum scattering will lead to shorter spin lifetimes [12, 13].

(ii) The D'yakonov-Perel' (DP) mechanism, in which spins precess along the magnetic field that is related to the momentum [14]. The spin direction and frequency change randomly at each scattering. Hence, more momentum scattering will lead to longer spin lifetimes.

(iii) The Bir-Aronov-Pikus mechanism [15]. It is due to the electron-hole exchange interaction, and plays an important role in semiconductors with a high overlap between the wafefunctions of electrons and holes. The fluctuating effective magnetic field generated by the total spin of holes is generated due to the different effective mass of holes.

(iv) The hyperfine interaction. This is due to the hyperfine interaction between the electrons and the nuclear spins.

In graphene, the band structures of electrons and holes are symmetric and the mass of the holes and electrons are the same. Hence, the Bir-Aronov-Pikus mechanism should be very small. Furthermore, in graphene, about 99% of the carbon atoms are C^{12}, which does not have nuclear spins. Also, the interaction between electrons/holes with the nuclei is

weak for free electrons/holes. Hence, the hyperfine interaction is probably also negligible. Therefore, there are two major spin relaxations (EY and DP) in graphene and will be discussed in detail in the following section.

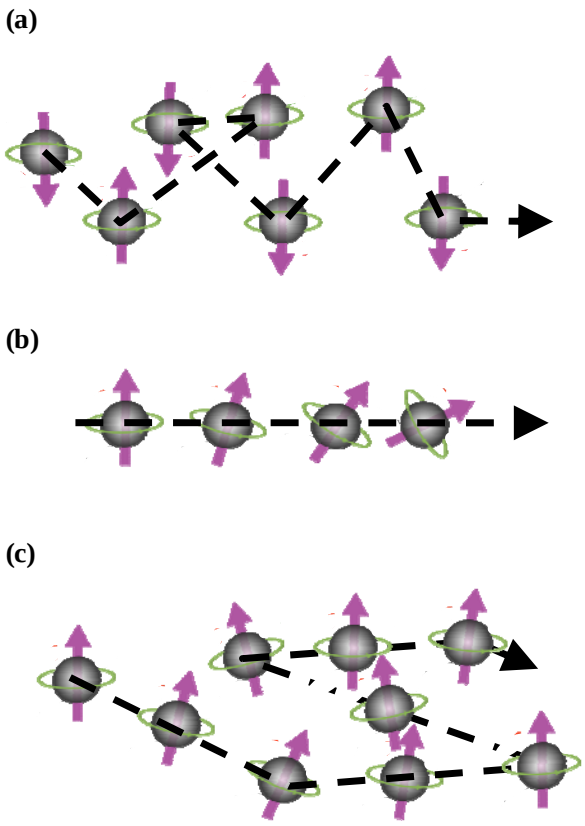

Fig. 2-5, spin relaxation mechanisms.

(a) The EY mechanism, in which electron has a chance to flip its spin at each scattering by impurities or phonons. (b) The DP mechanism, in which the spin precesses along the induced magnetic field. (c) The DP mechanism, The spin direction and precession frequency change randomly at each scattering. Hence, more momentum scattering will lead to longer spin lifetimes. The arrow indicates the momentum direction.

2.4.1 Spin relaxation and precession

There are two main spin relaxation processes, one requires energy exchange, and one does not. Assume the total spin is **S** and the external magnetic field is B in the z direction, the spins diffuse, decay and precess:

$$\frac{dS_z}{dt} = \frac{g\mu_B}{\hbar}(B \bullet S)_z - S_z / T_1 + D\nabla^2 S_z \tag{2-30}$$

$$\frac{dS_x}{dt} = \frac{g\mu_B}{\hbar}(B \bullet S)_x - S_x / T_2 + D\nabla^2 S_x \tag{2-31}$$

$$\frac{dS_y}{dt} = \frac{g\mu_B}{\hbar}(B \bullet S)_y - S_y / T_2 + D\nabla^2 S_y \tag{2-32}$$

in which the g is the electron g factor, μ_B is the Bohr magneton, and D is the spin diffusion coefficient. T_1 is the longitudinal relaxation time and T_2 is the transverse relaxation time, also known as spin dephasing time. Electrically, T_2 could be measured in a spin precession measurement, such as the Hanle measurement, with the magnetic field perpendicular to the spin direction. T_1 could be measured through spacing dependence of the spin signal. Both T_1 and T_2 are affected by the interaction of spins with other degrees of freedom.

2.4.2 EY mechanism

First proposed by Elliot and Yafet, the EY mechanism is due to the local atomic electric field induced by the lattice ions flipping the spins via spin-orbit coupling [12, 13]. As shown in fig. 2-5, the electron has a chance to flip its spin at each scattering by impurities or phonons. The EY mechanism leads to a linear relationship of the spin

relaxation rate and momentum scattering rate, and the spin diffusion length ($\lambda_{sf} = \sqrt{D\tau_{sf}}$) will be linearly proportional to the mean free path.

2.4.3 DP mechanism

The DP mechanism exists in a crystal lacking inversion symmetery with spin orbit coupling. In such systems, a finite electric field will induce a momentum-dependent effective magnetic field *B(k)*. And the spins precess around this effective mangnatic field with a Larmor frequency ω(k) = e/m *B(k)*, as shown in fig. 2-5b. However, random changes of the direction and frequency of the spins will lead to less spin relaxation and longer spin lifetimes (fig. 2-5c). In other words, the spin relaxation rate will be inversely proportional to the momentum scattering rate, which is the opposite of EY mechanism.

2.4.4 Spin orbit coupling in graphene

The spin-orbit (SO) coupling in graphene is given by a Rashba-like term in the Hamiltonian [16]: $H_{SO} = -\frac{\Delta}{2}(\hat{\boldsymbol{\sigma}} \times \hat{\mathbf{s}})_z$, where Δ is the SO coupling strength, $\hat{\mathbf{s}} = (\hat{s}_x, \hat{s}_y)$ are the Pauli matrices for the electron spin and $\hat{\boldsymbol{\sigma}} = (\hat{\sigma}_x, \hat{\sigma}_y)$ are the Pauli matrices for the pseudospin which is associated with the A-B sublattices. There are three types of SO couplings: the intrinsic SO coupling (Δ_{int}), the electrical field (ε_z) induced Rashba SO coupling (Δ_{ε}), and the curvature induced SO coupling (Δ_{curv}). Typical calculated values are Δ_{int} = 0.01 K (10^{-6} eV) [17-19], Δ_{ε} = 0.07 - 0.13 K, (~10^{-5} eV) for ε = 50 V/300 nm, and Δ_{curv} = 0.20 K (1.7x10^{-5} eV) for radius of curvature of 100 nm. The total SO coupling will be the sum of these three parts ($\Delta = \Delta_{int} + \Delta_{\varepsilon} + \Delta_{curv}$).

Typically, the EY mechanism should be more important for "dirty" samples and the DP mechanism should be more important for "clean" samples. The spin relaxation time for the EY mechanism, τ_{EY}, is given by $\tau_{EY} \sim \tau(\hbar v_F k_F)^2 / \Delta^2$, where τ is the momentum scattering time [16]. The spin relaxation time for the DP mechanism, τ_{DP}, is given by $\tau_{DP} \sim \tau^{-1}(\hbar / \Delta)^2$ [16]. The total spin relaxation time, τ_S, is given by $\tau_S^{-1} = \tau_{EY}^{-1} + \tau_{DP}^{-1}$. The spin relaxation is estimated using reasonable graphene parameters ($v_F = 10^6$ m/s, carrier density $n = 10^{12}$ cm^{-2} , $k_F = \sqrt{2\pi n}$). For the intrinsic SO coupling ($\Delta = \Delta_{int} = 10^{-6}$ eV), τ_S can be as high as ~100 μs (at electron mean free path of 4 nm). For the curvature-enhanced SO coupling ($\Delta = \Delta_{curv} = 1.7 \times 10^{-5}$ eV), τ_S can be as high as ~200 ns.

References:

[1] R. Meservey, and P. M. Tedrow, Phys. Rep **238**, 173 (1994).

[2] L. Piraux, S. Dubois, and A. Fert, J. Magn. Magn. Mater. **159**, L287 (1996).

[3] M. Johnson, and R. H. Silsbee, Phys. Rev. Lett. **55**, 1790 (1985).

[4] F. J. Jedema, A. T. Filip, and B. J. van Wees, Nature **410**, 345 (2001).

[5] M. Johnson, and R. H. Silsbee, Physical Review B **76**, 153107 (2007).

[6] F. L. Bakker, A. Slachter, J.-P. Adam, and B. J. Van Wees, Phys. Rev. Lett. **105**, 136601 (2010).

[7] S. Garzon, I. Zutic, and R. A. Webb, Phys. Rev. Lett. **94**, 176601 (2005).

[8] S. Takahashi, and S. Maekawa, Phys. Rev. B **67**, 052409 (2003).

[9] A. Fert, and S.-F. Lee, Phys. Rev. B **53**, 6554 (1996).

[10] N. Tombros, S. J. v. d. Molen, and B. J. van Wees, Phys. Rev. B **73**, 233403 (2006).

[11] J. Fabian, and M. W. Wu, arXiv:1012.2205 (2011).

[12] R. J. Elliott, Phys. Review **96**, 266 (1954).

[13] Y. Yafet, in Solid State Physics, edited by F. Seitz and D. Turnbull (Academic Press Inc., New York, 1963), Vol. 14, p. 1.

[14] M. I. D'yakonov, and V. I. Perel', Sov. Phys. State **13**, 3023 (1972).

[15] G. L. Bir, A. G. Aronov, and G. E. Pikus, Sov. Phys. JETP **42**, 705 (1976).

[16] D. Huertas-Hernando, F. Guinea, and A. Brataas, Phys. Rev. Lett. **103**, 146801 (2009).

[17] H. Min, J. E. Hill, N. A. Sinitsyn, B. R. Sahu, L. Kleinman, and A. H. MacDonald, Phys. Rev. B **74**, 165310 (2006).

[18] D. Huertas-Hernando, F. Guinea, and A. Brataas, Phys. Rev. B **74**, 155426 (2006).

[19] Y. Yao, F. Ye, Y.-L. Qi, S.-C. Zhang, and Z. Fang, Phys. Rev. B **75**, 041401(R) (2007).

Chapter 3.

Experimental techniques

Abstract

In this section, I present the detailed device fabrication of graphene spin valves with either transparent contacts, or tunneling contacts. Two major experimental techniques are briefly discussed, including molecular beam epitaxy (MBE), and electron beam lithography (EBL). At the end, I will describe the set up for the electrical measurement.

3.1 Fabrication of graphene spin valves

The detailed fabrication of graphene spin valves includes the following steps:

3.1.1 Preparation of the graphene

The graphene are prepared by the following steps:

1) Cut SiO_2/Si wafers into ~ 0.7 cm × 1 cm pieces with diamond scribe. Use Silicon wafers with a 300nm thick SiO_2 surface layer.

2) Clean these pieces of wafers by ultrasonic cleaning in Acetone twice and IPA once for ~ 10 min, and blow dry using nitrogen gas. Then bake dry on a hotplate at 150 °C for ~ 30 mins.

3) Prepare scotch tape with thin graphite sheet attached to it. Place the tape on top of the HOPG (SPI supplies, ZYA) and rub it with tweezers using light pressure for about 1 min, until there are no air bubbles between the tape and the graphite. Fold and peel he tape several times to create progressively thinner layers of graphite.

4) Rub graphene. Place the tape on top of SiO_2/Si wafer and rub it with tweezers using light pressure for about 1 min, until there are no air bubbles between the tape and the wafer. Then detach the tape very slowly, leaving graphene or graphite on top of SiO_2/Si by the Van der Waals force.

6) Locate the SLG or other multilayer graphene with the optical microscope. The thickness of the graphene could be identified by optical microscope, AFM and Raman spectroscopy [1](fig. 3-1a, b, c).

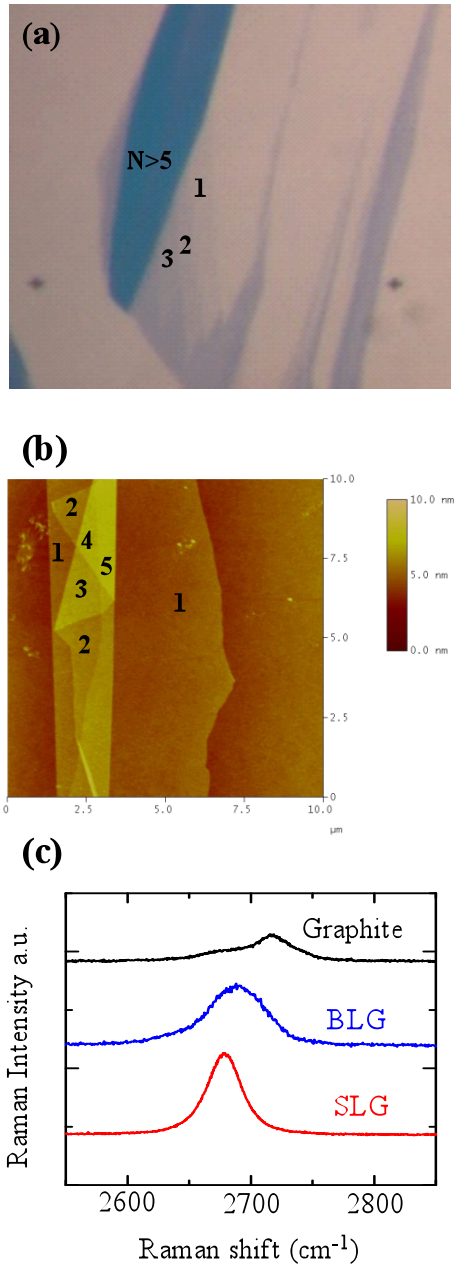

Fig. 3-1, characterization of the graphene thickness.

(a) Optical image of single layer graphene, bilayer graphene, and multilayer graphene. (b) AFM of 1-5 layers graphene. The height of the SLG is ~0.8 nm, and the interlayer height is ~0.37 nm.(c) Raman spectrum of SLG, BLG, and graphite respectively.

3.1.2 Write alignment marks by electron beam lithography (EBL)

The alignment marks are shown in fig. 3-2a including numbers and crosses. The spacing between the numbers and crosses are 500 μm and 50 μm, respectively. The SEM images of the number and cross are shown in fig. 3-2b and 3-2c. The detailed steps are as follows:

1) Calculate the position of graphene using the edge of the Si wafer as the origin.

2) Spin coating of the ebeam resist MMA (MMA 8.5 MAA EL9) using the following recipe. First, increase the rotating speed from 0 to 3000 rpm with an acceleration of 500 rmp/s. Then, keep it at 3000 rmp for 45s. At the end, stop the rotation to 0 with 500 rmp/s deceleration.

3) Bake the sample on a hotplate at 150 °C for 2min and then cool down the sample for 1 min on the work station.

4) Spin coating of the ebeam resist PMMA (950 A4) using the same recipe as MMA.

5) Bake the sample on Hotplate at 170 °C for 20min and cool for 2 min.

6) Use diamond scribe to make some scratches on the top-right corner of the sample for focusing later in EBL.

7) Do EBL and write the align marks on top of the wafer.

8) Develop the sample using MIBK:IPA (1:3) for 80 s, IPA for 60 s, and DI water (~20 s), and then blow dry the sample using N_2 gas.

Now the optical images of the sample are shown in fig. 3-3a (× 900 times) and fig. 3-3b (× 150 times). The contrast between PMMA and SiO_2 is clear enough for alignment in the next step. If one uses other substrates other than SiO_2 that has low contrast with

PMMA, one should grow gold film and then do lift-off. The contrast between Au markers and the substrate should be high enough.

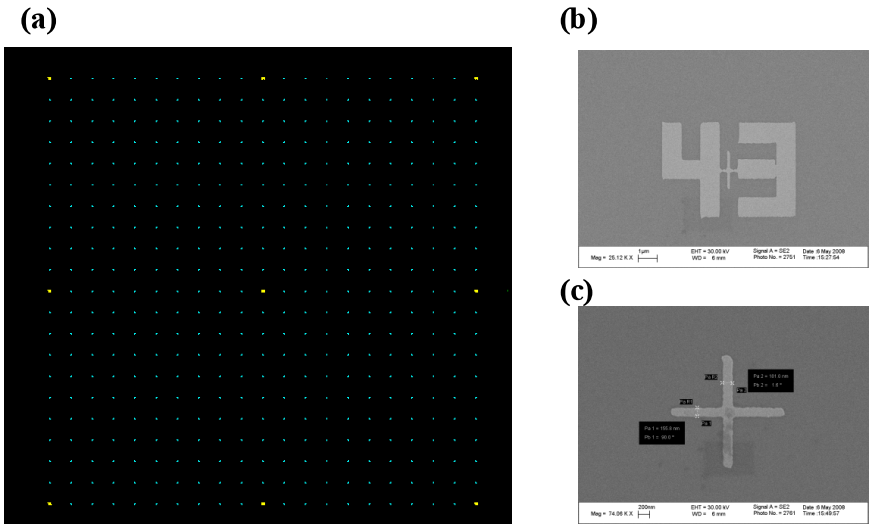

Fig. 3-2, alignment marks.

(a) The align marks consisting of numbers and crosses. (b-c) The SEM images of the number and cross.

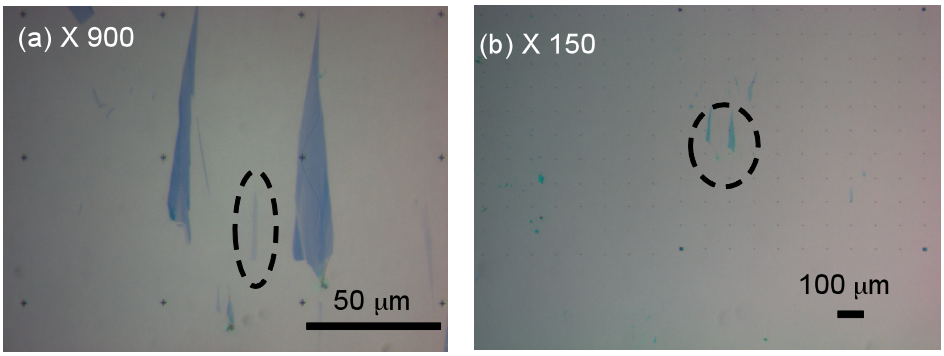

Fig. 3-3, the image of graphene in the alignment marks.

(a) The optical images of the sample × 900 times. (b) The optical images of the sample × 150 times.

3.1.3 Design the pattern using NPGS and Design CAD software

In this step, the NPGS and Design CAD software are used to design the device pattern, as shown in fig. 3-4a. Fig 3-4b shows the center part consists of several electrodes across the graphene. The Co electrodes are of different width from 90 nm to 500 nm to achieve distinct coercive fields.

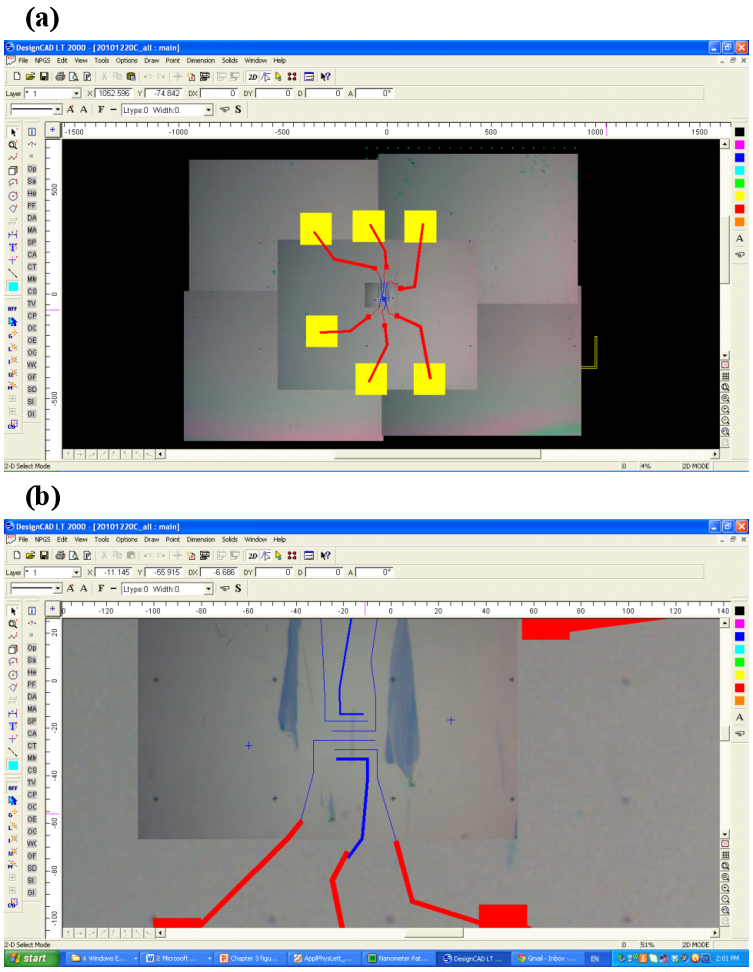

Fig. 3-4, NPGS design of the graphene spin vale pattern.

(a) The whole pattern. (b) The center pattern.

3.1.4 Define the electrodes by EBL

1) A second step of EBL is used to write the device pattern. The center pattern is written using the aperture 20 μm, and the outer pattern uses the aperture 120 μm.

2) Develop the sample using MIBK:IPA (1:3) for 80 s, IPA for 60 s, and DI water (~20 s), and then blow dry the sample using N_2 gas.

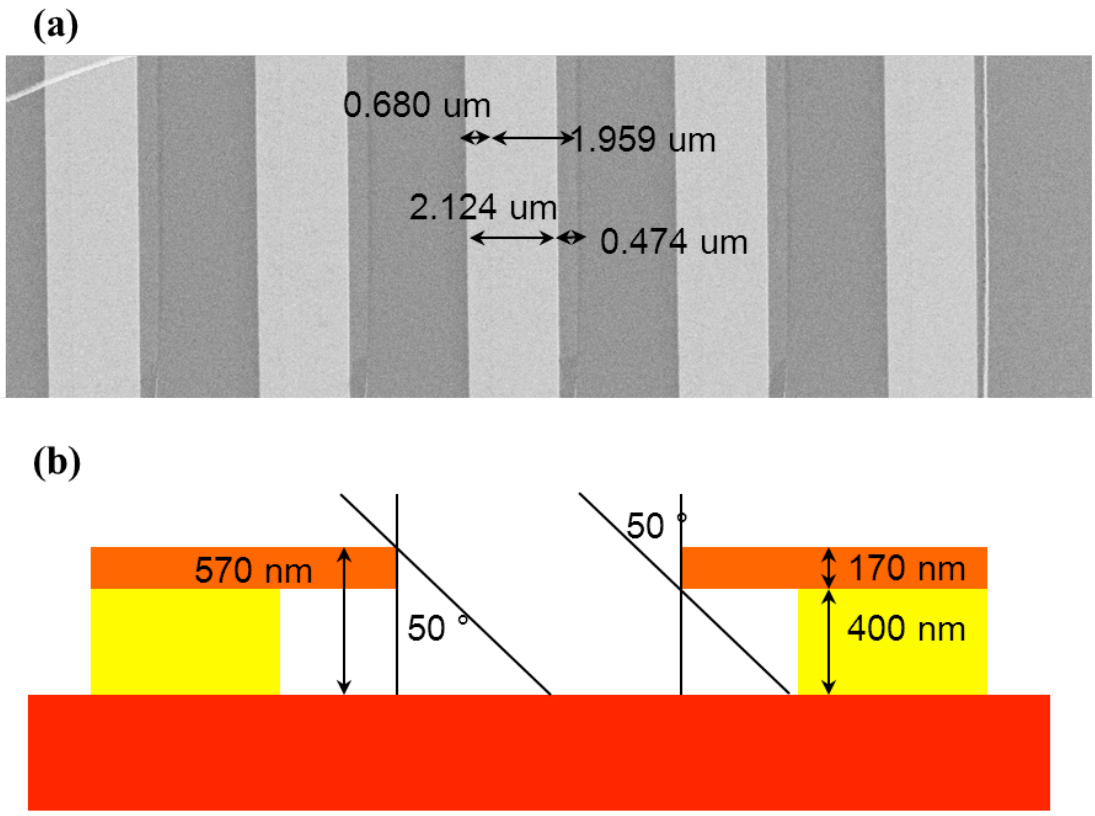

Fig. 3-5, characterization of the undercut formed by the bilayer ebeam resist.

(a) The SEM image of the two Au layer grown by angle deposition of 50 ° and 0 °.

(b) The schematic for the calculation of the thickness of the MMA and PMMA layer.

3) Quickly load the device into MBE chamber for angle evaporation of Co transparent/tunneling contacts. The angle evaporation takes the advantage of the slightly undercut formed due to the different sensitivity of MMA and PMMA to the electron beam. The undercut is characterized by SEM (fig. 3-5a). The two steps of angle evaporation are done at 0 and 50 degrees. Using the length measured by SEM, it is very easy to calculate the height of MMA and PMMA layer. The thickness are of 400 nm and 170 nm, respectively (fig. 3-5b).

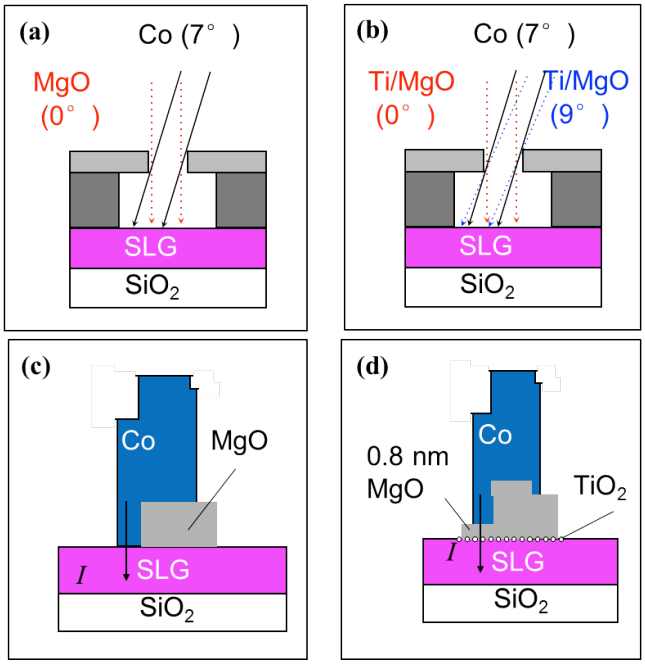

Fig. 3-6, transparent contacts (Co/SLG) and tunneling contacts (Co/MgO, TiO_2/SLG).

(a) The angle evaporation for transparent contacts. (b) The angle evaporation for tunneling contacts. (c-d) The final structures for transparent contacts and tunneling contacts.

3.1.5 Graphene spin valve with transparent contacts

The electrodes are deposited in a molecular beam epitaxy (MBE) system with a base pressure ~ 2×10^{-10} torr. MgO is deposited from a single crystal source by electron-beam evaporation. Co is deposited by thermal evaporation. The typical rates for MgO and Co are ~ 1 Å/min.

The detailed growth steps are shown below (fig. 3-6a):

1) Deposit a 2 nm MgO masking layer with an angle of 0° from normal incidence.

2) Deposit a 80 nm Co layer with an angle of 7°. This angle evaporation reduces the width of the contact area to ~50 nm, which is expected to increase the spin signal [2].

The final structure of the transparent contact is shown in fig. 3-6c. The spin valves with transparent contacts had a yield of 70%, defined as the percentage of electrodes that exhibit spin transport.

3.1.6 Graphene spin valve with tunneling contacts

For this type of contacts, another cell (Ti) in the MBE chamber is used. The Ti cell is a home-made cell with electron-beam evaporation of a Ti rod. The typical rate for Ti is about 0.4 Å /min. The detailed growth steps are shown below (fig. 3-6b):

1) Deposit a 0.12 nm of Ti at both 0° and 9°.

2) Oxidize the Ti in 5×10^{-8} torr of O_2 for 30 minutes to convert the metallic Ti into insulating TiO_2 to promot the growth of ultrathin atomically smooth MgO films [3].

3) A 3 nm of MgO is deposited at an angle of 0° for the masking layer and 0.8 nm of MgO is deposited at an angle of 9° for the tunnel barrier.

4) A 80 nm thick Co electrode is deposited with an angle of 7°.

The final structure of the tunneling contact is shown in fig. 3-6d. The yield of these tunneling contacts is ~5%, defined as the percentage of electrodes that exhibit spin transport and tunneling characteristics.

3.1.7 Al_2O_3 caping

Prior to lift-off, graphene spin valves with either transparent contacts or tunneling contacts are capped with 5 nm Al_2O_3 to protect the Co from further oxidation (in the cleanroom, evaporation angle is 7 °, the same as the Co growth angle). The pressure during growth is about 8×10^{-7} torr and the rate is ~ 1 Å/s.

3.1.8 Lift-off

The lift-off process is done in PG remover at 70 °C for ~ 30 mins. Then rinse with IPA, and blow dry using N_2 gas.

3.1.9 Graphene spin valve in the relaxation study

In the spin relaxation study with tunneling contacts, we used Au contacts as the outer two electrodes, instead of Co, in order to achieve symmetric Hanle curves. The steps are in the follows:

1) Use NPGS to design only two electrodes at the two ends of the graphene strip after the EBL of alignment marks.

2) Write the pattern using EBL and develop afterwards.

3) Grow Au/Ti (50nm /5 nm) film in cleanroom. The pressure during growth is about 8×10^{-7} torr and the rate is ~ 1.5 Å/s.

4) Lift-off. Note: for this step, the Au film is hard to do lift-off, sometimes, after 1 hour of lift-off, I spray IPA to wash off the Au film and MMA/ PMMA ebeam resist.

Now, the graphene spin valve looks like fig. 3-7a and 3-7b.

5) Anneal the device on the buffer heater at 150 °C for 1 hour in vacuum (10^{-9} torr) (The temperature change rate is 5 °C/min).

6) Spin coating MMA/PMMA as discussed earlier.

7) Write the pattern using EBL for Co electrodes.

8) Grow the tunneling contacts as discussed in 3.1.6.

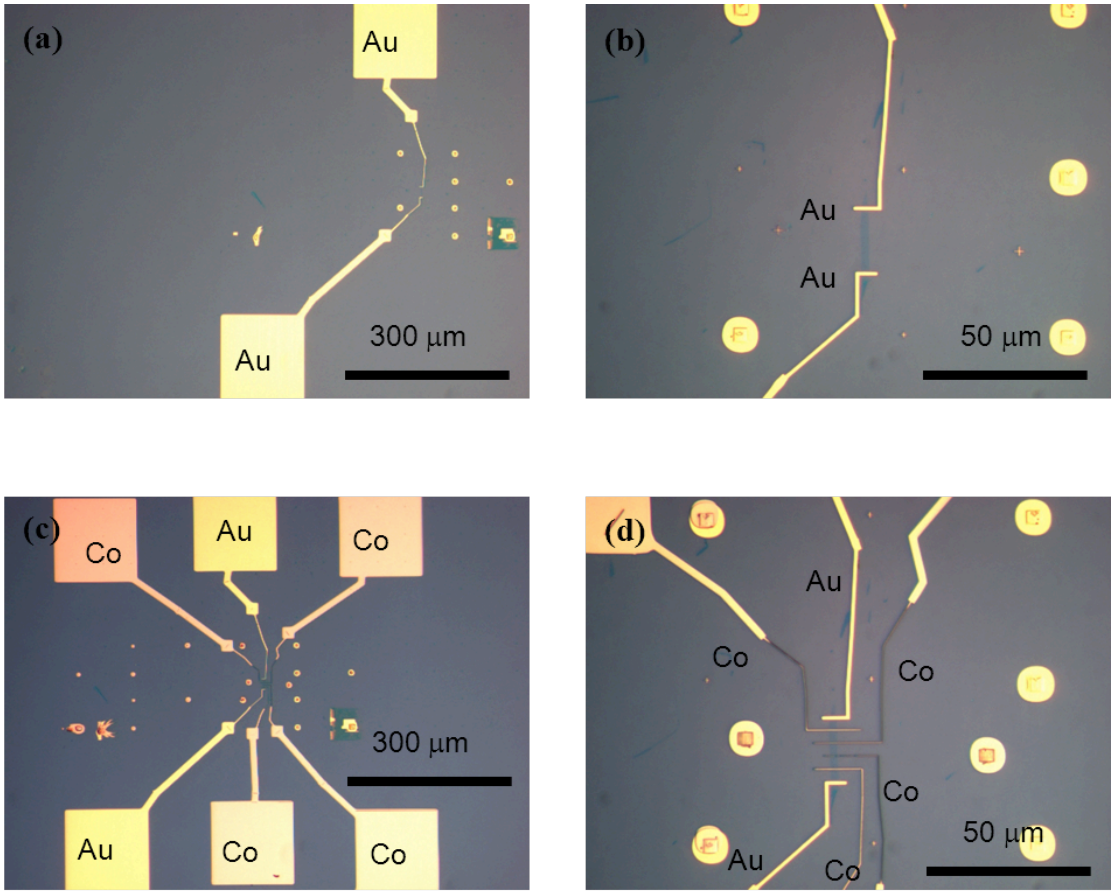

Fig. 3-7, fabrication of graphene spin valve for spin relaxation study.

(a-b) Graphene spin valves with Au contacts. (c-d) Graphene spin valves with Co electrodes.

9) Cap the devices with Al_2O_3, and lift-off. The optical images of the graphene spin valve are shown in fig. 3-7c and 3-7d. It is found that the yield of the tunneling contacts increased to ~30% when the Au electrode fabrication and surface cleaning in vacuum were added.

3.2 Molecular beam epitaxy (MBE)

MBE was invented in the late 1960s at Bell Telephone Laboratories by J. R. Arthur and Alfred Y. Cho [4]. It deposits materials layer by layer with atomic thickness, by creating a "molecular beam" of the growing material (fig. 3-8). It has several properties:

1) Typically in ultra-high vacuum

2) Low deposition rates

3) Good crystal structure.

4) Usually under well control by RHEED.

5) Very expensive.

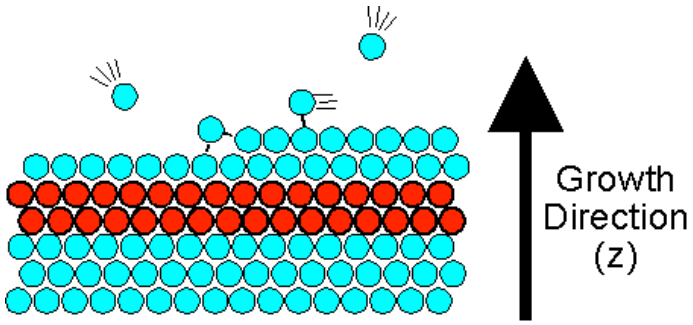

Fig. 3-8, MBE.

In our vacuum system, what we are using are two types of cells. One is thermal evaporation by thermal effusion (Knudsen cell), such as our Co. The Ta filament generates power and heats the Co material over 1000 °C to form a molecular beam. A Eurotherm temperature controller and a Sorensen power supply are used to control the temperature, and thus the growth rate. The other cell is ebeam evaporation, such as our MgO and Ti. The MgO cell is bought from MDC vacuum INC, with a 90 ° angle beam bending. Typical high voltage and emission current for this cell with a rate of 1 Å/min are 4.8 kV, 8-14 mA. The Ti cell is a home-build cell using triode electron bombardment deposition with Ta filament, Ta grid, and the Ti rod [5]. During the growth, the current in the filament is ~ 5 A and kept at the grounded potential, the grid is at a high voltage of ~ 0.25 kV, and the Ti rod is a high voltage of ~ 2 kV. Roughly, the power for the Ti rod is about 50 W to generate a growth rate of 0.5 Å /min.

3.3 Electron beam lithography

Electron beam lithography (EBL) is used to creating tiny structures down to nano scale. The procedure is as follows:

1) A polymer thin film, such as PMMA/MMA bilayer resist covers the surface of the wafer (fig. 3-9a).

2) The film is selectively exposed to the electron beam (fig. 3-9b).

3) After exposure, a solvent (MIBK: IPA, 1:3) is used to wash away the PMMA exposed part. Now the pattern is shown in fig. 3-9c.

4) A thin metal film (Au) used for conducting electrodes is deposited on the wafer (fig. 3-9d).

5) Lift-off in Acetone or PG remover to remove the PMMA resist.

At the end, the electrodes are left on top of the wafer (fig. 3-9e).

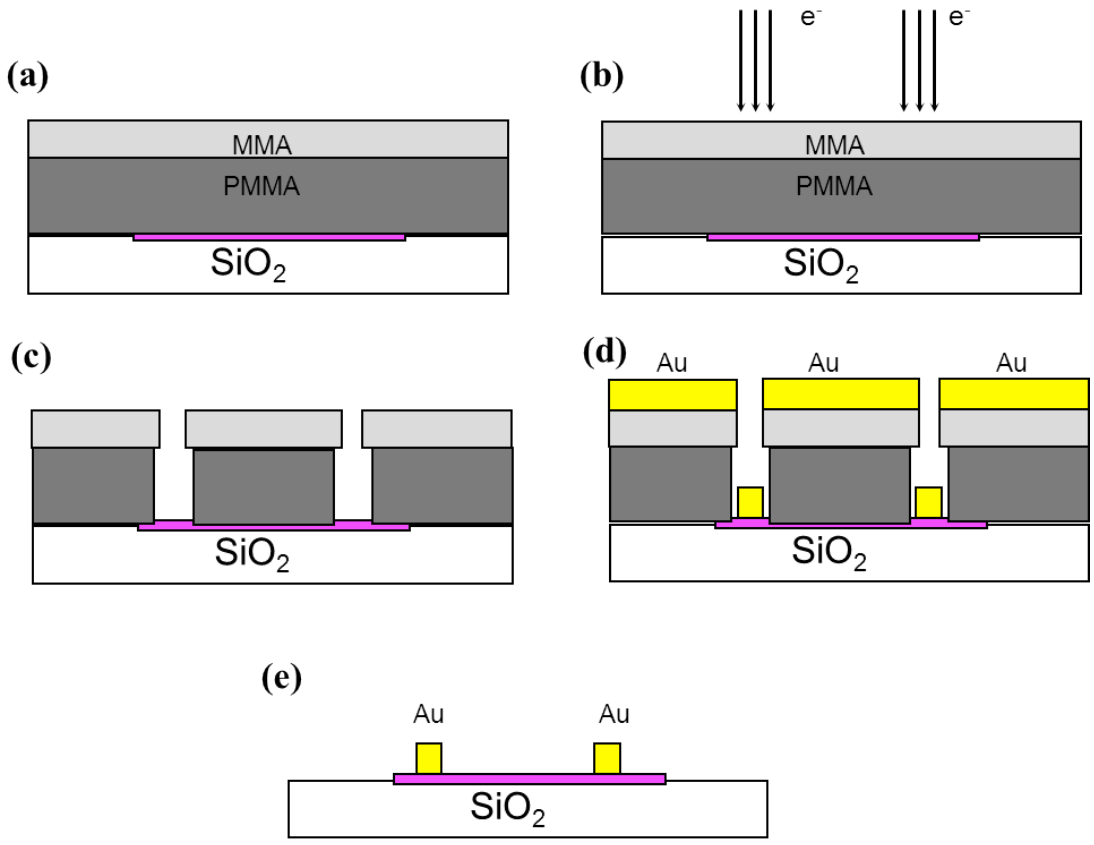

Fig. 3-9, the example of an EBL process.

(a) The SiO_2 wafer is covered with PMMA and MMA bilayer E-beam resist. (b) The bilayer resist is exposed with highly energetic electrons (5 keV to 30 keV). (c) The device after development in MIBK and IPA solutions. (d) Evaporation of gold film on top of the wafer. (e) After lift-off to remove the ebeam resist and the gold covering it.

The most important parameter in E-beam lio is the dose of the E-beam current. It follows

$$D \times A = T \times I \tag{1}$$

in which the D is the dosage, A is the area for exposure, I is the ebeam current, and T is the time needed for the exposure.

3.4 The electrical measurements set up

There are two types of electrical nonlocal MR measurement: DC current spin injection [6] and AC current spin injection [7, 8]. AC current spin injection takes advantage of lock-in techniques, which has better signal to noise ratio. Hence, the AC lock-in techniques are used to measure the nonlocal MR.

The electrical set-up consist of several pieces of equipment (fig. 3-10a), including a current source (Keithley 6221 or a home-made current source), a voltage source (Keithley 2400), a voltage amplifier (Stanford research 560), a home-made breakout box, and a lock-in (Signal recovery 7265). For the measurement in this thesis, the home-made current source is used. It uses operational amplifiers and resistors to generate the AC/DC current from the oscillator or the DC output on the lock-in (fig. 3-10b). The input voltage on the left side is the sum of DC and AC voltage, and current output on the right side is equal to:

$$I = -\left(\frac{V_{AC} + V_{DC}}{R}\right) \tag{2}$$

under the condition that $\frac{R_2}{R_1} = \frac{R_3}{R_4}$.

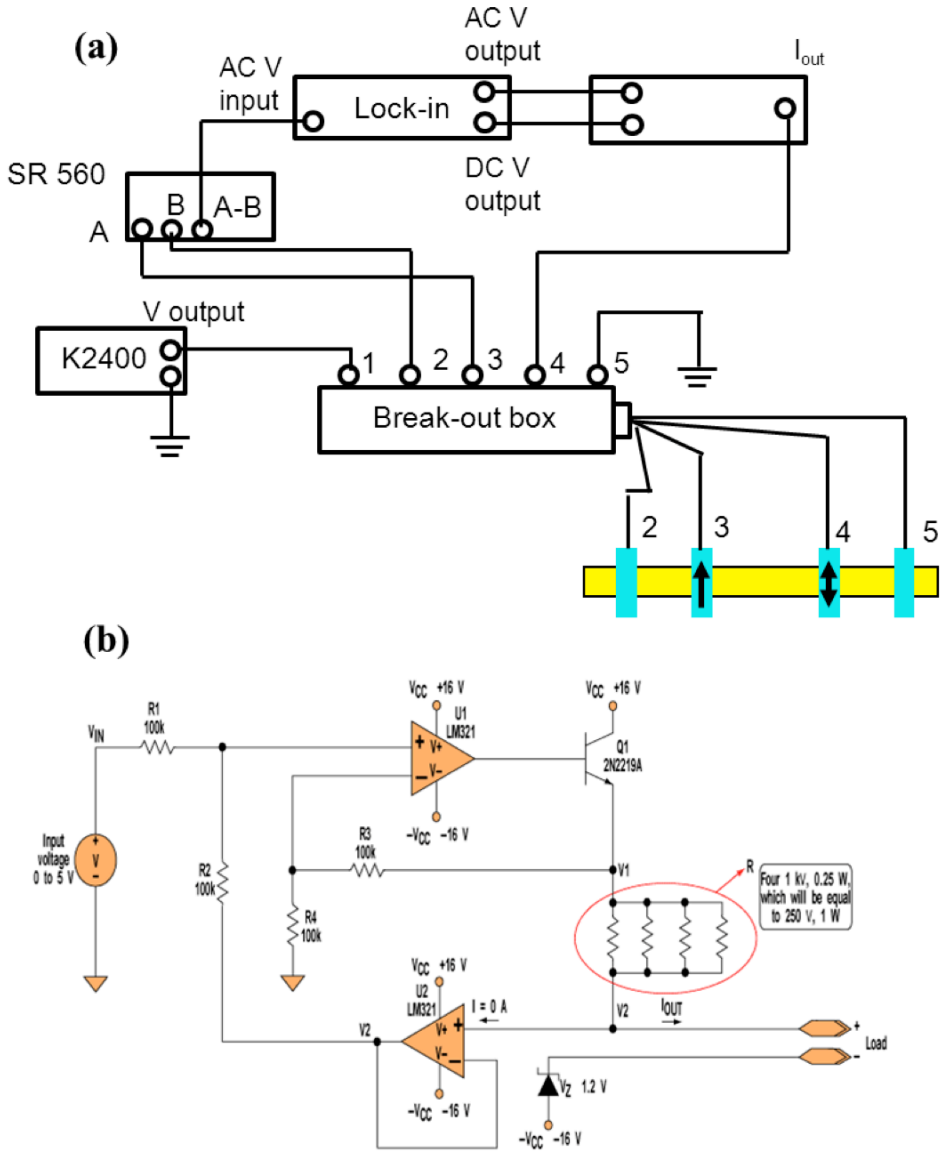

Fig. 3-10, the electrical measurement setup.

(a) The electrical measurement setup. The K2400 applies a voltage between Si and graphene across the SiO_2. (b) The circuit diagram of the home made current source.

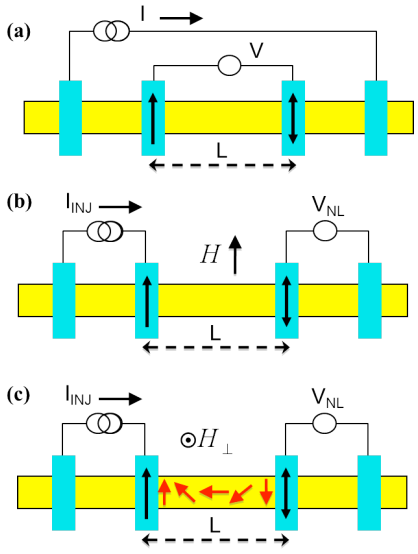

Fig. 3-11, the electrical measurement geometries.

(a) Graphene resistivity measurement. (b) Nonlocal MR measurement. (c) Hanle spin precession measurement.

The electrical set up for the graphene resistivity measurement is shown in fig.3-11a. A small AC current (~ 1 μA) is applied across the two outer electrodes, and the voltage is measured between the center two electrodes.

For the nonlocal MR and Hanle measurement, the AC current is applied across on the left two electrodes, and the voltage is measured on the right two electrodes. For the MR measurement (fig. 3-11b), the magnetic field is applied along the easy axis of the Co electrodes. For the Hanle measurement (fig. 3-11c), the magnetic field is applied perpendicular to the graphene surface. The detailed measurement and fitting are discussed in the later chapters.

The nonlocal MR loops (fig. 3-12b) are calculated from the nonlocal voltage loops fig. 3-12a).

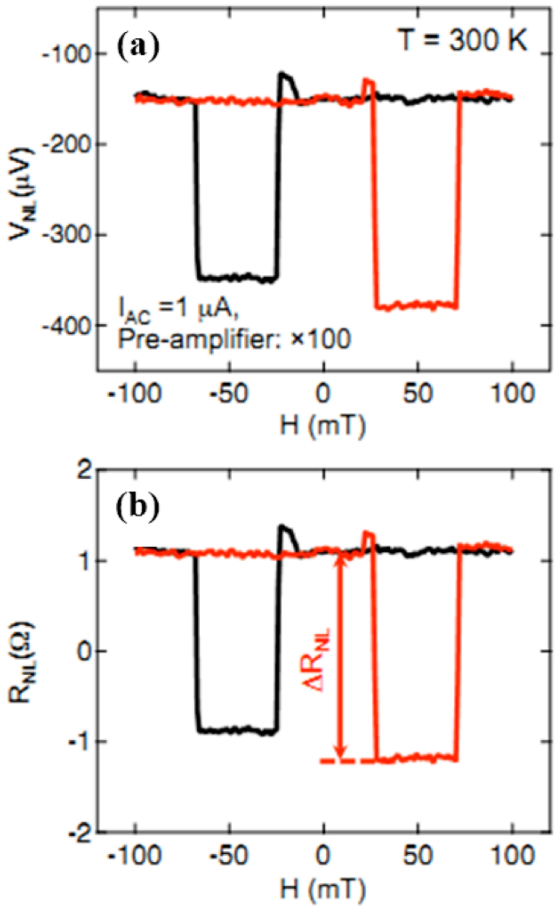

Fig. 3-12, the nonlocal MR measurement.

(a) Raw data of nonlocal voltage as the magnetic field is swept up and down. (b) The corresponding nonlocal MR curve. The arrow indicates the nonlocal MR.

The nonlocal resistance baseline is highly dependent on the frequency of the AC current. I test this using a graphene spin valve with transparent contacts. The smallest baseline is obtained around 10 Hz (fig. 3-13a and 3-13b). we use the frequency of 11 Hz,

13 Hz, 17 Hz for the electrical measurement of the MR to avoid the resonances with the 60 Hz electrical outlets.

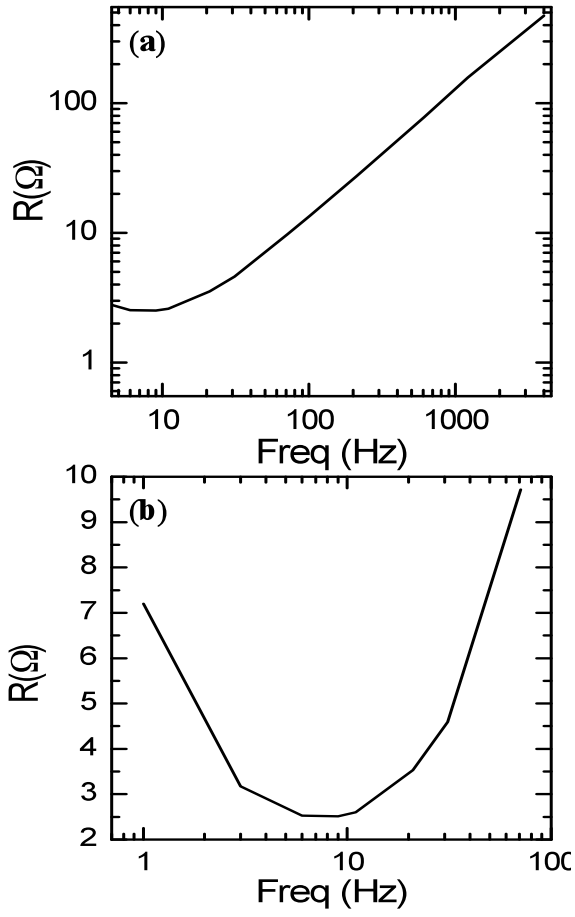

Fig. 3-13, the nonlocal MR background as a function of the frequency for graphene spin valve with transparent contacts.

REFERENCES:

[1] A. K. Geim, and K. S. Novoselov, Nature Materials **6**, 183 (2007).

[2] T. Kimura, Y. Otani, and J. Hamrle, Phys. Rev. B **73**, 132405 (2006).

[3] W. H. Wang, W. Han, K. Pi, K. M. McCreary, F. Miao, W. Bao, C. N. Lau, and R. K. Kawakami, Appl. Phys. Lett. **93**, 183107 (2008).

[4] J. R. A. A.Y. Cho, Progress in Solid State Chemistry **10**, 157 (1975).

[5] R. Verucchi, and S. Nannarone, Rev. Sci. Instrum. **71**, 3444 (2000).

[6] X. Lou, C. Adelmann, S. A. Crooker, E. S. Garlid, J. Zhang, K. S. M. Reddy, S. D. Flexner, C. J. Palmstrom, and P. A. Crowell, Nature Physics **3**, 197 (2007).

[7] M. Johnson, and R. H. Silsbee, Phys. Rev. Lett. **55**, 1790 (1985).

[8] F. J. Jedema, A. T. Filip, and B. J. van Wees, Nature **410**, 345 (2001).

Chapter 4.

Spin injection and precession in single layer graphene[1]

Abstract

In this section, I investigate the spin-dependent properties of single-layer graphene (SLG) spin valves with transparent Co/SLG contacts. First, I study the dependence of the non-local magnetoresistance on electrode spacing. The results indicate a spin diffusion length of ~1.6 μm and a spin injection/detection efficiency (*P*) of 0.013. Second, I observe the Hanle spin precession, which confirms that the non-local spin signal originates from spin injection and transport. Fitting of the Hanle spin precession data yields a spin relaxation time of ~84 ps and a spin diffusion length of ~1.5 μm, which is consistent with the value obtained through the spacing dependence.

---

[1]Published as: Wei Han, K. Pi, W. Bao, K. M. McCreary, Yan Li, W. H. Wang, C. N. Lau, and R. K. Kawakami, Appl. Phys. Lett. 94, 222109 (2009).

4.1 Introduction

Graphene is a unique system for spintronics due to its gate tunable carrier densities, weak spin-orbit coupling, and its quasi-relativistic band structure with symmetric electron and hole bands [1-3]. Recently, there has been considerable experimental success related to spin injection and spin transport in single layer graphene (SLG) and multilayer graphene (MLG) [4-10]. These spin valve devices can be classified into two categories according to the nature of the interfacial junctions between the ferromagnetic (FM) electrodes and the graphene. The first type is the tunnel junction, where the interfacial resistance is much higher than that of graphene. The advantage of this type of contact is that it produces a large spin valve effect by inserting a thin insulating layer to solve the conductivity mismatch problem [4, 11, 12]. The second type is the transparent junction, where the FM is in direct contact with the graphene. Low resistance junctions are advantageous for high-speed applications, and substantial currents can be generated without applying high voltages. Previous studies of electron spin precession in graphene have utilized tunnel junction contacts on SLG [4] and transparent contacts on MLG [13].

Here, we investigate electron spin precession and the spacing dependence of the spin transport in SLG spin valves with transparent contacts via non-local magnetoresistance and Hanle measurements at room temperature. First, the transparent properties are characterized by measuring the contact resistance of the Co/SLG junction. Second, the spacing dependence on the non-local MR spin signal is studied on a single SLG device consisting of several electrodes separated by various distances (1 μm, 2 μm, 3 μm). From this measurement, we obtain a spin diffusion length of ~1.6 μm and a spin

injection/detection efficiency (P) of 0.013. Next, an out-of-plane magnetic field is applied to induce spin precession, which generates Hanle curves in the non-local spin signal. These measurements yield a spin relaxation time of ~84 ps and a spin diffusion length of ~1.5 μm, which is consistent with the value obtained through the spacing dependence.

4.2 Experimental details

The SLG spin valve devices are fabricated using a micromechanical cleavage technique followed by electron-beam lithography and ultra high vacuum deposition of metals. The SLG sheets are mechanically exfoliated from Kish graphite onto a SiO_2(300 nm)/Si substrate where the degenerately doped Si acts as a back gate [14]. The graphene thickness is identified by Raman spectroscopy [15]. The electrodes are defined by eletron-beam lithography using PMMA/MMA bilayer resist. Because the non-local spin signal should be enhanced by decreasing the contact area [16], we utilize angle evaporation to deposit a 2 nm MgO masking layer prior to the deposition of an 80 nm Co layer to reduce the width of the Co/SLG contact area to ~50 nm, which can enhance the spin signal. Prior to lift-off, the device is capped with 5 nm Al_2O_3 to protect the Co from further oxidation. Fig. 4-1a shows a scanning electron microscope (SEM) image of the completed device. The seven Co electrodes labeled “E1”, “E2”, “E3”, “E4”, “E5”, “E6”, and “E7” with widths of 265 nm, 225 nm, 175 nm, 225 nm, 210 nm, 185 nm, and 320 nm respectively. The spacings between the electrodes are 1 μm, 2 μm, 1 μm, 1 μm, 1 μm, 3 μm, and 1 μm, respectively. Fig. 4-1b shows the non-local MR measurement geometry. To achieve different values for the spacing (L) between the central spin-injector and spin-

detector electrodes, we employ three different wiring configurations as indicated in the figure: "configuration A" for L = 1 μm, "configuration B" for L = 2 μm, and "configuration C" for L = 3 μm.

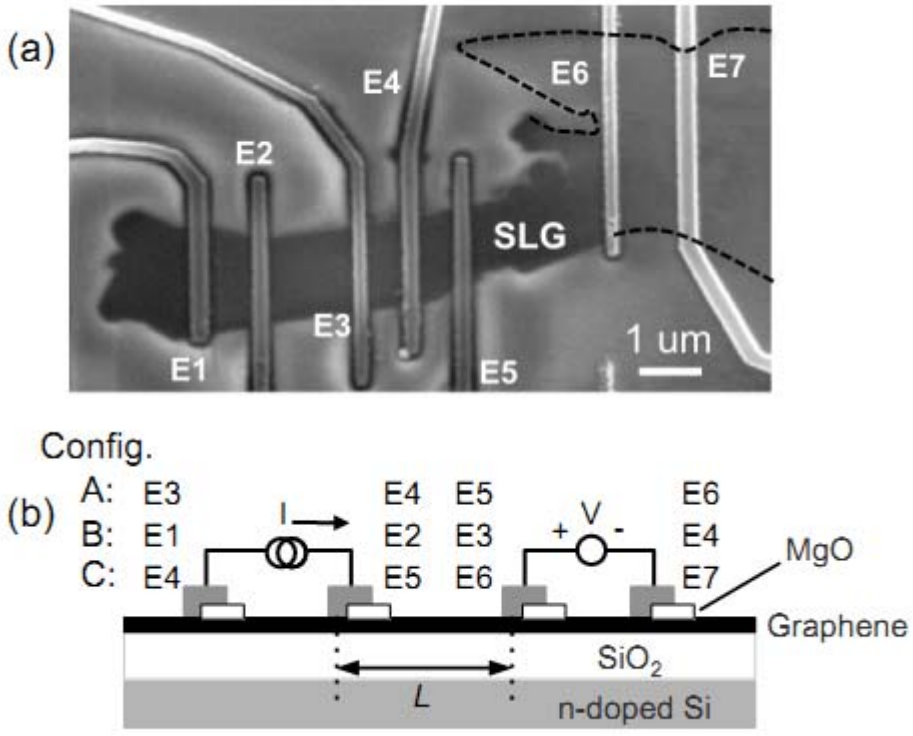

Fig. 4-1, graphene spin valves with transparent contacts.

(a) SEM image of the SLG spin valve device. The darker region corresponds to the SLG. E1, E2, E3, E4, E5, E6, E7 are seven Co electrodes. Dashed lines show the edge of the SLG in a region of the image which has poor contrast. (b) Schematic diagram of the SLG spin valve device and nonlocal MR measurment. Three configurations A, B, C provide different spacing (L) between the central spin-injector and spin-detector electrodes.

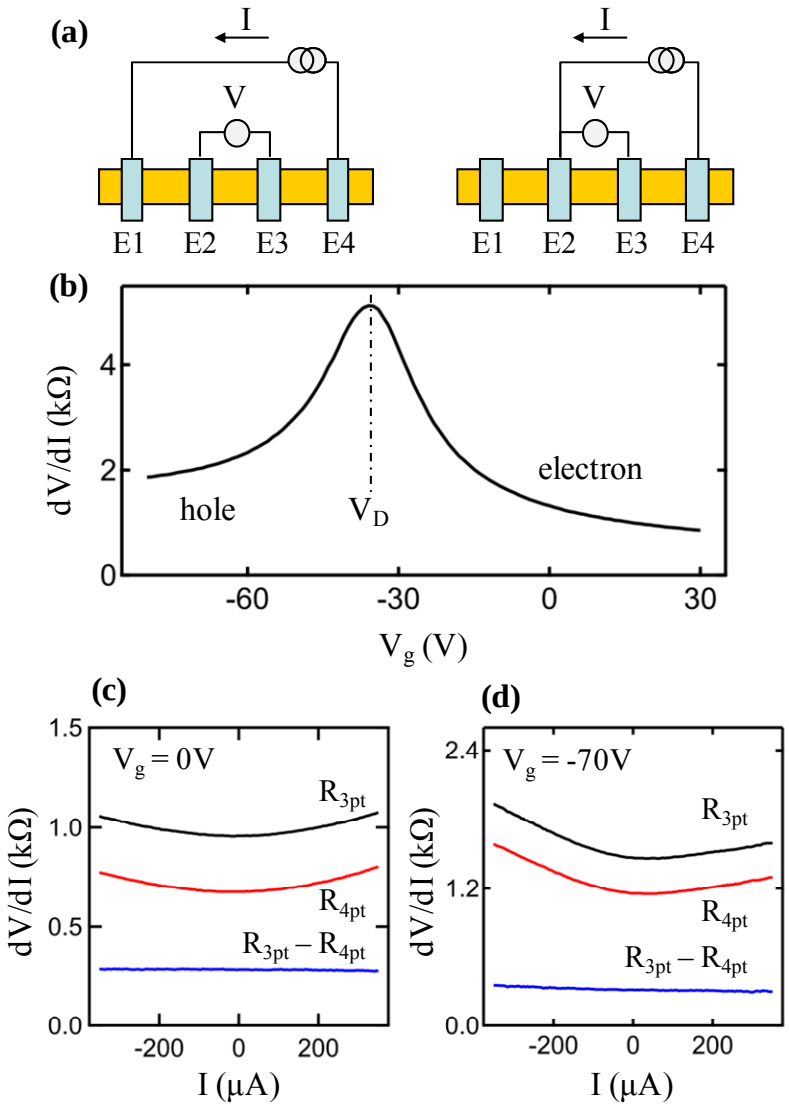

Fig. 4-2, electrical characteristics of the SLG spin valves with transparent contacts.

(a) Geometry of 4-point and 3-point resistance measurements. R_{4pt} measures the differential resistance of the SLG, while $R_{3pt} - R_{4pt}$ measures the differential resistance of the E2/SLG contact and the E2 electrode. (b) SLG resistivity vs. gate voltage. (c) Differential resistance vs. current bias at zero gate voltage at electron-doped regime V_g = 0V. (d) Differential resistance vs. current bias at zero gate voltage at hole-doped regime V_g = -70V.

4.3 Results and discussion

Electrical and magnetoresistance characteristics are measured at room temperature and in vacuum. Electrical characterization is performed using 4-point and 3-point differential resistance measurements as shown in fig. 4-2a. The gate-voltage dependence of the SLG resistivity indicates that the Dirac point is at -38 V (fig. 4-2b). The gate voltage is set to zero for all subsequent measurements. R_{4pt} measures the resistance of the graphene, and R_{3pt} measures the total resistance of the graphene, Co/SLG contact, and the Co electrode. Separating out the resistance contributions of SLG, we find that the contact resistance is ohmic with a value less than 400 Ω for both the electron-doped and hole-doped regime, which indicate that the junctions between the Co and SLG are transparent.

Fig. 4-3 shows the spin injection and spin transport properties investigated in the non-local geometry (fig. 4-1b) [16-18] using standard ac lock-in techniques. The spin injection current, I_{INJ}, is 30 μA rms for the L = 1 μm and L = 2 μm measurements and 50 μA rms for L = 3 μm. The non-local voltage, V_{NL}, is measured as an in-plane magnetic field is applied along the long axes of the Co electrodes and swept through their magnetic hysteresis loops. Fig. 4-3a shows the non-local resistance ($R_{NL} = V_{NL}/I_{INJ}$) as a function of magnetic field for configuration A (L = 1 μm), where a constant background level has been subtracted. Several non-local resistance values are observed which can be associated with the different magnetization alignments of the multiple Co electrodes, as indicated by the arrows. The primary effect, labeled as "ΔR_{NL}" in the figure, compares the parallel and antiparallel states of the central electrodes and is defined as the non-local magnetoresistance (MR). The value of ΔR_{NL} = 112 mΩ is due to spin injection and

transport across the L = 1 μm gap between the central electrodes. Fig. 4-3b and 4-3c are non-local MR scans for L = 2 μm and L = 3 μm, yielding values of 61 mΩ and 2.1 mΩ, respectively, for ΔR_{NL}.

Fig. 4-3d shows the dependence of the non-local MR on the spacing between two center electrodes. The non-local spin signal decreases as a function of spacing and the data is fit using the equation

$$\Delta R_{NL} = \frac{P^2 \lambda_s}{W\sigma} \exp(-L/\lambda_s) \qquad (1)$$

where W is the width for graphene (~1.9 μm), P is the spin injection/detection efficiency, λ_s is the spin diffusion length, and σ is the conductivity of the graphene [4, 19]. Initially, we perform a fit to all the three data points (red/grey curve in fig. 4-3d) and obtain best fit parameters of λ_s = 0.5 μm and P = 0.061. However, the curve itself does not appear to represent the data very well. The problem appears to be the unusually small value of ΔR_{NL} for the 3 μm spacing. This is probably due to a geometrical effect, as the width of the graphene at the detector electrode (E6 for configuration C) increases considerably, so the one-dimensional modeling (equation 1) is probably not appropriate. The top part of electrode E6 in the SEM image is in fact a long distance away from the injection electrode E5, and therefore would tend to reduce the value of ΔR_{NL}. Therefore, we perform the fit without the L = 3 μm data (black curve in fig. 4-3d), and the obtained fit (λ_s = 1.6 μm and P = 0.013) provides a more reasonable representation of the data.

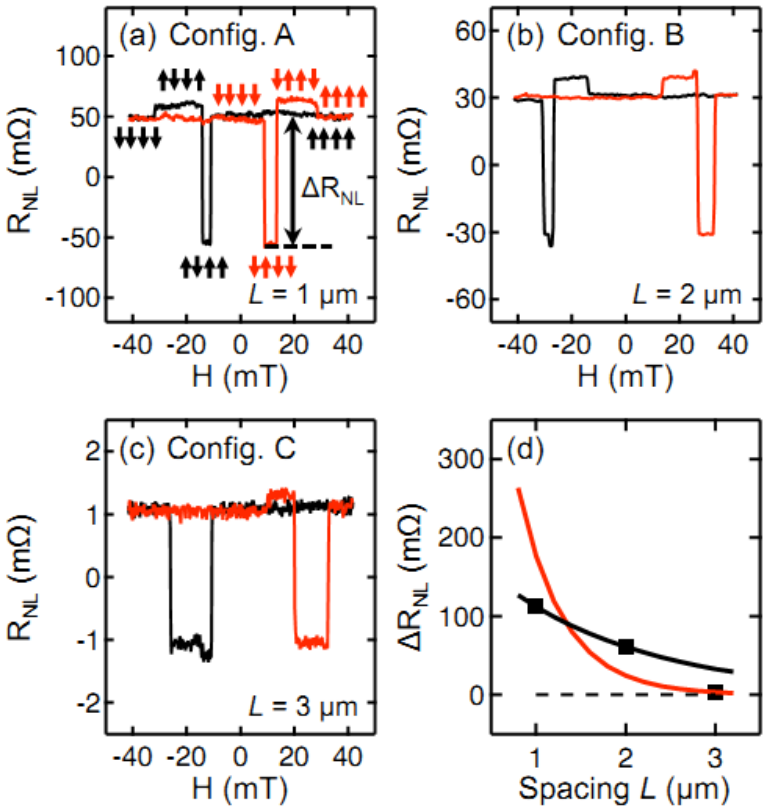

Fig. 4-3, nonlocal MR of SLG spin valves with transparent contacts.

(a-c) Non-local magnetoresistance (MR) scans for the three different configurations: "configuration A" for L = 1 μm, "configuration B" for L = 2 μm, and "configuration C" for L = 3 μm, respectively. A constant background has been subtracted from each curve. The arrows show the magnetization of the four Co electrodes. (d) The dependence of non-local MR on the spacing between the central injector and detector electrodes. The red curve is a fit based on equation 1 using all three data points and the black curve is a fit without the L = 3 μm data.

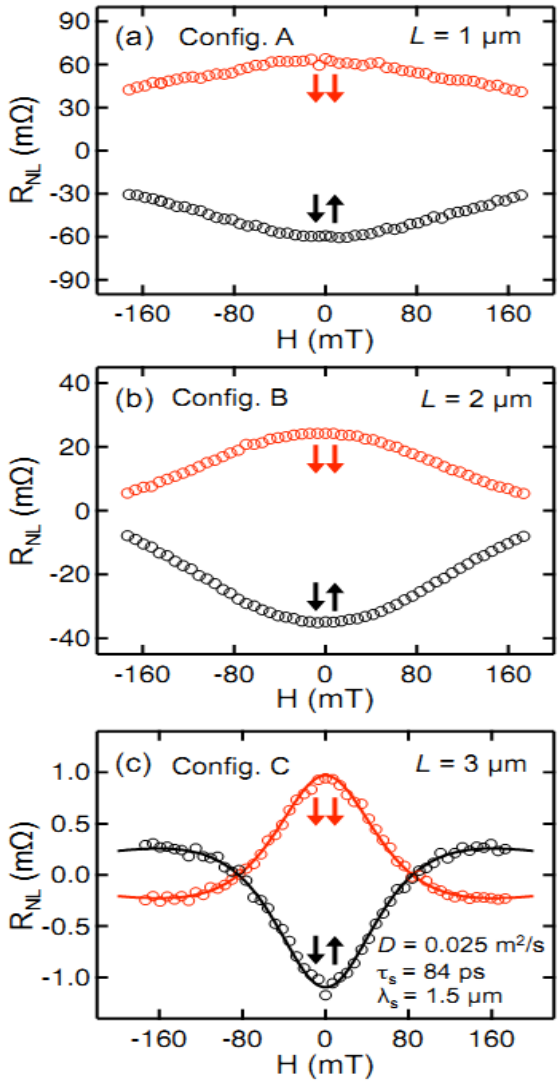

Fig. 4-4, Hanle spin precession.

(a-c) Non-local resistance as a function of the out-of-plane magnetic field for the three different wiring configurations: "configuration A" for L = 1 μm, "configuration B" for L = 2 μm, and "configuration C" for L = 3 μm, respectively. The red (black) circles are data for parallel (antiparallel) alignment of the central electrodes. The red/grey and black lines for the L = 3 μm data are curve fits based on equation 2.

The Hanle effect provides an independent measure of the spin diffusion length and also yields the values of the spin lifetime and diffusion constant [4, 13, 20, 21]. This is achieved by applying an out-of-plane magnetic field ($H_\perp$) that induces spin precession at a Larmor frequency of $\omega_L = g\mu_B H_\perp / \hbar$, where g is the g-factor, μ_B is the Bohr magneton, and $\hbar$ is the reduece Planck's constant. Fig. 4-4a, 4-4b, and 4-4c show Hanle spin precession curves which are obtained by measuring the non-local resistance as a function of $H_\perp$ for configurations A, B, and C, respectively. The top branches (red/gray curves) are for the parallel magnetization state of the central electrodes, and the bottom branches (black curves) are for the antiparallel magnetization state. The characteristic reduction in the spin signal with increasing magnitude of $H_\perp$ is a result of spin-precession induced by the out-of-plane field, which reduces the spin polarization reaching the detector electrode. For L = 3 μm, a nearly complete Hanle curve is obtained (fig. 4-4c). For the smaller spacings, the transit time is reduced so that the Hanle peak is broadened and cannot be fully measured within the range of our electromagnet (fig. 4-4a and 4-4b). Quantitatively, the Hanle curve depends on spin precession, spin diffusion, and spin relaxation and is given by:

$$R_{NL} \propto \pm \int_0^\infty \frac{1}{\sqrt{4\pi D t}} \exp\left[-\frac{L^2}{4Dt}\right] \cos(\omega_L t) \exp(-t/\tau_s) dt \qquad (2)$$

where the + (-) sign is for the parallel (antiparallel) magnetization state, D is the diffusion constant, and τ_s is the spin lifetime [20]. Using this equation, we fit the L = 3 μm data, which is a nearly complete Hanle curve (solid lines in fig. 4-2c). The fitting parameters

obtained are D =2.5×10^{-2} m^{2}s^{-1} and τ_s = 84 ps, which corresponds to a spin diffusion length of $\lambda_s = \sqrt{D\tau_s}$ = 1.5 μm. This value agrees with the spin diffusion length obtained by the spacing dependence (λ_s = 1.6 μm).

4.4 Conclusion

In summary, we performed electrical detection of spin accumulation and spin precession in SLG spin valves with transparent junctions. The dependence of the non-local spin signal on the electrode spacing has been measured on a single SLG device consisting of multiple Co electrodes. This study yields a spin diffusion length of 1.6 μm. Spin precession is detected in the non-local signal by apply an out-of-plane field to generate a Hanle curve. This yields a spin lifetime of 84 ps and a spin diffusion length of 1.5 μm, which is consistent with the value from the spacing dependence. In addition, the observation of the Hanle effect confirms that the observed non-local signals are due to spin injection and transport.

References:

[1] K. S. Novoselov, A. K. Geim, S. V. Morozov, D. Jiang, Y. Zhang, S. V. Dubonos, I. V. Grigorieva, and A. A. Firsov, Science **306**, 666 (2004).

[2] K. S. Novoselov, A. K. Geim, S. V. Morozov, D. Jiang, M. I. Katsnelson, I. V. Grigorieva, S. V. Dubonos, and A. A. Firsov, Nature **438**, 197 (2005).

[3] Y. Zhang, Y.-W. Tan, H. L. Stormer, and P. Kim, Nature **438**, 201 (2005).

[4] N. Tombros, C. Jozsa, M. Popinciuc, H. T. Jonkman, and B. J. van Wees, Nature **448**, 571 (2007).

[5] M. Ohishi, M. Shiraishi, R. Nouchi, T. Nozaki, T. Shinjo, and Y. Suzuki, Japanese Journal of Applied Physics **46**, L605 (2007).

[6] M. Nishioka, and A. M. Goldman, Appl. Phys. Lett. **90**, 252505 (2007).

[7] S. Cho, Y.-F. Chen, and M. S. Fuhrer, Appl. Phys. Lett. **91**, 123105 (2007).

[8] W. H. Wang, K. Pi, Y. Li, Y. F. Chiang, P. Wei, J. Shi, and R. K. Kawakami, Phys Rev. B (Rapid Comm.) **77**, 020402 (2008).

[9] H. Goto, A. Kanda, T. Sato, S. Tanaka, Y. Ootuka, S. Odaka, H. Miyazaki, K. Tsukagohi, and Y. Aoyagi, Appl. Phys. Lett. **92**, 212110 (2008).

[10] W. Han, W. H. Wang, K. Pi, K. M. McCreary, W. Bao, Y. Li, F. Miao, C. N. Lau, and R. K. Kawakami, Phys. Rev. Lett. **102**, 137205 (2009).

[11] A. Fert, and H. Jaffres, Phys. Rev. B **64**, 184420 (2001).

[12] G. Schmidt, D. Ferrand, L. W. Molenkamp, A. T. Filip, and B. J. van Wees, Phys. Rev. B (Rapid Communications) **62**, 4790 (2000).

[13] M. Shiraishi, M. Ohishi, R. Nouchi, T. Nozaki, T. Shinjo, and Y. Suzuki, arXiv:0810.4592, (2008).

[14] F. Miao, S. Wijeratne, Y. Zhang, U. C. Coskun, W. Bao, and C. N. Lau, Science **317**, 1530 (2007).

[15] A. C. Ferrari, J. C. Meyer, V. Scardaci, C. Casiraghi, M. Lazzeri, S. Piscanec, D. Jiang, K. S. Novoselov, S. Roth, and A. K. Geim, Phys. Rev. Lett. **97**, 187401 (2006).

[16] T. Kimura, Y. Otani, and J. Hamrle, Phys. Rev. B. **73**, 132405 (2006).

[17] M. Johnson, and R. H. Silsbee, Phys. Rev. Lett. **55**, 1790 (1985).

[18] F. J. Jedema, A. T. Filip, and B. J. van Wees, Nature **410**, 345 (2001).

[19] S. Takahashi, and S. Maekawa, Physical Review B **67**, (2003).

[20] F. J. Jedema, H. B. Heersche, A. T. Filip, J. J. A. Baselmans, and B. J. van Wees, Nature **416**, 713 (2002).

[21] X. Lou, C. Adelmann, S. A. Crooker, E. S. Garlid, J. Zhang, K. S. Madhukar Reddy, S. D. Flexner, C. J. Palmstrom, and P. A. Crowell, Nature Physics **3**, 197 (2007).

Chapter 5.

Electron-hole asymmetry of spin injection and transport in single layer graphene[1]

Abstract

In this section, I study the spin-dependent properties of single-layer graphene (SLG) spin valves with transparent Co/SLG contacts. I observe that the nonlocal magnetoresisatnce (MR) is proportional to the conductivity of the SLG, which is predicted for transparent ferromagnetic/nonmagnetic contacts. Furthermore, I observe an electron-hole asymmetry of spin injection and transport in SLG, although the electron and hole bands in SLG are symmetric. The non-local MR is roughly independent of DC bias current for electrons, but varies significantly with DC bias current for holes.

---

[1]Published as: Wei Han, W. H. Wang, K. Pi, K. M. McCreary, W. Bao, Yan Li, F. Miao, C. N. Lau, and R. K. Kawakami, Phys. Rev. Lett. 102, 137205 (2009).

5.1 Introduction

A special property of SLG is that the band structure of the electrons and holes are ideally symmetric (similar to carbon nanotubes [1]), so their spin-dependent properties are expected to match. This differs from conventional semiconductors such as GaAs and Si, whose electron and hole bands are highly asymmetric (e.g. different atomic orbital states, different spin-orbit coupling, different effective masses), which leads to very different spin-dependent properties. Thus, the observation of electron-hole asymmetry of a spin-dependent property in SLG would create a unique opportunity to investigate the relationship between carrier charge and spin, separated from the typical effects of band asymmetries found in conventional semiconductors.

In this chapter, I present the observation of electron-hole asymmetry for spin injection and transport in SLG at room temperature, as determined by non-local magnetoresistance (MR) measurements on SLG spin vales with transparent Co contacts [2, 3]. A systematic investigation of the gate voltage dependence and bias dependence of the non-local MR signal shows that when the carriers in the SLG are electrons, the non-local MR is roughly constant as a function of dc current bias, which is consistent with the standard one dimensional (1D) drift-diffusion model of spin injection and transport [3-7]. When the carriers in the SLG are holes, however, the non-local MR is strongly reduced in the negative bias regime (i.e. spin extraction [8]). This differing behavior between the electrons and the holes is a clear demonstration of spin-dependent electron-hole asymmetry, which is most likely due to an interfacial effect at the Co/SLG contact. Understanding the origin of this asymmetry will be crucial for the development of bipolar

spin transport devices utilizing both electrons and holes.

5.2 Experimental details

The devices consist of exfoliated SLG sheets [9, 10] and Co electrodes fabricated by electron-beam lithography using PMMA/MMA bilayer resist (fig. 5-1a). The SiO_2(300 nm)/Si substrate is used as a gate. These spin valves are made of transparent contacts, as discussed in chapter 3. For the two representative samples (A and B), the widths of the electrodes are 225 nm, 210 nm, 175 nm, and 225 nm for sample A and 350 nm, 160 nm, 210 nm, and 180 nm for sample B. The spacings between electrodes for sample A are L_{12} = 1.0 μm, L_{23} = 1.0 μm, and L_{34} = 2.0 μm and for sample B are L_{12} = 1.6 μm, L_{23} = 1.0 μm, and L_{34}= 1.1 μm. The widths of the SLG are ~2 μm for both samples. Raman spectroscopy is used to verify the thickness of the graphene [11]. Fig. 5-1b shows typical spectra from SLG measured on our devices and from bulk graphite for reference. Fig. 5-1c shows a scanning electron microscope image of a completed device, in which the darker region corresponds to the SLG.

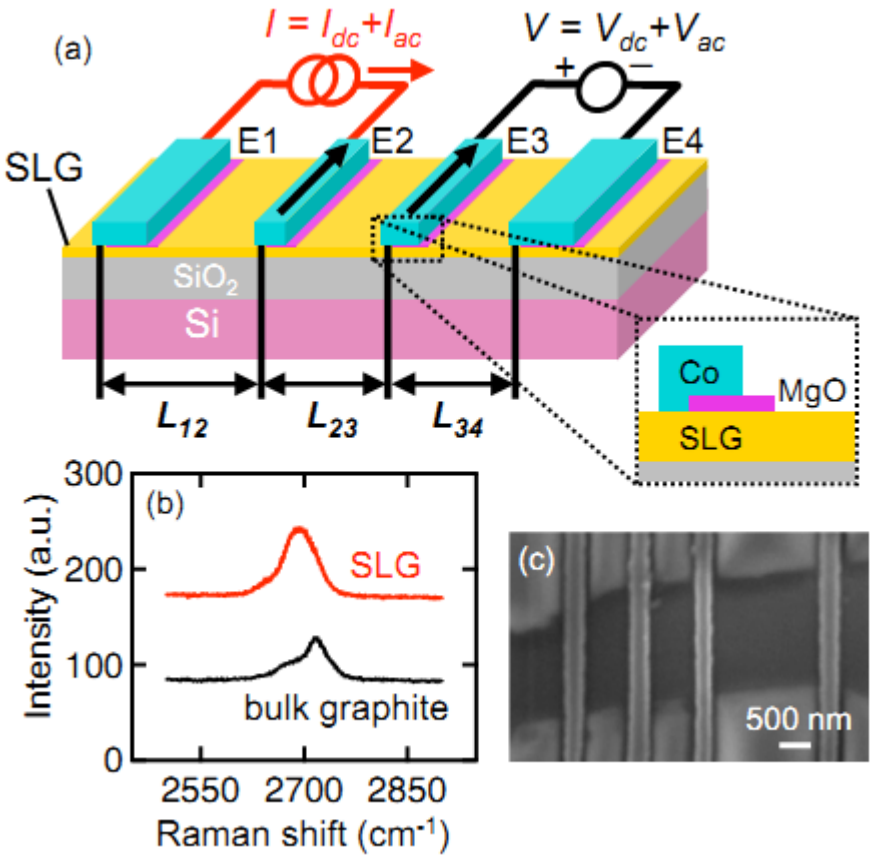

Fig. 5-1, graphene spin valves.

(a) Schematic diagram of the single layer graphene (SLG) spin valve. E1, E2, E3, are E4 are four cobalt electrodes. The Si substrate acts as a back gate. Detail: A MgO layer deposited by angle evaporation to reduce the width of the contact area to ~50 nm. (b) Raman spectroscopy of SLG and bulk graphite. (c) SEM image of a completed device. The darker region corresponds to the SLG.

5.3 Result and discussion

The electrical and non-local magnetoresistance (MR) characteristics are measured in

vacuum at room temperature. Fig. 5-2a and 5-2b show the resistivity of the SLG as a function of gate voltage for samples A and B. Both samples exhibit a peak in resistivity which define the Dirac point, with V_{Dirac} = -34 V for sample A and V_{Dirac} = -32 V for sample B. Sample A has a mobility of 900-1700 cm^2/Vs, while sample B has a mobility of 800-1300 cm^2/Vs. The *I-V* curves measured across electrodes E1 and E2 at different gate voltages indicate transparent contacts between the Co and SLG (Fig. 5-2c and 5-2d). Spin injection and transport are investigated using standard lock-in techniques. A current source applies a dc bias (I_{dc}) and ac excitation (I_{ac} = 30 μA) across electrodes E1and E2 (fig. 5-1a) to generate spin polarization in the SLG beneath electrode E2 by spin injection or extraction. This spin-polarization propagates to E3 via spin diffusion and generates a non-local voltage across electrodes E3 and E4 ($V = V_{dc} + V_{ac}$) due to the spin-sensitive nature of the ferromagnetic electrodes [2-7]. To separate the spin signal from a constant background level, R_{NL} ($\equiv V_{ac}/I_{ac}$) is measured as the magnetic field is swept up and swept down fig. 5-2e and 5-2f) to generate parallel and antiparallel alignments of the central electrodes (E2 and E3). The non-local MR is defined as $\Delta R_{NL} = R_{NL}^{P} - R_{NL}^{AP}$, where R_{NL}^{P} (R_{NL}^{AP}) is the non-local resistance for the parallel (antiparallel) state. Fig. 5-2e shows representative non-local MR scans on sample A measured at zero bias. Comparing the scans, we see that ΔR_{NL} is smallest near the Dirac point (V_g = -30 V) and larger for electron doping (V_g = 0 V) and hole doping (V_g = -70 V). The non-local MR of sample B shows similar behavior, with ΔR_{NL} smallest when V_g is close to the Dirac point, and higher for larger carrier densities (fig. 5-2f).

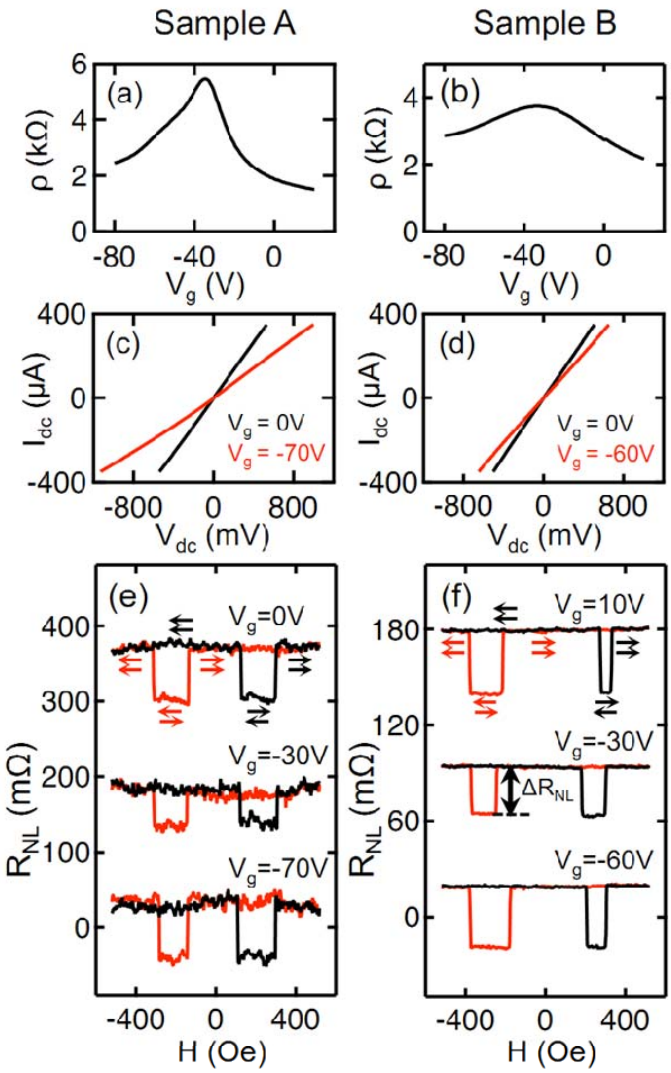

Fig. 5-2, electrical characteristics and non-local MR scans of samples A and sample B. (a,b) SLG resistivity vs. gate voltage of sample A and sample B. (c,d) I-V curves between electrodes E1 and E2 of sample A and sample B. (e) Non-local MR scans of sample A at three different gate voltages (Vg = 0 V, -30 V, and -70 V), as the magnetic field is swept up (black curve) and swept down (red curve). A constant background is subtracted and the curves are offset for clarity. (f) Non-local MR scans of sample B at Vg = 10 V, -30 V, and -60 V.

Fig. 5-3a and 5-3b show the detailed gate-dependence of ΔR_{NL} at zero bias on samples A and B (circles). ΔR_{NL} has a minimum near the Dirac point and has increasing values for increasing electron density ($V_g > V_{Dirac}$) as well as for increasing hole density ($V_g < V_{Dirac}$). This behavior can be understood in terms of the 1D drift-diffusion model, which predicts that ΔR_{NL} should be proportional to the conductivity of the nonmagnetic material, σ_N, (SLG in our case) for transparent ferromagnetic/nonmagnetic contacts (e.g. equation 4 in ref. [6], equation 1 in ref. [3] with $M >> 1$). The solid lines in fig. 5-3a and 3b show the conductivity as a function of gate voltage. The good agreement indicates that we have realized the $\Delta R_{NL} \sim \sigma_N$ dependence for transparent contacts. This illustrates a powerful aspect of graphene as a material to examine spin-polarized transport, where the ability to tune the conductivity provides a novel approach to investigate theoretical predictions.

To gain insight into the characteristics of spin injection and transport in SLG, we systematically investigate the gate dependence and bias dependence of ΔR_{NL}. Fig. 5-3c and 5-3d show the gate-dependence of ΔR_{NL} for samples A and B for I_{dc} = +300 μA (squares), 0 μA (circles), and -300 μA (triangles). The polarity of I_{dc} is defined in fig. 5-1a. For positive bias, the gate-dependence of ΔR_{NL} follows the zero bias data. On the other hand, when the bias is negative and the carriers are holes (triangles, $V_g < V_{Dirac}$), a strong reduction of ΔR_{NL} is observed in both samples. In this case, the holes in the SLG are driven toward electrode E2 and become spin-polarized due to spin-dependent reflection from the ferromagnetic interface (i.e. spin extraction [8]). A very interesting aspect is that the reduction of ΔR_{NL} is observed for spin extraction of holes, but not for

the spin extraction of electrons.

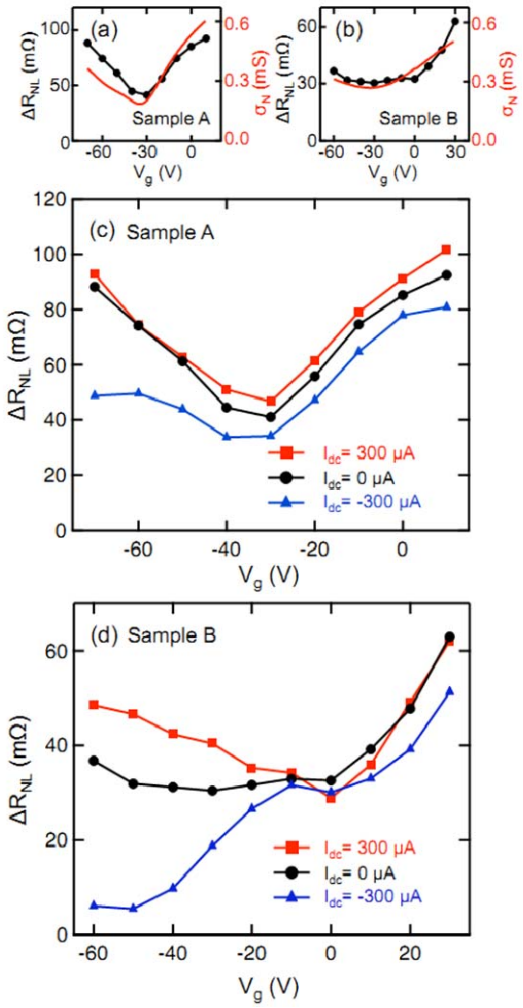

Fig. 5-3, nonlocal MR as a function of gate voltage.

(a) Non-local MR at zero bias (black circles) and conductivity (red) vs. gate voltage for sample A. (b) Non-local MR at zero bias (black circles) and conductivity (red) vs. gate voltage for sample B. (c) The dependence of non-local MR on the gate voltage for sample A at bias current 300 μA (red squares), 0 μA (black circles), -300 μA (blue triangles). (d) The dependence of non-local MR on the gate voltage for sample B at bias current 300 μA (red squares), 0 μA (black circles), -300 μA (blue triangles).

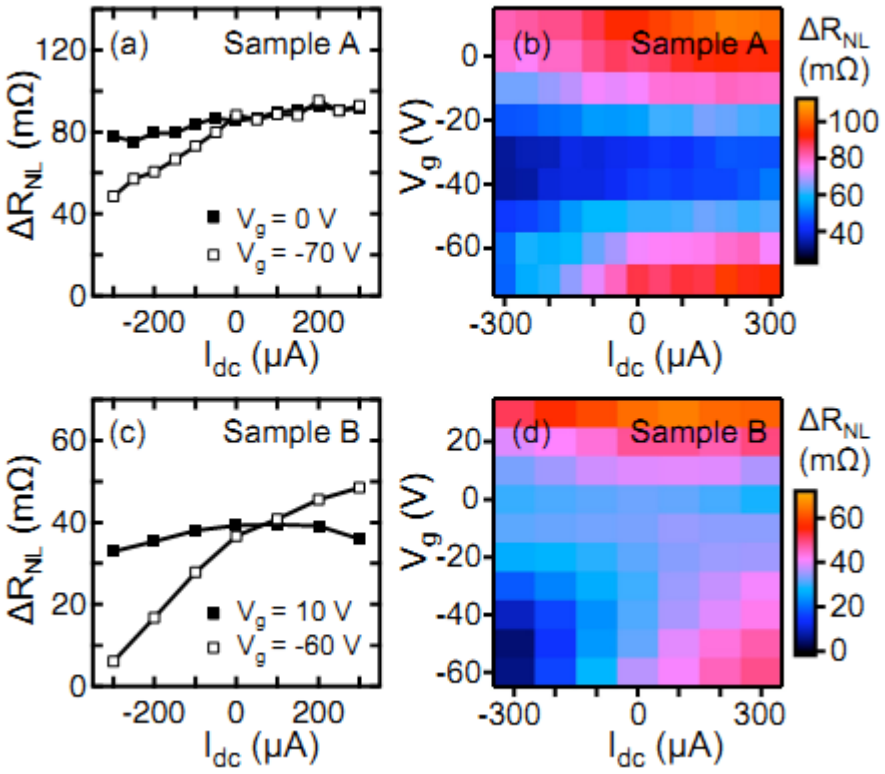

Fig. 5-4, electron-hole asymmetry.

(a) Non-local MR as a function of dc bias current for sample A at Vg = 0 V (electrons, solid squares) and -70 V (holes, open squares). (b) Non-local MR as a function of gate voltage and dc bias current for sample A. (c) Non-local MR as a function of dc bias current for sample B at Vg = 10 V (electrons, solid squares) and -60 V (holes, open squares). (d) Non-local MR as a function of gate voltage and dc bias current for sample B.

Fig. 5-4a shows the bias dependence of ΔR_{NL} on sample A for V_g = 0 V (electrons, solid squares) and for V_g = -70 V (holes, open squares). For electrons, there is only a slight variation in ΔR_{NL} as a function of I_{dc}. For holes at positive bias, the behavior of ΔR_{NL} is similar to the electron case. For holes at negative bias, however, there is a significantly stronger variation of ΔR_{NL} as a function of dc current bias, with decreasing ΔR_{NL} at larger negative biases. Fig. 5-4c shows the bias dependence of ΔR_{NL} on sample B for V_g = 10 V (electrons, solid squares) and for V_g = -60 V (holes, open squares). Similar to sample A, for electrons the value of ΔR_{NL} is roughly constant as a function of dc bias current. For holes under negative bias, there is a very strong change of ΔR_{NL} with dc current bias, nearly approaching zero at I_{dc} = -300 μA. The images in fig. 5-4b and 5-4d show the dependence of ΔR_{NL} as a function of both gate voltage and dc current bias for samples A and B, respectively. The two main trends, namely the roughly constant ΔR_{NL} vs. I_{dc} for electrons and the reduced ΔR_{NL} for hole spin extraction, can be clearly seen in the two images. By increasing the negative dc bias current to −660 μA for device B, a sign reversal of ΔR_{NL} at approximately 450 μA was observed as shown in fig. 5-5.

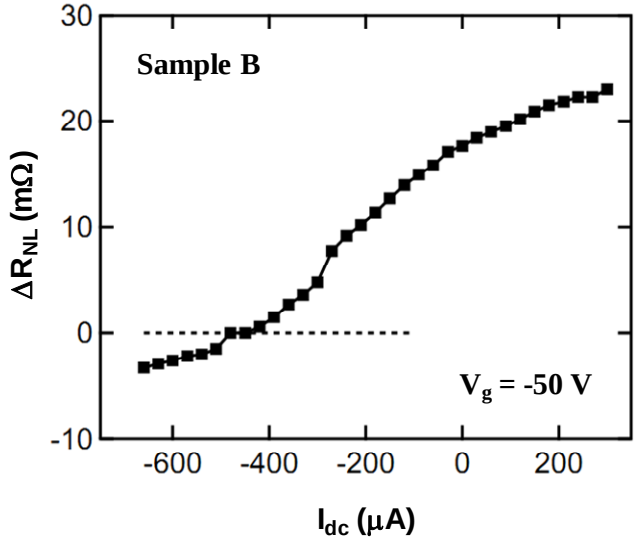

Fig. 5-5. sign reversal of nonlocal MR as a function of bias current for sample B. The dashed line shows the zero value.

The roughly constant ΔR_{NL} vs. I_{dc} can be understood in terms of the 1D drift-diffusion model [3-7], which predicts that the non-local voltage $\Delta V = \Delta V^{P} - \Delta V^{AP}$ is proportional to the injection current I. For the ac lock-in measurement, this behavior will lead to a constant ΔR_{NL} vs. I_{dc} because the lock-in measures the slope of the ΔV vs. I curve. The reduction of ΔR_{NL} for hole spin extraction represents a deviation from the standard behavior. Similar deviations from the standard behavior have been observed for spin extraction in Fe/n-GaAs [12], CoFe/Al_2O_3/Al [13], and very recently in Co/Al_2O_3/graphene [14], NiFe/Al_2O_3/p-Si [15], as shown in fig. 5-6. In these studies, tunnel barriers between the ferromagnet and non-magnetic materials play a prominent role in explaining the unusual behavior [8, 13, 16]. In our devices, the contact resistances are less than 300 Ω and have linear I-V characteristics, so the behavior is not related to interfacial barriers and must originate from a different physical mechanism.

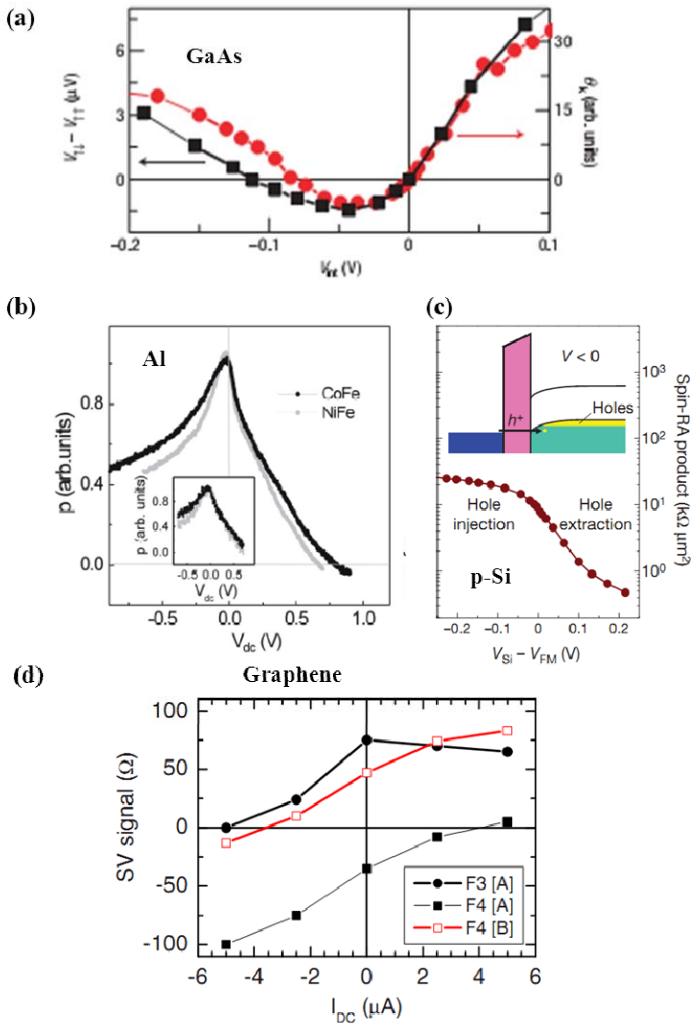

Fig. 5-6, bias dependence in GaAs, Al, Si, graphene spin valves.

(a) Spin signal as a function of bias current in Fe/GaAs system, adapted from Lou et al, Ref. [12]. (b) Spin injection efficiency as a function of bias voltage in NiFe (CoFe)/Al_2O_3/Al system, adapted from Valenzuela et al, Ref. [13]. (c) Spin-RA product as a funcation of bias voltage in Co/Al_2O_3/p-Si system, adapted from Dash et al, Ref. [15].(d) nonlocal spin signal as a function of bias current for graphene spin valves with pinhole Al_2O_3 contact, adapted from Josza et al, Ref. [14].

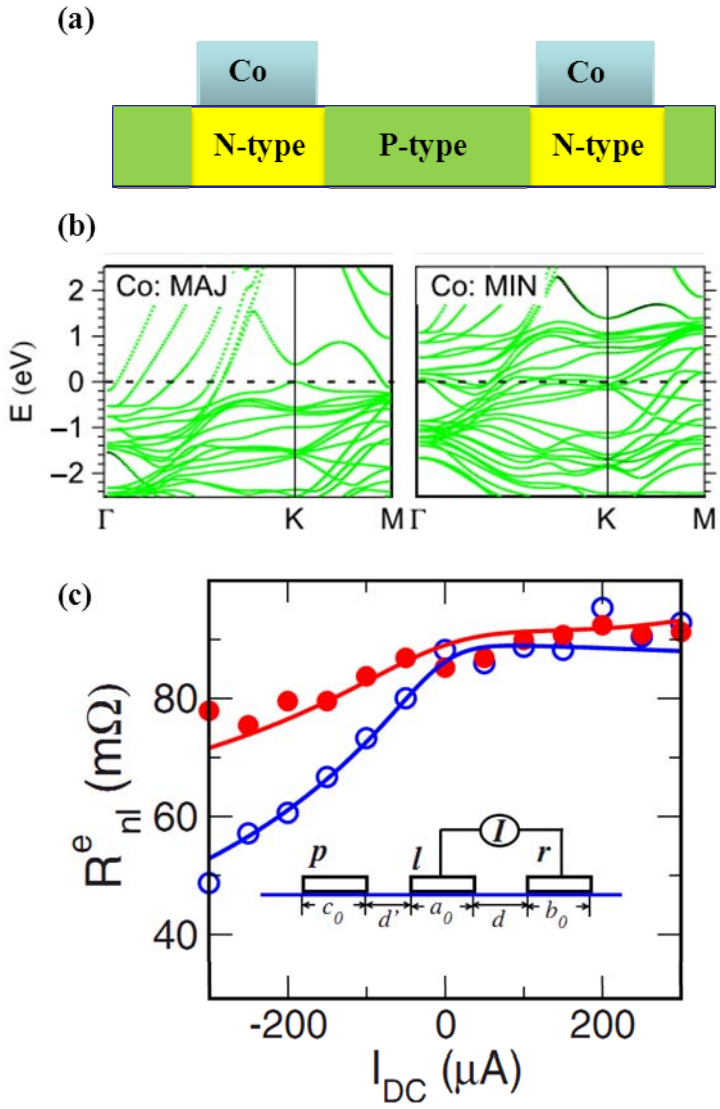

Fig. 5-7, origin of the electron-hole asymmetry.

(a) Local doping could generate potential steps that vary with gate voltage and may introduce non-linearity in the lateral spin transport in the SLG. (b) Strong Co-SLG hybridization calculated by Giovannetti et al, adapted from Ref. [19]. (c) Theoretical calculated nonlocal MR for graphene spin valves with a transparent interface. The red circles are for electrons, while the blue dots are for holes, adapted from Ref. [21].

We believe an interfacial effect at the Co/SLG contact such as local doping or wavefunction hybridization (illustrated in fig. 5-7a and 5-7b) could be important [17-20]. With a strong Co-SLG hybridization, it is possible for the spin-dependent density of states of the Co to break the electron-hole symmetry of the SLG [18]. Apart from band structure effects, local doping has been shown to generate electron-hole asymmetry of the conductance [17, 19, 20], but its influence on the spin-dependent properties is currently unclear. Later theoretical studies on this indicate that redistribution of the spin current near the ferromagnetic electrode (illustrated in fig. 5-7c) plays an important role in this bias dependence of the spin signal [21]. Further theoretical and experimental studies will be needed to understand the origin of the electron-hole asymmetry of the spin signal.

5.4 Conclusion

In summary, I have measured non-local MR on SLG spin valves with transparent contacts as a function of gate voltage and dc current bias. The gate dependence of the non-local MR at zero bias is found to scale with the SLG conductivity, consistent with the predicted behavior for transparent contacts. For electrons, the non-local MR is roughly independent of bias, but for holes under negative bias the non-local MR is strongly reduced. Understanding the origin of this effect should be important for further theoretical developments in spintronics.

REFERENCES

[1] P. Jarillo-Herrero, S. Sapmaz, C. Dekker, L. P. Kouwenhoven, and H. S. J. van der Zant, Nature **429**, 389 (2004).

[2] M. Johnson, and R. H. Silsbee, Phys. Rev. Lett. **55**, 1790 (1985).

[3] F. J. Jedema, A. T. Filip, and B. J. van Wees, Nature **410**, 345 (2001).

[4] P. C. van Son, H. van Kempen, and P. Wyder, Phys. Rev. Lett. **58**, 2271 (1987).

[5] T. Valet, and A. Fert, Phys. Rev. B **48**, 7099 (1993).

[6] S. Takahashi, and S. Maekawa, Phys. Rev. B. **67**, 052409 (2003).

[7] T. Kimura, Y. Otani, and J. Hamrle, Phys. Rev. B **73**, 132405 (2006).

[8] H. Dery, and L. J. Sham, Phys. Rev. Lett. **98**, 046602 (2007).

[9] F. Miao, S. Wijeratne, Y. Zhang, U. C. Coskun, W. Bao, and C. N. Lau, Science **317**, 1530 (2007).

[10] W. H. Wang, W. Han, K. Pi, K. M. McCreary, F. Miao, W. Bao, C. N. Lau, and R. K. Kawakami, Appl. Phys. Lett. **93**, 183107 (2008).

[11] A. C. Ferrari, J. C. Meyer, V. Scardaci, C. Casiraghi, M. Lazzeri, F. Mauri, S. Piscanec, D. Jiang, K. S. Novoselov, S. Roth, and A. K. Geim, Phys. Rev. Lett. **97**, 187401 (2006).

[12] X. Lou, C. Adelmann, S. A. Crooker, E. S. Garlid, J. Zhang, K. S. Madhukar Reddy, S. D. Flexner, C. J. Palmstrom, and P. A. Crowell, Nature Physics **3**, 197 (2007).

[13] S. O. Valenzuela, D. J. Monsma, C. M. Marcus, V. Narayanamurti, and M. Tinkham, Phys. Rev. Lett. **94**, 196601 (2005).

[14] C. Jozsa, M. Popinciuc, N. Tombros, H. T. Jonkman, and B. J. van Wees, Phys. Rev. B **79**, 081402(R) (2008).

[15] S. P. Dash, S. Sharma, R. S. Patel, M. P. d. Jong, and R. Jansen, Nature **462**, 26 (2009).

[16] A. N. Chantis, K. D. Belashchenko, D. L. Smith, E. Y. Tsymbal, M. van Schilfgaarde, and R. C. Albers, Phys. Rev. Lett. **99**, 196603 (2007).

[17] B. Huard, N. Stander, J. A. Sulpizio, and D. Goldhaber-Gordon, Phys. Rev. B **78**, 121402 (2008).

[18] G. Giovannetti, P. A. Khomyakov, G. Brocks, V. M. Karpan, J. van den Brink, and P. J. Kelly, Phys. Rev. Lett. **101**, 026803 (2008).

[19] J. Cayssol, B. Huard, and D. Goldhaber-Gordon, Phys. Rev. B **79**, 075428 (2008).

[20] P. Blake, R. Yang, S. V. Morozova, F. Schedina, L. A. Ponomarenko, A. A. Zhukov, R. R. Nair, I. V. Grigorieva, K. S. Novoselov, and A. K. Geim, Solid State Commun. **149**, 1068 (2009).

[21] Z. G. Yu, J. Baker, and S. Krishnamurthy, Phys. Rev. B **82**, 035425 (2010).

Chapter 6.

Growth of atomically smooth MgO films on graphene by molecular beam epitaxy[1]

Abstract

In this section, I investigate the growth of MgO films on graphene by molecular beam epitaxy and find that surface diffusion promotes a rough morphology. To reduce the mobility of surface atoms, the graphene surface is dressed by Ti atoms prior to MgO deposition. With as little as 0.5 monolayers of Ti, the MgO overlayer becomes atomically smooth. Furthermore, no aggregation of MgO is observed at the edges of the graphene sheet. This result is a key advance for the development of pinhole free tunneling contacts for spin injection into graphene.

---

[1]Published as: W. H. Wang*, W. Han*, K. Pi, K. M. McCreary, F. Miao, W. Bao, C. N. Lau, and R. K. Kawakami, Appl. Phys. Lett. 93, 183107 (2008).

6.1 Introduction

Graphene has emerged as a fascinating material for nanoelectronics and spintronics due to its high electronic mobility, quasi-relativistic band structure, and the possibility of long spin coherence times associated with low spin-orbit and hyperfine couplings [1-6]. To realize its full potential, one of the most critical challenges is the synthesis of high quality insulating layers on graphene to serve as dielectric layers for electrostatic gates and as tunnel barriers for spin injection. For local gates on graphene, current approaches utilize evaporation of SiO_2 [7, 8], atomic layer deposition of Al_2O_3 or HfO_2 on treated surfaces [9-12], air-gap under suspended bridges [13, 14], and thick polymer films (PMMA) [15]. By comparison, the development of tunnel barriers for spintronic devices, which are expected to enhance spin injection from ferromagnetic contacts by alleviating possible conductivity mismatch problems [16-18], is considerably more demanding. This is because smooth layers are required at a much lower film thickness (1-5 nm) as compared to gate dielectrics (>20 nm), and initial stages of overlayer growth on graphite often follow a Volmer-Weber growth mode (island formation) [19]. So far, two groups have utilized tunnel barriers for spin injection into graphene/graphite [6, 20, 21]. Tombros *et. al.* achieve room temperature spin transport in graphene using aluminum oxide tunnel barriers fabricated by cryogenic deposition of aluminum followed by oxidation, but it is stated that the barriers very likely contain pinholes [6, 20]. In our previous studies on spin injection into mesoscopic graphite [21], we employed magnesium oxide (MgO) tunnel barriers and found that the presence of pinholes was the most common failure mode. Systematic investigations on the role of the tunnel barrier in

spin injection into graphene has been lacking, mostly due to the difficulty of growing uniform, ultrathin insulating layers on the graphene surface.

In this chapter, I demonstrate the growth of atomically smooth MgO films on graphene surfaces by molecular beam epitaxy (MBE). By examining atomic force microscopy (AFM) images of MgO films with different growth rates on highly oriented pyrolytic graphite (HOPG) substrates, we find that the high surface diffusion leads to non-uniform MgO films (rms roughness > 0.8 nm). To reduce the mobility of surface atoms, we deposit titanium (Ti) atoms to dress the graphene surface prior to the MgO deposition. Remarkably, with as little as a 0.5 monolayer (ML) coverage of Ti, the rms roughness of a 1 nm MgO film is dramatically reduced to be near the atomic spacing in MgO (0.211 nm). Because metallic Ti islands on graphene may be undesirable for lateral transport, we oxidize the Ti prior to MgO growth and find that the MgO layer is atomically smooth under this condition as well. Finally, we grow MgO films on isolated graphene sheets using the Ti dressing layer and find that the MgO film is atomically smooth and free of aggregation at the edges of the graphene.

6.2 Experimental details

The samples are grown by MBE in an ultrahigh vacuum (UHV) system with base pressure of 5×10^{-10} torr, unless otherwise noted. All the material growth is performed without removing the sample from UHV. For the HOPG samples, a fresh graphite surface is generated by peeling off the top layers with scotch tape and the sample is immediately inserted into UHV. For the graphene samples, the graphene is micromechanically extracted from Kish graphite onto SiO_2/Si(001) substrates and immediately inserted into

UHV [22]. MgO films are grown either by depositing Mg from a Knudsen cell while leaking O_2 into the MBE system or by depositing MgO from an electron-beam (e-beam) source. The Ti is deposited from an e-beam source.

6.3 Result and discussion

We first investigate the role of substrate preparation on film morphology by comparing MgO films grown on HOPG with and without substrate degassing at 160°C. For both samples, 1 nm thick MgO films are grown by introducing oxygen gas (6×10^{-6} torr) into the UHV chamber and depositing Mg at a rate of 0.065 nm/min with the substrate held at room temperature. In both cases, the Auger electron spectra exhibits a peak at 35 eV, which is characteristic of Mg within an MgO crystal, but no peak at 45 eV which is characteristic of elemental Mg, thus confirming the complete oxidation of the Mg [23]. For the MgO/HOPG sample without substrate degassing (fig. 6-1a), the AFM image indicates a non-uniform but quasi-continuous film with rms roughness of 1.37 nm. The dark areas of the image correspond to regions of the HOPG substrate which are not covered by MgO. Some aggregation of MgO to the step edges on the HOPG is observed. For the MgO/HOPG sample with substrate degassing (fig. 6-1b), the AFM image shows a highly discontinuous film and the coverage of the HOPG substrate is much less uniform than the previous case. The aggregation of the MgO into large islands probably results from an increase in the surface diffusion due to the removal of adsorbed gases.

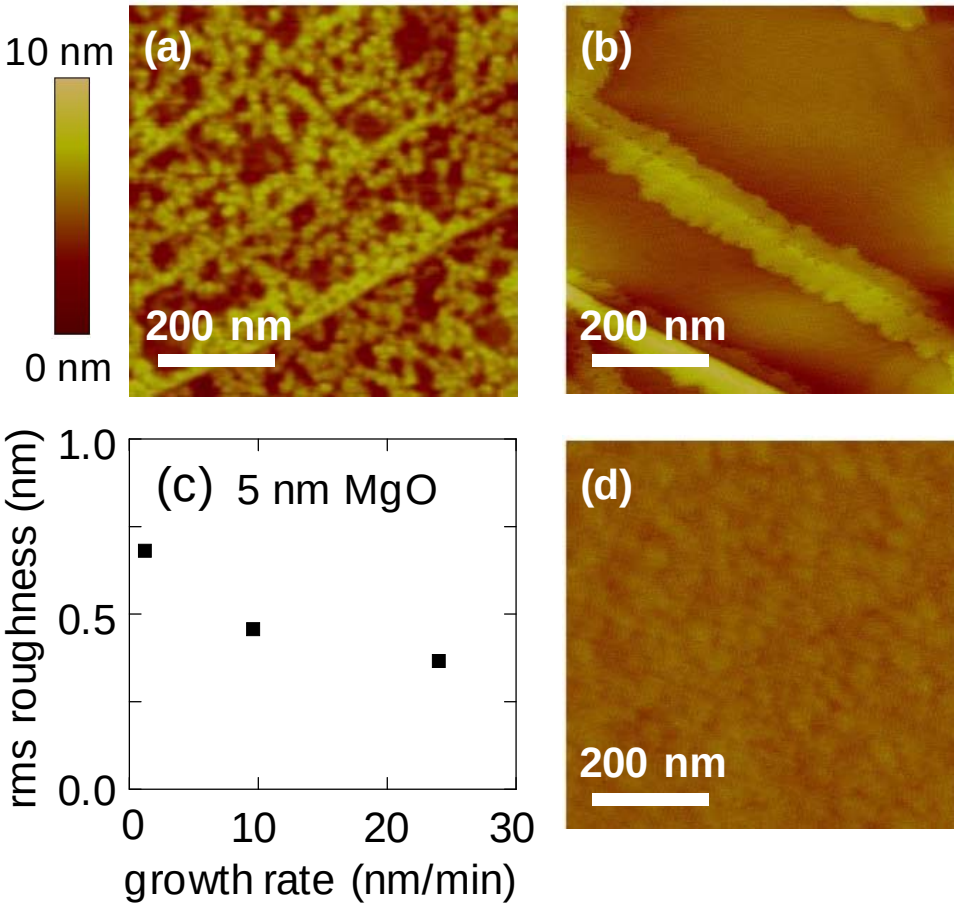

Fig. 6-1, the role of surface diffusion on MgO film morphology.

(a) AFM image of 1 nm MgO grown on HOPG without degassing. MgO is deposited by Mg evaporation with oxygen gas in the chamber. (b) AFM image of 1 nm MgO grown on HOPG degassed at 160 °C. MgO is deposited by Mg evaporation with oxygen gas in the chamber. (c) Dependence of rms roughness on growth rate for 5 nm MgO films deposited by e-beam evaporation. (d) AFM image of 5 nm MgO grown by e-beam evaporation on HOPG without degassing at 24 nm/min.

To test whether the surface diffusion is the main cause of the highly non-uniform morphology, we investigate its dependence on growth rate. Using a cleanroom e-beam evaporation system to achieve high deposition rates for the MgO, we deposit 5 nm of MgO at 1.2 nm/min, 9.6 nm/min, and 24 nm/min on freshly peeled HOPG (without substrate degassing). AFM measurements indicate that the rms roughness decreases with increasing growth rate (fig. 6-1c). Fig. 6-1d shows the AFM image of the MgO film grown at 24 nm/min, which is much smoother than the samples in fig. 6-1a and 6-1b. The dependence on growth rate confirms that the surface diffusion is an important factor in determining the film morphology. The fact that the films become smoother at higher growth rates indicates that the surface diffusion tends to promote a rougher morphology. Thus, a strategy to improve the film smoothness is to reduce the mobility of the surface atoms.

In an attempt to reduce the surface diffusion, we explore the use of Ti atoms to dress the graphene surface prior to MgO deposition. Ti is often used in device fabrication as an adhesion layer to help inert materials such as gold maintain good contact to other materials. Therefore, it is likely that Ti atoms will bind more strongly to the graphene surface (compared to MgO on graphene) and serve as an agent to reduce the mobility of subsequently deposited MgO (as illustrated in fig. 6-3a and 6-3b). In the UHV system, Ti atoms are deposited onto a freshly peeled HOPG substrate that has received no additional treatment. Then MgO is deposited from an e-beam source at a growth rate of ~0.2 nm/min. Fig. 6-2a and 6-2c show AFM images of 1 nm thick MgO films grown on the HOPG substrate dressed with 0 ML, 0.25 ML, and 0.5 ML of Ti, respectively [1 ML =

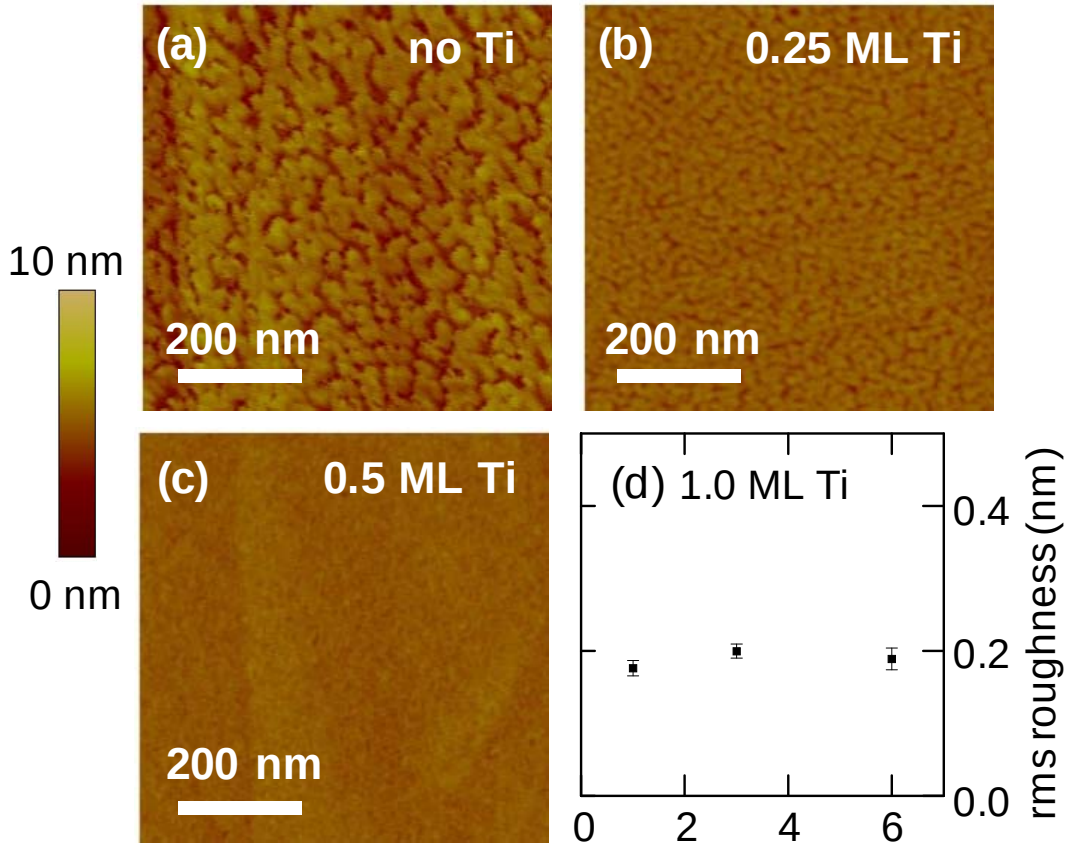

Fig. 6-2, morphology of MgO films grown on HOPG dressed by Ti atoms.

(a) AFM image of 1 nm MgO without the Ti dressing. (b) AFM image of 1 nm MgO grown on 0.25 ML Ti/HOPG. (c) AFM image of 1 nm MgO grown on 0.5 ML Ti/HOPG. (d) Dependence of rms roughness on MgO thickness. Here, the Ti coverage is 1.0 ML.

0.234 nm for Ti(0001)]. A dramatic improvement in the film morphology is observed with as little as 0.5 ML of Ti dressing the HOPG substrate. Fig. 6-4 shows the dependence of rms roughness of a 1 nm MgO film as a function of the Ti coverage (open circles). The rms roughness is obtained by taking the average of three 1 μm × 1 μm AFM images, and the error bars reflect the variation among these images. From 0 to 0.5 ML, a

sharp reduction in rms roughness from ~0.8 nm to ~0.2 nm is observed. Between 0.5 and 1.0 ML the roughness decreases gradually, and above 1.0 ML there is no further improvement. The roughness value of ~0.2 nm is significant because the atomic spacing in MgO is 0.211 nm, so the film is smooth at the atomic scale. For applications as a tunnel barrier, it is important to know how the MgO film morphology depends on its thickness. Fig. 6-2d shows the dependence of rms roughness on MgO thickness. These samples all use 1.0 ML of Ti which is subsequently oxidized by 30 L of O2. The rms roughness shows little change with the MgO thickness, which is favorable for future studies of spin injection as a function of tunnel barrier thickness.

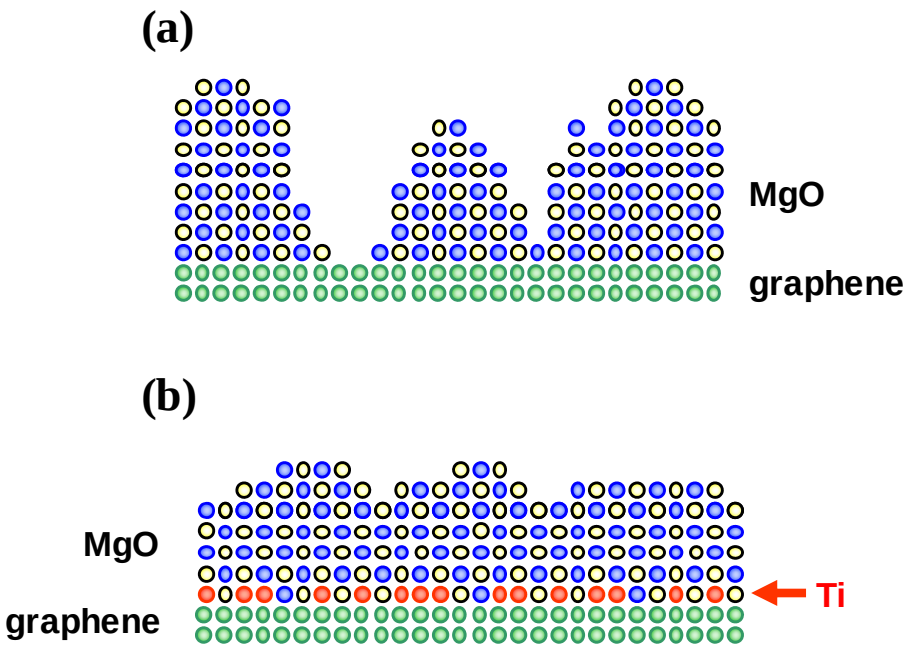

Fig. 6-3. MgO films grown on HOPG without or with seeding Ti atoms.

(a) Rough MgO film without Ti dressing. (b) Smooth MgO film with Ti dressing layer.

Because we plan to use the MgO films in lateral spin transport devices, there is some concern that the Ti could form small metallic islands at the MgO/graphene interface, which may generate a parallel conduction path. However, due to the small amount of Ti and its high reactivity with oxygen, it is likely that Ti is converted to insulating TiO_2 (band gap > 3 eV) during the initial stages of MgO deposition. To ensure that the Ti is fully oxidized, we add an extra step to the growth procedure. Prior to the MgO deposition, oxygen gas is introduced into the UHV system at a pressure of 5×10^{-8} torr for 10 minutes (i.e. 30 Langmuirs) which is sufficient to completely convert the Ti into insulating TiO_2 [24]. The open triangles in fig. 6-4 illustrate the dependence of rms roughness for a 1 nm MgO film grown on oxidized Ti/graphene as a function of the Ti coverage. The results for oxidized Ti (open trianges) are nearly identical to the case of Ti without post-oxidation (open circles).

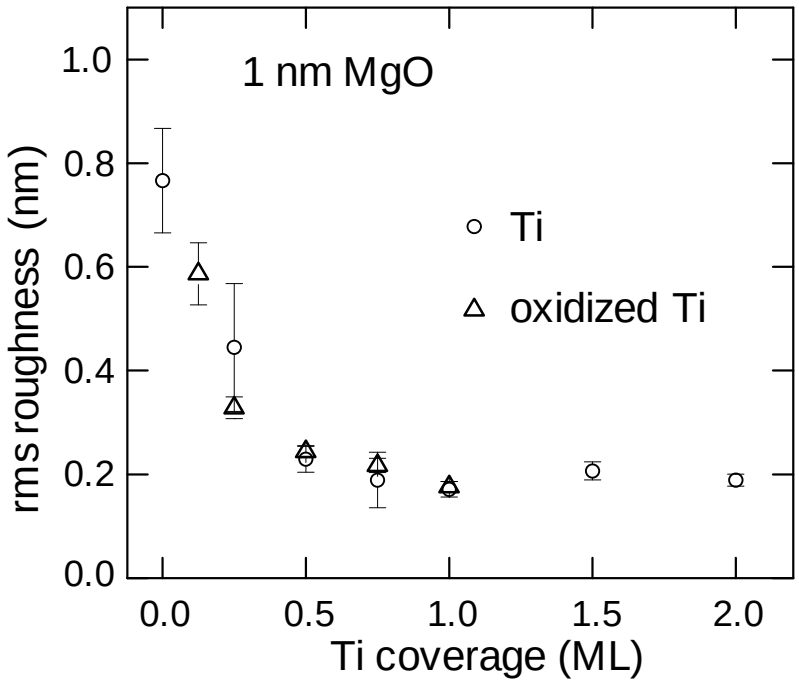

Fig. 6-4, the rms roughness of 1 nm MgO films as a function of Ti coverage.

Open circles are for samples in which the MgO is deposited immediately after Ti. Open triangles are for samples that are exposed to 30 L of O_2 gas to fully oxidize the Ti prior to MgO growth.

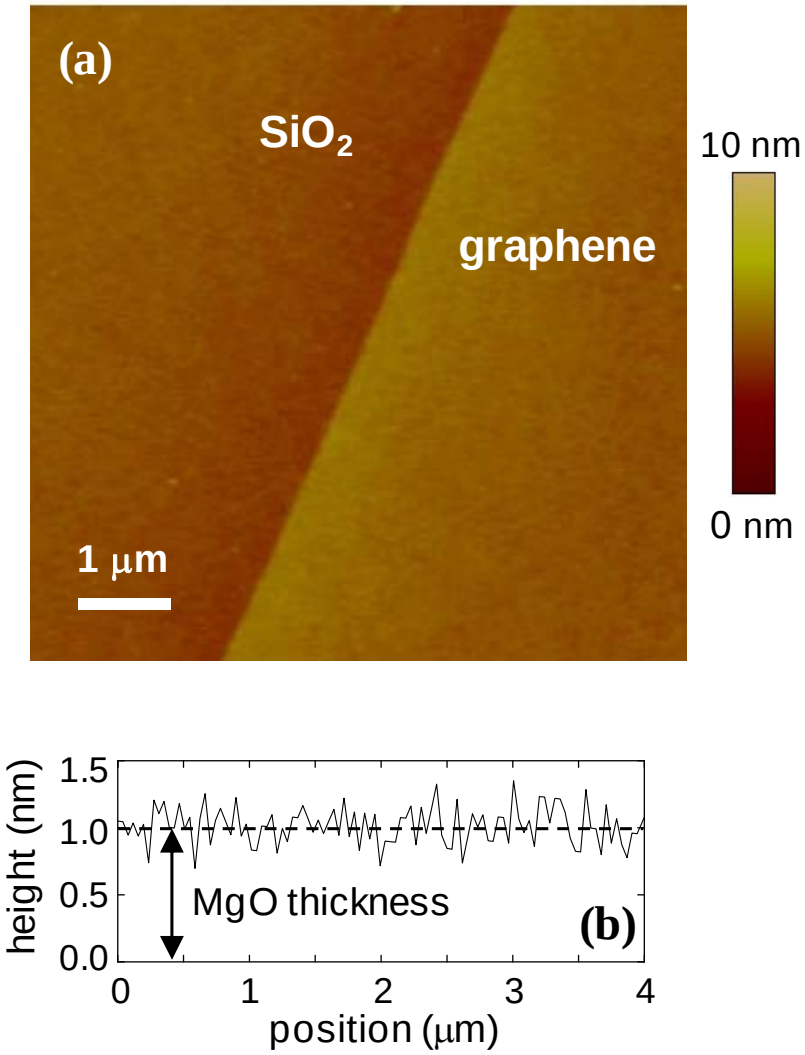

Fig. 6-5, MgO film on single layer graphene.

(a) AFM image of 1 nm MgO grown by e-beam deposition in UHV on a graphene sheet dressed by 1.0 ML Ti (with post-oxidation). There is no aggregation of MgO at the edges of the graphene. The rms roughness of the MgO film on the graphene surface is 0.17 ± 0.01 nm. (b) Typical AFM line cut of MgO film on graphene surface.

Finally, we investigate the growth of MgO films on isolated graphene sheets. The graphene is produced by mechanical extraction onto SiO_2/Si(001) substrate and is identified by optical microscopy [1-3, 22]. After depositing a 1.0 ML Ti dressing layer and oxidizing in 30 L of O_2, a 1 nm MgO film is grown by e-beam deposition. The AFM image (fig. 6-5) shows the absence of aggregation at the lateral boundary of the graphene sheet. The MgO film on graphene is atomically smooth with an rms roughness of 0.17 ± 0.01 nm, equal to the best MgO films grown on HOPG. These results demonstrate the ability to produce atomically smooth MgO films on graphene.

6.4 Conclusion.

In summary, we have determined that surface diffusion tends to promote rough morphology in the MBE growth of MgO films on HOPG. This effect can be overcome by dressing the graphene surface with Ti atoms. We find that as little as 0.5 ML of Ti greatly improves the MgO film smoothness to be on the order of a single atomic spacing. The MgO films also exhibit no aggregation at the edges of the graphene sheet. These results are a key advance towards realizing tunneling spin injection in graphene [25], as discussed in the following chapter.

REFERENCES:

[1] K. S. Novoselov, A. K. Geim, S. V. Morozov, D. Jiang, Y. Zhang, S. V. Dubonos, I. V. Grigorieva, and A. A. Firsov, Science **306**, 666 (2004).

[2] K. S. Novoselov, A. K. Geim, S. V. Morozov, D. Jiang, M. I. Katsnelson, I. V. Grigorieva, S. V. Dubonos, and A. A. Firsov, Nature **438**, 197 (2005).

[3] Y. Zhang, Y.-W. Tan, H. L. Stormer, and P. Kim, Nature **438**, 201 (2005).

[4] C. Berger, Z. Song, X. Li, X. Wu, N. Brown, C. Naud, D. Mayou, T. Li, J. Hass, A. N. Marchenkov, E. H. Conrad, P. N. First, and W. A. de Heer, Science **312**, 1191 (2006).

[5] A. K. Geim, and K. S. Novoselov, Nature Materials **6**, 183 (2007).

[6] N. Tombros, C. Jozsa, M. Popinciuc, H. T. Jonkman, and B. J. Van Wees, Nature **448**, 571 (2007).

[7] M. C. Lemme, T. J. Echtermeyer, M. Baus, and H. Kurz, IEEE Electron Device Letters **28**, 282 (2007).

[8] Y. Q. Wu, P. D. Ye, M. A. Capano, Y. Xuan, Y. Sui, M. Qi, J. A. Cooper, T. Shen, D. Pandey, G. Prakash, and R. Reifenberger, Appl. Phys. Lett. **92**, 092102 (2008).

[9] J. R. Williams, L. DiCarlo, and C. M. Marcus, Science **317**, 638 (2007).

[10] B. Özyilmaz, P. Jarillo-Herrero, D. Efetov, D. A. Abanin, L. S. Levitov, and P. Kim, Phys. Rev. Lett. **99**, 166804 (2007).

[11] B. Lee, S. Y. Park, H. C. Kim, K. J. Cho, E. M. Vogel, M. J. Kim, R. M. Wallace, and J. Kim, Appl. Phys. Lett. **92**, 203102 (2008).

[12] X. Wang, S. M. Tabakman, and H. Dai, J. Amer. Chem. Soc. **130**, 8152 (2008).

[13] G. Liu, J. Velasco Jr., W. Bao, and C. N. Lau, Appl. Phys. Lett. **92**, 203103 (2008).

[14] R. V. Gorbachev, A. S. Mayorov, A. K. Savchenko, D. W. Horsell, and F. Guinea, Nano Lett. **8**, 1995 (2008).

[15] B. Huard, J. A. Sulpizio, N. Stander, K. Todd, B. Yang, and D. Goldhaber-Gordon, Phys. Rev. Lett. **98**, 236803 (2007).

[16] G. Schmidt, D. Ferrand, L. W. Molenkamp, A. T. Filip, and B. J. van Wees, Phys. Rev. B (Rapid Communications) **62**, 4790 (2000).

[17] E. I. Rashba, Phys. Rev. B (Rapid Communications) **62**, 16267 (2000).

[18] A. Fert, and H. Jaffres, Phys. Rev. B **64**, 184420 (2001).

[19] C. Binns, S. H. Baker, C. Demangeat, and J. C. Parlebas, Surf. Sci. Rep. **34**, 105 (1999).

[20] N. Tombros, S. Tanabe, A. Veligura, C. Jozsa, M. Popinciuc, H. T. Jonkman, and B. J. van Wees, ArXiv:cond-mat: , 0802.2892 (2008).

[21] W. H. Wang, K. Pi, Y. Li, Y. F. Chiang, P. Wei, J. Shi, and R. K. Kawakami, Phys Rev. B (Rapid Comm.) **77**, 020402 (2008).

[22] F. Miao, S. Wijeratne, Y. Zhang, U. C. Coskun, W. Bao, and C. N. Lau, Science **317**, 1530 (2007).

[23] M. Suleman, and E. B. Pattinson, Surf. Sci. **35**, 75 (1973).

[24] I. Vaquila, M. C. G. Passeggi Jr., and J. Ferron, Phys. Rev. B **55**, 13925 (1997).

[25] W. Han, K. Pi, K. M. McCreary, Y. Li, J. J. I. Wong, A. G. Swartz, and R. K. Kawakami, Phys. Rev. Lett. **105**, 167202 (2010).

Chapter 7.

Tunneling spin injection into single layer graphene[1]

Abstract

In this section, I study tunneling spin injection from Co into single layer graphene (SLG) using TiO_2 seeded MgO barriers. I observe a non-local magnetoresistance (ΔR_{NL}) of 130 Ω at room temperature, which is the largest value observed in any graphene spin valve. I also investigate the ΔR_{NL} vs. SLG conductivity from the transparent to the tunneling contact regimes, which is consistent with the drift-diffusion theory of spin transport. Furthermore, I find that tunnel barriers reduce the contact-induced spin relaxation and are therefore important for future investigations of spin relaxation in graphene.

---

[1]Published as: Wei Han, K. Pi, K. M. McCreary, Yan Li, Jared J. I. Wong, A. G. Swartz, and R. K. Kawakami, Phys. Rev. Lett. 105, 167202 (2010).

7.1 Introduction

Spintronics utilizes the electron's spin degree of freedom in addition to its charge in electronic devices for advanced approaches to information storage and processing [1]. Single layer graphene (SLG) is a promising material for spintronics due to the low intrinsic spin-orbit and hyperfine couplings [2], long spin diffusion lengths (~2 μm) [3], and predictions of fascinating spin dependent behavior [4, 5]. Furthermore, SLG is the first material to achieve gate tunable spin transport at room temperature [3, 6, 7]. However, to realize its full potential for spintronics, there are two critical challenges. First, the measured spin lifetimes in SLG (50-200 ps) are orders of magnitude shorter than expected from the intrinsic spin-orbit coupling [2, 3, 8-11]. Consequently, substantial theoretical and experimental effort is focused on identifying the extrinsic mechanism of spin scattering [9, 11, 12]. The second important challenge is to achieve tunneling spin injection into SLG. This will produce efficient spin injection by overcoming the conductance mismatch between the ferromagnetic (FM) metal electrodes and the SLG [13-15]. Up to now, enhancing the spin injection efficiency has focused on reducing the conductance mismatch by decreasing the contact area using MgO masking layers or barriers with pinholes [7, 8, 10, 16-18]. However, tunneling spin injection has not been achieved due to the difficulty to growing uniform, pinhole-free tunnel barriers on graphene.

In this chapter, I demonstrate tunneling spin injection in SLG spin valves and report large spin signals and enhanced spin lifetimes. Using TiO_2 seeded MgO films as the tunnel barrier, we observe a non-local magnetoresistance (ΔR_{NL}) as high as 130 Ω at

room temperature, which is the largest value observed in any graphene spin valve. The *I-V* characteristics of the contact resistance are highly non-linear and ΔR_{NL} varies inversely with the SLG conductivity, which are the two principal characteristics of tunneling spin injection. Furthermore, the spin lifetimes (450-500 ps) are considerably longer than previously observed for transparent and pinhole contacts (50-200 ps) [3, 8-10], which suggests that the tunnel barrier greatly reduces the contact-induced spin relaxation. These results are important for applications such as spin-based logic [19] and for fundamental studies of spin relaxation in graphene.

7.2 Experimental details

Graphene spin valves are fabricated using mechanically exfoliated SLG flakes on SiO_2/Si substrate, where the Si is used as a back gate. Co electrodes are defined by electron-beam lithography using PMMA/MMA bilayer resist to produce an undercut, followed by angle evaporation in a molecular beam epitaxy system with a base pressure of 2×10^{-10} torr. Tunneling contacts are fabricated in the following manner. First, 0.12 nm of Ti is deposited at both 0° and 9° angles (fig. 7-1a), followed by oxidation in 5×10^{-8} torr of O_2 for 30 minutes to convert the metallic Ti into insulating TiO_2. The presence of TiO_2 was shown in Chapter 6 to greatly improve the surface mopology of the MgO overlayer [20]. A 3 nm MgO masking layer is deposited at an angle of 0° and a 0.8 nm MgO tunnel barrier is deposited at an angle of 9°. Then the 80 nm thick Co electrode is deposited with an angle of 7°. Fig. 7-1b illustrates the geometry of the tunneling contact, where the current flows across the 0.8 nm MgO tunnel barrier of width ~50 nm. Approximately 20% of the tunneling electrodes possess pinholes, which are utilized for investigating the

characteristics of spin injection through pinhole contacts. For the transparent contacts, the Co is directly contacted to SLG with a 2 nm MgO masking layer [7, 8].

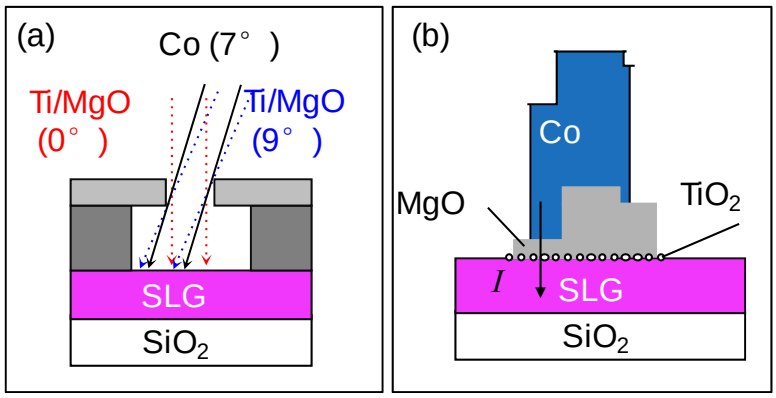

Fig. 7-1, tunneling contact for graphene spin valve.

(a) Schematic diagram of the angle evaporation geometry. The grey layers are PMMA/MMA resist with an undercut. (b) Schematic drawing of the Co/MgO/TiO_2/SLG tunneling contacts. The arrow indicates the current flow through the MgO tunnel barrier.

7.3 Characterization of the tunneling contact

The tunneling contact is characterized by 3-probe electrical measurement, in which the current is applied across E1 and E2, while the voltage is measured between E3 and E2 (fig. 7-2a). The resistance measured is equal to the sum of the contact resistance and the Co electrode resistance. Since the Co electrode resistance is very small (~ 100 Ω) compared to the contact resistance of the junction (> 5 k Ω), here, I use the measured resistance for the contact resistance of the Co/MgO/Graphene junction.

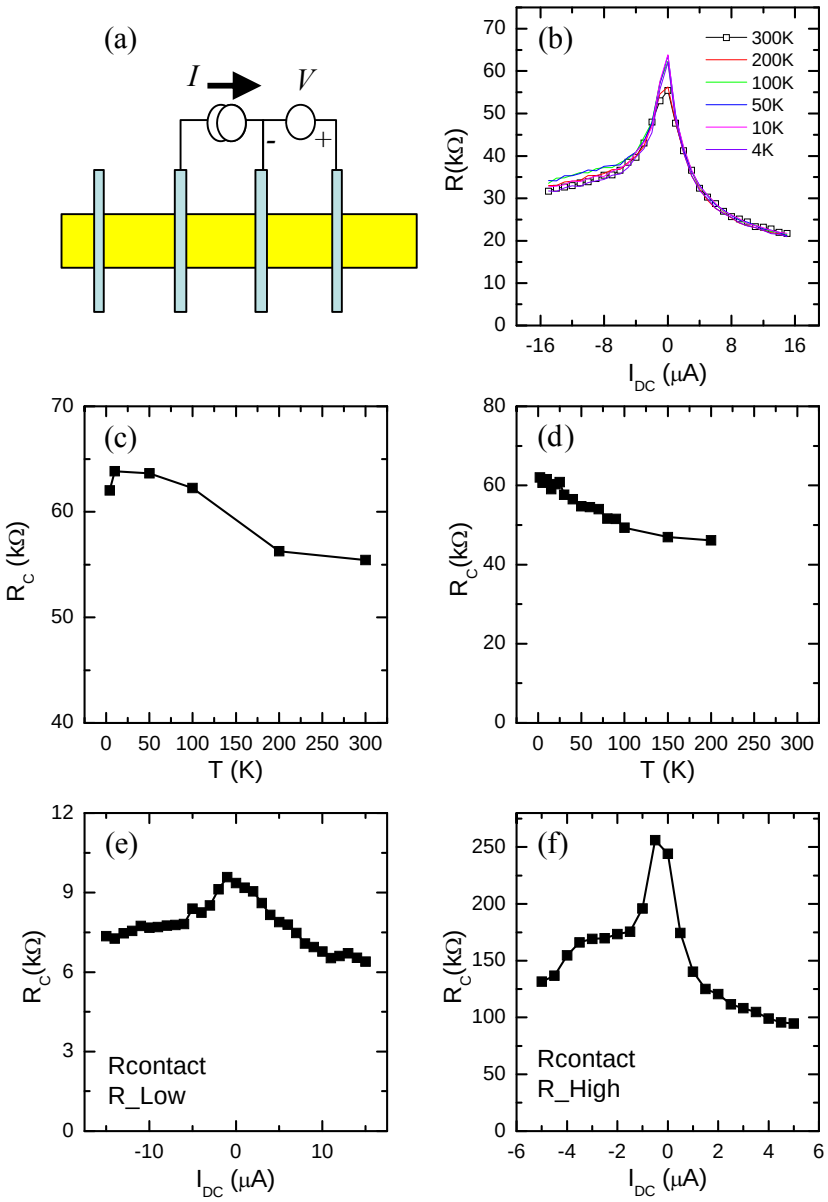

Fig. 7-2, electrical characterization of the tunneling contact.

(a) Schematic diagram of 3-probe electrical measurement. (b) Typical differential contact resistance of the Co/MgO/SLG junctions at different temperatures. (c-d) Temperature dependence of the peak resistance at I_{dc} = 0 μA for the tunneling contact. (e) Typical low resistance tunneling contact. (f) Typical high resistance tunneling contact.

Fig. 7-2b shows the typical contact resistance of the Co/MgO/Graphene junction. At room temperature, the dV/dI shows peak at I_{DC} = 0 μA, with a resistance of ~ 50 k Ω, and decreases with the increase of bias current. When the temperature decreases, the dV/dI data shows little temperature dependence. At 2 K, the peak resistance increases to 65 k Ω. The temperature dependence of the contact resistance is shown in fig. 7-2c. A detailed scan of another Co/MgO/Graphene junction is shown in fig. 7-2d. As the temperature decreases, the peak resistance displays a modest increase. Both the nonlinear properties of the differential contact resistance and the temperature dependence of the peak resistance demonstrate the tunneling behavior of the Co/MgO/graphene junction [21]. The fabrication of tunneling contact junction is not as easy as for transparent contacts. Also, the tunneling contact resistance has a large range from 10 kΩ to 200 kΩ at the 0 bias current, as shown in fig. 7-2e and fig. 7-2f.

7.4 Nonlocal MR and local MR measurement

Spin injection and transport are measured on samples held at 300 K in helium atmosphere using the non-local geometry with standard AC lock-in techniques [3, 22]. The inset of fig. 7-3a shows the non-local measurement where the spin is injected at electrode E2 and detected at E3. The non-local resistance, R_{NL}, is defined as the measured voltage signal (V_{NL}) divided by the injection current (I). Fig. 7-3a shows R_{NL} as the magnetic field is swept up (black curve) and swept down (red curve) for a device with tunneling contacts. ΔR_{NL} is defined as the difference of R_{NL} between the parallel and antiparallel magnetization states of E2 and E3. For spin transport across the 2.1 μm electrode gap (L), ΔR_{NL} is 130 Ω, which is the largest value observed in any lateral spin valve including metals and semiconductors [3, 6, 7, 16, 23].

For tunneling contacts [3],

$$\Delta R_{NL} = \frac{1}{\sigma_G}\frac{P_J^2 \lambda_G}{W} e^{-L/\lambda_G} \qquad (1)$$

where P_J is the spin injection/detection efficiency, and σ_G, W, and λ_G are the conductivity, width, and spin diffusion length of the SLG, respectively. P_J is calculated to be 28 ± 2% using experimental values of σ_G = 0.35 mS, W = 2.2 μm, L = 2.1 μm, and typical values of λ_G = 2.5-3.0 μm (see fig. 7-8a and fig. 7-8b). This compares favorably with the tunneling spin polarization of 35-42% measured by spin-dependent tunneling from Co into a superconductor across polycrystalline Al_2O_3 barriers [24-27]. The spin injection efficiency is larger than observed in previous studies using barriers with pinholes (2% – 18% at low bias) [3, 10, 16] and transparent contacts (1%) [8].

The tunnel barrier enhances the efficiency of spin injection from Co into the SLG by alleviating the conductance mismatch problem [13-15]. For spin injection without tunnel barriers, the spins that are injected from the Co electrode into the SLG can diffuse within the SLG (toward neighboring electrodes) or diffuse back into the Co electrode. The flow of spin via diffusion is governed by the spin resistances [18] which are $R_G = \lambda_G /(\sigma_G W)$ for the SLG, and $R_F = \rho_F \lambda_F / A_J$ for the Co, where ρ_F is the Co resistivity, λ_F is the spin diffusion length of Co, and A_J is the junction area [28]. Using typical parameters (W = 2 μm, λ_G = 2-3 μm, σ_G = 0.5 mS, $\rho_F = 6 \times 10^{-8}$ Ω m [29], λ_F = 0.06 μm [30]), the R_F/R_G ratio has values between ~10^{-3} and ~10^{-5} depending on the value of A_J [28]. Because $R_F << R_G$, the spin diffusion is dominated by the back flow of spins into the Co electrode, which leads to a low spin injection efficiency. The insertion of a tunnel barrier increases the spin injection efficiency by blocking the back flow of spins into the Co electrode.

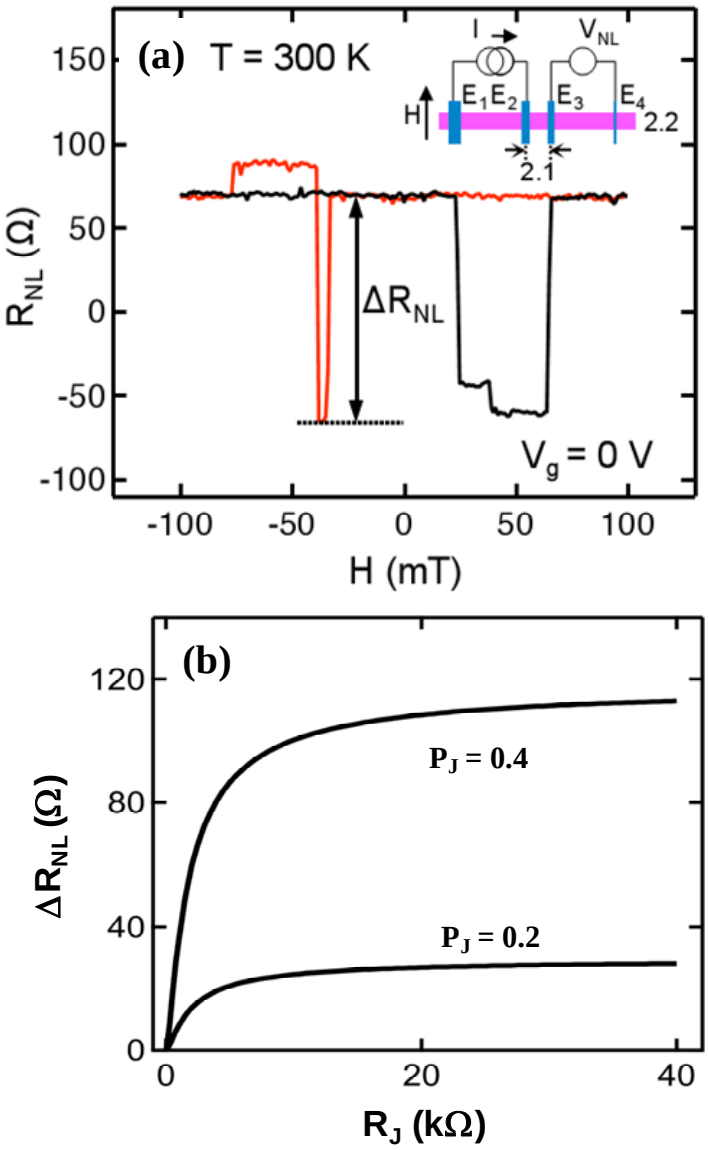

Fig. 7-3, nonlocal MR for SLG spin valve with tunneling contacts.

(a) Non-local MR scans of a SLG spin valves measured at room temperature. The black (red) curve shows the non-local resistance as the magnetic field is swept up (down). The nonlocal MR (ΔR_{NL}) of 130 Ω is indicated by the arrow. Inset: the non-local spin transport measurement on this device with a spacing of L = 2.1 μm and SLG width of W = 2.2 μm. (b) The non-local MR as a function of contact resistance (R_J) with P_J = 0.4 and P_J = 0.2, based on equation 2 and parameters given in the text.

Quantitatively, the role of the tunnel barrier is explained in the one-dimensional drift-diffusion theory of spin transport [18]. Assuming the injector and detector are identical for simplicity, ΔR_{NL} is given by

$$R_{NL} = 4R_G e^{-L/\lambda_G} \left(\frac{P_J \frac{R_J}{R_G}}{1-P_J^2} + \frac{P_F \frac{R_F}{R_G}}{1-P_F^2} \right)^2 \times \left(\left(1 + \frac{2\frac{R_J}{R_G}}{1-P_J^2} + \frac{2\frac{R_F}{R_G}}{1-P_F^2} \right)^2 - e^{-2L/\lambda_G} \right)^{-1} \quad (2)$$

where $R_G = \lambda_G / (\sigma_G W)$ and $R_F = \rho_F \lambda_F / A_J$ are the spin resistances of the SLG and FM electrodes, respectively, W is the width of the SLG, A_J is the junction area between the FM and SLG, λ_G (λ_F) is the spin diffusion length in the SLG (FM), σ_G is the conductivity of SLG, ρ_F is the resistivity of the FM, P_F is the spin polarization of the FM, P_J is the polarization of the interfacial current, R_J is the contact resistance between FM and SLG, and L is the spacing between the injector and detector electrodes. This equation shows that increasing the contact resistance produces a strong enhancement of ΔR_{NL} that saturates as R_J becomes significantly larger than R_G. Fig. 7-3b shows the non-local MR as a function of contact resistance based on equation 2 with typical values of W = 2 μm, L = 2 μm, λ_G = 2 μm, σ_G = 0.5 mS, P_F = 0.4 [31], $\rho_F = 6 \times 10^{-8}$ Ω m [29], and λ_F = 0.06 μm [30]. We plot two curves corresponding to junction polarizations of P_J = 0.4 and 0.2.

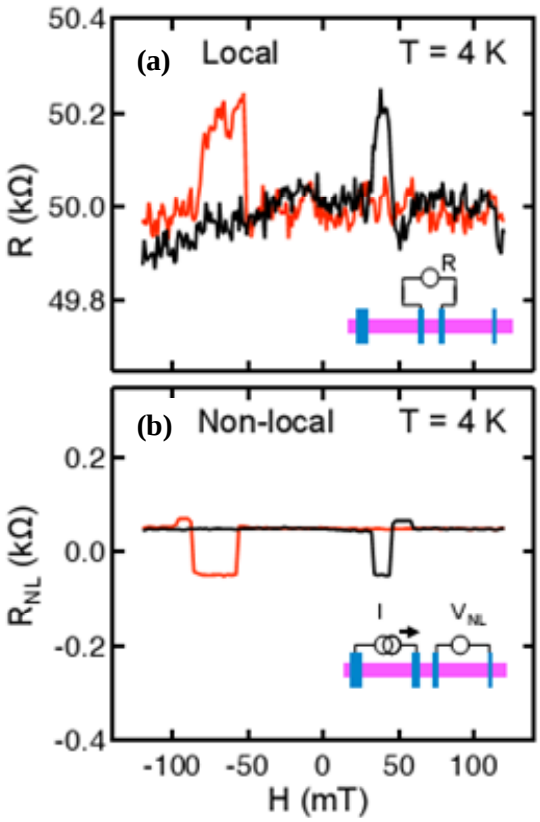

Fig. 7-4, local and nonlocal MR for SLG spin valve with tunneling contacts at 4K.

(a) Local MR measurements of a graphene spin valve. (b) Non-local MR measurements of the same graphene spin valve. Insets: Measurement geometries.

At 4 K, we measure a local MR signal of 0.4% at V_g = 0 V (fig. 7-4a), obtained by measuring the resistance across E2 and E3 as the magnetic field is ramped. Comparing the local and non-local MR scans (fig. 7-4a and 7-4b), the magnetization switching fields of the injector and detector electrodes match. It is also observed that the resistance change for the local MR is ~200 Ω, which is roughly twice the non-local MR (~100 Ω). This relationship between local MR and the non-local MR is expected theoretically [32, 33].

7.5 gate dependence of spin transport

Equation 2 also shows that the relationship of ΔR_{NL} vs. σ_G is strongly dependent on the contact resistance. Although the ΔR_{NL} vs. σ_G relation is applicable to any material system, it has never been verified experimentally across different contact regimes. The gate tunable conductivity of SLG provides a unique opportunity to investigate this behavior.

For transparent contacts ($R_J << R_G$), equation 2 reduces to:

$$\Delta R_{NL} = 4\frac{1}{R_G}\left(\frac{P_F R_F}{(1-P_F^2)}+\frac{P_G R_J}{(1-P_j^2)}\right)^2 \frac{e^{-L/\lambda_G}}{1-e^{-2L/\lambda_G}} \sim \sigma_G \qquad (3)$$

The top curve of Fig. 7-5 shows the calculated gate dependence of the non-local MR (normalized by its value at zero gate voltage) for transparent contacts. The conductivity is assumed to vary linearly with V_g away from the Dirac point according to $\sigma_G = \sigma_0 + \mu\alpha|V_g|$ [34], where σ_0 is the minimum conductivity (assumed to be $4e^2/h$ [34]), μ is the mobility (taken to be 2000 cm^2/Vs), e is the electron charge, and α is the capacitance per area (taken to be 1.15×10^{-8} F/cm^2 for 300 nm of SiO_2). Due to the proportionality of ΔR_{NL} and σ_G, the gate dependence of the non-local MR has a minimum at the Dirac point. For simplicity, we have assumed that λ_G is independent of V_g. Intuitively, the increase of non-local MR with increasing conductivity occurs because the conductance mismatch between the Co and SLG is reduced [13].

For intermediate contact resistance ($R_J \sim R_G$, $R_F << R_G$, $R_F << R_J$), equation 2 reduces to:

$$\Delta R_{NL} = 4R_G \left(\frac{P_J \frac{R_J}{R_G}}{1-P_J^2} \right)^2 \left(\left(1+\frac{2\frac{R_J}{R_G}}{1-P_J^2} \right)^2 - e^{-2L/\lambda_G} \right)^{-1} e^{-L/\lambda_G} \qquad (4)$$

The middle curve of Fig 7-5 shows the gate dependence of non-local MR calculated from equation 4 using R_J = 1 kΩ, P_J = 0.2, and σ_G defined above. The non-local MR exhibits a relatively weak dependence on gate voltage with a shallow minimum at the Dirac point.

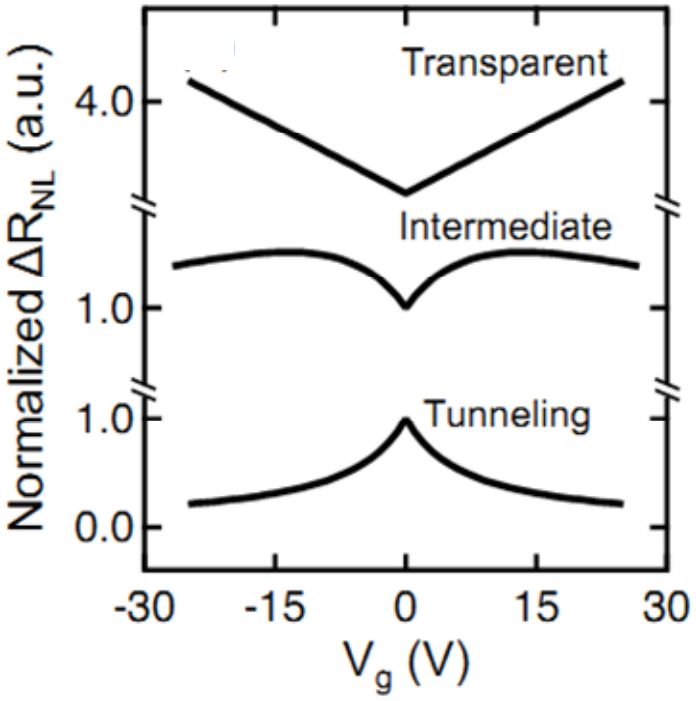

Fig. 7-5, predictions of the drift-diffusion theory of spin transport.

The non-local MR as a function of gate voltage for three different types of contacts between Co and SLG: transparent, intermediate, and tunneling. The curves are normalized by their value at zero gate voltage.

For tunneling contacts ($R_J >> R_G$), equation 2 reduces to:

$$\Delta R_{NL} = \frac{1}{\sigma_G}\frac{P_J^2 \lambda_G}{W} e^{-L/\lambda_G} \sim \frac{1}{\sigma_G} \qquad (5)$$

The bottom curve of fig .7-5 is a plot of the normalized non-local MR as a function of gate voltage based on equation 5. The presence of the tunnel barrier alleviates the conductance mismatch between the Co and SLG, as seen by the absence of the term $(R_F/R_G)^2$ in equation 5. This leads to the increase in the non-local MR observed experimentally in fig. 7-3a and theoretically in fig. 7-3b. Notably, the non-local MR has a maximum at the Dirac point and is inversely proportional to the SLG conductivity.

Experimentally, the gate dependence of ΔR_{NL} (black squares) and σ_G (red curve) for tunneling contacts at 300 K is shown in fig. 7-6a. Interestingly, ΔR_{NL} exhibits a maximum at V_g = 2 V near the Dirac point, which is the first time this has been observed experimentally. The origin of the asymmetry of ΔR_{NL} vs. V_g is unclear and varies from sample to sample. The observed peak structure in the gate dependence is a key characteristic of tunneling spin injection (Fig. 7-5, bottom curve), and has been reliably reproduced on four different devices. This inverse scaling of ΔR_{NL} with σ_G is associated with the spin injection process as opposed to spin detection. Specifically, spin injection produces a difference in the spin-dependent chemical potential at the tunnel barrier/SLG interface given by $\Delta\mu = \mu_\uparrow - \mu_\downarrow = eP_J R_G I$ [18]. Thus, a larger R_G will increase ΔR_{NL} due to a greater difference in the spin-dependent chemical potential.

The spin injection efficiency is calculated to be in the range of 20-30% for all gate voltages using equation 1 (assuming the spin diffusion length is 2.5 μm for all gate

voltages), as shown in the inset of fig. 7-6a. The reverse relationship is robust to low temperatures, and the 4 K results are shown in fig. 7-6b.

For comparison, the experimental results for the gate dependence of ΔR_{NL} the SLG spin valves with transparent contact and pinhole and pinhole contacts are shown in fig. 7-7a and 7-7b, respectively. The *I-V* characteristic of the contact resistance is determined by a three-probe lock-in measurement (current is applied across E1 and E2, voltage measured across E3 and E2). For both cases, the nearly constant bias dependence of $(dV/dI)_C$ (insets of fig. 7-6a and 7-6b) corresponds to a nearly linear *I-V* characteristic. For transparent contacts, ΔR_{NL} (black squares) exhibits a minimum at the Dirac point, and a linear relationship with σ_G (red curve), which verifies the theoretical prediction (Fig. 7-5, top curve). For pinhole contacts, ΔR_{NL} (black squares) shows relatively little variation and has a weak minimum near the Dirac point which is similar to the case of intermediate contact resistance as calculated in fig. 7-5 (middle curve). For both the transparent and pinhole contacts, the non-local MR and *I-V* characteristics are consistent with previous studies [3, 7, 8, 10, 16] which exhibit a minimum in ΔR_{NL} at the Dirac point and nearly linear I-V curves for the contacts.

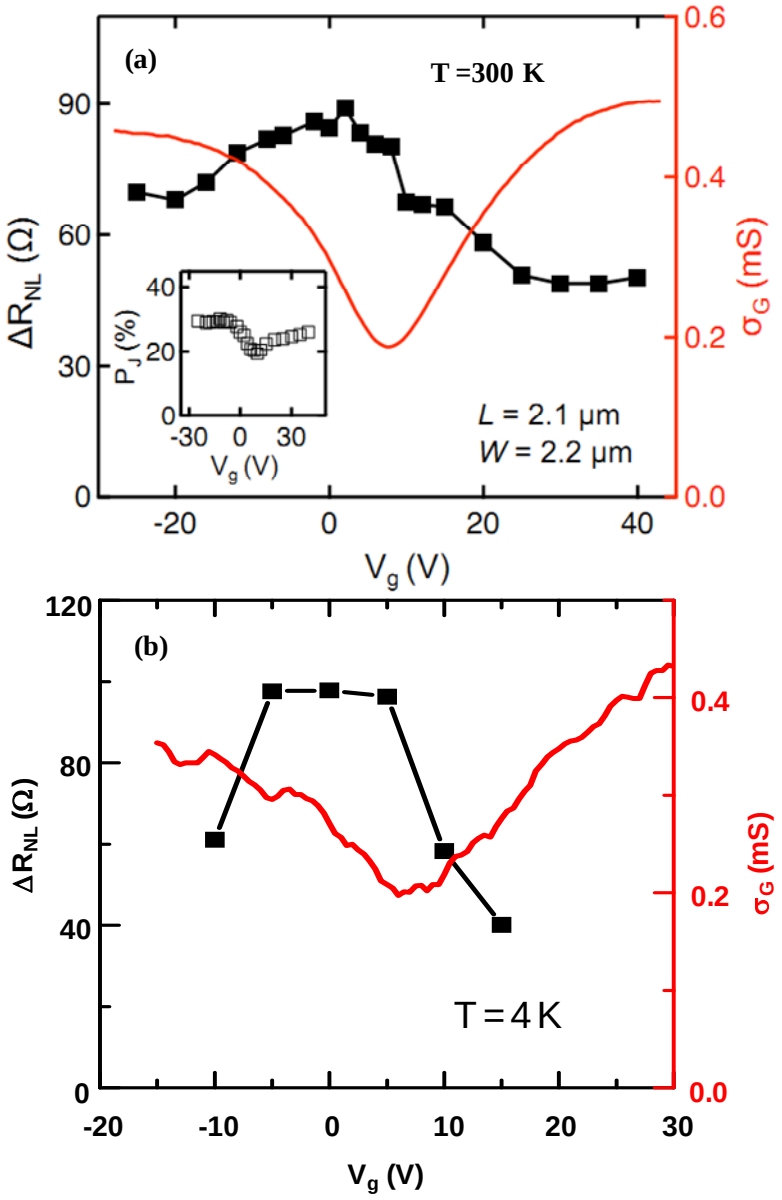

Fig. 7-6, gate dependence of the nonlocal MR at 300 K and 4 K.

(a) Non-local MR (black squares) and conductivity (red lines) as a function of gate voltage for SLG spin valves with tunneling contacts at 300 K. Inset: the spin injection efficiency calculated based on equation 1. (b) Non-local MR (black squares) and conductivity (red lines) as a function of gate voltage for SLG spin valves with tunneling contacts at 4 K.

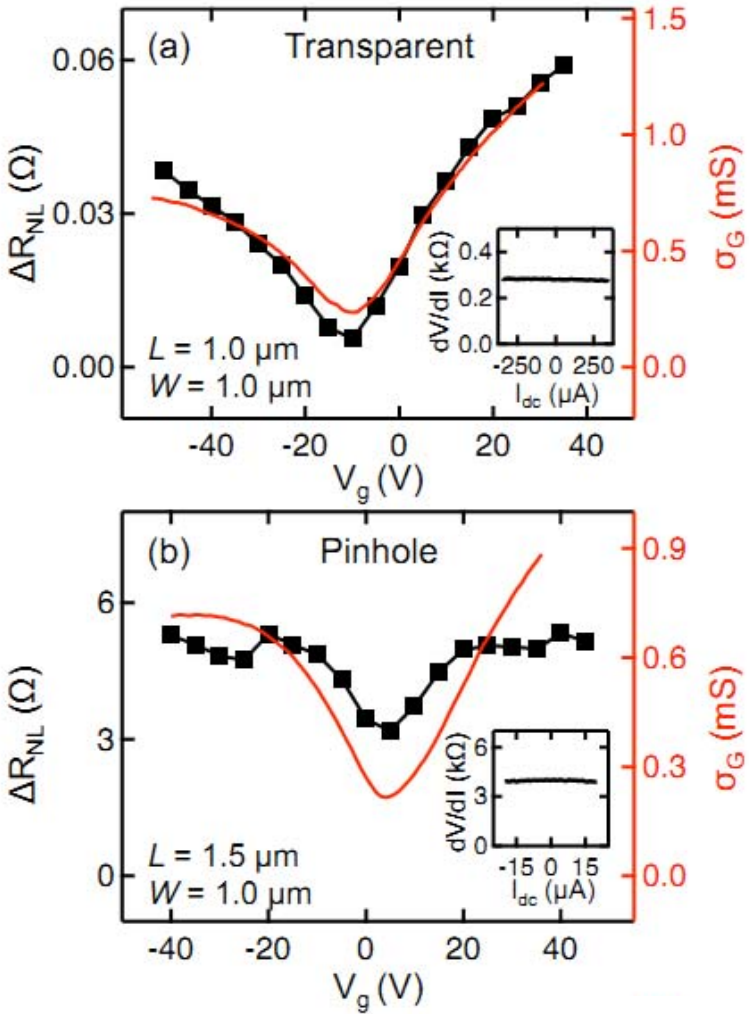

Fig. 7-7, gate dependence of the nonlocal MR at 300K for SLG spin valves with transparent contacts (a) and pinhole contacts (b). Insets: contact resistance as a function of bias current.

7.6 Spin lifetime measurement with different contacts

While the achievement of tunneling spin injection will be important for applications in spintronics, it will also have a strong impact on fundamental studies of spin relaxation in graphene. As shown in fig. 7-8a and 7-8b, the spin lifetimes measured at the Dirac point are 495 ps and 448 ps for tunneling SLG spin valves with 2.1 μm and 5.5 μm spacing, respectively. These are much longer than the spin lifetimes of 134 ps for pinhole contacts (fig. 7-8c) and 84 ps for transparent contacts (fig. 7-8d), which are consistent with the values reported in previous studies (50 - 200 ps) [3, 8-10]. The spin lifetimes are obtained by applying an out-of-plane magnetic field ($\boldsymbol{H}_{\perp}$) to induce spin precession and fitting the resulting Hanle curves (see [11] and Chapter 4 for details) with

$$R_{NL} \propto \pm \int_0^{\infty} \frac{1}{\sqrt{4\pi D t}} \exp\left[-\frac{L^2}{4Dt}\right] \cos(\omega_L t) \exp(-t/\tau_s) dt \qquad (3)$$

where the + (-) sign is for the parallel (antiparallel) magnetization state, D is the diffusion constant, τ_s is the spin lifetime, and $\varpi_L = g\mu_B H_{\perp} / \hbar$ is the Larmor frequency.

The ferromagnetic contacts can theoretically introduce spin relaxation through a number of mechanisms. One mechanism is through the inhomogeneous magnetic fringe fields. Roughness of the Co film could produce inhomogeneous local magnetic fields that vary with the morphology, which will generate spin relaxation through inhomogeneous spin precession about the spatially-varying local fields. This mechanism has been proposed to be significant in semiconductor systems [35]. A second mechanism is interfacial spin scattering, which is possible because of the direct contact between the FM and graphene for the transparent and pinhole contacts. A third mechanism for contact-

induced spin relaxation is related to the Hanle measurement itself. With metallic Co in contact with graphene, the spins diffuse from the graphene to the Co with a characteristic escape time, τ_{esc}. Due to the conductance mismatch between Co and graphene, the escape time can become comparable to or less than the actual spin lifetime (denoted as the spin-flip time, τ_{sf}). In this case, the Hanle lifetime (τ_s) in equation 2 is determined by both the spin-flip time and the escape time, with a simple relationship of $\tau_s^{-1} = \tau_{sf}^{-1} + \tau_{esc}^{-1}$ when the spin diffusion length is much larger than the sample size [36]. Because the Hanle lifetime is determined mostly by the smaller of τ_{sf} and τ_{esc}, it can only provide a lower bound of the spin lifetime. More accurate measurement of the true spin lifetime in graphene is made possible by the insertion of good tunnel barriers to reduce the out-diffusion of spins. This greatly increases τ_{esc} to yield $\tau_s^{-1} \approx \tau_{sf}^{-1}$ when $\tau_{esc} >> \tau_{sf}$, so that the measured Hanle lifetime τ_s more accurately measures the actual spin-flip time in graphene τ_{sf}. We note that it is possible to model this type of contact-induced spin relaxation numerically (see appendix of [37]) but an analytic expression for the Hanle curves including escape time effects is currently unavailable.

Based on the Hanle data in fig. 7-8 with much longer lifetimes for tunneling contacts compared to pinhole and transparent contacts, it is likely that for spin valves with lifetimes in the 50-200 ps range, the dominant spin relaxation is generated by the contacts. Thus, future studies of spin relaxation will require the use of tunneling contacts to suppress the contact-induced spin relaxation.

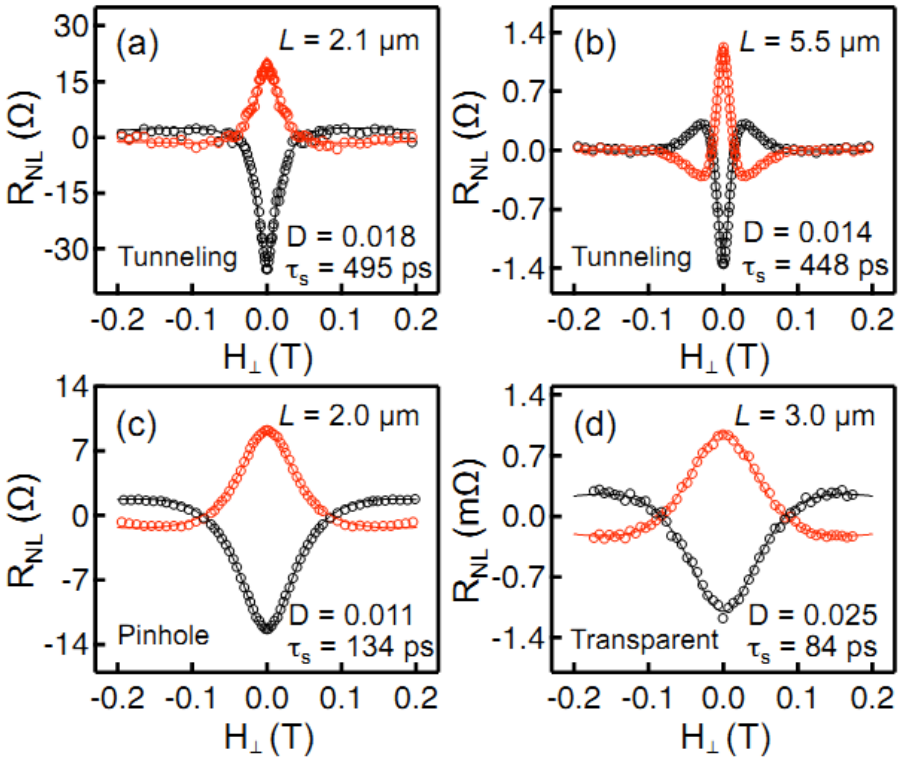

Fig. 7-8, Hanle spin precession for SLG spin valves with different contacts.

(a) Hanle spin precession for SLG spin valves with tunneling contacts (R_J = 30-70 kΩ, non-linear) for L=2.1 μm. (b) Hanle spin precession for tunneling contacts (R_J = 20-40 kΩ, non-linear) with L=5.5 μm. (c) Hanle spin precession for pinhole contacts (R_J = 6 kΩ, linear) with L=2.0 μm. (d) Hanle spin precession for transparent contacts (R_J < 0.3 kΩ, linear) with L=3.0 μm. The top (red/grey) and bottom (black) curves correspond to Hanle curves of the parallel and anti-parallel states, respectively. The solid lines are best fit curves based on equation 3. The units for D are m^2/s.

7.7 Conclusion

In conclusion, we have successfully achieved tunneling spin injection into SLG using TiO_2 seeded MgO barriers and observe enhanced spin injection efficiencies and large ΔR_{NL}. Investigating ΔR_{NL} vs. σ_G for the different contact regimes (from transparent to tunneling) realizes the contrasting behaviors predicted by the drift-diffusion theory. Finally, tunnel barriers reduce the contact-induced spin relaxation and are therefore important for future investigations of spin relaxation in graphene.

References:

[1] S. A. Wolf, D. D. Awschalom, R. A. Buhrman, J. M. Daughton, S. von Molnar, M. L. Roukes, A. Y. Chtchelkanova, and D. M. Treger, Science **294**, 1488 (2001).

[2] D. Huertas-Hernando, F. Guinea, and A. Brataas, Phys. Rev. B **74**, 155426 (2006).

[3] N. Tombros, C. Jozsa, M. Popinciuc, H. T. Jonkman, and B. J. van Wees, Nature **448**, 571 (2007).

[4] Y.-W. Son, M. L. Cohen, and S. G. Louie, Nature **444**, 347 (2006).

[5] W. Y. Kim, and K. S. Kim, Nature Nanotech. **3**, 408 (2008).

[6] S. Cho, Y.-F. Chen, and M. S. Fuhrer, Appl. Phys. Lett. **91**, 123105 (2007).

[7] W. Han, W. H. Wang, K. Pi, K. M. McCreary, W. Bao, Y. Li, F. Miao, C. N. Lau, and R. K. Kawakami, Phys. Rev. Lett. **102**, 137205 (2009).

[8] W. Han, K. Pi, W. Bao, K. M. McCreary, Y. Li, W. H. Wang, C. N. Lau, and R. K. Kawakami, Appl. Phys. Lett. **94**, 222109 (2009).

[9] C. Józsa, T. Maassen, M. Popinciuc, P. J. Zomer, A. Veligura, H. T. Jonkman, and B. J. van Wees, Phys. Rev. B **80**, 241403(R) (2009).

[10] M. Popinciuc, C. Jozsa, P. J. Zomer, N. Tombros, A. Veligura, H. T. Jonkman, and B. J. van Wees, Phys. Rev. B **80**, 214427 (2009).

[11] K. Pi, W. Han, K. M. McCreary, A. G. Swartz, Y. Li, and R. K. Kawakami, Phys. Rev. Lett. **104**, 187201 (2010).

[12] A. H. Castro Neto, and F. Guinea, Phys. Rev. Lett. 103, 026804 (2009); D. Huertas-Hernando, F. Guinea, and A. Brataas, Phys. Rev. Lett. 103, 146801 (2009); C. Ertler et al., Phys. Rev. B 80, 041405(R) (2009).

[13] G. Schmidt, D. Ferrand, L. W. Molenkamp, A. T. Filip, and B. J. van Wees, Phys. Rev. B **62**, 4790(R) (2000).

[14] E. I. Rashba, Phys. Rev. B **62**, 16267(R) (2000).

[15] A. Fert, and H. Jaffres, Phys. Rev. B **64**, 184420 (2001).

[16] C. Jozsa, M. Popinciuc, N. Tombros, H. T. Jonkman, and B. J. van Wees, Phys. Rev. B **79**, 081402(R) (2009).

[17] T. Kimura, Y. Otani, and J. Hamrle, Phys. Rev. B **73**, 132405 (2006).

[18] S. Takahashi, and S. Maekawa, Phys. Rev. B **67**, 052409 (2003).

[19] H. Dery, P. Dalal, L. Cywinski, and L. J. Sham, Nature **447**, 573 (2007).

[20] W. H. Wang, W. Han, K. Pi, K. M. McCreary, F. Miao, W. Bao, C. N. Lau, and R. K. Kawakami, Appl. Phys. Lett. **93**, 183107 (2008).

[21] B. J. Jonsson-Akerman, R. Escudero, C. Leighton, S. Kim, and I. K. Schuller, Appl. Phys. Lett. **77**, 1870 (2000).

[22] M. Johnson, and R. H. Silsbee, Phys. Rev. Lett. **55**, 1790 (1985).

[23] T. Kimura, and Y. Otani, Phys. Rev. Lett. 99, 196604 (2007); X. Lou et al., Nature Phys. 3, 197 (2007); O. M. J. van't Erve et al., Appl. Phys. Lett. 91, 212109 (2007).

[24] R. Meservey, and P. M. Tedrow, Phys. Rep. **238**, 173 (1994).

[25] D. J. Monsma, and S. S. P. Parkin, Appl. Phys. Lett. **77**, 720 (2000).

[26] C. H. Kant, J. T. Kohlhepp, H. J. M. Swagtden, and W. J. M. d. de Jonge, Appl. Phys. Lett. **84**, 1141 (2004).

[27] C. Kaiser, S. van Dijken, S.-H. Yang, H. Yang, and S. S. P. Parkin, Phys. Rev. Lett. **94**, 247203 (2005).

[28] Because of the ultrathin nature of the SLG, the current density experiences a significant change at the junction. Thus, the effective AJ should have a value between the Co/SLG contact area and W × (SLG thickness). For the estimation of RF/RG, the range is determined using AJ = W × 50 nm and AJ = W × (SLG thickness).

[29] D. R. Lide, CRC Handbook of Chem. and Phys., CRC Press, Boca Raton, Florida, USA, (1998).

[30] L. Piraux, S. Dubois, A. Fert, and L. Belliard, Eur. Phys. J. B. **4**, 413 (1998).

[31] R. J. Soulen Jr., J. M. Byers, M. S. Osofsky, B. Nadgorny, T. Ambrose, S. F. Cheng, P. R. Broussard, C. T. Tanaka, J. Nowak, J. S. Moodera, A. Barry, and J. M. D. Coey, Science **282**, 85 (1998).

[32] A. Fert, and S.-F. Lee, Phys. Rev. B **53**, 6554 (1996).

[33] F. J. Jedema, M. S. Nijboer, A. T. Filip, and B. J. v. Wees, Phys. Rev. B **67**, 085319 (2003).

[34] A. K. Geim, and K. S. Novoselov, Nature Mater. **6**, 183 (2007).

[35] S. P. Dash, S. Sharma, J. C. L. Breton, H. Jaffrès, J. Peiro, J.-M. George, A. Lemaître, and R. Jansen, Phys. Rev. B **84**, 054410 (2011).

[36] M. Zaffalon, and B. J. van Wees, Phys. Rev. B **71**, 125401 (2005).

[37] M. Popinciuc, C. Jozsa, P. J. Zomer, N. Tombros, A. Veligura, H. T. Jonkman, and B. J. van Wees, Phys. Rev. B **80**, 214427 (2009).

Chapter 8.

Spin relaxation in single layer and bilayer graphene[1]

Abstract

In this section, I investigate spin relaxation in graphene spin valves and observe strongly contrasting behavior for single layer graphene (SLG) and bilayer graphene (BLG). In SLG, the spin lifetime (τ_s) varies linearly with the momentum scattering time (τ_p) as carrier concentration is varied, indicating the dominance of Elliot-Yafet (EY) spin relaxation at low temperatures. In BLG, τ_s and τ_p exhibit an inverse dependence, which indicates the dominance of Dyakonov-Perel spin relaxation at low temperatures. The different behavior could be due to enhanced screening and/or reduced surface sensitivity of BLG, which greatly reduces the impurity-induced EY spin relaxation.

---

[1]Published as: Wei Han, and R. K. Kawakami, Phys. Rev. Lett. 105, 167202 (2011).

8.1 Introduction

Graphene is an attractive material for spintronics due to the possibility of long spin lifetimes arising from low intrinsic spin-orbit coupling and weak hyperfine coupling [1-5]. However, Hanle spin precession experiments in graphene spin valves report spin lifetimes that are orders of magnitude shorter than expected theoretically [6-12]. This has prompted theoretical studies of the extrinsic sources of spin relaxation such as impurity scattering [13], ripples [5], and substrate effects [14]. Experimentally, several studies have investigated spin relaxation including the roles of impurity scattering [7, 11] and graphene thickness [15]. Recently, it has been shown that ferromagnet (FM) contact-induced spin relaxation is responsible for the short spin lifetimes observed in experiments [12]. Therefore, high quality tunneling contacts are necessary to suppress the contact-induced effects for systematic investigations of spin relaxation in graphene.

Here, I perform systematic studies of spin relaxation in single layer graphene (SLG) and bilayer graphene (BLG) spin valves with tunneling contacts. The dependence of spin lifetime on temperature and carrier concentration (tuned by gate voltage) reveals rather different spin relaxation mechanisms in the two systems. In SLG, the temperature dependence shows similar trends of the spin lifetime and momentum scattering time, and the low temperature gate voltage dependence shows a strong linear scaling of the two quantities. This indicates the dominance of Elliot-Yafet (EY) spin relaxation, which most likely comes from impurity scattering. In BLG, the temperature dependence and low temperature gate voltage dependence show a nearly inverse relationship between the spin lifetime and momentum scattering time. This indicates the dominance of Dyakonov-Perel

(DP) spin relaxation, which can be generated by ripples in the graphene. The contrasting behaviors of SLG and BLG can be understood as a reduction of the impurity scattering in BLG due to the enhanced screening of the impurity potential and reduced surface sensitivity. This leads to longer spin lifetimes (~6.2 ns, the highest value observed in graphene spin valves to date) and the greater role of DP spin relaxation observed in BLG.

8.2 Experimental details

The graphene flakes are mechanically exfoliated from HOPG onto an SiO_2 (300 nm thickness)/Si substrate (fig. 8-1a)[16]. Gate voltage is applied to the Si substrate to tune the carrier concentration in graphene. SLG and BLG are identified by optical microscopy and Raman spectroscopy [17]. Standard e-beam lithography with PMMA/MMA bilayer resist is used to define the Au and Co electrodes. First, two Au electrodes are put down on the two ends of the graphene (fig. 8-1c and 8-1d). Then a second step of e-beam lithography is used for the Co electrodes, where subsequent angle evaporations of TiO_2, MgO, and Co produce the ferromagnetic electrodes with tunneling contacts [12, 18]. In ultrahigh vacuum, 0.12 nm of Ti is deposited at an angle of 9° and is converted to TiO_2 by exposure to oxygen partial pressure of 5×10^{-8} torr for 30 min. A 0.8 nm layer of MgO is deposited at 9° for the tunnel barrier and 3 nm of MgO is deposited at 0° for a masking layer. 80 nm of Co is deposited at 7° for the ferromagnetic electrodes, which are capped with 5 nm of Al_2O_3 prior to lift-off. The Ti, MgO, and Al_2O_3 are deposited by electron beam evaporation and the Co is deposited from a thermal effusion cell. Typically several Co electrodes are fabricated in between the two Au electrodes, but only two Co

electrodes are wired up for the nonlocal measurement (fig. 8-1e and 8-1f). The widths of the Co electrodes vary between 80 nm and 300 nm to have different coercivities.

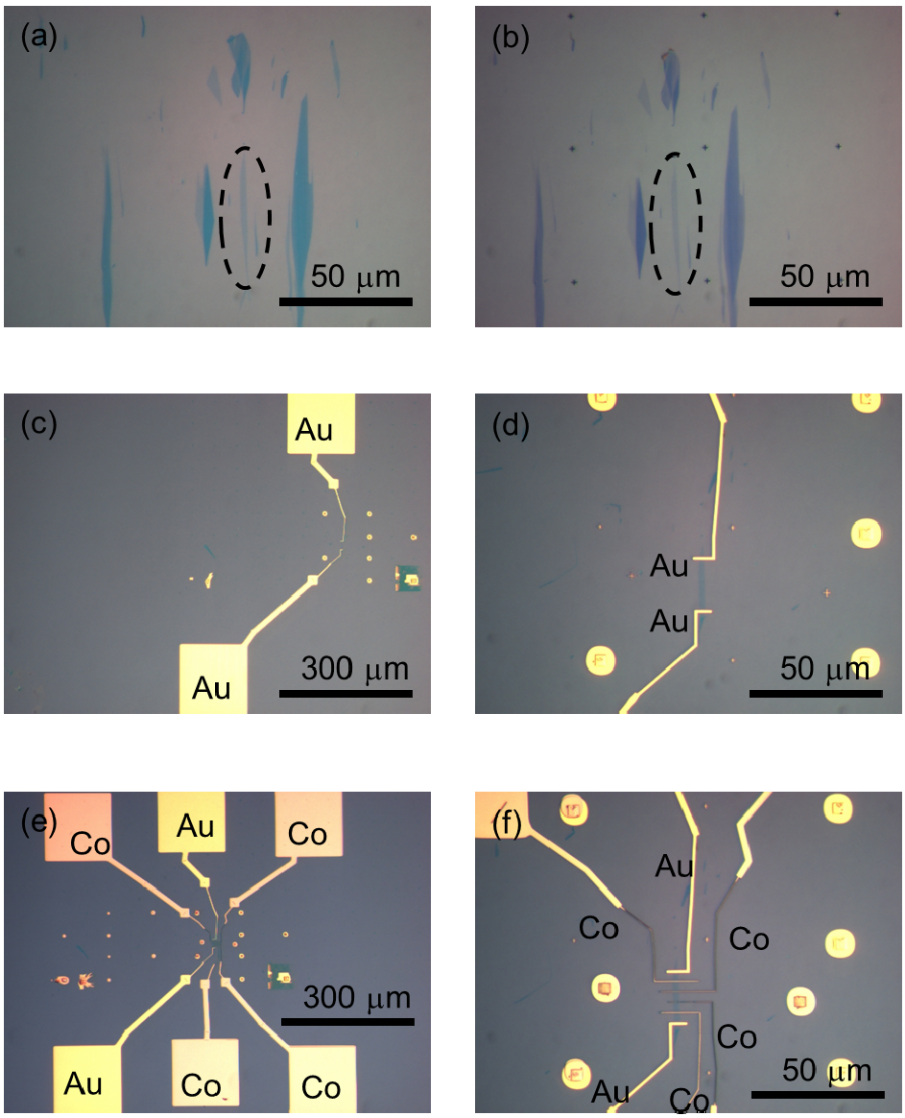

Fig. 8-1, device fabrication.

(a) Graphene on SiO2/Si; (b) Graphene on SiO2/Si with alignment marks on PMMA/MMA bilayer resist; (c-d) Graphene spin valves with only Au contacts. (e-f) Graphene spin valves with Co electrodes.

8.3 Results and discussion

Studies of spin transport and spin relaxation are performed on graphene spin valves consisting of two spin-sensitive Co electrodes (E2, E3) and two Au electrodes (E1, E4), as shown in fig. 8-2a. Nonlocal voltages (V_{NL}) are measured using lock-in detection with an ac injection current of I = 1 μA rms at 13 Hz [18]. For the nonlocal measurement of spin transport, spin-polarized carriers are injected into the graphene at electrode E2 [6, 19-24]. The spins subsequently diffuse to electrode E3 where they are detected as a voltage V_{NL} measured across electrodes E3 and E4. The nonlocal resistance ($R_{NL} = V_{NL}/I$) is measured as a function of in-plane magnetic field (fig. 1a inset) to detect the spin injection and transport (fig. 8-2b). Fig. 8-2c and 8-2d show the nonlocal magnetoresistance (MR) curves for two SLG devices (Device A and Device B), in which the sharp changes in R_{NL} are due to the magnetization switching of the Co electrodes. The nonlocal MR is indicated by the red arrow in fig. 8-2c, which is the magnitude of the sharp change in R_{NL}. Devices A and B have nonlocal MRs of 24 Ω and 5 Ω corresponding to spin injection efficiencies of 24% and 7%, respectively [12].

The spin lifetime (τ_s), diffusion coefficient (D), and spin diffusion length ($\lambda_G = \sqrt{D\tau_s}$) are determined by the nonlocal Hanle spin precession measurement (fig. 8-1e)[20]. Applying an out-of-plane magnetic field ($H_\perp$) causes the spins to precess as they diffuse from E2 to E3, which results in characteristic Hanle curves as shown in Figures 1f and 1g for devices A and B at 300 K. The red circles (black circles) are for the parallel (antiparallel) alignment of the Co magnetizations.

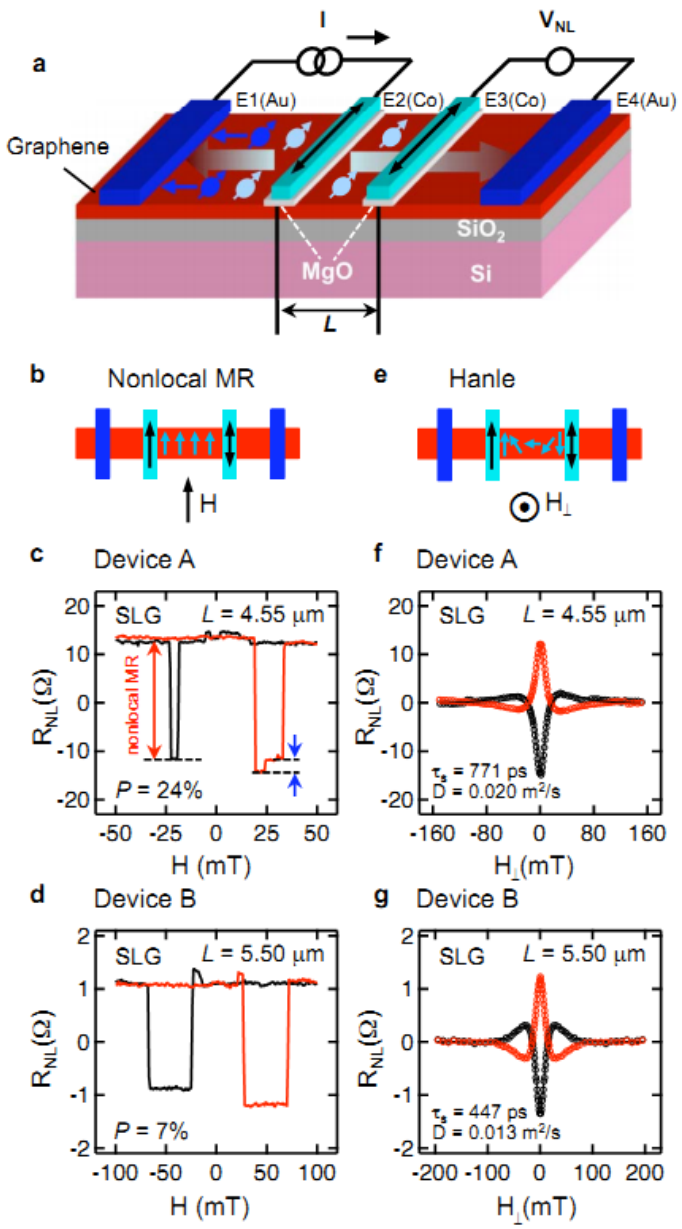

Fig. 8-2, measurement of spin transport and spin relaxation.

(a) Schematic device geometry for a graphene spin valve. (b) Nonlocal MR measurements. (c, d) Nonlocal MR measurement of device A (SLG) and device B (SLG), respectively, at 300 K. (e) Hanle measurement to determine the spin lifetime and diffusion coefficient (f, g) Hanle measurements of device A and device B, respectively, at 300 K. The red (black) circles are data taken for parallel (antiparallel) Co magnetizations.

τ_s and D are determined by fitting the Hanle curves with

$$R_{NL} \propto \pm \int_0^\infty \frac{1}{\sqrt{4\pi Dt}} \exp[-\frac{L^2}{4Dt}] \cos(\omega_L t) \exp(-t/\tau_s) dt \quad (1)$$

where the + (-) sign is for the parallel (antiparallel) magnetization state, L is the spacing between the Co electrodes, $\omega_L = g\mu_B H_\perp / \hbar$ is the Larmor frequency, g is the g-factor, μ_B is the Bohr magneton, and $\hbar$ is the reduced Planck's constant. For device A, the best fit parameters are D = 0.020 m^2/s and τ_s = 771 ps, which yields λ_G = 3.9 μm. For device B, D = 0.013 m^2/s, τ_s = 447 ps, and λ_G = 2.4 μm.

Fig. 8-3a and 8-3b show the 300 K nonlocal MR loops and Hanle spin precession curves for device B at different carrier concentrations. The carrier concentration is tuned by gate voltage (V_g) and is given by $n = -\alpha(V_g - V_{CNP})$ where $\alpha = 7.2\times10^{10}$ cm^{-2} V^{-1} for a 300 nm SiO_2 dielectric layer and V_{CNP} is the gate voltage for charge neutrality[11, 25]. Fig. 8-3c summarizes the nonlocal MR (black squares) and SLG conductivity (red line) as a function of gate voltage. The peak in nonlocal MR at the charge neutrality point is consistent with previous studies on tunneling spin injection [12, 26-28]. The τ_s and D obtained from the Hanle curves are plotted as a function of gate voltage in fig. 8-3d. At 300 K, there is no obvious correlation between τ_s and D. Interestingly, when the device is cooled to T = 4 K, τ_s and D exhibit a strong correlation, with both quantities increasing with carrier concentration (fig. 8-3f). One consequence of this increase is the enhancement of the nonlocal MR at high carrier concentrations (fig. 8-3e). More importantly, the correlation of τ_s and D implies a linear relation between τ_s and the momentum scattering time, τ_p ($D \sim \tau_p$ as discussed in ref. [7]). This indicates that at low

temperatures the spin scattering is dominated by momentum scattering through the Elliot-Yafet (EY) mechanism (i.e. finite probability of a spin-flip during a momentum scattering event) [29-31]. This behavior has been observed in five SLG devices.

The temperature dependences of τ_s and D at different carrier concentrations are shown in fig. 8-4a and 8-4b. As the temperature decreases from 300 K to 4 K, τ_s shows a modest increase at higher carrier densities (e.g. from ~0.5 ns to ~1 ns for $V_g - V_{CNP} = +60$ V) and little variation for lower carrier densities. The temperature dependence of D shows a similar behavior as τ_s. To analyze the relationship between the spin scattering and momentum scattering, we plot τ_s vs. D for temperatures below or equal to 100 K (fig. 8-4c) and for temperatures above 100 K (fig. 8-4d). The main trend is that for lower temperatures (fig. 8-4c), τ_s scales linearly with D, which indicates that an EY spin relaxation mechanism is dominant at lower temperatures (≤100 K). For higher temperatures (fig. 8-4d), τ_s and D do not follow the linear relationship as shown at low temperatures, which suggests that multiple sources of spin scattering are present. If there is more than one source of EY spin scattering (e.g. impurities of different species, phonons, etc.), the linear relationship between τ_s and τ_p does not necessarily hold; for example, with two EY scattering mechanisms obeying $\tau_{s,1}^{-1} = k_1 \tau_{p,1}^{-1}$ and $\tau_{s,2}^{-1} = k_2 \tau_{p,2}^{-1}$, the overall spin relaxation rate $\tau_s^{-1} = \tau_{s.1}^{-1} + \tau_{s,2}^{-1} = k_1 \left(\tau_{p,1}^{-1} + \frac{k_2}{k_1} \tau_{p,2}^{-1} \right)$ is not proportional to the overall momentum scattering rate $\tau_p^{-1} = \tau_{p,1}^{-1} + \tau_{p,2}^{-1}$ except in some special cases (e.g. $k_1 = k_2$, $\tau_{p,1} << \tau_{p,2}$, etc.).

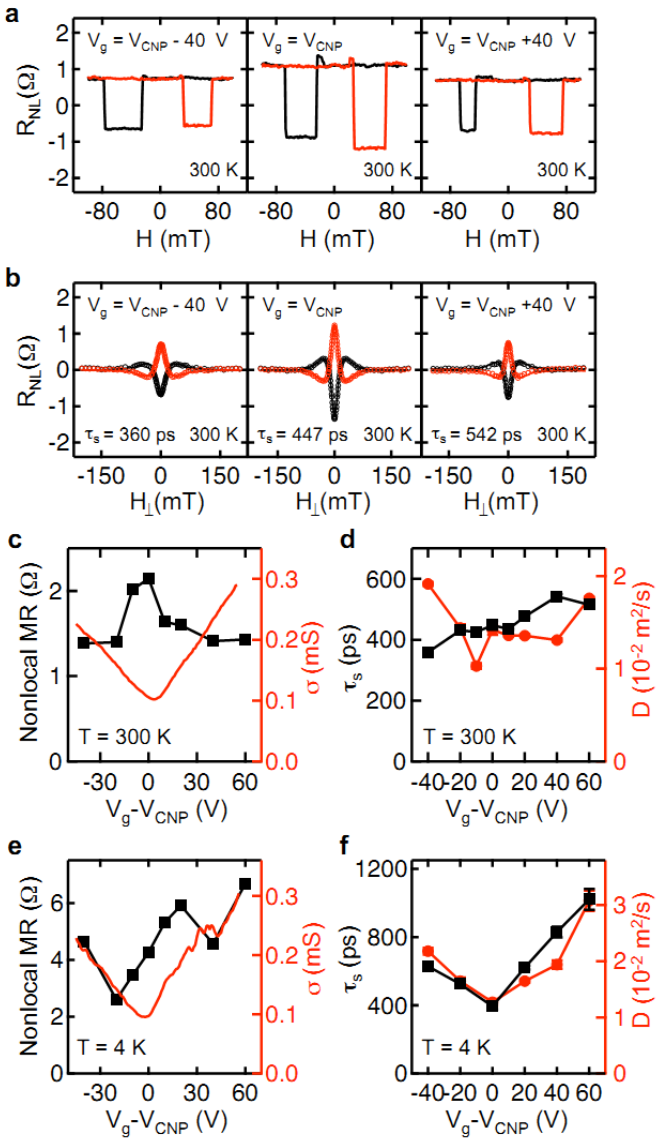

Fig. 8-3, gate dependence of SLG spin valves.

(a-b) Nonlocal MR measurements and Hanle measurements of device B at 300 K for different gate voltages. (c) Nonlocal MR (black squares) and SLG conductivity (red curve) as a function of gate voltage at 300 K. (d) Spin lifetime (black squares) and diffusion coefficient (red circles) as a function of gate voltage at 300 K. (e) Nonlocal MR (black squares) and SLG conductivity (red curve) as a function of gate voltage at 4 K. (f) Spin lifetime (black squares) and diffusion coefficient (red circles) as a function of gate voltage at 4 K.

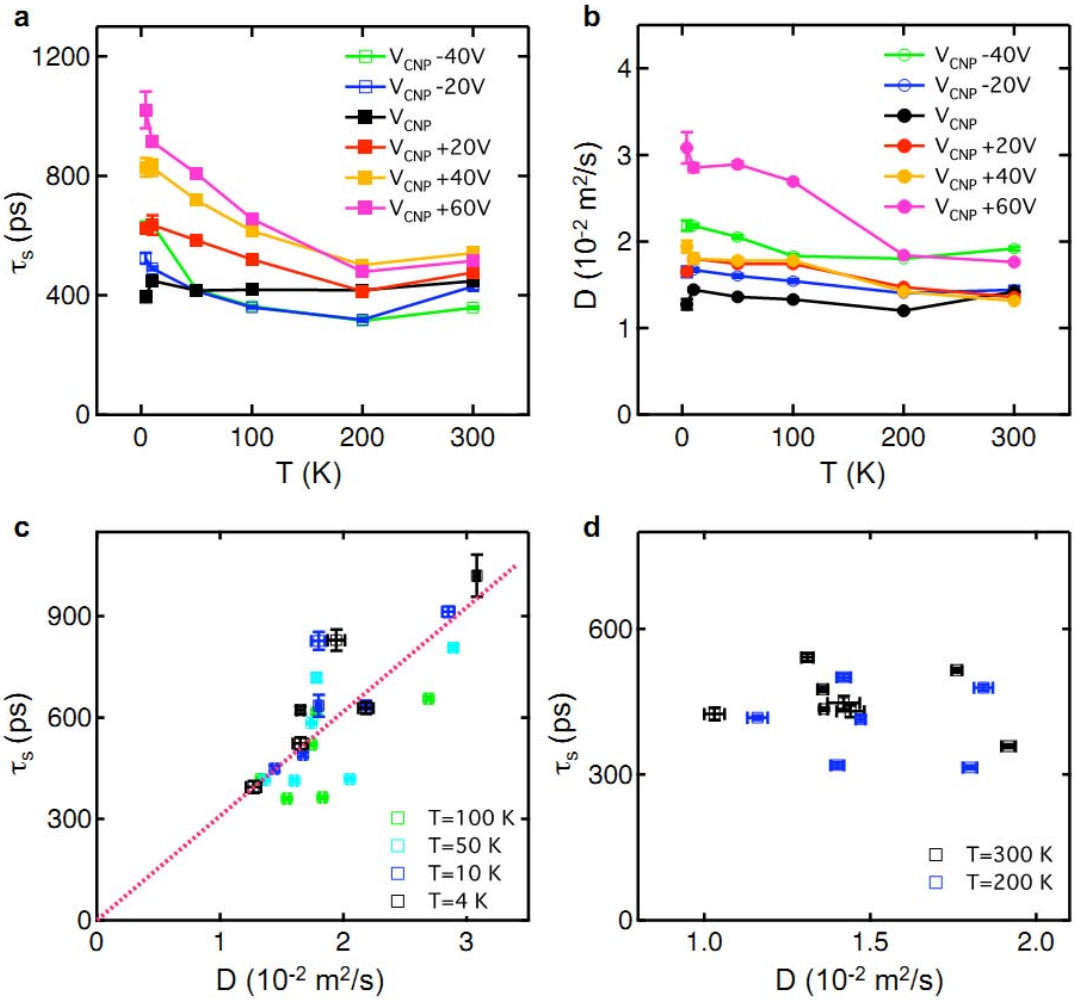

Fig. 8-4, temperature dependence of SLG spin valves.

(a) Temperature dependence of the spin lifetime at different gate voltages for device B. (b) Temperature dependence of the diffusion coefficient at different gate voltages for device B. (c) Plot of spin lifetime vs. diffusion coefficient for $T \leq 100$ K. The dashed line shows the best linear fit. (d) Plot of spin lifetime vs. diffusion coefficient for $T \geq 200$ K.

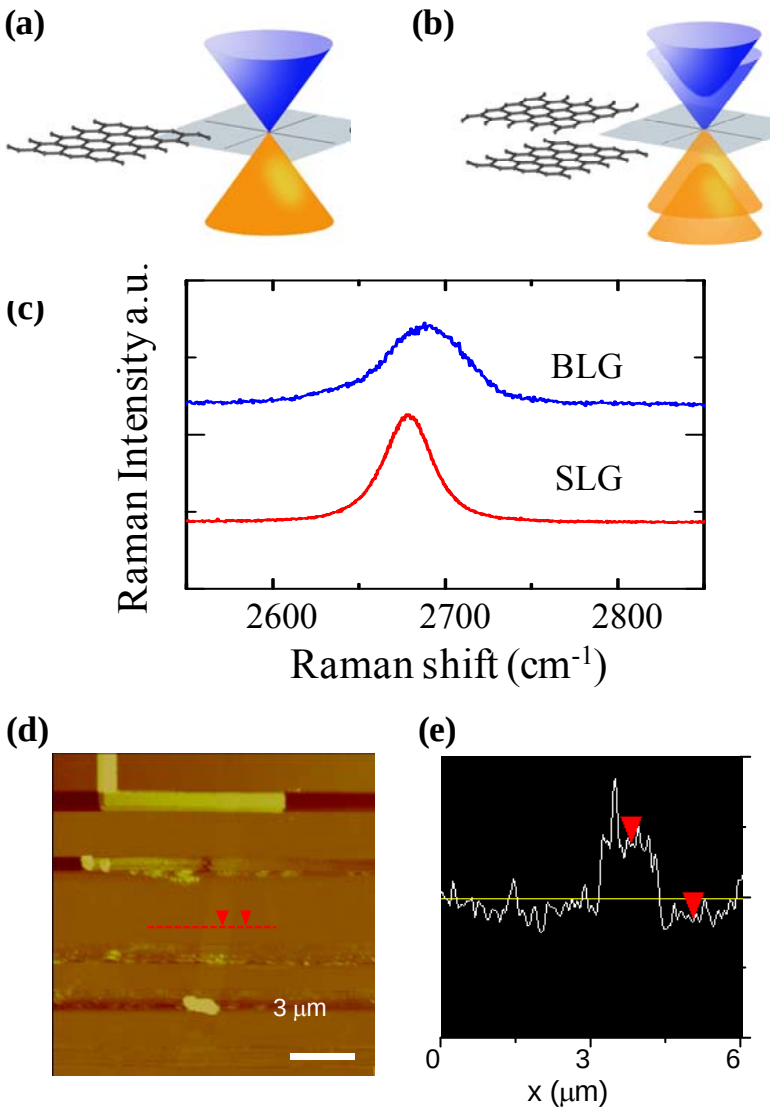

Fig. 8-5, bilayer graphene.

(a-b) Band structure of single layer and bilayer grpahene. (b) Raman spectrum of SLG and BLG. (c) AFM image of a BLG spin valve device. (e) line cut of the BLG shown in fig. 8-5d. The step height is 1.28 nm.

Next, we investigate spin relaxation in BLG spin valves, which differs from SLG not just in thickness but also in band structure (linear for SLG, parabolic for BLG, as shown in fig. 8-5a and fig. 8-5b) and intrinsic spin-orbit coupling [32, 33]. BLG is identified by micro-Raman spectroscopy [17] (fig. 8-5c) and atomic force microscopy (fig. 8-5d and 8-5e). Fig. 8-6a shows a representative nonlocal MR curve of a BLG spin valve (Device C, L=3.05 μm) measured at 300 K (the nonlocal MR is 0.6 Ω at $V_g = V_{CNP}$). Fig 8-6b shows the corresponding Hanle curve at 300 K with best fit parameters of D = 0.008 m^2/s and τ_s = 268 ps. Fig. 8-6d shows the Hanle curve of the longest observed spin lifetime of 6.2 ns, which is obtained on device C for the charge neutrality point at 20 K. Fig. 8-6c and 8-6e show the Hanle curves at 20 K for gate voltages of V_{CNP} − 40 V and V_{CNP} + 40 V, respectively. The gate dependences of τ_s and D at 300 K and 20 K are shown in fig. 8-6f and 8-6g, respectively. At 300 K, τ_s varies from 250 ps to 450 ps as a function of gate voltage and exhibits no obvious correlation with D. At 20 K, τ_s varies from 2.5 ns to 6.2 ns, showing a peak at the charge neutrality point. On the other hand, the gate dependence of D exhibits lower values near the charge neutrality point and increasing values at higher carrier densities. This opposite trend of τ_s and D is robust even under an irreversible sample change experienced by this device. The opposite behaviors of τ_s and D suggest the importance of D'yakonov-Perel (DP) spin relaxation (i.e. spin relaxation via precession in internal spin-orbit fields) where τ_s scales inversely with τ_p [31, 34]. This behavior has been observed in four BLG devices.

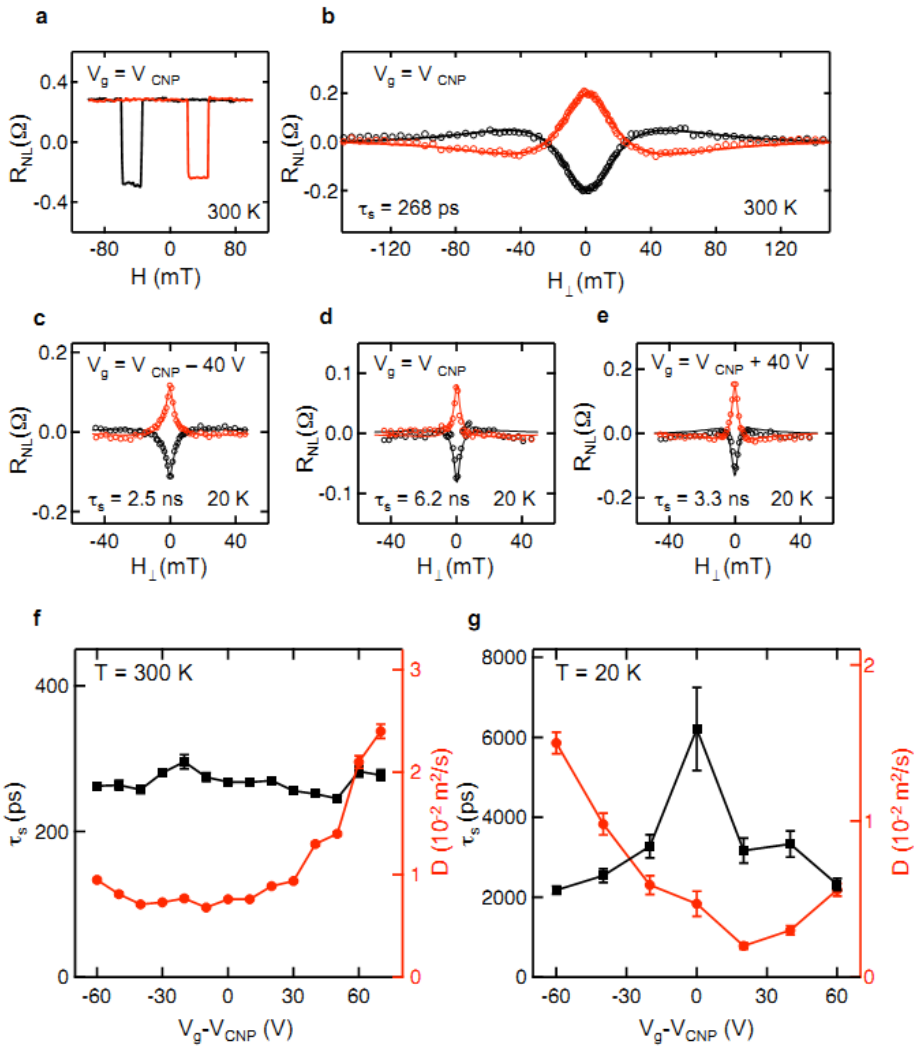

Fig. 8-6, gate dependence of BLG spin valves.

(a) Nonlocal MR measurement of device C (BLG) at 300 K (L = 3.05 mm). (b) Hanle measurement for device C at 300 K for $V_g = V_{CNP}$. (c, d, e) Hanle measurement for device C at 20 K for $V_g - V_{CNP}$ = –40 V, 0 V, and +40 V, respectively. (f) Spin lifetime (black squares) and diffusion coefficient (red circles) as a function of gate voltage at 300 K. (g) Spin lifetime (black squares) and diffusion coefficient (red circles) as a function of gate voltage at 20 K.

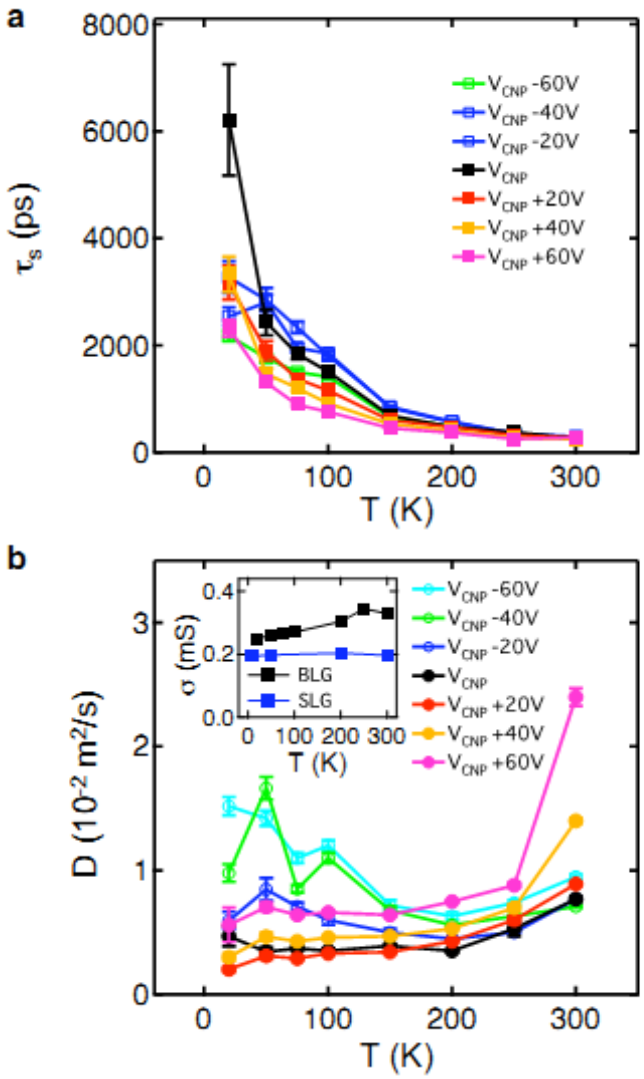

Fig. 8-7, temperature dependence of BLG spin valves.

(a) Temperature dependence of spin lifetime at different gate voltages for device C. (b) Temperature dependence of diffusion coefficient at different gate voltages for device C. Inset: temperature dependence of the graphene conductivity at the charge neutrality point for BLG device C (black squares) and SLG device B (blue squares).

Fig 8-7a and 8-7b show the temperature dependences of τ_s and D, respectively. At low temperatures, τ_s is enhanced while D is reduced, which is different from SLG where both D and τ_s increase as temperature decreases for most gate voltages. The opposite trends of the temperature dependences of τ_s and D suggest the strong contributions of spin relaxation mechanisms of the DP type, which is also suggested in ref. [35].

To investigate the spin relaxation in BLG quantitatively, we perform a detailed measurement of the gate voltage dependence of a BLG spin valve (device D) at 4 K. In fig 8-8a, τ_s and D exhibit opposite dependences as a function of gate voltage, indicating the importance of DP spin relaxation. Quantitatively, it is known that the scattering rate for EY spin relaxation scales as $\frac{1}{\tau_s^{EY}} \sim \frac{1}{\tau_p} \sim \frac{1}{D}$, while the scaling for DP spin relaxation is $\frac{1}{\tau_s^{DP}} \sim \tau_p \sim D$ [7, 15, 29-31, 34, 36]. Hence, if both EY and DP spin scattering are present, the spin lifetime is:

$$\frac{1}{\tau_s} = \frac{1}{\tau_s^{EY}} + \frac{1}{\tau_s^{DP}} = \frac{K_{EY}}{D} + K_{DP} D \qquad (2)$$

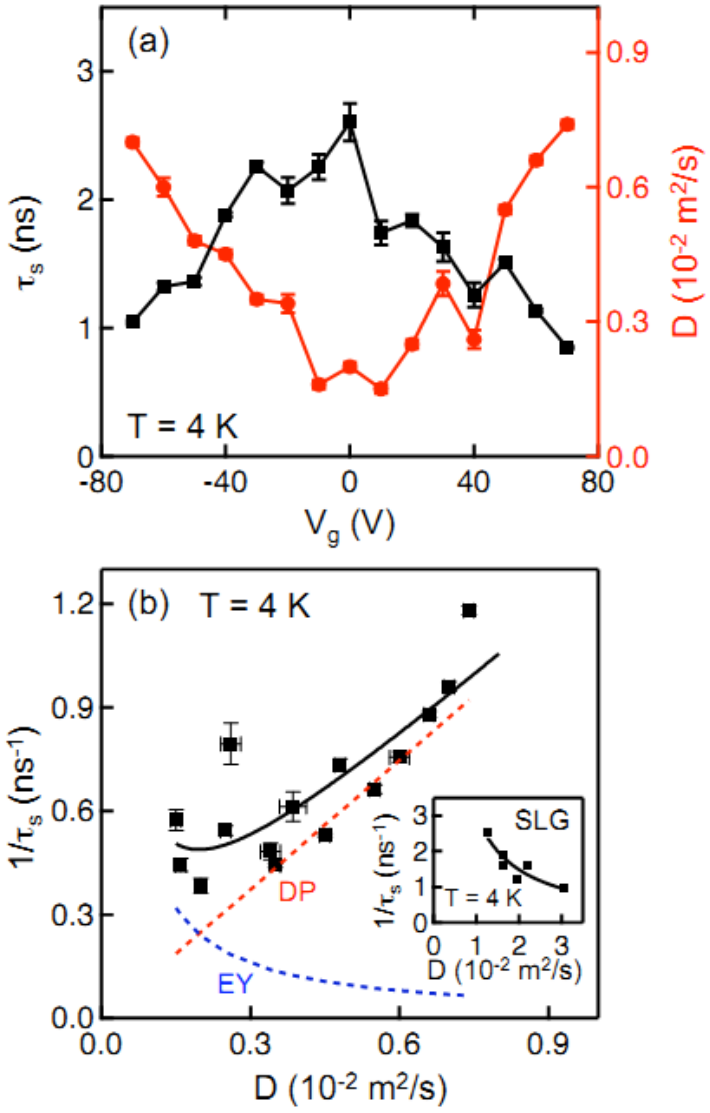

Fig. 8-8, gate dependence of BLG spin valves (device D).

(a) Spin lifetime (squares) and diffusion coefficient (circles) as a function of gate voltage at 4 K. (b) Spin relaxation rate as a function of diffusion coefficient. The black solid line is the best fit based on equation 2. The dashed red (blue) line is the contribution of DP (EY) spin relaxation. Inset: Spin relaxation rate as a function of diffusion coefficient for SLG (device B) at 4K with the best fit (solid line) based on equation 2.

Fig. 8-8b shows the spin relaxation rate ($1/\tau_s$) as a function of D for BLG (device D at 4 K). The best fit by equation 2 yields $K_{EY} = 0.05 \pm 0.01$ (10^{-2} m^2s^{-1}) ns^{-1}, and $K_{DP} = 1.24 \pm 0.09$ (10^{-2} m^2s^{-1})$^{-1}$ ns^{-1}. The contributions from EY spin relaxation are shown by the blue dashed line, and the contributions from DP spin relaxation are shown by the red dashed line. For the experimental range of D, the DP contribution to spin relaxation is much stronger than the EY contribution. For comparison, we plot the spin relaxation rate ($1/\tau_s$) as a function of D (fig. 8-8b inset) for SLG (device B at 4 K). The best fit parameters are $K_{EY} = 3.05 \pm 0.35$ (10^{-2} m^2s^{-1})ns^{-1}, and $K_{DP} = -0.02 \pm 0.10$ (10^{-2} m^2s^{-1})$^{-1}ns^{-1}$, which is zero within the error bars.

It is noted that longer spin lifetimes are observed in BLG (up to 6.2 ns) than in SLG (up to 1.0 ns). Theoretically, the intrinsic spin-orbit coupling in BLG is an order of magnitude larger than in SLG, which predicts shorter spin lifetimes for BLG [33]. The opposite experimental trend verifies that the spin relaxation in graphene is of extrinsic origin and the SLG is more sensitive to the extrinsic spin scattering than BLG. Possible sources of extrinsic EY spin relaxation include long-range (Coulomb) impurity scattering and short-range impurity scattering [13], while an extrinsic DP spin relaxation could arise from curvature of the graphene film [1, 5]. The transition from EY-dominated SLG to the DP-dominated BLG could be due to a strong reduction of the EY contribution because of enhanced screening of the impurity potential in thicker graphene [15, 37] and the smaller surface-to-volume ratio. However, a quantitative explanation for the substantial differences in spin relaxation between SLG and BLG will require further theoretical and experimental studies. Specifically, understanding the relationship between spin relaxation

and the characteristics that differentiate SLG from BLG (e.g. band structure, lattice symmetry, bandgap formation in BLG, etc.) may be essential.

8.4 Conclusion

In summary, spin relaxation in SLG and BLG spin valves has been investigated. By studying the spin lifetime and diffusion coefficient in SLG and BLG as a function of temperature and carrier concentration, contrasting behaviors are observed. For SLG, the EY spin scattering (e.g. impurity scattering) is dominant at low temperatures leading to the linear scaling of τ_s and τ_p. For BLG, the temperature dependence shows an opposite trend between the spin lifetime and momentum scattering time, and the low temperature gate voltage dependence shows an inverse relationship of the two quantities, which indicate the dominance of DP spin relaxation.

References:

[1] D. Huertas-Hernando, F. Guinea, and A. Brataas, Phys. Rev. B **74**, 155426 (2006).

[2] H. Min, J. E. Hill, N. A. Sinitsyn, B. R. Sahu, L. Kleinman, and A. H. MacDonald, Phys. Rev. B **74**, 165310 (2006).

[3] Y. Yao, F. Ye, X.-L. Qi, S.-C. Zhang, and Z. Fang, Phys. Rev. B **75**, 041401(R) (2007).

[4] B. Trauzettel, D. V. Bulaev, D. Loss, and G. Burkard, Nature Physics **3**, 192 (2007).

[5] D. Huertas-Hernando, F. Guinea, and A. Brataas, Phys. Rev. Lett. **103**, 146801 (2009).

[6] N. Tombros, C. Jozsa, M. Popinciuc, H. T. Jonkman, and B. J. van Wees, Nature **448**, 571 (2007).

[7] C. Józsa, T. Maassen, M. Popinciuc, P. J. Zomer, A. Veligura, H. T. Jonkman, and B. J. van Wees, Phys. Rev. B **80**, 241403(R) (2009).

[8] M. Popinciuc, C. Jozsa, P. J. Zomer, N. Tombros, A. Veligura, H. T. Jonkman, and B. J. van Wees, Phys. Rev. B **80**, 214427 (2009).

[9] M. Shiraishi, M. Ohishi, R. Nouchi, T. Nozaki, T. Shinjo, and Y. Suzuki, Adv. Funct. Mater. **19**, 3711 (2009).

[10] W. Han, K. Pi, W. Bao, K. M. McCreary, Y. Li, W. H. Wang, C. N. Lau, and R. K. Kawakami, Appl. Phys. Lett. **94**, 222109 (2009).

[11] K. Pi, W. Han, K. M. McCreary, A. G. Swartz, Y. Li, and R. K. Kawakami, Phys. Rev. Lett. **104**, 187201 (2010).

[12] W. Han, K. Pi, K. M. McCreary, Y. Li, J. J. I. Wong, A. G. Swartz, and R. K. Kawakami, Phys. Rev. Lett. **105**, 167202 (2010).

[13] A. H. Castro Neto, and F. Guinea, Phys. Rev. Lett. **103**, 026804 (2009).

[14] C. Ertler, S. Konschuh, M. Gmitra, and J. Fabian, Phys. Rev. B **80**, 041405(R) (2009).

[15] T. Maassen, F. K. Dejene, M. H. Guimaraes, C. Jozsa, and B. J. van Wees, arXiv:1012.0526, (2010).

[16] K. S. Novoselov, A. K. Geim, S. V. Morozov, D. Jiang, Y. Zhang, S. V. Dubonos, I. V. Grigorieva, and A. A. Firsov, Science **306**, 666 (2004).

[17] A. C. Ferrari, J. C. Meyer, V. Scardaci, C. Casiraghi, M. Lazzeri, F. Mauri, S. Piscanec, D. Jiang, K. S. Novoselov, S. Roth, and A. K. Geim, Phys. Rev. Lett. **97**, 187401 (2006).

[18] A. Csik, G. A. Langer, D. L. Beke, and Z. Erdelyi, J. Appl. Phys. **89**, 804 (2001).

[19] M. Johnson, and R. H. Silsbee, Phys. Rev. Lett. **55**, 1790 (1985).

[20] F. J. Jedema, H. B. Heersche, A. T. Filip, J. J. A. Baselmans, and B. J. van Wees, Nature **416**, 713 (2002).

[21] X. Lou, C. Adelmann, S. A. Crooker, E. S. Garlid, J. Zhang, K. S. M. Reddy, S. D. Flexner, C. J. Palmstrom, and P. A. Crowell, Nature Physics **3**, 197 (2007).

[22] S. Cho, Y.-F. Chen, and M. S. Fuhrer, Appl. Phys. Lett. **91**, 123105 (2007).

[23] W. Han, W. H. Wang, K. Pi, K. M. McCreary, W. Bao, Y. Li, F. Miao, C. N. Lau, and R. K. Kawakami, Phys. Rev. Lett. **102**, 137205 (2009).

[24] H. Goto, A. Kanda, T. Sato, S. Tanaka, Y. Ootuka, S. Odaka, H. Miyazaki, K. Tsukagoshi, and Y. Aoyagi, Appl. Phys. Lett. **92**, 212110 (2008).

[25] A. K. Geim, and K. S. Novoselov, Nature Materials **6**, 183 (2007).

[26] S. Takahashi, and S. Maekawa, Phys. Rev. B **67**, 052409 (2003).

[27] A. Fert, and H. Jaffres, Phys. Rev. B **64**, 184420 (2001).

[28] H. Jaffres, J.-M. George, and A. Fert, Phys. Rev. B **82**, 140408(R) (2010).

[29] R. J. Elliott, Phys. Review **96**, 266 (1954).

[30] Y. Yafet, in Solid State Physics, edited by F. Seitz and D. Turnbull (Academic Press Inc., New York, 1963), Vol. 14, p. 1.

[31] F. Meier, and B. P. Zachachrenya, Optical Orientation, Modern Problems in Condensed Matter Science (North-Holland, Amsterdam, 1984), Vol. 8.

[32] A. K. Geim, and K. S. Novoselov, Nature Materials **6**, 183 (2007).

[33] F. Guinea, New J. of Phys. **12**, 083063 (2010).

[34] M. I. D'yakonov, and V. I. Perel', Sov. Phys. State **13**, 3023 (1972).

[35] T.-Y. Yang, J. Balkrishnna, F. Volmer, A. Avsar, M. Jaiswal, J. Samm, S. R. Ali, A. Pachoud, M. Zeng, M. Popinciuc, G. Guntherodt, B. Beschoten, and B. Ozyilmaz, Phys. Rev. Lett. **107**, 047206 (2010).

[36] J. Fabian, A. Matos-Abiague, C. Ertler, P. Stano, and I. Zutic, Acta Physica Slovaca **57**, 565 (2007).

[37] F. Guinea, Phys. Rev. B **75**, 235433 (2007).

Chapter 9.

Spin relaxation in single layer graphene with tunable mobilites[1]

Abstract

In this section, I investigate spin relaxation in single layer graphene (SLG) spin valves with tunable mobilities. The SLG spin valve is first decorated with a layer of ligand-bound nanoparticles (Fe_2O_3). It is demonstrated that the charges are able to transfer between graphene and Fe_2O_3 nanoparticales reservoir at room temperature, which could be indicated by the mobility tenability at low temperature (10 K). Hanel spin precession results show that the spin lifetimes in SLG are always in the range of 0.5-2 ns for SLG at 10 K although the mobility of the SLG varies from 2000-12000 $cm^2V^{-1}s^{-1}$. These results indicate that the charged impurity scattering is not the dominant spin relaxation in SLG.

---

[1] Wei Han, Jen-Ru Chen, Deqi Wang, Kathy McCreary, Adrian Swartz, Jing Shi, and Roland Kawakami, in preparation.

9.1 Introduction

Graphene is attractive for spintronics for the possibility of long spin lifetimes and long spin transport length due to low intrinsic spin-orbit and weak hyperfine couplings [1-5]. However, Hanle spin precession experiments in single layer graphene (SLG) spin valves report spin lifetimes that are orders of magnitude shorter than expected theoretically [6-12]. This has prompted theoretical studies of the extrinsic sources of spin relaxation such as impurity scattering [13], ripples [5], and substrate effects [14]. Experimentally, several studies have investigated spin relaxation in SLG including the roles of contact-induced spin relaxation [8, 12, 15], nano ripples [16], linear relationship band structure [7, 15, 17], spin relaxation due to the edge effects [8] and impurity scattering [7, 11]. However, all these studies are done on low mobility SLG (< 5000 $cm^2V^{-1}s^{-1}$), and are performed on different sheets of SLG, different carrier concentration or the low spin lifetimes regime (50-200 ps). Since different sheets of graphene are of different edges, different contact-induced spin relaxation, and different amounts of the defects. This makes the conclusion related to the impurity scattering questionable. To directly study the relationship of spin lifetimes and mobility due to charged impurity scattering, it would be necessary to study the spin relaxation in the same SLG spin valve with a large range of mobilities.

In this chapter, I perform systematic studies of spin relaxation in the same SLG in which the mobility is tuned by controlling the amount of charged impurities. First, the SLG spin valve is decorated with a layer of ligand-bound nanoparticles (iron oxide, mainly γ-Fe_2O_3 with a diameter of 13 nm). The mobility is able to be tuned, similar to

previous studies [18]. Then, the spin relaxation is measured using Hanle spin precession, in which the spin lifetimes turn out to be in the same range of 0.5-2 ns for SLG at 10 K with mobility from 2000-12000 $cm^2V^{-1}s^{-1}$. These results indicate that the charged impurity scattering is not the dominant spin relaxation in SLG with the mobility less than 12000 $cm^2V^{-1}s^{-1}$. This result is important for further investigation of the spin relaxation in graphene.

9.2 Experimental details

The graphene flakes are mechanically exfoliated from HOPG onto an SiO_2 (300 nm thickness)/Si substrate [19], in which the Si substrate is used as a gate to tune the carrier concentration in graphene. SLG is identified by optical microscopy and Raman spectroscopy [20]. The Au and Co electrodes are defined with standard e-beam lithography with PMMA/MMA bilayer resist. A first step of e-beam lithography is sued for the Au electrodes, which are put on the two ends of the SLG. Then the Co electrodes are defined using a second step of e-beam lithography and grown by angle evaporations of TiO_2, MgO, and Co to produce the ferromagnetic electrodes with tunneling contacts [12]. In ultrahigh vacuum, 0.12 nm of Ti is deposited at an angle of 9° and is converted to TiO_2 by exposure to oxygen partial pressure of 5×10^{-8} torr for 30 min. A 0.8 nm layer of MgO is deposited at 9° for the tunnel barrier and 3 nm of MgO is deposited at 0° for a masking layer. 80 nm of Co is deposited at 7° for the ferromagnetic electrodes, which are capped with 5 nm of Al_2O_3 prior to lift-off. Typically several Co electrodes are fabricated in between the two Au electrodes, but only two Co electrodes are wired up for the

nonlocal measurement. The widths of the Co electrodes vary between 80 nm and 300 nm to have different coercivities.

To control the density of NPs on graphene, we first dilute iron oxide NPs with toluene in various ratios ranging from 1:10 to 1:2000 [18].. After we put ~ 10 drops of NPs solution on graphene, we leave the device at room temperature until it is completely dried. Then the device is measured using an Oxford He 4 system.

9.3 Results and discussion

Studies of spin transport and spin relaxation are performed on graphene spin valves consisting of two spin-sensitive Co electrodes (E2, E3) and two Au electrodes (E1, E4). Nonlocal voltages (V_{NL}) are measured using lock-in detection with an ac injection current of I = 1 μA rms at 13 Hz. First, nonlocal MR measurement of spin transport is performed and the two states, parallel and anti-parallel are defined. Then, the Hanle spin precession is performed by applying an out-of-plane magnetic field to cause the spins to precess as they diffuse from E2 to E3, which results in characteristic Hanle curves as shown for devices A at 300 K (fig. 9-1b). The red circles (black circles) are for the parallel (antiparallel) alignment of the Co magnetizations. The spin lifetime (τ_s), diffusion coefficient (D), and spin diffusion length ($\lambda_s = \sqrt{D\tau_s}$) are determined by the fitting the Hanle curves with the following equation [21]:

$$R_{NL} \propto \pm \int_0^\infty \frac{1}{\sqrt{4\pi Dt}} \exp\left[-\frac{L^2}{4Dt}\right] \cos(\omega_L t) \exp(-t/\tau_s) dt \qquad (1)$$

where the + (-) sign is for the parallel (antiparallel) magnetization state, D is the diffusion constant, and τ_s is the spin lifetime. Using this equation, we fitted the parallel

and anti-parallel Hanle curves (solid lines). The fitting parameters obtained were D $=2.0\times10^{-2}$ m^2s^{-1} and τ_s = 0.77 ns, which corresponded to a spin diffusion length of $\lambda_s=\sqrt{D\tau_s}$ = 3.9 μm.

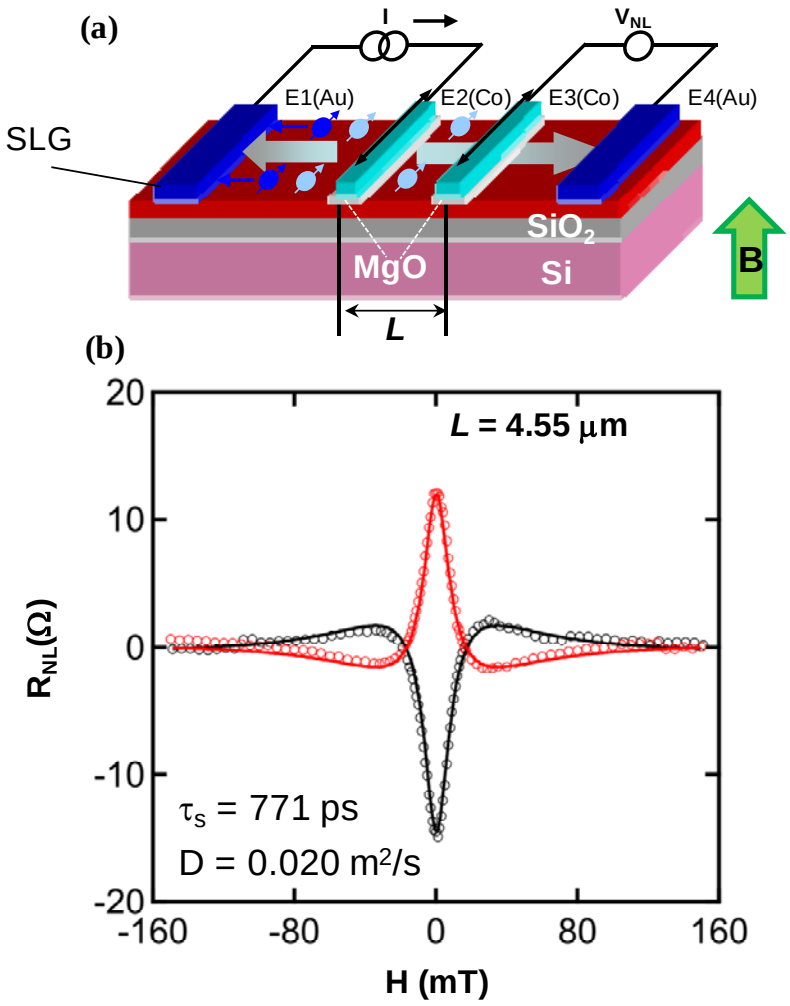

Fig. 9-1, Hanle spin precession.

(a) Schematic device geometry for a graphene spin valve. (b) Representative Hanle measurements of a SLG spin valve at 300 K. The red (black) circles are data taken for parallel (antiparallel) Co magnetizations.

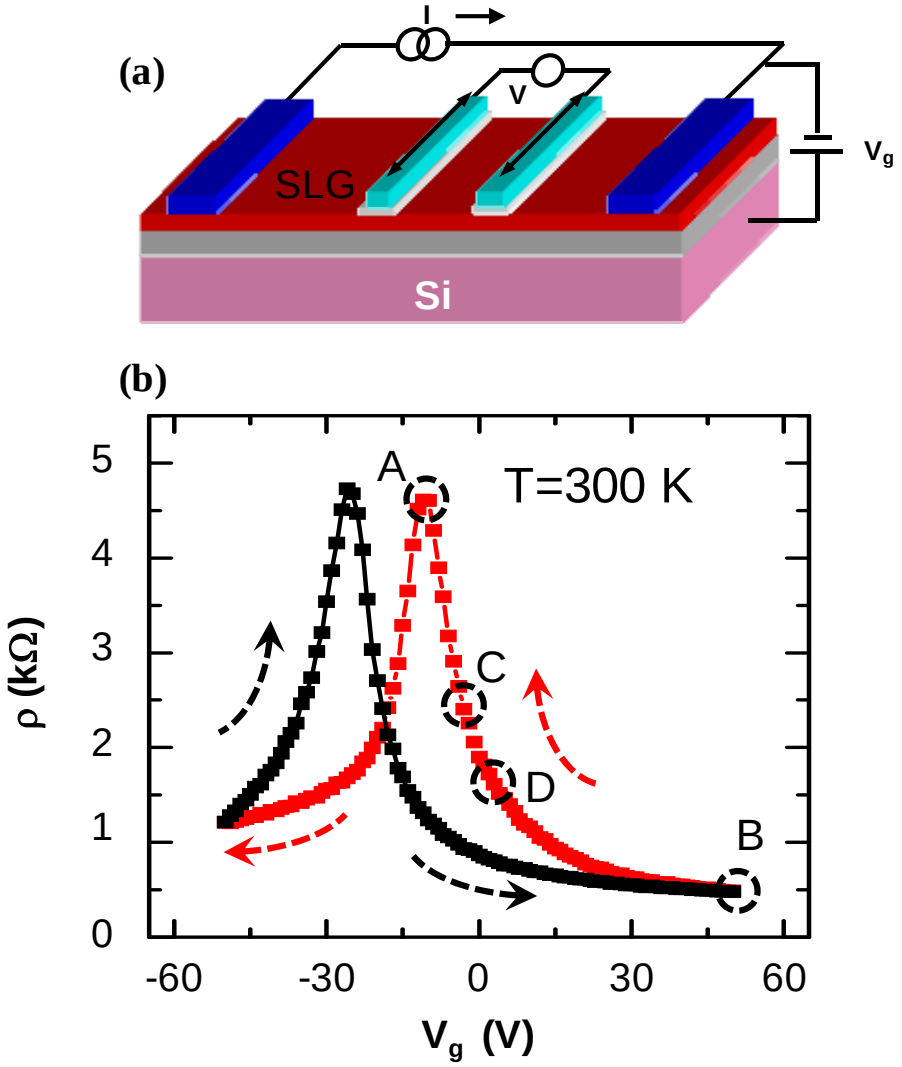

Fig. 9-2, electrical properties of SLG after iron oxide NPs doping.

(a) Schematic resistivity measurement geometry. (b) Resistivity as a function of the gate voltage at room temperature (device A). Two Dirac points indicates the charge transferring between SLG and iron oxide NPs. The black/red curve shows the resistance curve as the gate voltage is swept up/down. A, B, C, D are four state of the graphene, with different resistivity.

The electrical properties of SLG are measured by measuring the graphene resistivity as a function of the gate voltage applied on the highly doped Si side (fig. 9-2a). The AC current (1 μA) is applied between two Au electrode, while the voltage is measured across the two central Co electrodes, while the gate voltage is swept with a rate of 0.2 V/s. After several drops of iron oxide NPs solution are applied and completely dried, as Vg is swept, two resistance peaks appear (blue curve in fig. 9-2b). As the Vg is swept from – 50 V to + 50 V, the resistivity peak shows up at – 28V, while as Vg is swept from + 50 V to – 50 V, the resistivity peak shows up at -10V. This means that the Vg alters the charge state in NPs and in turn results in the hysteresis in graphene resistivity, which is consistent with previous studies [18]. It should be pointed out that the addition of NPs on graphene does not provide a parallel current path due to the high resistive nature of the molecular links.

The graphene mobility is tuned by the following procedure: First, we set Vg at an arbitrary value (eg. A state in fig. 9-2b) and then quickly cool the device to low temperatures while holding the Vg constant. At 10 K, only one Dirac peak shows up (fig. 9-3a), and no time dependence is observed, which reveal that varying Vg only changes the carrier density in graphene due to the freezing of the charges in the NPs. By choosing the different initial states to cool down quickly, the graphene mobilities can be tuned from 2200 to 7140 $cm^2V^{-1}s^{-1}$ (fig.9-3a to fig. 9-3d), in which the mobility of the SLG (μ) is calculated by the average of the electron and hole mobilities ($\mu=(\mu_e+\mu_h)/2$), which are determined using the relation $\mu_{e,h}=\left|\Delta\sigma/e\Delta n\right|$, where the carrier concentration, *n*, is directly related to the gate voltage, Vg, by $n=-\alpha(V_g-V_D)$ with

$\alpha = 7.2\times10^{10} V^{-1}cm^{-2}$. The key to tuning the mobility of SLG is the precooled charge state. Clearly, the higher mobility is achieved by cooling down at the initial state with maximum resistivity (low amount of charged impurity in SLG). When the excess charges are transferred to NPs, the stored charges in NPs appear to cause less scattering to carriers in graphene. These results support that the charged impurities stuck to graphene are one main limiting factor to graphene mobility.

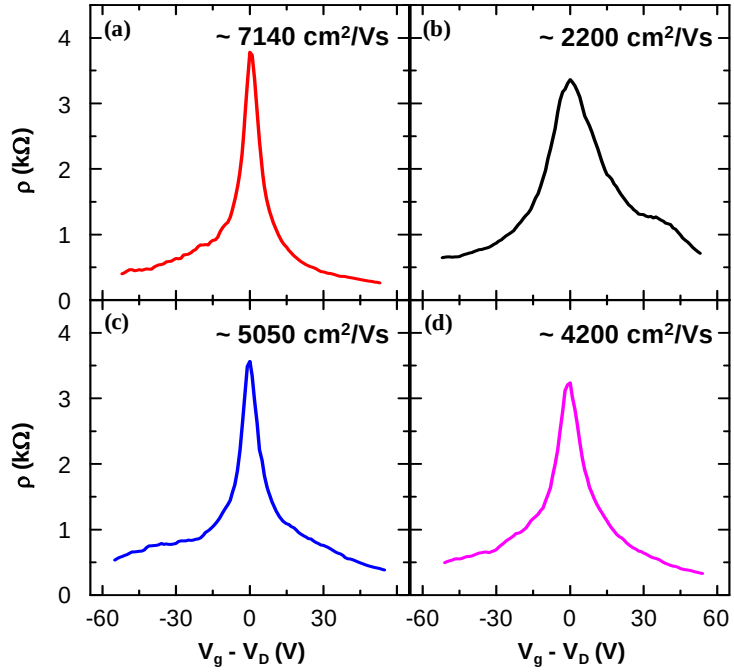

Fig. 9-3, electrical properties of SLG after iron oxide NPs doping at 10 K.

(a-d) The same SLG spin valve (device A) with different mobilities after cooling down from diferent states at 300 K. The 10 K mobilites are 7140 $cm^2V^{-1}s^{-1}$, 2200 $cm^2V^{-1}s^{-1}$, 5050 $cm^2V^{-1}s^{-1}$, 4200 $cm^2V^{-1}s^{-1}$, respectively, which are obtained by cooling down from A, B, C, D states, indicated in fig. 9-2b.

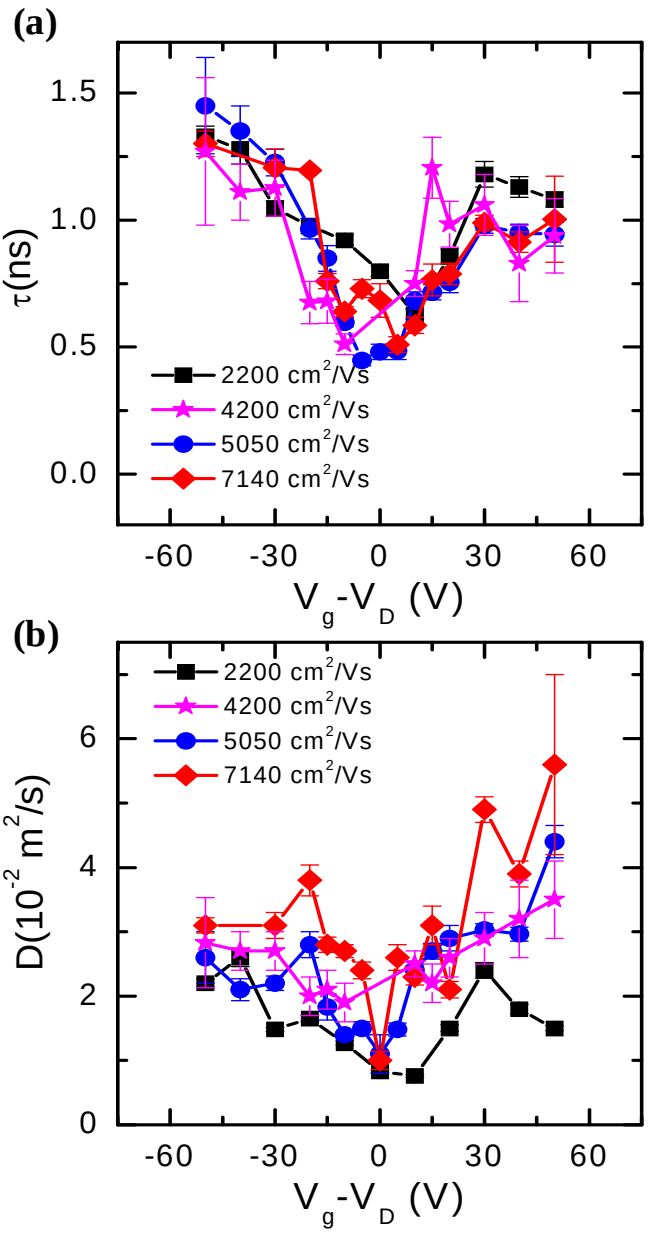

Fig. 9-4, spin dependtent properties of the same SLG spin valve (device A) with different mobilities measured from Hanle spin precession at 10 K.

(a) The spin lifetimes as a function of the gate voltage for the mobilities from 2200 to 7140 $cm^2V^{-1}s^{-1}$. (b) The corresponding diffusion coefficients as a function of gate voltage.

Fig. 9-4a and 9-4b summarize the spin lifetimes and the diffusion coefficients of the SLG spin valve (device A) measured by Hanle spin precession. It is clearly seen that for all the different mobilities, the spin lifetimes show a minimum at the Dirac point, and increase as the carrier densities increase. These behaviors follow the same trend as the diffusion coefficients, which are consistent with previous studies [15]. Interestingly, the spin lifetimes are almost the same for the device with mobilities from 2200 to 7140 $cm^2V^{-1}s^{-1}$. While for the diffusion coefficients, it turns out that larger diffusion coefficients are observed in SLG spin valve with higher mobility. These results clearly demonstrate that the spin transport (spin lifetimes) and charge transport (mobility and diffusion coefficients) of graphene are dominated by different mechanisms.

To further investigate the spin lifetimes with higher mobility, we fabricated device B (fig. 9-5) with much higher mobility. The minimum and maximum mobilities tuned are 4200 $cm^2V^{-1}s^{-1}$ and 12000 $cm^2V^{-1}s^{-1}$. Interestingly, for 12000 $cm^2V^{-1}s^{-1}$, exhibiting higher mobility, the spin lifetimes are still in the range of 0.5-1.8 ns, which are exactly the same as the low mobility values. Our observations clearly show that the spin lifetimes are not dependent on the mobility in the 2000 – 12000 $cm^2V^{-1}s^{-1}$ regimes.

As we know, the mobility in our study is an indication of the amount of charged impurities in SLG. The higher mobility corresponds to lower amounts of charged impurities in SLG, and more charged impurities frozen in the iron oxide NPs. On the other hand, the lower mobility corresponds to higher amounts of charged impurity in SLG. The spin lifetimes for SLG with mobility from 2000 to 12000 $cm^2V^{-1}s^{-1}$ are all in the range of 0.5-2 ns, despite the amount of charged impurities are present in SLG. This

result clearly demonstrates that the charged impurities are not the dominant spin relaxation in SLG with the mobility from 2000 to 12000 $cm^2V^{-1}s^{-1}$.

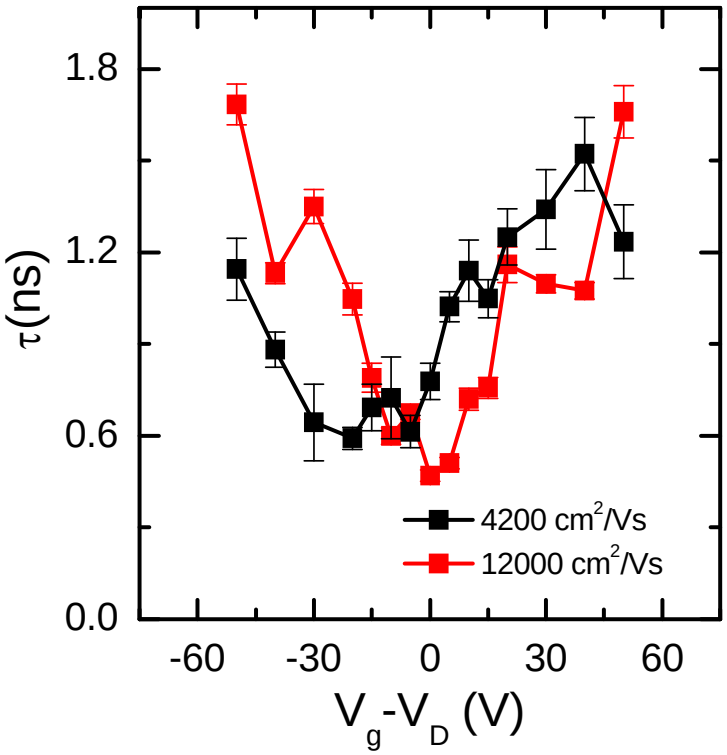

Fig. 9-5, spin lifetimes of the same SLG spin valve (device B) measured from Hanle spin precession at 10 K. The spin lifetimes are in the range of 0.5-2 ns as a function of the gate voltage, which are the same for both high mobility (4200 $cm^2V^{-1}s^{-1}$) and low mobility (12000 $cm^2V^{-1}s^{-1}$).

9.4 Conclusion

In summary, spin relaxation in SLG with tunable mobilities is investigated by taking advantage of charged impurity freezing or releasing from iron oxide NPs to SLG. The spin lifetimes are all in the range of 0.5-1.2 ns for the SLG mobility from 2000 to 12000

$cm^2V^{-1}s^{-1}$. Our results demonstrate that the charged impurities are not the dominant spin relaxation in SLG with the mobility from 2000 to 12000 $cm^2V^{-1}s^{-1}$.

References:

[1] D. Huertas-Hernando, F. Guinea, and A. Brataas, Phys. Rev. B **74**, 155426 (2006).

[2] H. Min, J. E. Hill, N. A. Sinitsyn, B. R. Sahu, L. Kleinman, and A. H. MacDonald, Phys. Rev. B **74**, 165310 (2006).

[3] Y. Yao, F. Ye, X.-L. Qi, S.-C. Zhang, and Z. Fang, Phys. Rev. B **75**, 041401(R) (2007).

[4] B. Trauzettel, D. V. Bulaev, D. Loss, and G. Burkard, Nature Physics **3**, 192 (2007).

[5] D. Huertas-Hernando, F. Guinea, and A. Brataas, Phys. Rev. Lett. **103**, 146801 (2009).

[6] N. Tombros, C. Jozsa, M. Popinciuc, H. T. Jonkman, and B. J. van Wees, Nature, **448**, 571 (2007).

[7] C. Józsa, T. Maassen, M. Popinciuc, P. J. Zomer, A. Veligura, H. T. Jonkman, and B. J. van Wees, Phys. Rev. B **80**, 241403(R) (2009).

[8] M. Popinciuc, C. Jozsa, P. J. Zomer, N. Tombros, A. Veligura, H. T. Jonkman, and B. J. van Wees, Phys. Rev. B **80**, 214427 (2009).

[9] M. Shiraishi, M. Ohishi, R. Nouchi, T. Nozaki, T. Shinjo, and Y. Suzuki, Adv. Funct. Mater. **19**, 3711 (2009).

[10] W. Han, K. Pi, W. Bao, K. M. McCreary, Y. Li, W. H. Wang, C. N. Lau, and R. K. Kawakami, Appl. Phys. Lett. **94**, 222109 (2009).

[11] K. Pi, W. Han, K. M. McCreary, A. G. Swartz, Y. Li, and R. K. Kawakami, Phys. Rev. Lett. **104**, 187201 (2010).

[12] W. Han, K. Pi, K. M. McCreary, Y. Li, J. J. I. Wong, A. G. Swartz, and R. K. Kawakami, Phys. Rev. Lett. **105**, 167202 (2010).

[13] A. H. Castro Neto, and F. Guinea, Phys. Rev. Lett. **103**, 026804 (2009).

[14] C. Ertler, S. Konschuh, M. Gmitra, and J. Fabian, Phys. Rev. B **80**, 041405(R) (2009).

[15] W. Han, and R. K. Kawakami, Phys. Rev. Lett. **107**, 047207 (2011).

[16] A. Avsar, T.-Y. Yang, S.-K. Bae, J. Balakrishnan, F. Volmer, M. Jaiswal, Z. Yi, S. R. Ali, G. Güntherodt, B.-H. Hong, B. Beschoten, and B. Özyilmaz, arXiv:1104.4715, (2011).

[17] S. Jo, D.-K. Ki, D. Jeong, H.-J. Lee, and S. Kettemann, Phys. Rev. B **84**, 075453 (2011).

[18] D. Wang, X. Liu, L. He, Y. Yin, D. Wu, and J. Shi, Nano Letters **10**, 4989 (2010).

[19] A. K. Geim, and K. S. Novoselov, Nature Materials **6**, 183 (2007).

[20] A. C. Ferrari, J. C. Meyer, V. Scardaci, C. Casiraghi, M. Lazzeri, F. Mauri, S. Piscanec, D. Jiang, K. S. Novoselov, S. Roth, and A. K. Geim, Phys. Rev. Lett. **97**, 187401 (2006).

[21] F. J. Jedema, H. B. Heersche, A. T. Filip, J. J. A. Baselmans, and B. J. van Wees, Nature **416**, 713 (2002).

Chapter 10.

Growth of single-crystalline, atomically smooth MgO films on Ge(001) by molecular beam epitaxy[1]

Abstract

In this section, I investigate the growth of MgO thin films on Ge(001) via molecular beam epitaxy and find that the growth temperature plays a key role in the quality of MgO thin films. Reflection high-energy electron diffraction (RHEED) and atomic force microscopy show that the single-crystal quality and atomically smooth morphology are optimized for a growth temperature of 250°C. Cross-sectional transmission electron microscopy (TEM) of Fe/MgO/Ge(001) is used to probe the single crystal ordering and atomic scale structure of the MgO/Ge interface. Analysis of the RHEED patterns and TEM images indicate that the MgO is (001)-oriented and the MgO unit cell has a 45° in-plane rotation with respect to that of Ge, which gives rise to a better lattice match and thus provides a high quality film and interface for potential spin injection experiments.

[1]Published as: Wei Han, Yi Zhou, Yong Wang, Yan Li, Jared. J. I. Wong, K. Pi, A.G. Swartz, K.M. McCreary, Faxian Xiu, Kang L. Wang, Jin Zou, and R.K. Kawakami, J. Crystal Growth 312, 44 (2010).

10.1 Introduction

Semiconductor spintronics aims to add novel functionality to electronic devices by utilizing the spin degree of freedom [1]. Group-IV semiconductors are of particular interest due to the potential compatibility with established silicon technologies, and Ge has shown favorable properties related to magnetic doping [2-7]. One of the main challenges for Ge-based spintronics is to achieve efficient spin injection from ferromagnetic (FM) metal contacts into Ge [8]. A promising avenue is to develop single-crystalline FM/MgO/Ge(001) heterostructures. In addition to alleviating the conductivity mismatch problem by introducing a tunnel barrier [9, 10], MgO(001) films possess a special spin filtering property based on wavefunction symmetry that greatly enhances the spin polarization when the FM is bcc Co_xFe_{1-x} (up to 85% spin polarization in some cases) [11-14]. When applied to spin injection into GaAs, the CoFe/MgO/GaAs(001) system has exhibited very high spin injection efficiency in spin-LED experiments [15, 16], so the MgO barrier is potentially beneficial for spin injection into Ge. Furthermore, the MgO can act a barrier to prevent diffusion of transition metals into Ge. The insertion of a thin layer of insulator can also alleviate the strong Fermi level pinning problem of metal/n-Ge contacts [17, 18]. While the growth of MgO on Si(001) and GaAs(001) has been well studied [16, 19-23], very little work has been done on Ge(001). Therefore, the epitaxial growth of MgO thin films on Ge(001) is an important issue for the development of Ge-based spintronics.

In this chapter, I demonstrate the growth of atomically smooth, single crystalline MgO thin films on Ge(001) by molecular beam epitaxy (MBE). Using *in situ* reflection

high energy electron diffraction (RHEED) and atomic force microscopy (AFM) to characterize the crystal structure and morphology, we find that the growth temperature plays a key role in determining the quality of the MgO film. The sharpest RHEED patterns are obtained for a growth temperature of 250°C and the root-mean-square (rms) roughness of 0.17 nm obtained by AFM is less than the atomic spacing of MgO (0.2106 nm). Deposition at room temperature or 400°C produces much rougher films. High resolution transmission electron microscopy (HRTEM) is used to characterize the single-crystal structure, atomic scale morphology, and interfacial structure of Fe/MgO/Ge(001). Interestingly, the MgO is (001)-oriented with a 45° in-plane rotation of the unit cell relative to that of Ge(001). This achieves the relatively small lattice mismatch of 5.1%, as opposed to a ~25% mismatch that would result from a cube-on-cube alignment as often seen in MgO/Si(001) and MgO/GaAs(001) [16, 19-23].

10.2 Experimental details

Samples are grown by MBE in an ultrahigh vacuum (UHV) system with a base pressure of 1×10^{-10} torr. The wafers are first cleaned in isopropyl alcohol, followed by successive washes in dilute NH_4OH_4, dilute H_2SO_4, and H_2O_2. The H_2O_2 produces a thin oxide protection layer on the Ge substrate. After loading the Ge substrate into the MBE chamber, the Ge substrate is annealed at 500 °C for 1 hour to remove the Ge-oxide layer. Auger electron spectroscopy after the oxide desorption (Fig. 10-1, black curve) shows the peak for Ge (52 eV) [24] but no oxygen peak at 505 eV, which confirms that the Ge-oxide layer is completely removed. The MgO is deposited by electron beam evaporation of a single crystal MgO source. For potential spin injection experiments, Fe and Al are

deposited from thermal effusion cells. Typical deposition rates of ~1.5 Å/min for MgO, ~1.0 Å/min for Fe, and ~1.5 Å/min for Al are measured by a quartz deposition monitor.

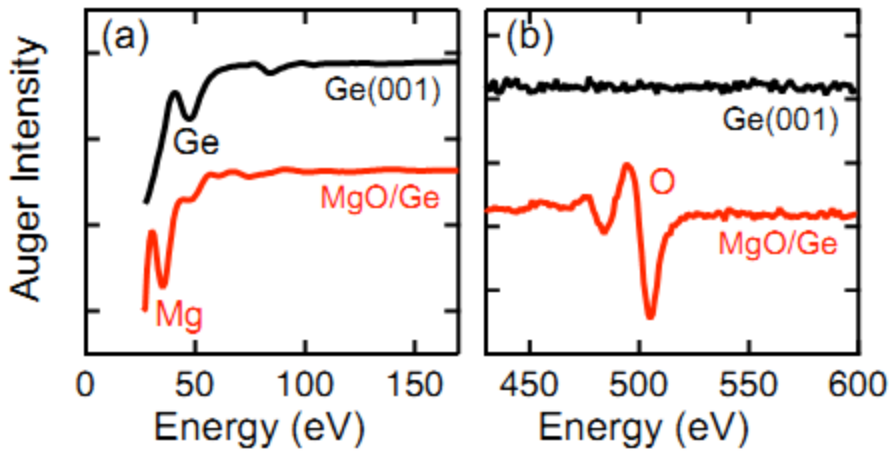

Fig. 10-1, Auger spectra of Ge substrate after annealing at 500 °C for 1 h (black curve) and the typical spectra of 3 nm MgO grown on Ge substrate (red/grey curve).

(a) The energy from 0 to 170 eV.

(b) The energy from 430 to 600 eV.

10.3 Results and discussion

We first utilize RHEED to investigate the effect of growth temperature on the crystalline quality of MgO thin films on Ge(001). Fig. 10-2a shows the RHEED patterns of the Ge(001) substrate after oxide desorption for the in-plane [110] and [100] azimuths. The sharp and streaky RHEED patterns indicate a high quality Ge surface. A series of 3 nm MgO/Ge(001) samples are grown at different substrate temperatures ranging from room temperature (RT) to 400°C. Fig. 10-2b to 10-2f show the RHEED patterns after the MgO deposition for growth temperatures of RT, 200°C, 250°C, 300°C, and 400°C, respectively. All RHEED patterns are taken after cooling the sample down to RT. With the exception of the 400°C growth, all RHEED patterns exhibit spots which indicate single-crystalline ordering. Between RT and 250°C, the RHEED patterns become sharper and streakier with increasing growth temperature, indicating an improvement of the crystal structure and epitaxial growth of the MgO thin film. For growth temperature of 300°C, the RHEED pattern starts to fade away and by 400°C the RHEED pattern vanishes. Thus, the crystal structure is optimized for a growth temperature of 250°C. The RHEED patterns also indicate that the MgO has (001) orientation with a 45° rotation of the unit cell relative to the Ge(001) unit cell (i.e. MgO[100](001)//Ge[110](001) as indicated in fig. 10-2), which will be discussed in detail later.

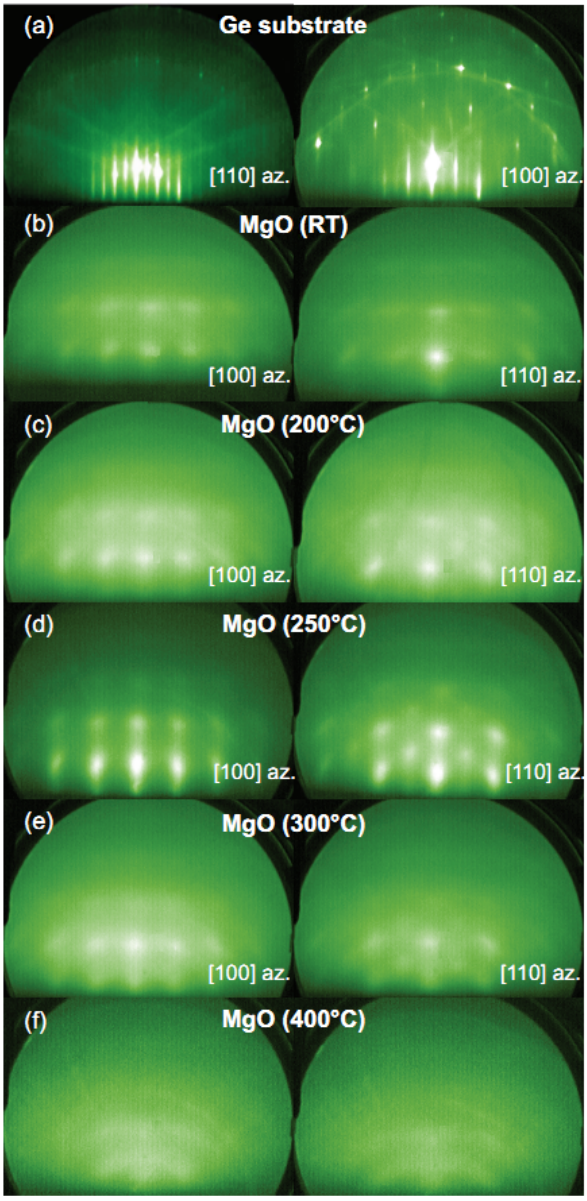

Fig. 10-2, RHEED patterns of Ge substrate and 3 nm MgO grown on Ge at different temperatures (left column in the Ge[1 1 0](0 0 1) and MgO[1 0 0](0 0 1) orientation; right column in the Ge[1 0 0](0 0 1) and MgO[1 1 0](0 0 1) orientation).

(a) Ge substrate; (b) 3 nm MgO grown on Ge at RT; (c) 3 nm MgO grown on Ge at 200 °C; (d) 3 nm MgO grown on Ge at 250 °C; (e) 3 nm MgO grown on Ge at 300 °C; and (f) 3 nm MgO grown on Ge at 400 °C.

Prior to removing the samples from UHV, Auger electron spectroscopy is performed on the MgO films. Fig. 10-1 (red/grey curve) shows a typical Auger spectrum of a 3 nm MgO film grown on Ge(001). Nearly identical spectra (with Mg peak at 35 eV and O peak at 505 eV) are observed for all growth temperatures. The key feature of the data is that the Mg peak appears at 35 eV (for Mg in MgO crystal) as opposed to 45 eV (for elemental Mg), which demonstrates that MgO is being grown on the Ge substrate [25].

We utilize *ex situ* AFM to investigate the morphology of the MgO films grown at different temperatures. Fig. 10-3a shows the AFM image of the Ge substrate and fig. 10-3 to 10-3e show the AFM images of 3 nm MgO grown on Ge(001) at RT, 250°C, 300°C, and 400°C, respectively. Clearly, the growths at RT and 400°C produce very rough MgO films, while the growths at 250°C and 300°C produce films with roughness comparable to the Ge substrate (RMS roughness of 0.093 nm). Fig. 10-3f displays the RMS roughness of the 3 nm MgO films as a function of growth temperature. Increasing the growth temperature from RT to 300°C causes the rms roughness to decrease. Between 250°C and 300°C the MgO film is atomically smooth (rms roughness < 0.2106 nm, the atomic spacing of MgO). When the substrate temperature is above 300°C, increasing the growth temperature results in a rougher MgO film. Based on the RHEED and AFM characterizations, the best single crystalline and atomically smooth MgO films are produced at a growth temperature of 250°C.

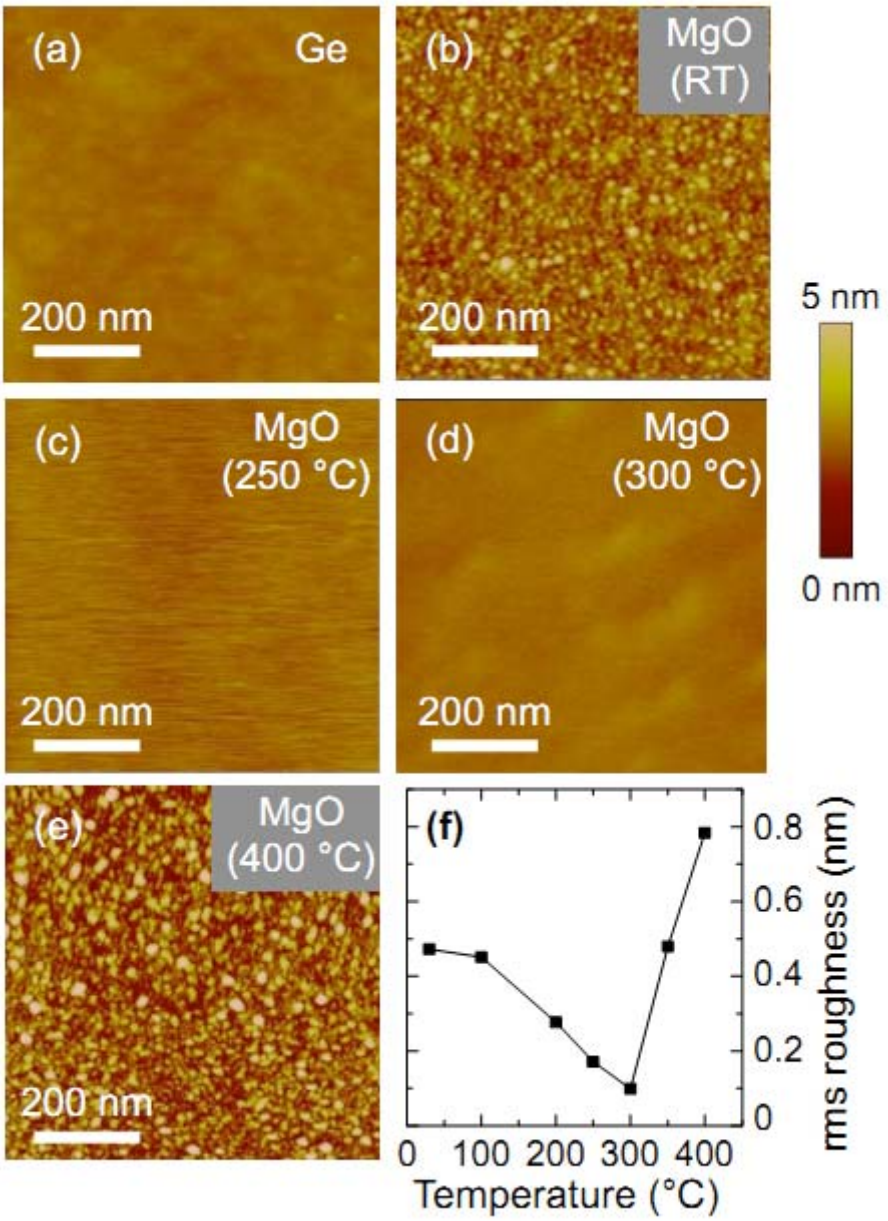

Fig. 10-3, AFM images of Ge substrate and 3 nm MgO grown on Ge at different temperatures.

(a) Initial Ge substrate; (b) 3 nm MgO grown on Ge at RT; (c) 3 nm MgO grown on Ge at 250 °C; (d) 3 nm MgO grown on Ge at 300 °C; (e) 3 nm MgO grown on Ge at 400 °C; and (f) rms roughness as a function of growth temperature.

Finally, we grow a complete Fe/MgO/Ge(001) heterostructure which consists of Al(15 nm)/Fe(10 nm)/MgO(10 nm)/Ge(001), where the MgO is grown at 250°C, the Fe is grown at 200°C, and the Al is grown at RT. The Al capping layer prevents oxidation of the Fe layer. Fig. 10-4a shows a cross-sectional HRTEM image, which confirms the single-crystal nature of the entire heterostructure. The atomic-scale morphology is smooth, consistent with the AFM studies (fig. 10-3). The HRTEM reveals a transition region at the Ge and MgO interface of a few atomic layers. This is consistent with the MgO RHEED patterns, which begin to appear after ~0.5 nm of MgO deposition. The white squares drawn on the HRTEM image indicate that the projected unit cells are cubic for MgO and rectangular for Ge, which supports an epitaxial alignment of MgO[100](001)//Ge[110](001).

Fig. 10-4b to 10-4d show RHEED patterns measured for the Ge substrate (fig. 10-4d), the MgO layer (fig. 10-4c), and Fe layer (fig. 10-4b) of the sample with the RHEED beam along the [110] azimuth of the Ge substrate. The sharp patterns are consistent with the single-crystal, atomically smooth films as illustrated in the HRTEM images. Analysis of the RHEED patterns supports the epitaxial relationship of Fe[110](001) // MgO[100](001) // Ge[110](001). The (001) orientation of the MgO and Fe layers is verified by the four-fold rotation symmetry of the RHEED patterns as the sample is rotated in-plane. The in-plane relationships are analyzed using line cuts of the RHEED patterns (fig. 10-4e), where the spacing of the RHEED streaks is inversely proportional to the lateral spacing of the surface atoms. For the RHEED beam along [110] of Ge and the in-plane epitaxial relationship of Fe[110]//MgO[100]//Ge[110], the relevant surface

lattice constants are $a^*_{Fe} = 2a_{Fe}/\sqrt{2}$ = 0.4059 nm, $a^*_{MgO} = a_{MgO}$ = 0.4212 nm, $a^*_{Ge} = a_{Ge}/\sqrt{2}$ = 0.3995 nm, where a_{Fe} = 0.287 nm, a_{MgO} = 0.4212 nm, and a_{Ge} = 0.565 nm are the bulk lattice constants at room temperature. The bulk lattice constants lead to predicted RHEED spacing ratios of $(a^*_{Fe})^{-1} : (a^*_{MgO})^{-1} : (a^*_{Ge})^{-1}$ = 0.9862 : 0.9506: 1. The experimental RHEED spacings from fig. 9-4e have ratios of $x_{Fe} : x_{MgO} : x_{Ge}$ = 0.9923 : 0.9644 : 1. The agreement between the predicted and measured RHEED spacings strongly supports the in-plane epitaxial relationship of Fe[110]//MgO[100]//Ge[110]. Additional support is given by the fact that Fe/MgO(001) is well-known to have a 45° rotation [13], so the observed lattice matching of the Fe and Ge supports the 45° rotation between the MgO and Ge.

We note that the 45° in-plane rotation of MgO on Ge(001) is rather interesting, as MgO/Si(001) and MgO/GaAs(001) are usually reported to have a cube-on-cube epitaxial relationship[16, 19-23]. For cube-on-cube, the ~25% lattice mismatch is accommodated by having four MgO unit cells match up with three Si or GaAs unit cells, leading to dangling bonds at the interface. A possible advantage of the 45° in-plane rotation of the MgO/Ge(001) is the reduction of dangling bonds, which may be favorable for electronic and spintronic properties.

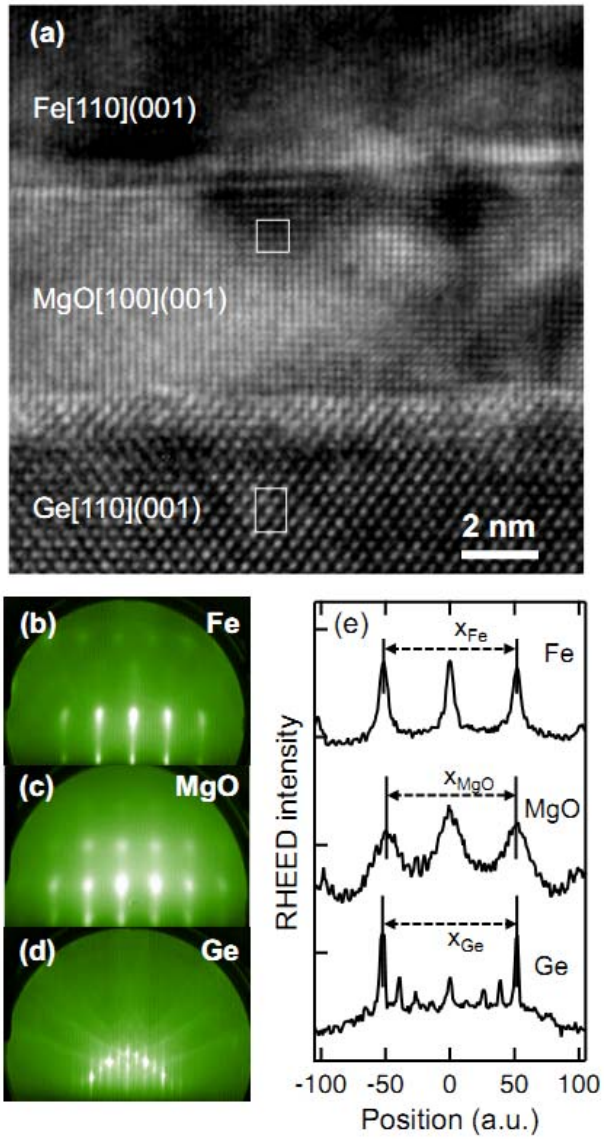

Fig. 10-4, HRTEM and RHEED of Fe/MgO/Ge(0 0 1).

(a) HRTEM image of Fe/MgO/Ge; (b) RHEED pattern of 10 nm Fe; (c) RHEED pattern of 7 nm MgO; (d) RHEED pattern of Ge substrate; and (e) Line cuts of RHEED intensity of Fe, MgO, and Ge. x_{Fe}, x_{MgO}, x_{Ge} are the experimental RHEED peak-to-peak spacings.

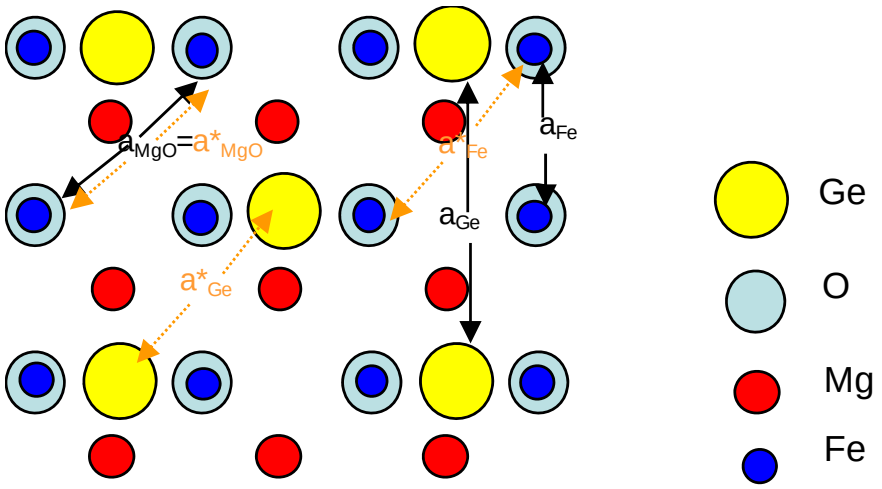

Fig. 10-5, Interface rotation of Fe/MgO/Ge(0 0 1).

10.4 Conclusion

In summary, we find that the growth temperature is a key factor in the growth MgO films on Ge (001). Based on RHEED and AFM, the single-crystal quality and atomic scale smoothness are optimized for a growth temperature of 250°C. Cross-sectional HRTEM images of Fe/MgO/Ge(001) heterostructures directly show the single crystal structure, atomically smooth morphology, and relatively sharp interfaces. The rotation of 45° in-plane between MgO and Ge (illustrated in fig. 9-5) gives rise to a better lattice match and thus provides a high quality film and interface for potential spin injection experiments.

References:

[1] S. A. Wolf, D. D. Awschalom, R. A. Buhrman, J. M. Daughton, S. von Molnar, M. L. Roukes, A. Y. Chtchelkanova, and D. M. Treger, Science **294**, 1488 (2001).

[2] I. Appelebaum, B. Huang, and D. J. Monsma, nature **447**, 295 (2007).

[3] B. T. Jonker, G. Kioseoglou, A. T. Hanbicki, C. H. Li, and P. E. Thompson, nature **3**, 542 (2007).

[4] R. Jansen, Nature physics **3**, 521 (2007).

[5] Y. D. Park, A. T. Hanbicki, S. C. Erwin, C. S. Hellberg, J. M. Sullivan, J. E. Mattson, T. F. Ambrose, A. Wilson, G. Spanos, and B. T. Jonker, Science **295**, 651 (2002).

[6] S. Cho, S. Choi, S. C. Hong, Y. Kim, J. B. Ketterson, B.-J. Kim, Y. C. Kim, and J.-H. Jung, Phys. Rev. B **66**, 033303 (2002).

[7] F. Tsui, L. He, L. Ma, A. Tkachuk, Y. S. Chu, K. Nakajima, and T. Chikyow, Phys. Rev. Lett. **91**, 177203 (2003).

[8] G. Schmidt, D. Ferrand, L. W. Molenkamp, A. T. Filip, and B. J. van Wees, Phys. Rev. B (Rapid Communications) **62**, R4790 (2000).

[9] E. I. Rashba, Phys. Rev. B (Rapid Communications) **62**, 16267 (2000).

[10] A. Fert, and H.Jaffres, Phys. Rev. B **64**, 184420 (2001).

[11] W. H. Butler, X.-G. Zhang, T. C. Schulthess, and J. M. Maclaren, Phys. Rev. B **63**, 054416 (2001).

[12] P. Mavropoulos, N. Papanikolaou, and P. H. Dederichs, Phys. Rev. Lett. **85**, 1088 (2000).

[13] S. Yuasa, T. Nagahama, A. Fukushima, Y. Suzuki, and K. Ando, Nature Materials **3**, 868 (2004).

[14] S. S. P. Parkin, C. Kaiser, A. Panchula, P. M. Rice, B. Hughes, M. Samant, and S.-H. Yang, Nature Materials **3**, 862 (2004).

[15] X. Jiang, R. Wang, R. M. Shelby, R. M. Macfarlane, S. R. Bank, J. S. Harris, and S. S. P. Parkin, Phys. Rev. Lett. **94**, 056601 (2005).

[16] Y. Lu, V. G. Truong, P. Renucci, M. Tran, H. Jaffres, C. Deranlot, J.-M. George, A. Lemaitre, Y. Zheng, D. Demaille, P.-H. Binh, T. Amand, and X. Marie, Appl. phys. Lett. **93**, 152102 (2008).

[17] Y. Zhou, M. Ogawa, X. Han, and K. L. Wang, Appl. phys. Lett. **93**, 202105 (2008).

[18] Y. Zhou, M. Ogawa, M. Bao, W. Han, R. Kawakami, and K. L. Wang, Appl. Phys. Lett. **94**, 242104 (2009).

[19] S. Kaneko, H. Funakubo, T. Kadowaki, Y. Hirabayashi, and K. Akiyama, Europhys. Lett. **81**, (2008).

[20] G. X. Miao, J. Y. Chang, M. J. v. Veenhuizen, K. Thiel, M. Seibt, G. Eilers, M. Munzenberg, and J. S. Moodera, Applied Physics Letters **93**, 142511 (2008).

[21] X. Y. Chen, K. H. Wong, C. L. Mak, X. B. Yin, M. Wang, J. M. Liu, and Z. G. Liu, J. Appl. Phys. **91**, 5728 (2002).

[22] L. D. Chang, M. Z. Tseng, E. L. Hu, and D. K. Fork, Appl. phys. Lett. **60**, 1753 (1992).

[23] L. S. Hung, L. R. Zheng, and T. N. Blanton, Appl. phys. Lett. **60**, 3129 (1992).

[24] A. Csik, G. A. Langer, D. L. Beke, and Z. Erdelyi, J. Appl. Phys. **89**, 804 (2001).

[25] M. Suleman, and E. B. Pattinson, Surf. Sci. **35**, 75 (1973).

Chapter 11.

Investigate the origin of Fermi level pinning in Ge Schottky junctions using epitaxially grown ultrathin MgO films[1]

Abstract

In this section, I investigate the Schottky characteristics of high quality metal/MgO/n-Ge junctions with the ultrathin MgO epitaxially grown on Ge. We find the depinning effect displays a weak dependence on the MgO thickness, indicating the interface states due to the native defects on Ge surface are likely to play the dominant role in Fermi level pinning.

---

[1]Published as: Yi Zhou*, Wei Han*, Yong Wang, Faxian Xiu, Jin Zou, R. K. Kawakami, and Kang. L. Wang, Appl. Phys. Lett. 96, 102103 (2010).

11.1 Introduction

Fermi level (FL) pinning inside the Ge bandgap leads to a weak dependence of the Schottky barrier height (SBH) on the metal work functions [1]. Even though a few groups have demonstrated depinning of the FL by various methods, an explicit explanation of the underlying mechanism is still unclear. One of the most conjectured origins of pinning is the metal-induced-gap-states (MIGS) [2, 3], which are energy states in the bandgap of the semiconductor due to the tailing of the metal electron wave functions into the semiconductor. If MIGS plays the dominant role in FL pinning, inserting an ultrathin oxide (UTO) or insulator between the metal and Ge should depin the FL since the UTO can block the tailing of the metal wave function into Ge and thus reduce the MIGS formation. More importantly, the depinning should be increasingly effective when the UTO thickness is increased until a saturation thickness is reached, at which all MIGS are eliminated. From the MIGS point of view, T. Nishimura *et al*. [4] and M. Kobayashi *et al*. [5] recently demonstrated such an increasing depinning effect with increasing thickness of a thin amorphous insulator (AlO_x, GeO_2 or SiN) between the metal and Ge via sputtering deposition. However, it should be noted that sputtering process could induce defects or intermixing in the films [6, 7]. And the amorphous state of the films could lead to inhomogeneous interfacial structures as well as a variation of the film thickness, all of which bring complications to a lucid characterization [8]. Another possible origin of FL pinning is due to the surface states which arise from unsatisfied dangling bonds or other defects on the semiconductor surface [9, 10]. Depinning could be achieved by passivating those surface states before metal deposition. Lieten *et al*. [11]have shown to depin the FL

by inserting a thin Ge_3N_4 layer, either amorphous or polycrystalline, between the metal and Ge. They attributed the depinning effect to the termination of dangling bonds at the Ge surface by the Ge_3N_4 layer. If surface states due to dangling bonds play the dominant role in FL pinning, the depinning effect should have a rather weak dependence on the insulator thickness. However, no Ge_3N_4 film thickness dependence of the depinning effect was reported. On the other hand, Ikeda *et al*. [12] have shown to depin the FL by passivating the Ge surface via implantation of sulfur atoms, which act as the dangling bond terminator at the interface. However, implantation induced defects or other disorders can also bring uncertainties, which make it difficult to draw an unambiguous conclusion. Therefore, it is evident that a homogenous, epitaxially grown metal/Ge or metal/UTO/Ge junction with a single crystalline order and an atomically smooth morphology is essential to explicitly reveal the FL pinning mechanism.

In this chapter, I report the Schottky characteristics of Fe/MgO/n-Ge junctions with the MgO epitaxially grown on Ge. The entire structure appears to be single crystalline and atomically smooth. The insertion of an ultrathin MgO film can indeed depin the FL, however the SBH displays a negligible dependence on the MgO thickness, suggesting the surface states plays the dominant role in the FL pinning. Further evidence is given by the fact that passivating the surface dangling bonds using aqueous $(NH_4)_2S$ solution depins the FL more effectively than inserting the MgO films, which would have been the opposite if MIGS played the dominant role.

11.2 Experimental details

Samples are grown by molecular beam epitaxy (MBE) in an ultrahigh vacuum

system with a base pressure of 1×10^{-10} torr. The Ge wafers (n type, resistivity of 16-20 Ω·cm) are first degreased in isopropyl alcohol, followed by successive washes in dilute NH_4OH_4, H_2SO_4, and H_2O_2. A H_2O_2 wash produces a thin oxide protection layer on the Ge substrate. After loading the substrate into the chamber, it is annealed at 500 °C for 1 hour to remove the Ge-oxide layer. The MgO films with various thicknesses (0.5 nm, 1nm, 2nm and 3nm) are deposited at the substrate temperature of 250 °C by electron beam evaporation of a single crystal MgO source. Then Fe and Al (capping layer) are deposited from thermal effusion cells. The detailed growth method and characterization will be published elsewhere [13]. After growth, Schottky contacts of 300 μm×300 μm square size are prepared by conventional photolithography and mesa etching. Ti/Au is deposited on the Ge backside for Ohmic contact.

11.3 Results and discussion

Fig. 11-1a shows the cross-sectional high resolution transmission electron microscopy (HRTEM) image of a Fe/MgO (3 nm)/n-Ge junction. The entire structure displays a single-crystalline order and an atomically smooth morphology, as also evidenced by the sharp *in-situ* reflection high energy electron diffraction (RHEED) patterns (fig. 11-1b) and *ex-situ* atomic force microscopy (AFM) scans (fig. 11-1c) of the MgO after growth. Such a high quality junction with well-defined MgO thicknesses and single crystalline order allows for a reliable characterization of the Schottky characteristics dependence on the MgO thickness.

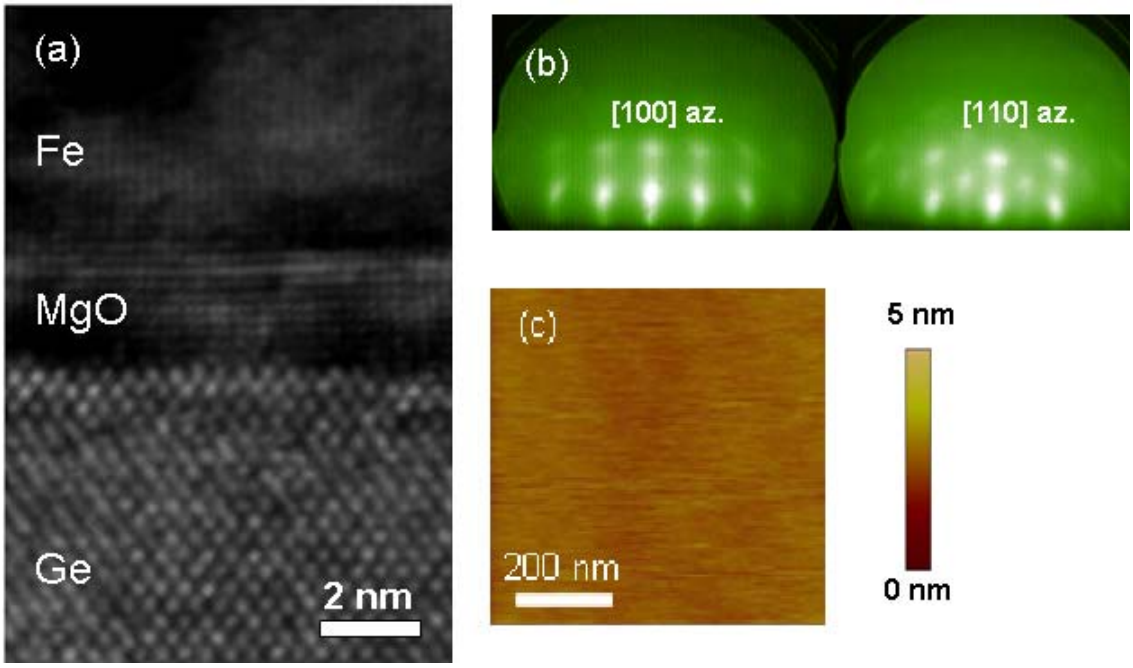

Fig. 11-1, epitaxial Fe/MgO/Ge junction.

(a) Cross-sectional HRTEM image of a Fe/MgO(3 nm)/n-Ge junction. The entire structure shows a single crystalline order and homogeheous interfaces. (b) in-situ RHEED patterns after the growth of 3 nm MgO. The sharp lines indicate high quality films. (c) ex-situ AFM scans after the growth of 3 nm MgO. The root-mean-square roughness is smaller than the atomic spacing of MgO (0.211 nm), indicating the film is atomically smooth.

Fig. 11-2 shows the room temperature J-V characteristics of the Fe/MgO/n-Ge junctions with different MgO thicknesses. With the insertion of the MgO layer, the reverse leakage currents increase as compared to the Fe/n-Ge (without surface passivation, black solid curve), which indicates the FL is indeed depinned. However, they display a weak dependence on the MgO thicknesses, which suggests the modulation of SBH by different MgO thickness is negligible.

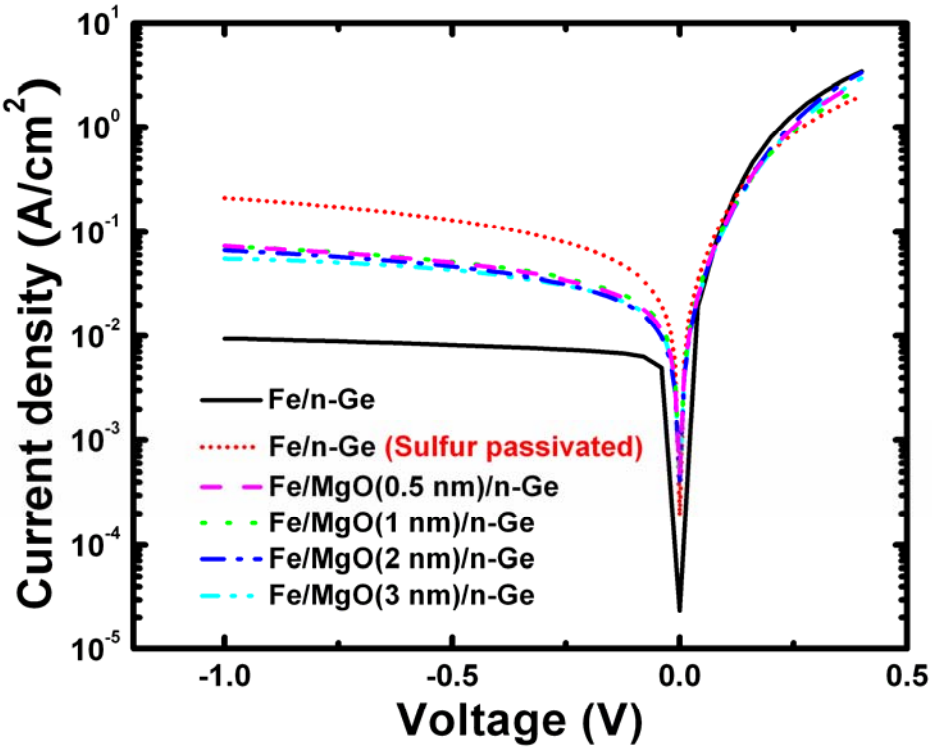

Fig. 11-2, J-V Characteristics. Room temperature J-V characteristics of Fe/MgO/n-Ge diodes with different MgO thicknesses and the Fe/n-Ge diode after sulfur passivation of the Ge surface.

Temperature dependent I-V characterization is performed to extract the SBH. According to the thermionic emission model, the J-V relation for a Schottky diode under the forward bias ($V_F > 3kT/q$) is given by [14]:

$$J = A^* T^2 \exp(-\frac{q\Phi_B}{kT}) \exp(\frac{qV_F}{nkT})[1 - \exp(-\frac{qV_F}{kT})] \approx A^* T^2 \exp(-\frac{q\Phi_B}{kT}) \exp(\frac{qV_F}{nkT}) \quad (1),$$

where A^* is the effective Richardson constant, T is the temperature, q is the electron charge, k is the Boltzmann constant, Φ_B is the effective Schottky barrier height, n is the ideality factor and V_F is the forward bias voltage. When plotting $ln(J/T^2)$ Versus q/kT, also called the Richardson plot, a linear function is found with the slope of $-E_A = V_F / n - \Phi_B$. A set of E_A are obtained with different forward bias V_F, at which the lnJ is a linear function of V_F. Plotting E_A as a function of V_F, a linear curve is obtained with the slope of $-1/n$ and the intercept of Φ_B. For example, fig. 11-3 shows the Richardson plots of the Fe/MgO (0.5 nm)/n-Ge under different forward bias (0.15 V to 0.22 V). The activation energy E_A is extracted from the slope of linear fitting of each plot. The E_A is then plotted with corresponding V_F as shown in fig. 11-3 inset. The Φ_B and n for this particular diode are extracted to be 0.35 eV and 1.03, respectively, from a linear fitting of the plot. This method assumes a temperature independent Φ_B and n. Indeed, within such a limited temperature range, the variation of Φ_B and n are negligible [15]. It should also be noted that the SBH extracted here is insensitive to the effective Richardson constant A^*. This is especially important to the characterization of junctions with the presence of an ultrathin interfacial insulator, for which the additional contribution from

the tunneling probability through the insulator could be viewed as a modification to the conventional A^* [15].

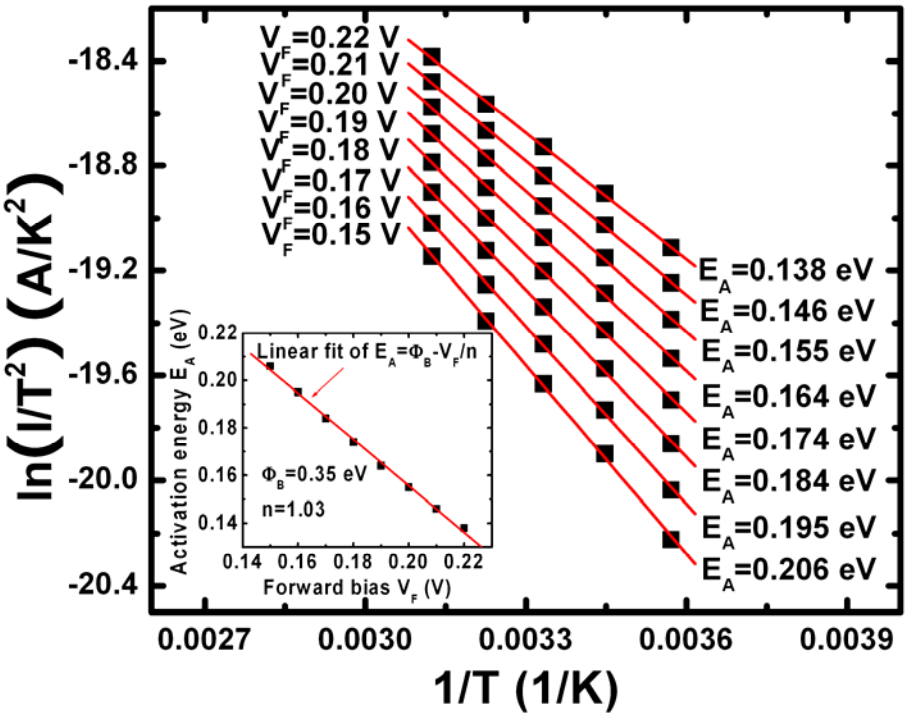

Fig. 11-3, Richardson plots of a Fe/MgO (0.5 nm)/n-Ge diode under different forward biases (0.15 V – 0.22 V). The activation energies (E_A) under each forward bias (V_F) are extracted from the slopes of the linear fits. The inset shows the plot of E_A versus the corresponding V_F, the SBH and ideality factor are extracted from the intercept and slope of the linear fit, respectively.

The SBHs of Fe/MgO/n-Ge with MgO thicknesses of 0.5 nm, 1 nm, 2nm and 3 nm are extracted to be 0.352 eV, 0.35 eV, 0.363 eV and 0.36 eV, respectively, as shown in

fig. 11-4 in solid red squares to the left axis. The corresponding ideality factors are shown to the right axis in open black squares. Both the SBH and *n* are values averaged over many diodes on each sample, with a typical root-mean-square-error less than 3%. Such a uniform distribution of the Schottky characteristics benefits from the homogeneous structure of the junctions. Increasing the MgO thickness causes an increase in n, which is consistent with the fact that the transport deviates from pure thermionic emission with the additional tunneling process [15]. However, the dependence of the SBH on the MgO thickness is negligible, which suggests the interface between MgO and Ge plays the dominant role in the Schottky barrier formation. We believe the large density of the surface states at the Ge surface is reduced by the insertion of MgO, which alleviates the FL pinning.

One argument could be that the MgO thicknesses in this study already exceed the saturation thickness and they would have blocked all the MIGS formation. To further confirm the importance of surface states in FL pinning, we investigate the Schottky characteristics of Fe/n-Ge junctions fabricated on a sulfur passivated Ge surface. Before metal deposition, the same n-Ge substrate is dipped into the aqueous $(NH_4)_2S$ solution (20%) at 80°C for 10 minutes. This treatment is supposed to form a sulfur passivation layer (<3 ML) in which the Ge dangling bonds are saturated by S via bridge-bonding formation [16, 17]. This surface passivation method has been demonstrated to be effective for reducing the interface state density in Ge MOS structures. The presence of S at the Ge surface is confirmed by auger electron spectroscopy as shown in fig. 11-5a. The HRTEM image (fig. 11-5b) shows an abrupt Fe/Ge interface, without appreciable

disorder or intermixing at the interface. Schottky diodes are fabricated and characterized by the same method described above. The depinning effect is found to be more effective than the insertion of MgO, as evidence by the higher reverse leakage current (dotted red in fig. 11-2) and a lower SBH (red star in fig. 11-4) for the sulfur passivated Fe/n-Ge diodes. This result further supports that the surface states due to native defects at the Ge surface, rather than the MIGS, plays the dominant role in the FL pinning.

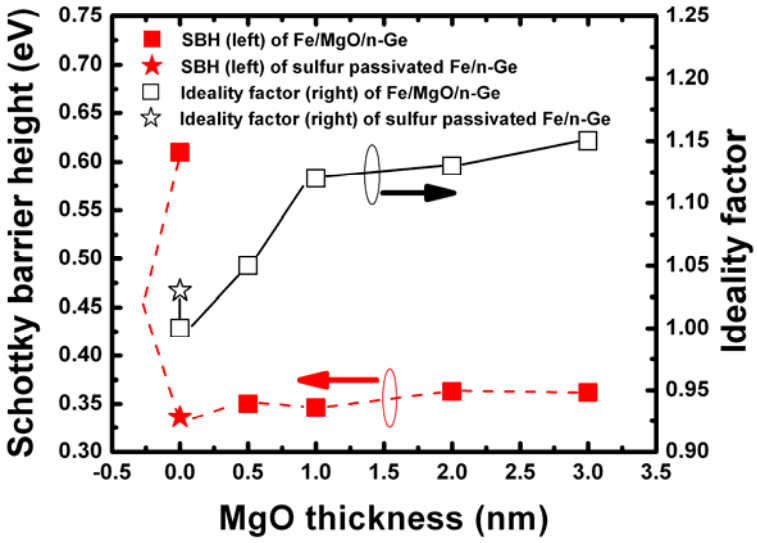

Fig. 11-4, the SBH as a function of the MgO thickness of the Fe/MgO/n-Ge diodes (solid red squares to the left axis). The dependence of SBH on the MgO thickness is rather weak. The red star shows the SBH of Fe/n-Ge formed on sulfur passivated Ge, which has a more effective depinning effect than the insertion of MgO. The black open squares and star show the ideality factors of the corresponding diode to the right axis.

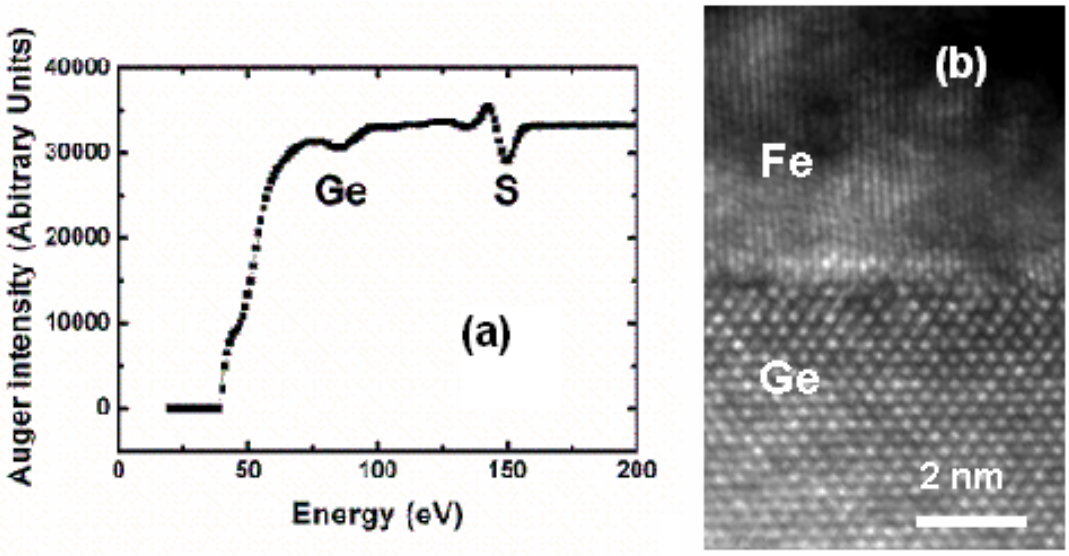

Fig. 11-5, Fe/n-Ge junction with sulfur passivation.

(a) Auger electron spectrum of the sulfur passivated Ge surface, which confirms the S presence. (b) The HRTEM image of the Fe/n-Ge junction with sulfur passivation.

10.4 Conclusion

In summary, we investigated the origin of FL pinning in Ge Schottky junctions by characterizing the Fe/MgO/n-Ge junctions with single-crystalline and atomically smooth MgO epitaxially grown on Ge. The weak dependence of the SBH on the MgO thickness suggests that the surface states due to native defects at Ge surface are likely to play the dominant role in the FL pinning. Sulfur passivation of the Ge dangling bonds by using aqueous $(NH_4)_2S$ solution was shown to be more effective in depinning than insertion of MgO, and this result further supports the dominant role of Ge surface states in FL pinning.

References:

[1] A. Dimoulas, P. Tsipas, A. Sotiropoulos, and E. K. Evangelou, Appl. Phys. Lett. **89**, 252110 (2006).

[2] S. G. Louie, and M. L. Cohen, Phys. Rev. B **13**, 2461 (1976).

[3] V. Heine, Phys. Rev. **138**, A1689 (1965).

[4] T. Nishimura, K. Kita, and A. Toriumi, Appl. Phys. Expr. **1**, 051406 (2008).

[5] M. Kobayashi, A. Kinoshita, K. Saraswat, H.-S. P. Wong, and Y. Nishi, Symposium on VLSI Technology, 54 (2008).

[6] W. Njoroge, T. Lange, H. Weis, B. Kohnen, and M. Wuttig, J. Vac. Sci. Technol. A **18**, 42 (2000).

[7] E. Simoen, K. Opsomer, C. Claeys, K. Maex, C. Detavernier, R. L. V. Meirhaeghe, and P. Clauws, J. Electrochem. Soc. **154**, H857 (2007).

[8] R. T. Tung, J. Vac. Sci. Technol. B **11**, 1546 (1993).

[9] W. E. Spicer, I. Lindau, P. Skeath, C. Y. Su, and P. Chye, Phys. Rev. Lett. **44**, 420 (1980).

[10] W. E. Spicer, P. W. Chye, P. R. Skeath, C. Y. Su, and I. Lindau, J. Vac. Sci. Technol. **16**, 1422 (1979).

[11] R. R. Lieten, S. Degroote, M. Kuijk, and G. Borghs, Appl. Phys. Lett. **92**, 022106 (2008).

[12] K. Ikeda, Y. Yamashita, N. Sugiyama, N. Taoka, and S.-i. Takagi, Appl. Phys. Lett. **88**, 152115 (2006).

[13] W. Han, Y. Zhou, Y. Wang, Y. Li, J. J. I. Wong, K. Pi, A. G. Swartz, K. M. McCreary, F. Xiu, K. L. Wang, J. Zou, and R. K. Kawakami, J. Crystal Growth **312**, 44 (2010).

[14] E. H. Rhoderick, and R. H. William, Metal-Semiconductor Contacts (Oxford, Clarendon, 1988).

[15] S. M. Sze, and K. K. Ng, Physics of Semiconductor Devices, 3rd ed. (Wiley, New Jersey, 2007).

[16] G. W. Anderson, M. C. Hanf, P. R. Norton, Z. H. Lu, and M. J. Graham, Appl. Phys. Lett. **66**, 1123 (1995).

[17] P. F. Lyman, O. Sakata, D. L. Marasco, T.-L. Lee, K. D. Breneman, D. T. Keane, and M. J. Bedzyk, Surface Science **462**, L594 (2000).

Chapter 12.

Electrical spin injection and transport in germanium[1]

Abstract

In this section, I investigate the electrical spin injection, transport and detection in bulk germanium (Ge). The non-local magnetoresistance in n-type Ge is observable up to 225 K. Our results indicate that the spin relaxation rate in the n-type Ge is closely related to the momentum scattering rate, which is consistent with the predicted Elliot-Yafet spin relaxation mechanism for Ge. The bias dependence of the nonlocal magnetoresistance and the spin lifetime in n-type Ge is also investigated. Furthermore, Three- terminal (3T) local method and nonlocal spin transport are compared, and the discrepancy between 3-T and nonlocal four-terminal (4T) spin lifetime shows that the 3-T spin relaxation is easily affected by extrinsic factors.

[1]Published as: Yi Zhou*, Wei Han*, Li-Te Chang, Faxian Xiu, Minsheng Wang, Michael Oehme, Inga A. Fischer, Joerg Schulze, Roland. K. Kawakami, and Kang L. Wang, Phys. Rev. B 84, 125323 (2011).

12.1 Introduction

Information processing based on the electron's spin degree of freedom is envisioned to offer a new paradigm of electronics beyond the conventional charge-based device technologies [1, 2]. Adding spin functionality into semiconductor-based field effect transistors (e.g. spin-FET) [3-5] is considered as one of the approaches to overcome the ultimate scaling limits of the mainstream silicon (Si)-based complementary metal-oxide-semiconductor (CMOS) technology [6]. Electrical injection and transport of spin-polarized electrons from ferromagnetic metals (FMs) into the semiconductors is a prerequisite for developing such an approach [1, 2]. Recently, significant progress has been made in Si [7-10], showing great promise for achieving spintronic devices beyond the CMOS technology. On the other hand, spintronics based on SiGe heterostructures would likely offer more opportunities by taking advantages of the higher carrier mobility, device design flexibility and tunable spin relaxation [11] rendered by the strain engineering, bandgap engineering as well as the quantum confinement effects while maintaining the CMOS compatibility. However, despite the success of Si spintronics, the feasibility of SiGe spintronics remains an open question because Ge is expected to have faster spin relaxation than that of Si due to the larger spin-orbit interaction. Furthermore, electrical spin injection and transport in either Ge or SiGe heterostructures have not yet been clearly demonstrated.

In this chapter, I investigate the electrical spin injection to bulk Ge by using an epitaxially grown Fe/MgO/n-Ge tunnel junction. The observation of Hanle spin precession in the non-local geometry provides unambiguous evidence of spin injection

and transport in Ge. The non-local magnetoresistance (MR) in Ge is observed up to 225 K. Both the non-local MR and the spin lifetime are found to be weakly dependent on temperature at low temperature region ($T < 30$ K). However, the dependence becomes much stronger as the temperature increases. This is attributed to the dominance of spin relaxation by ionized impurity scattering at low temperatures and phonon scattering at higher temperatures. Our results show a close relation between the spin relaxation rate and the momentum relaxation rate, which is consistent with the predicted Elliot-Yafet spin relaxation mechanism for Ge [12, 13]. We also examine the bias dependence of the non-local MR and spin lifetime. The smaller non-local MR under forward biases are attributed to the fast spin relaxation rate in the highly doped Ge surface layer and a possible lower spin injection efficiency due to the unscreened electric field in the semiconductor. Furthermore, we report three-terminal (3T) Hanle measurements and compare the results with the nonlocal four-terminal (4T) measurements. τ_{3T} and τ_{4T} are extracted from 3T and 4T Hanle measurement, respectively. The temperature dependence of spin lifetime are consistent with Sasaki's work at low temperature, $T < 10$K; however, clear discrepancy between τ_{3T} and τ_{4T} shows up at higher temperature, $T > 10$K. This indicates that 3T Hanle measurements are easily affected by extrinsic effects, therefore do not provide an accurate characterization of the intrinsic spin injection. Our results show that Ge is also a promising candidate for spintronics and thus opens up the possibility of using SiGe for spintronic applications.

12.2 Experimental details

An unintentionally doped *n*-type Ge wafer is used as the starting substrate. A lightly doped n^- ($n = 1\times10^{16} cm^{-3}$) Ge layer (300 nm) is grown on this substrate as the spin transport channel. Above this layer is a transition layer (15 nm) to a degenerately doped n^+ ($n = 2\times10^{19} cm^{-3}$) surface layer (15 nm). All these layers are grown by low temperature solid source molecular beam epitaxy [14]. Two devices for the 4T measurement (A and B) are fabricated on this wafer with the same processes. First, a device channel is defined by photolithography and etched by reactive ion etching. The width of the channel is 5 μm and 15 μm for device A and B, respectively. The height of the channel mesa is 60 nm for both devices. Four electrodes are then fabricated on the channel by the standard e-beam lithography and liftoff process. The outer two electrodes are made of Au/Ti. The center two spin-dependent electrodes are made of MgO (1nm) and Fe (100 nm), which are deposited in a molecular beam epitaxy system, and capped by 5 nm Al_2O_3. The as-grown MgO is single crystalline and possessing 45 degree in-plane rotation of the unit cell with respect to that of the Ge [15]. A schematic of the atomic configuration is shown in fig. 12-1a. This high quality Fe/MgO/Ge junction not only alleviates the Fermi level pinning at the Ge surface to favor electronic transport [16], but also leads to an enhanced spin polarization of the injected electrons due to the symmetry induced spin filtering [17]. To characterize the spin injection and transport in Ge, we employ the non-local measurement technique [18-22]. The center-to-center distance (*L*) between the spin injector (E2) and spin detector (E3) is 420 nm and 1 μm for device A and device B, respectively. A schematic diagram of the device structure and

measurement scheme is shown in fig. 12-1b. For 3T devices (device C), the MgO (1nm) and Fe(20nm) films are subsequently grown on Ge and capped by a 20 nm Al layer. Then the electrodes are patterned by photolithography and defined by reactive ion etching and wet chemical etching. Finally, Ti/Au bonding pads are fabricated by electron beam evaporation and lift-off. Silver epoxy is applied to the whole wafer backside for the back contact. The standard low-frequency lock-in technique is used for the measurement.

12.3 Nonlocal (4T) MR measurement

Fig. 12-1c shows a scanning electron microscope (SEM) image of the device A. The widths of the spin injector (E2) and spin detector (E3) are 400 nm and 250 nm, respectively. Temperature dependent *I-V* characteristics measured between the spin injector (E2) and E1 are shown in fig. 12-1d. Since E1 is made of Au/Ti and the size is much larger than E2, we consider the *I-V* characteristics are dominated by the contact resistance of the spin injector (E2). The nonlinearity and weak temperature dependence of the I-V characteristics confirm the tunneling nature of this contact [23], which is necessary to overcome the conductivity mismatch problem for spin injection from FMs to semiconductors [24-26].

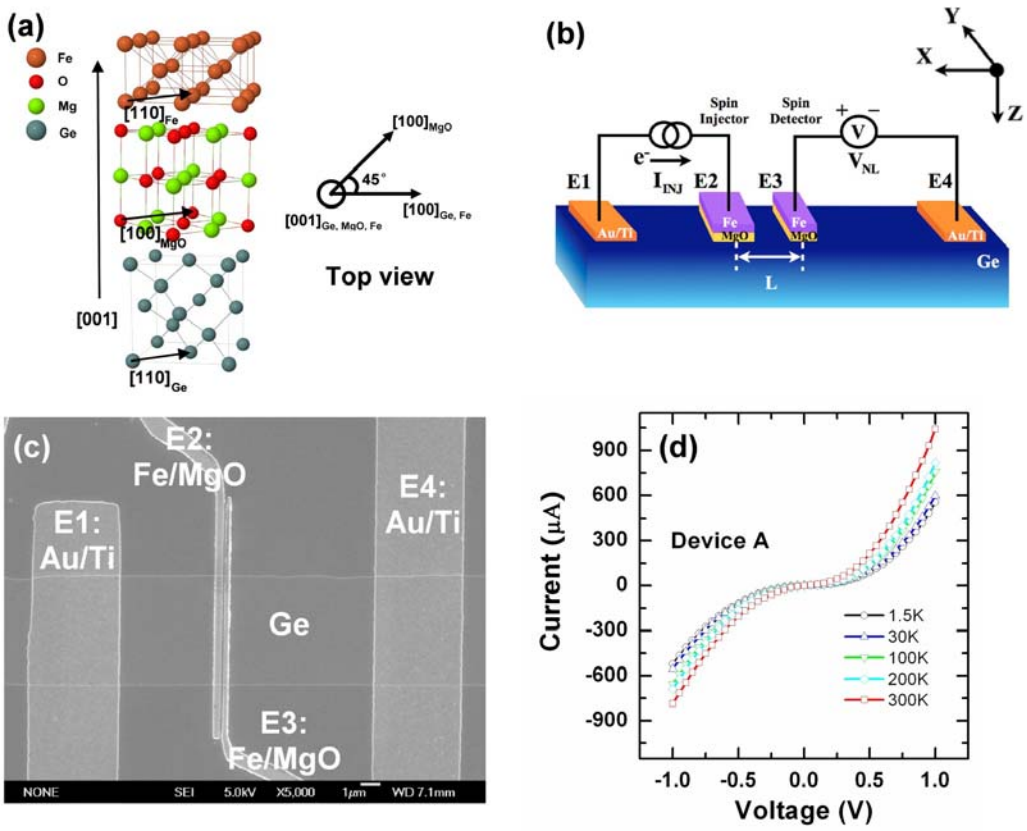

Fig. 12-1, Ge spin valve device with Fe/MgO/Ge tunnel junction.

(a) Schematic atomic configuration of the Fe/MgO/Ge junction, showing 45 degree rotation of the MgO unit cell with respect to that of the Ge. (b) A schematic diagram of the device structure and the non-local measurement scheme. The center-to-center distances between the spin injector and detector are 420 nm and 1 μm for device A and B, respectively. (c) A SEM image of device A. The widths of the injector (E2) and detector (E3) are 400 nm and 250 nm, respectively. (d) Temperature dependent I-V curves measured between spin injector (E2) and E1.

To characterize spin injection and transport in Ge, we first perform the non-local spin valve measurement. In this measurement, a charge current is applied between the spin injector (E2) and E1 (as shown in fig. 12-1b), resulting in a spin accumulation in the Ge at E2 by means of spin injection (E2 under a reverse bias) or spin extraction (E2 under a forward bias) [27, 28]. In either case, once spin accumulation is created, the spin-polarized electrons start to diffuse isotropically in the Ge channel. The spin detector (E3) is placed outside the charge current path, and it detects a voltage potential which is proportional to the projection of the spin accumulation in the Ge onto its magnetization direction. Therefore, if the spin accumulation of the injected electrons is sizeable when they diffuse to E3, a bipolar non-local voltage V_{NL} should be observed which changes sign when the magnetization directions of the spin injector (E2) and detector (E3) switch from parallel to anti-parallel. To modulate the magnetization directions of the spin injector (E2) and detector (E3), an external magnetic field (B_y) along the easy axis of the electrodes (y direction as indicated in fig. 12-1b is swept and the V_{NL} is recorded as a function of B_y. Fig. 12-2a shows the non-local spin valve signal measured on device A at 4K, with a reverse DC bias current (I_{DC}) of -20 μA and AC current (I_{AC}) of 10 μA. The non-local resistance R_{NL} is defined as the V_{NL} divided by I_{AC}. The difference of R_{NL} between the parallel and antiparallel configuration is defined as the non-local MR (ΔR_{NL}) and measured to be 0.94 Ω in this case. The spin injection efficiency of the Fe/MgO/Ge tunnel junction is estimated to be 0.23% using the Equation 1 in Ref 19 with a spin diffusion length $\lambda_{sf} = 0.58\ \mu m$ (calculated from non-local Hanle measurement), Ge conductivity $\sigma = 1\ S \cdot m^{-1}$ (estimated from Ref [29]), cross-sectional area $A = 1.5\ \mu m^2$,

and $L = 420\ nm$. The possible methods for improving the spin injection efficiency include the optimization the MgO film thickness and the Ge surface passivation technique.

Fig. 12-2b shows the non-local spin valve signals measured on device A at different temperatures. The signal is observable up to 225K. Fig. 12-2c summarizes the ΔR_{NL} as a function of the temperature for device A. The ΔR_{NL} is weakly dependent on temperature at low temperature region, which increases slightly from 0.83 Ω at 1.5K to 1.04 Ω at 10K, and then decreases to 0.72 Ω at 30K. However, as the temperature further increases, the ΔR_{NL} drops abruptly and is not observable for T>225 K. Similar temperature dependence of ΔR_{NL} is also observed in device B with a longer transport channel (L = 1 μm, as shown in fig. 12-2d).

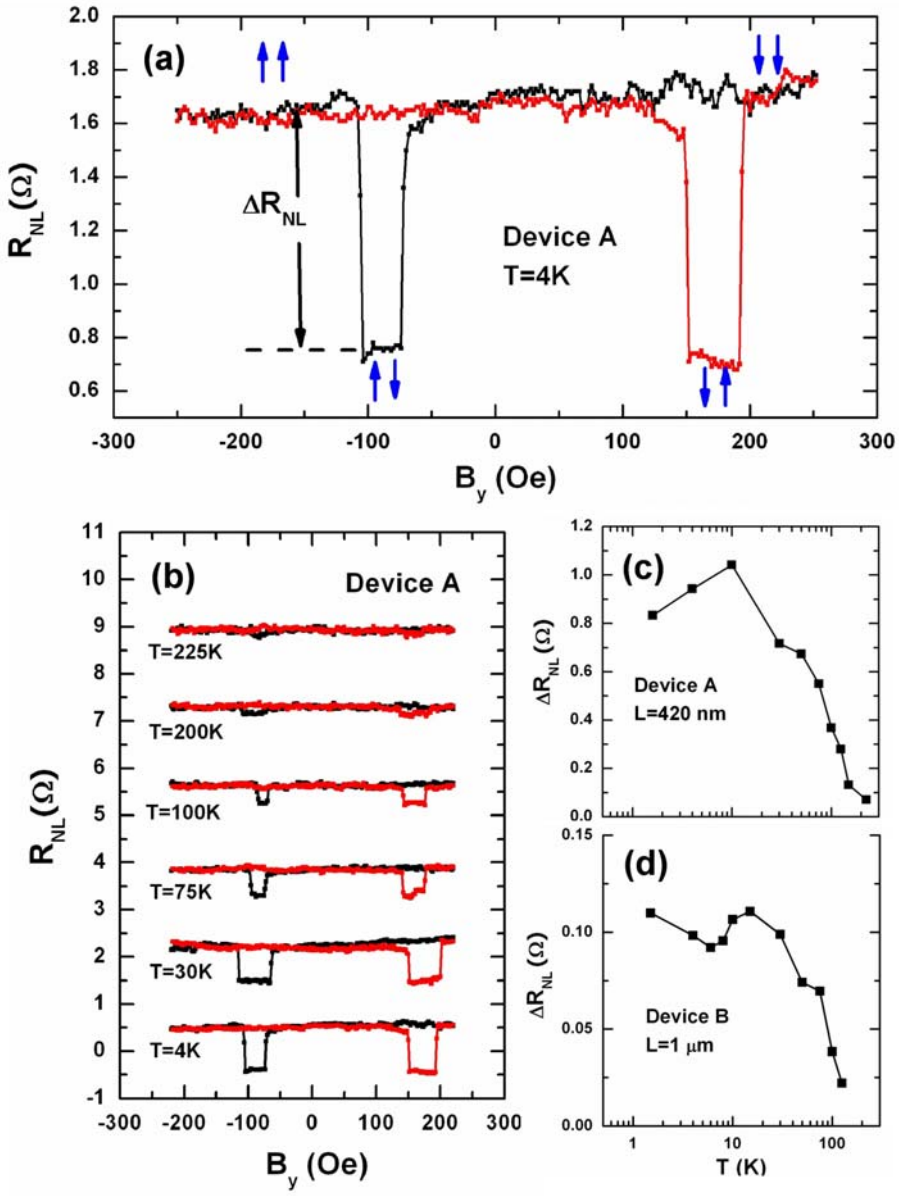

Fig. 12-2, nonlocal MR measurement.

(a) Non-local spin valve signal measured on device A at 4K with a DC injection current of -20 μA and AC injection current of -10 μA. The blue arrows indicate the magnetization directions of the injector and detector. (b) Temperature dependent non-local spin valve signals on device A. The curves are offset for clarity. (c) and (d), Temperature dependent non-local magnetoresistance (ΔR_{NL}) of device A and B, respectively.

To further explore the spin transport properties in Ge, we perform the non-local Hanle measurement. In this measurement, a small transverse (in *z* direction as shown in fig. 12-1b) magnetic field (B_z) is applied to induce the precession of the injected spin by the Hanle effect [21, 30]. The precession and dephasing of the spins during their transport in Ge is manifested as the magnetic field (B_z) dependence of the V_{NL} (or R_{NL}, equivalently). Fig. 12-3a shows the Hanle precession curves of device B at 4K under a reverse bias of -130 μA. The red and black symbols are for signals taken when the injector/detector magnetizations are in parallel and anti-parallel configurations, respectively. A spin lifetime (τ_s) of 1.08 ns is extracted by fitting the Hanle curves based on the 1-D spin drift diffusion model [18, 19, 22], under which

$$R_{NL} \propto \pm\int_0^\infty \frac{1}{\sqrt{4\pi Dt}} \exp[-\frac{L^2}{4Dt}]\cos(\omega_L t)\times\exp(-\frac{t}{\tau_s})dt \qquad (1)$$

In the above equation, + (-) sign is for the parallel (antiparallel) magnetization configuration, D is the diffusion constant, $\omega_L = g\mu_B B_z/\hbar$ is the Larmor frequency (where g=1.6 is the Landé g-factor for Ge [31], μ_B is the Bohr magneton and $\hbar$ is the reduced Planck constant). The temperature dependent spin lifetimes for device A and device B (obtained under reverse biases) are shown in fig. 12-3b in solid circles and open squares, respectively. Similar to the temperature dependence of ΔR_{NL}, the dependence of the spin lifetime on temperature is rather weak at low temperatures, while it becomes much stronger as the temperature increases. This can be explained as in the following. For Ge, which possesses the lattice inversion symmetry, the spin relaxation is predicted to be dominated by the Elliot-Yafet mechanism Ge [12, 13]. Under which the spin

relaxation rate ($1/\tau_s$) is proportional to the momentum relaxation rate. The two major sources of momentum relaxation are the ionized impurity scattering and the phonon scattering. And the temperature dependence of the ionized impurity scattering rate is found to be much weaker than that of the phonon scattering in n-type Ge [29]. It is expected that at low temperature region, ionized impurity is the dominant scattering source, therefore a weak temperature dependence of the spin relaxation rate (or spin lifetime, equivalently) is observed. As the temperature increases, phonon scattering becomes dominant, resulting in a much higher temperature dependence of the spin lifetime. Our results are consistent with the predicted Elliot-Yafet spin relaxation mechanism for Ge.

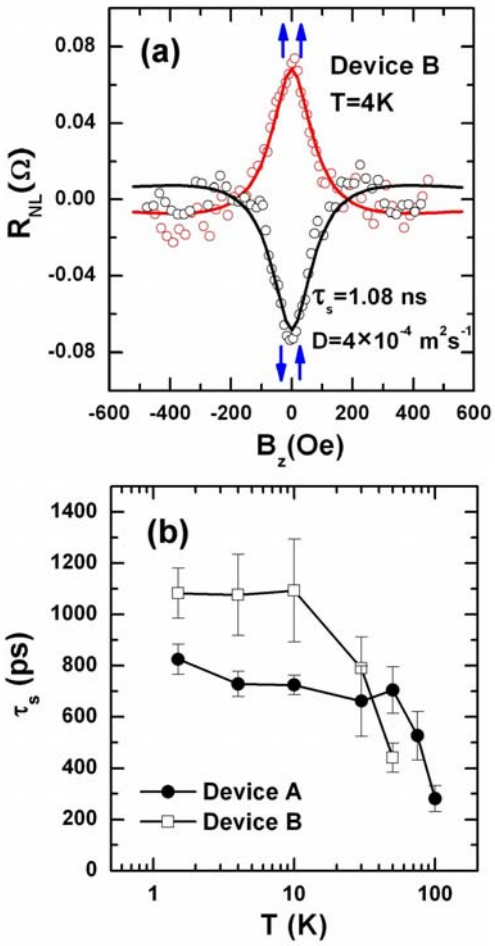

Fig. 12-3, nonlocal Hanle spin recession measurement.

(a) Non-local Hanle precession curves measured on device B at 4K with a DC injection current of -130 μA. The red and black symbols are for signals measured when the injector and detector are in parallel and antiparallel configurations, respectively. The solid lines are fitting based on the 1-D spin drift diffusion model, from which the spin lifetime is extracted to be 1.08 ns. (b) Temperature dependent spin lifetimes measured on device A (solid circles) and B (open squares), respectively.

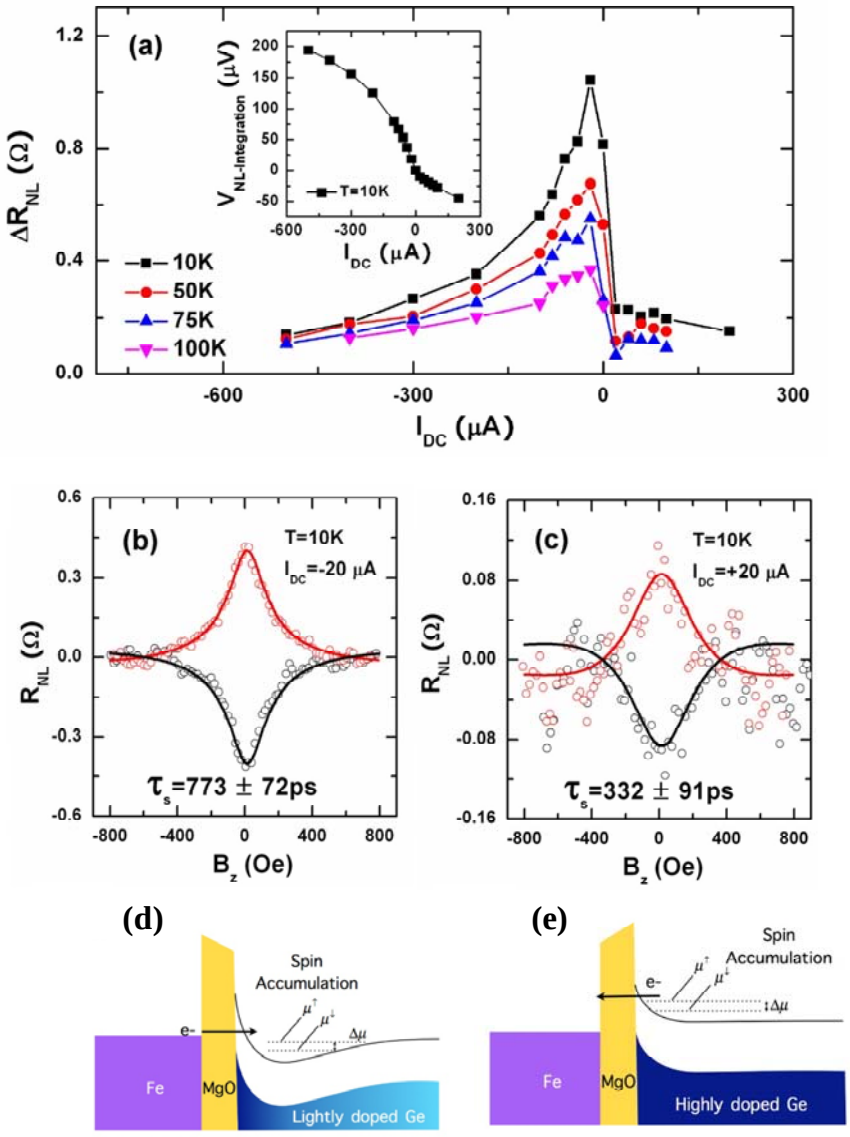

Fig. 12-4, bias dependence of the spin transport in Ge.

(a) The DC bias dependent ΔR_{NL} of device A at different temperatures. The inset shows the restored DC relation between the V_{NL} and I_{DC} at 10K by numerically integrating our V_{NL} over I_{DC}. (b) and (c), Hanle precession curves measured on device A at 10K under a reverse bias of -20 μA and a forward bias of +20 μA, respectively. (d-e) The locations of the spin accumulation under negative/positive bias (spin injection/extraction).

Finally we study the bias dependence of the ΔR_{NL} and the spin lifetime. Fig. 12-4a shows the DC bias dependent ΔR_{NL} of device A at different temperatures. Since we use the lock-in technique, the measured V_{NL} is characteristic of the slope of V_{NL} versus I_{DC} curve from the DC measurement. The inset of fig. 12-4a shows the restored DC relation between the V_{NL} and I_{DC} at 10K by numerically integrating our V_{NL} over I_{DC}. The bias dependence of V_{NL} at reverse bias is consistent with the reported results on the Fe/GaAs system [18]. However, our data do not display the nonmonotonic behavior at forward biases, which was attributed to the localized electrons in the surface bands due to the doping profile in the Fe/GaAs system [32]. It is noted that the ΔR_{NL} is much smaller at forward biases as compared to those at reverse biases. Fig. 12-4b and 12-4c show the Hanle precession curves at 10K with a DC reverse bias of -20 μA and a forward bias of +20 μA, respectively. It is also found that the spin lifetime extracted from forward bias (332 ps) is shorter than that from the reverse bias (773 ps). The bias dependence of the ΔR_{NL} and spin lifetime can be explained by the doping dependent spin relaxation as in the following. When a reverse bias is applied, the depletion region in the Ge extends and spin polarized electrons are injected into the lightly doped Ge channel (inset of fig. 12-4b). However, when a forward bias is applied, the depletion region is reduced and the spin accumulates mainly at the highly doped surface layer (inset of fig. 12-4c), where a faster spin relaxation rate is expected due to the larger momentum scattering by ionized impurities. In addition to the doping dependent spin relaxation, the bias dependence of the ΔR_{NL} could also be due to the following possible effects. First, it could be due to the spin drift effect which arises from the unscreened electric field in the nondegenerate

semiconductors. Since there is no charge current between injector and detector, the spin diffusion length does not change with bias in the direction towards to the detector. However, in the other direction, the spin diffusion length will be highly dependent on the bias current, in which it will be longer when the electric field is along the diffusion direction (downstream), while it will be shorter when the electric field is opposite to the diffusion direction (upstream). The change of the spin diffusion length will have a significant effect on the spin injection efficiency, as explained by Yu and Flatte [33, 34], when the electric field is higher than the critical field (E_c ~15 V/cm) in our case. Second, it could also be due to interfacial tunneling asymmetry of the electrons tunneling out of and into the semiconductors from FM electrodes, in which the spin polarization in lower because of the reduced spin polarization at the hot electron states [35]. Third, the spin-dependent interfacial electronic structure may also lead to a bias dependent ΔR_{NL} [36]. Further theoretical and experimental studies are needed to elucidate the origin of the observed bias dependence of the spin signal.

11.4 Three-terminal (3T) Hanle measurement

We also utilize 3T Hanle measurement, as shown in fig. 12-5a, to probe the spin dynamics in the degenerately doped n^+ Ge. One-dimensional (1-D) lateral spin drift-diffusion model is commonly used to extract the spin dynamics in various systems [18, 19, 37]; the spin polarized electrons are created at the injector location x_1, and their spin polarization is detected after they diffuse and/or drift to a detector location x_2. During this process, the spin loses certain degree of polarization due to spin relaxation and precession

under a transverse magnetic field B (Hanle effect). The steady-state spin polarization $S_x(B)$ of single interface Hanle measurement is given by [37]:

$$S_x(B) = \int_0^L \int_0^L \int_0^\infty \frac{S_0}{\sqrt{4\pi Dt}} e^{-(x_2 - x_1 + v_d t)^2/4Dt - t/\tau_s} \times \cos(\frac{g\mu_B B}{\hbar} t) dt dx_1 dx_2 \qquad (1),$$

where S_0 is the spin creation rate per unit length, D is the diffusion constant, v_d is the drift velocity, τ_s is the spin lifetime, $g = 1.6$ is the g factor for electrons in Ge, μ_B is the Bohr magneton, $\hbar$ is the reduced Planck constant and L is the contact lateral size. The integration yields a peak at zero magnetic field, with a width determined by the time scales of τ_s, L^2/D, L/v_d, and $4D/v_d^2$ [37]. Having D ($1\times10^{-3} m^2 s^{-1}$) calculated from the generalized Einstein relation for degenerate semiconductors with a known mobility value, and using S_0 and τ_s as the fitting parameters, we fit the Hanle spin resistances (See method for definition) of the n^+ Ge at different temperatures based on the above integration (in red), which are shown in fig. 12-5b – 12-5e (device C). Drift transport is neglected since the time scales related to v_d (L/v_d and $4D/v_d^2$) are more than one order of magnitude longer than that of spin diffusion (L^2/D) or spin lifetime (τ_s). For comparison, we also fit the data using a Lorentzian function $\Delta\mu(B) = \Delta\mu(0)/[1+(\omega_L\tau_s)^2]$ (in blue, where $\Delta\mu$ is the spin accumulation and $\omega_L = g\mu_B B/\hbar$ is the Larmor frequency), which is often used to extract the spin lifetime in single interface Hanle measurement [9]. Since the Lorentzian fitting neglects spin diffusion, it is valid only when the contact lateral size is much larger than the spin diffusion length. For $T \geq 15K$, the integration fitting and Lorentzian fitting essentially

yield the same spin lifetime. At lower temperatures (1.5K, 10K), the two fitting yield different values because the spin diffusion lengths (~1μm at 1.5K, ~0.4μm at 10K) become comparable to the contact size (3μm), where the Lorentzian fitting is invalid.

Fig. 12-6 summarizes the temperature dependence of spin lifetime for both geometries. It appears 3T Hanle can measure spin related phenomenon, however when we compare 3T results with 4T, there is a huge discrepancy between τ_{3T} and τ_{4T} at higher temperature (T > 10K). It could be due to the following effects: First, for 3-T device, the active contact is used as spin injector and detector, so the carrier density under spin detector is much higher than that of the 4-T device. When the temperature increases and carrier density is high, collisions between carriers are an important scattering mechanism [38]. Second, 3T Hanle measurement might be affected by the localized states (LS) [39] between MgO/Ge interface, so that the sequential tunneling process through LS must be taken into account, and τ3T is an average of spin lifetime and escape tunneling time. Third, the surface roughness between Fe/MgO interface might induces local magnetostatic field [40]. These inhomogeneous magnetic field make spin precess and reduce the spin polarization near the interface, causing additional broadening of 3T Hanle peaks.

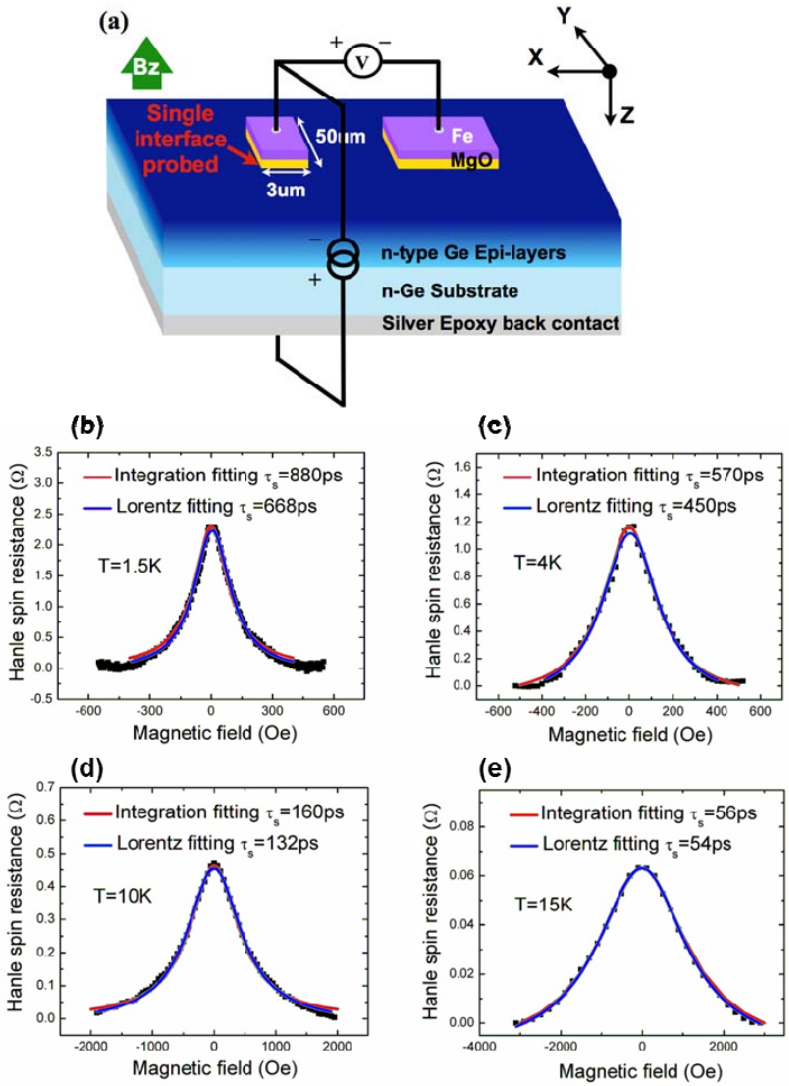

Fig. 12-5, three-terminal Hanle measurement on device C.

(a) Three-terminal device with lateral conduction for detection of spin polarization in the n^+-Ge under a single contact. (b-e) Hanle spin resistancesat 1.5 K, 4 K, 10K and 15K of the n^+ Ge (at DC bias current of 0.5 μA for 1.5 K, ~ 1 μA for 4 K, 1.2 μA for 10 K and 3.2 μA for 15 K). To extract the spin lifetimes, fittings based on the 1-D lateral spin drift-diffusion model (red) and a Lorentzian function (blue) are applied and compared.

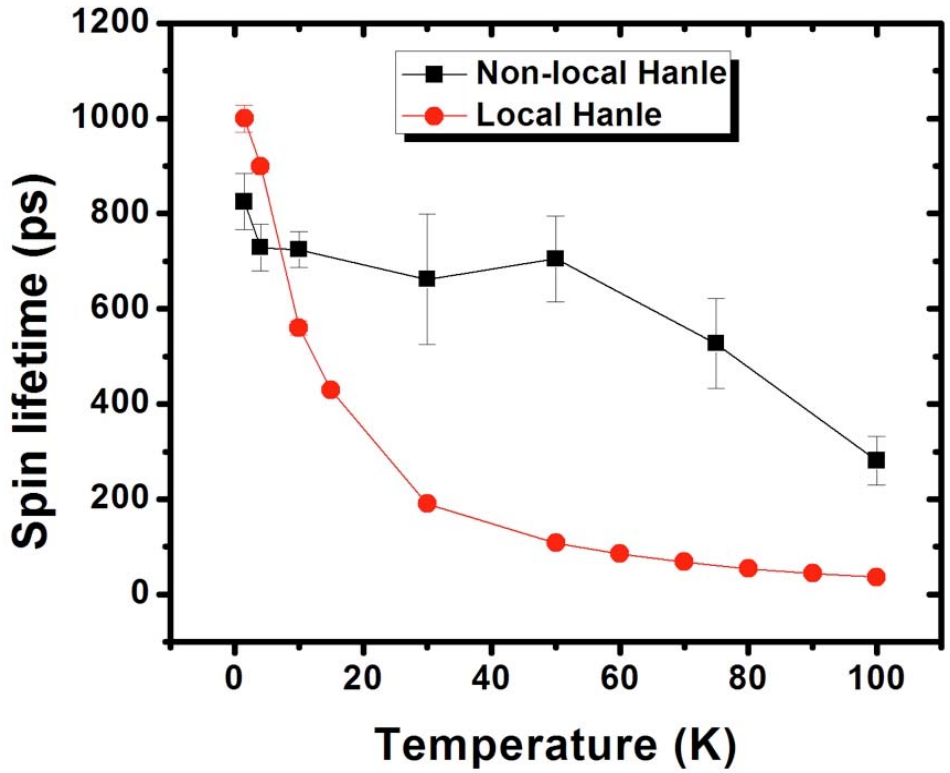

Fig. 12-6, comparison of nonlocal four-terminal and three-terminal spin transport in Ge. Temperature dependence of spin lifetime extracted from non-local Hanle and local Hanle measurements. The spin lifetime of local Hanle measurement is further decreased at higher temperature (>10K) due to enhanced phonon scattering by local electrical field.

11.5 Conclusion

In conclusion, we have successfully achieved electrical spin injection, transport and detection in bulk n-type Ge by using an Fe/MgO/n-Ge tunnel junction. Investigating the temperature and bias dependence of the non-local spin valve signals and the spin lifetimes, we show that the spin relaxation in Ge is consistent with the predicted Elliot-

Yafet mechanism. Our results present a major step towards achieving Ge and SiGe-based Spintronics devices for a new paradigm of non-volatile electronics beyond CMOS technology.

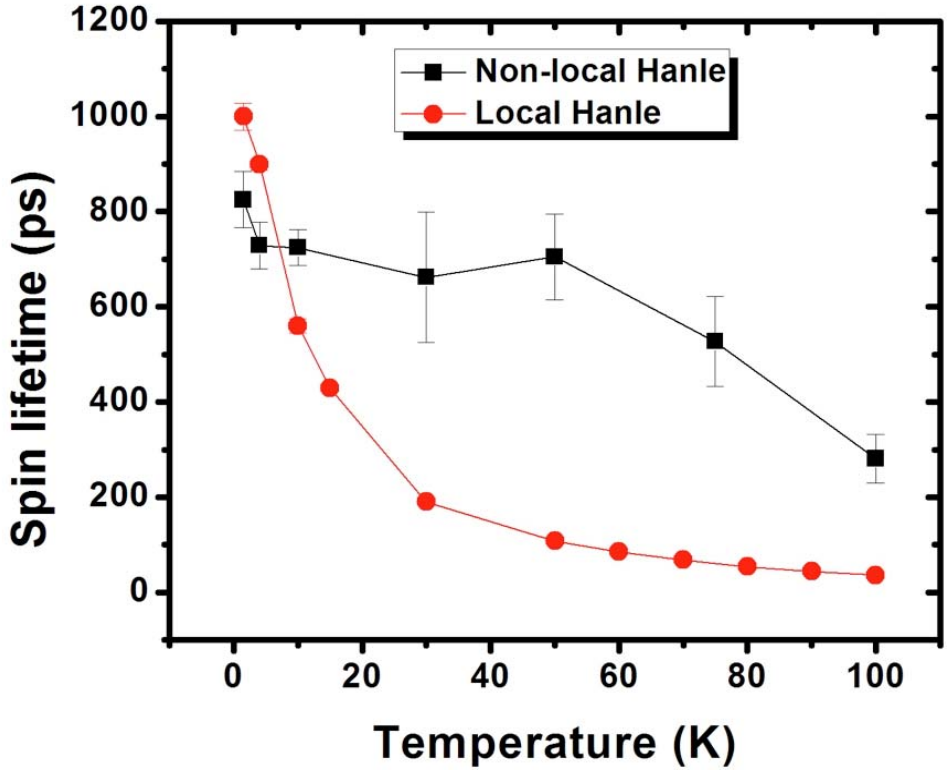

Fig. 12-6, comparison of nonlocal four-terminal and three-terminal spin transport in Ge. Temperature dependence of spin lifetime extracted from non-local Hanle and local Hanle measurements. The spin lifetime of local Hanle measurement is further decreased at higher temperature (>10K) due to enhanced phonon scattering by local electrical field.

References:

[1] S. A. Wolf, D. D. Awschalom, R. A. Buhrman, J. M. Daughton, S. von Molnar, M. L. Roukes, A. Y. Chtchelkanova, and D. M. Treger, Science **294**, 1488 (2001).

[2] I. Zutic, J. Fabian, and S. Das Sarma, Rev. Mod. Phys **76**, 323 (2004).

[3] S. Datta, and B. Das, Appl. Phys. Lett. **56**, 665 (1990).

[4] S. Sugahara, and M. Tanaka, Appl. Phys. Lett. **84**, 2307 (2004).

[5] K. C. Hall, and M. E. Flatté, Appl. Phys. Lett. **88**, 162503 (2006).

[6] International Technology Roadmap for Semiconductors, 2009 Edition, http://www.itrs.net/reports.html. See Emerging Research Devices.

[7] I. Appelbaum, B. Huang, and D. J. Monsma, Nature **447**, 295 (2007).

[8] B. T. Jonker, G. Kioseoglou, A. T. Hanbicki, C. H. Li, and P. E. Thompson, Nature Physics **3**, 542 (2007).

[9] S. P. Dash, S. Sharma, R. S. Patel, M. P. d. Jong, and R. Jansen, Nature **462**, 26 (2009).

[10] T. Suzuki, T. Sasaki, T. Oikawa, M. Shiraishi, Y. Suzuki, and K. Noguchi, Appl. Phys. Expr. **4**, 023003 (2011).

[11] J.-M. Tang, B. T. Collins, and M. E. Flatté, arXiv:1104.0975v1, (2011).

[12] R. J. Elliott, Phys. Review **96**, 266 (1954).

[13] Y. Yafet, in Solid State Physics, edited by F. Seitz and D. Turnbull (Academic Press Inc., New York, 1963), Vol. 14, p. 1.

[14] M. Oehme, J. Werner, and E. Kasper, J. Crystal Growth **310**, 4531 (2008).

[15] W. Han, Y. Zhou, Y. Wang, Y. Li, J. J. I. Wong, K. Pi, A. G. Swartz, K. M. McCreary, F. Xiu, K. L. Wang, J. Zou, and R. K. Kawakami, J. Crystal Growth **312**, 44 (2010).

[16] Y. Zhou, W. Han, Y. Wang, F. Xiu, J. Zou, R. K. Kawakami, and K. L. Wang, Appl. Phys. Lett. **96**, 102103 (2010).

[17] W. H. Butler, X.-G. Zhang, T. C. Schulthess, and J. M. MacLaren, Phys. Rev. B **63**, 054416 (2001).

[18] X. Lou, C. Adelmann, S. A. Crooker, E. S. Garlid, J. Zhang, K. S. M. Reddy, S. D. Flexner, C. J. Palmstrom, and P. A. Crowell, Nature Physics **3**, 197 (2007).

[19] F. J. Jedema, H. B. Heersche, A. T. Filip, J. J. A. Baselmans, and B. J. van Wees, Nature **416**, 713 (2002).

[20] O. van 't Erve, C. Awo-Affouda, A. T. Hanbicki, C. H. Li, P. E. Thompson, and B. T. Jonker, IEEE. Trans. Electron. Device **56**, 2343 (2009).

[21] N. Tombros, C. Jozsa, M. Popinciuc, H. T. Jonkman, and B. J. van Wees, Nature, 571 (2007).

[22] W. Han, K. Pi, K. M. McCreary, Y. Li, J. J. I. Wong, A. G. Swartz, and R. K. Kawakami, Phys. Rev. Lett. **105**, 167202 (2010).

[23] B. J. Jonsson-Akerman, R. Escudero, C. Leighton, S. Kim, and I. K. Schuller, Appl. Phys. Lett. **77**, 1870 (2000).

[24] G. Schmidt, D. Ferrand, L. W. Molenkamp, A. T. Filip, and B. J. van Wees, Phys. Rev. B **62**, 4790(R) (2000).

[25] E. I. Rashba, Phys. Rev. B **62**, 16267(R) (2000).

[26] A. Fert, and H.Jaffres, Phys. Rev. B **64**, 184420 (2001).

[27] C. Ciuti, J. P. McGuire, and L. J. Sham, Applied Phyiscs Letters **81**, 4781 (2002).

[28] J. Stephens, J. Berezovsky, J. P. McGuire, L. J. Sham, A. C. Gossard, and D. D. Awschalom, Phys. Rev. Lett. **93**, 097602 (2004).

[29] P. P. Debye, and E. M. Conwell, Phys. Rev **93**, 693 (1954).

[30] M. Johnson, and R. H. Silsbee, Phys. Rev. Lett. **55**, 1790 (1985).

[31] G. Feher, D. K. Wilson, and E. A. Gere, Phys. Rev. Lett. **3**, 25 (1959).

[32] H. Dery, and L. J. Sham, Phys. Rev. Lett. **98**, 046602 (2007).

[33] Z. G. Yu, and M. E. Flatte, Phys. Rev. B (Rapid Comm.) **66**, 201202 (2002).

[34] Z. G. Yu, and M. E. Flatte, Phys. Rev. B **66**, 235302 (2002).

[35] S. O. Valenzuela, D. J. Monsma, C. M. Marcus, V. Narayanamurti, and M. Tinkham, Phys. Rev. Lett. **94**, 196601 (2005).

[36] A. N. Chantis, K. D. Belashchenko, D. L. Smith, E. Y. Tsymbal, M. v. Schilfgaarde, and R. C. Albers, Phys. Rev. Lett. **99**, 196603 (2007).

[37] X. Lou, C. Adelmann, M. Furis, A. C. S, C. J. Palmstrom, and P. A. Crowell, Phys. Rev. Lett. **96**, 176603 (2006).

[38] M. Lundstrom, Fundamentals of carrier transport 2000, New York: Cambridge University Press.

[39] T. Tran, H. Jaffres, C. Deranlot, J.-M. George, A. Fert, A. Miard, and A. Lemaitre, Phys. Rev. Lett. **102**, 036601 (2009).

[40] S. P. Dash, S. Sharma, J. C. L. Breton, H. Jaffrès, J. Peiro, J.-M. George, A. Lemaître, and R. Jansen, Phys. Rev. B **84**, 054410 (2011).